CORTICAL MECHANISMS UNDERLYING THE EFFECTS OF TRANSCRANIAL MAGNETIC STIMULATION

Ajay Venkateswaran

Doctor of Philosophy

Department of Biomedical Engineering

McGill University

Montreal, Canada

December 2016

A thesis submitted to McGill University in partial fulfillment of the requirements for the degree of Doctor of Philosophy

Table of Contents

ABSTRACT

Transcranial magnetic stimulation (TMS) involves the application of time-pulsed magnetic fields to cortical tissue using a coil located near the head. In the first part of the thesis, we use numerical analysis and finite element modeling (FEM) to investigate the fields induced by TMS in the brain. The field results are compared to electric fields (E-fields) measured in a phantom filled with saline. We used two phantoms, one smaller and the other much larger than the wing-span of the coil. High correlation (0.97) was observed between simulated and measured induced E-fields in the larger phantom. The correlation values for the smaller phantom were low (0.10). We hypothesize that the low correlation achieved in the experiment involving the small phantom was caused because (1) the FEM analysis yields accurate total E-fields (a combination of primary and secondary E-fields) whereas the measurements provide an estimate of only the primary E-fields, and (2) secondary E-fields come into existence when the conducting volume is smaller than the coil span.

FEM simulations were then used to estimate fields induced on the motor cortex due to TMS on realistic human and non-human primate (NHP) head models at resting motor threshold (RMT). Since the RM potential (approximately -70 mV) is similar across mammals, we hypothesized that approximately the same magnitude of induced E-field should allow reaching RMT in human and NHP. Based on the previously reported average RMT intensity in humans (44% of maximum stimulator output (MSO)) and a realistic human head FEM, we estimated the induced E-field on the motor cortex of humans at RMT as 176 V/m. We then used an NHP FEM model to simulate the current needed in order to induce the same electric field on the motor cortex of NHPs. The stimulation intensity required to induce 176 V/m on the NHP motor cortex was 55.4% of MSO. This estimated motor threshold value obtained from simulation was then compared to results obtained in-vivo in NHPs. The measured value of RMT was 51±5.2 % (Mean±SD) of MSO. We hypothesize that the reasonable difference between the simulated and measured RMT is due to inaccuracies in the NHP FEM model.

The second part of the dissertation quantifies the effect of a repetitive TMS (rTMS) continuous theta burst (cTBS) protocol on cortical activity in area S1 of NHPs. Although cTBS suppressed somatosensory evoked potential (SEP) amplitude for an average duration of ~40 minutes, the spatial pattern of the responses remained approximately unchanged. Namely, TMS induced a linear suppressive gain. There was no correlation between changes in SEP amplitudes and spontaneous LFP BLM. These results suggest that cTBS TMS reduces the capacity of cortical neurons to respond synchronously to potent sensory stimuli.

To further test our proposed model of linear gain effect by rTMS, continuous and intermittent theta bursts (iTBS) and 15 Hz conditioning was applied to area 18 of the feline visual cortex. We investigated whether the gain effect of TMS extended to neuronal populations with diverse and selective functional characteristics. cTBS and 15 Hz rTMS suppressed evoked spiking activity response to oriented grating stimuli, whereas iTBS enhanced this response. The spatial pattern and the orientation tuning of the multi-unit activity response remained unaffected. Our findings

demonstrate that rTMS does not modify the functional selectivities of ensembles of neurons; rather, it has a linear gain effect on their responses.

We expect that incorporating simulations for planning subject-specific TMS for equalizing the elicited current density across subjects will reduce the variability of the effects of TMS on human brain activity and behavior. We propose and discuss the advantages of involving numerical analyses such as FEM simulations combined with predictions of the effect of TMS on neuronal activity in experimental studies, and their subsequent implications on future clinical studies.

RÉSUMÉ

La stimulation magnétique transcranienne (SMT) utilise une bobine proximale à la tête afin d'appliquer des champs magnétiques pulsés temporellement au tissu cortical. Dans la première partie de cette thèse, une technique numérique basée sur les éléments finis (EF) est utilisée afin de modéliser les champs induits par la SMT. Les champs obtenus sont ensuite comparés et validés par des mesures de champs électriques dans des fantômes simples en utilisant des électrodes. Deux fantômes de tailles différentes ont été utilisés: un plus petit que l'étendue de la bobine de stimulation et un plus grand. Les résultats montrent une bonne corrélation (0.97) entre les résultats simulés et les mesures dans le fantôme de grande taille. Toutefois, ces corrélations diminuent significativement (0.10) pour le fantôme de petite taille. Pour expliquer ces résultats, nous émettons l'hypothèse dans laquelle : (1) l'analyse par EF permet d'estimer le champ électrique E total (incluant le champ primaire et secondaire) tandis que les mesures n'estiment que le champ primaire, et (2) le champ secondaire est plus apparent lorsque le volume conducteur est plus petit que la taille de la bobine.

Les simulations par EF ont ensuite été utilisées afin d'estimer les champs induits dans le cortex moteur utilisant des modèles anatomiques humains et de primates réalistes sous les conditions de seuil moteur au repos (SMR). Puisque le potentiel membranaire neuronal (environ -70mV) est similaire entre mammifères, l'amplitude du champ électrique généré au niveau du cortex devrait être le même pour atteindre le SM chez les primates et chez les humains. Basé sur les études antérieures chez l'humain déterminant le seuil (44% de la sortie maximale du stimulateur) et une simulation utilisant un modèle anatomique réaliste, nos simulations estiment qu'un champ de 176 V/m est nécessaire pour atteindre le SM. Nous avons ensuite utilisé un modèle anatomique de primate pour prédire l'amplitude du stimulateur nécessaire afin d'atteindre le même champ qui s'est révélée être 55.4% de la sortie maximale. Cette prédiction est ensuite comparée aux données obtenues sur trois primates montrant un seuil de 51±5.2%, une valeur proche de la prédiction étant donné que la segmentation du modèle par EF peut produire des erreurs.

La deuxième partie de cette thèse quantifie l'effet d'une protocole, qui consiste d'une stimulation d'ondes theta sous forme de bouffées, sur le cortex moteur de primates. Quoique la stimulation continue ait pour effet de diminuer l'amplitude des potentiels évoqués pour une période de 40 minutes, la distribution spatiale de la réponse est restée inchangée. Spécifiquement, la stimulation a induit un effet de gain suppressive linéaire. Ces résultats sont consistants avec un modèle suggérant que la SMT module la réponse en modifiant l'excitabilité corticale.

Afin de valider ce modèle, des stimulations continue et intermittente d'ondes theta de même qu'une stimulation répétitive à 15Hz ont été faites sur un modèle félin dans la zone 18 du cortex visuel afin d'évaluer si l'observation faite précédemment se généralisait. La stimulation theta sous forme de bouffées et la stimulation continue à 15Hz menaient toutes les deux à une diminution de la réponse à un stimulus visuel sous forme de grille tandis que la stimulation intermittente ne menait pas à une telle diminution. L'effet de suppression était aussi plus fort sur les neurones qui répondaient plus fortement aux stimuli avant l'application de la SMT. Toutefois, l'étiologie de la réponse, i.e. étendue spatiale, sélectivité, est restée sensiblement la même. Ces résultats montrent

que la SMT répétée ne mène pas à une modification de la fonction neuronale, elle agit plutôt sur l'amplitude de la réponse.
L'intégration de simulations spécifiques à un sujet à la planification de traitement pourrait permettre d'uniformiser l'effet de la SMT et contribuer à une diminution de la variance dans les études humaines.

ACKNOWLEDGEMENTS

First and foremost, I would like to thank my doctoral program supervisor, Dr. Amir Shmuel, for his able guidance and support in the completion of this journey. I could not have asked for a better person to be my supervisor. Through all the ups and downs during the course of the past six years, he stood by me and was always prepared to lend out a helping hand, even during his times of tragic personal loss. I will never forget it. I would also like to thank my co-supervisor, Dr. Frederic Lesage, for his immense help, critical insight and support in the successful completion of this dissertation. Both gentlemen made my learning process through this program immensely productive by providing me with sound advice, a wealth of knowledge and most importantly, their invaluable time as and when I needed it. I would also like to thank my PhD committee members for supervision and support.

I would also like to thank my family, whose constant support and encouragement formed the backbone of my work ethic.

Words cannot begin to describe what I owe to my parents, Mrs. Rajeshwari Venkateswaran and Mr. P.N. Venkateswaran, who inspire me every day with unbounded love and faith. I have so much to learn from you. Thank you, for being you and for being my parents. This work involves as much of your blood, sweat, tears and prayers, as it does mine. To you, I dedicate this thesis.

PREFACE

This dissertation is ultimately based on the experimental apparatus and data pertaining to transcranial magnetic stimulation (TMS) approved by McGill's ethics committee. None of the contributions of the dissertation is taken directly from previously published or collaborative articles. This dissertation shows the relevance of numerical simulations to experimental work. It also addresses the difficulties and impediments one may when implementing solutions obtained from simulations in in-vivo research. It also shows how TMS affects a large population of neurons with similar and discrete functional characteristics.

Original contributions

Contribution of this doctoral dissertation to the field of transcranial magnetic stimulation has been provided in relevant sections of each chapter. Here we present a summary of the significant points:

Chapter 3 is the first to validate and calibrate simulations of current density induced by TMS. The validation and calibration were carried out over a large volume of interest with a high resolution of observation points in order to enable us to quantify our claims better.

In Chapter 4, finite element model (FEM) simulations on realistic non-human primate (NHP) head models, pertaining to TMS, has been demonstrated for the first time. This is also the first time that the magnitude and spatial distribution of induced electric field (E-field) on the motor cortex of humans, at specifically resting motor threshold (RMT) TMS intensity, has been reported. The ease and speed of these simulations has been highlighted. Fast simulations to yield approximate induction values have also been demonstrated. The key aspect which made the simulations more conducive to faster analysis was the design of a simpler single loop coil model. The single loop model not only reduced computational nodes in the simulation (thereby making the simulations faster),

but it also did not compromise the accuracy of the induced E-fields, compared to the E-fields induced using realistic coils. Based on such FEM simulations and data available on % MSO required for reaching RMT in human subjects, we estimated the E-field required for that purpose. Since resting membrane potential (RMP) is approximately constant across mammals, we hypothesized that the E-field required for reaching RMT in humans and primates should be similar. We tested this hypothesis by measuring RMT and simulating the E-field required for reaching RMT in primates. It is a novel approach with regard to TMS studies and has been presented for the first time.

In Chapters 5 and 6, the effect of different TMS protocols on global response pattern, using neurophysiology from a large region of interest, has been demonstrated for the first time, first over a population of neurons that have similar response properties (somatosensory cortex of NHPs) and then over a population of neurons having distinct response properties (orientation selective neurons in the visual cortex of felines). Although information exists in the literature about the effect of different TMS protocols on neuronal responses, the effect of TMS on a relatively large cortical area, the neuronal populations of which encompass varied functionality, has not been studied so far. We are the first to show that in the effective region of ~13 mm^2 the performance of all the neurons is affected by a gain effect to the same extent, without any change or disruption in their actual functional selectivity.

In Chapter 5, the effect of continuous theta burst (cTBS) TMS paradigm on the primary somatosensory cortex on NHPs was demonstrated for the first time. In addition, we show that cortical processing over a large area of the cortex is affected to the same extent by cTBS.

In Chapter 6, the effect of continuous theta burst (cTBS), intermittent theta burst (iTBS) and 15 Hz repetitive transcranial magnetic stimulation (rTMS) paradigm on cat visual cortex was

demonstrated for the first time. We show that the effect of TMS paradigms over a large region of neuronal populations remains the same, even if the region of interest consists of neuronal populations with distinct functional selectivity. In other words, the effect of cTBS, iTBS and 15 Hz TMS can be modeled as a linear gain effect.

Author contributions

Validation and calibration of TMS fields in Chapter 1:

I wrote the introduction and Dr. Shmuel edited it.

Background of TMS in Chapter 2:

I wrote the literature review and Dr. Shmuel edited it.

Validation and calibration of TMS fields in Chapter 3:

Dr. Amir Shmuel and Dr. Frederic Lesage initiated the study. The project was designed by Dr. Shmuel, Dr. Lesage and me. The experimental and system setup, testing and data collection was done primarily by me. Part of the data was collected by Mr. Niladri Mohanty. The analyses on the data were done by me and reviewed by Drs. Shmuel and Lesage. Mr. Mirza Abdel Baig had created a LabView platform to trigger TMS pulses in synchrony with neurophysiological recordings, which was modified by me to suit my experiment and to synchronize three different modules (Neuralynx Digital Lynx SX data acquisition system (DAQ), Labview and Magstim TMS stimulator module). The chapter was written by me and reviewed by Drs. Shmuel and Lesage.

Simulation of TMS fields on head geometries in Chapter 4:

The project was designed by Dr. Shmuel and me. Dr. Shmuel provided the MRI data of the NHPs whereas the MRI for humans was obtained from the website of the Brain Imaging Centre (http://www.bic.mni.mcgill.ca/ServicesAtlases/ICBM152NLin6) of the Montreal Neurological Institute. All the object creation, data processing and simulations were performed by me.

Effect of TMS on the somatosensory cortices of NHPs in Chapter 5:

Dr. Amir Shmuel initiated and designed the project. Mr. Mirza Abdel Baig had created a LabView platform to trigger TMS pulses in synchrony with neurophysiological recordings. Dr. Thomas and I were responsible for data collection. Conversion of the neuronal data (acquired on a Tucker-Davis Technologies' (TDT) data acquisition system) to a format compatible with MATLAB was performed by Dr. Thomas. All subsequent analyses on the data were done by me and reviewed by Dr. Shmuel. The chapter was written by me and reviewed by Dr. Shmuel.

Effect of TMS on the visual cortices of felines in Chapter 6:

Dr. Amir Shmuel initiated and designed the study. The experimental and system setup as well as testing of equipment involved was done by me and Mr. Sujay Neupane. Surgeries were performed by Mr. Ze Shan Yao and array implantation was done by me. Data were collected and analyzed by myself. Mr. Sujay Neupane wrote part of the analysis code. The data analysis was reviewed by Dr. Shmuel. The chapter was written by me and reviewed by Dr. Shmuel.

Summary and conclusions in Chapter 7:

I summarized the dissertation contents and wrote out the salient observations and potential work that can be done in the future. Dr. Shmuel edited it.

List of Figures

List of Tables

List of Acronyms

AMT	Active motor threshold
BLM	Band limited magnitude
CSF	Cerebro-spinal fluid
cTBS	Continuous theta burst
CV	Circular variance
DAQ	Data acquisition system
EEG	Electroencephalogram
E-field	Electric field
EM	Electro magnetic
FEM/FEA	Finite element model/ Finite element analysis
FFT	Fast Fourier transform
FOE	Figure-of-eight
FR	Firing rate
FWHM	Full width at half maximum
GM	Gray matter
HWHM	Half width at half maximum
iTBS	Intermittent theta burst
MC	Magnetic coil
MEA	Multi electrode array
MEP	Motor evoked potential

MSO	Maximum stimulator output
MT	Motor threshold
MUA	multi-unit activity
NHP	Non-human primate
RMT	Resting motor threshold
ROI	Region of interest
rTMS	Repetitive transcranial magnetic stimulation
SEP	Somatosensory evoked potential
TBS	Theta burst
tDCS	Transcranial direct current stimulation
TES	Transcranial electric stimulation
TMS	Transcranial magnetic stimulation
VEP	Visual evoked potential
WM	White matter

List of Units

Quantity	Name	Symbol
Current	Ampere	A
Temperature	Degree Centigrade	^{o}C
Capacitance	Farad	F
Inductance	Henry	H
Resistance	Ohm	Ω
Time	Second	s
Frequency	Hertz	Hz
Energy	Joule	J
Power	Watt	W
Distance	Meter	m
Potential Difference	Volt	V
Magnetic Field Strength	Tesla	T

Note : All vector notations are in bold font-type and scalar notations are in non-bold font-type.

Chapter 1 Introduction

Electricity and physiology have shared a long communion and have seen a plethora of techniques trying to consummate this marriage. From Scribonius Largus' pioneering technique of treating pain related to headaches and gout using electric pulses delivered by a torpedo fish (a species belonging to the family of electric rays) to the affected area ; through the demonstration, bordering on genius and macabre, of bringing back dead cadavers to life by Giovanni Aldini; to the current modern day techniques of magnetic field stimulation, non-invasive stimulation has been through a gamut of transitions (Pascual-Leone and Wagner, 2007).

Non-invasive brain stimulation involves generation of an electric field in the cortex and changing the potential outside neuronal membranes. This results in disruption of the transmembrane ionic equilibrium. The brain is a vast and complex network consisting of numerous cell bodies (glial cells, neurons interneurons, astrocytes, vessels, etc.). Every feature of the generated current, for example, whether it is time varying or constant amplitude, what is the orientation of the electric fields, what is the duration of time for which the fields exist, what is the intensity or magnitude of the electric fields etc., has a bearing on not only the cortical entity that will be influenced by it, but also how that cortical entity will be influenced by the particular feature of the induced current. For example, if the intensity of the induced current is not sufficient, it will not create a sufficient concentration of ions in the extracellular fluid around a neuron to disrupt the established equilibrium membrane potential. Thus, an action potential will not be generated. Similarly, if the orientation of the induced currents is such that it does not influence a disturbance in the equilibrium membrane potential of a neuron, an action potential will not be generated.

1.1 Motivations and Objectives

Transcranial magnetic stimulation (TMS) generates a time varying current in the brain resulting from a time varying current in a coil placed in close proximity, based on Faraday's law of electro-magnetic induction. TMS studies have been predominantly categorized into numerical studies and neurophysiological/behavioral studies. Numerical studies are mostly associated with aspects pertaining to the stimulating coil and the profile of currents the coils induced in the brain. Experimental studies have been conducted primarily to understand neuronal behavior in response to currents induced by TMS. However, a substantial study incorporating the strengths of these two domains together has eluded scientists primarily due to the lack of generic method that could link them together, thereby enabling quantification of the effects of TMS. A few studies have tried to bridge this gap but even in a rudimentary stage, the problems posed by the inability to record high amplitude currents induced by TMS in conjunction with relatively extremely low amplitude neuronal responses, are quite apparent. Our objective was to validate simulated induced current density with the induced currents measured using a standard neurophysiology system, in order to establish confidence in the simulated results. With that done, future work could incorporate simulations directly in their experiment plans, relying on the knowledge that the simulation results would give an accurate description of the currents that would be induced in the cortex during the subsequent experiment. Once this objective is achieved, we could focus on demonstrating an actual TMS experiment in conjunction with simulation. Current literature available with regard to TMS has numerous reports of contradictory effects of TMS on neuronal processing. For instance, when

cTBS is used to condition the left primary somatosensory cortex (S1) in humans, it was reported to result in a decrease in somatosensory evoked potential amplitude of S1 (Ishikawa et al., 2007). When the same experiment was repeated by another group, cTBS was reported to not have any influence on the SEP amplitude (Katayama et al., 2010). What causes such discrepancy? Due to the potential therapeutic applications of this non-invasive technique, interests in TMS related studies have been on the rise and because of this reason, several TMS protocols have been proposed, with the goal to increase the duration of the effects of TMS. More number of TMS pulses result in longer duration of effects. But with more number of pulses come problems of coil overheating, patient discomfort and in extreme cases, induction of epileptic seizures. We would like to study the effect of established high frequency TMS protocols on a large population of neurons to try and understand the underlying mechanisms of the effects of those TMS protocols.

1.2 Methodology

The current dissertation aims at achieving the following goals

i. *Decrease the complexity of numerical simulations of induced E-field by TMS, so that they can be seamlessly incorporated in experimental studies. Validate the simulations in a simple medium.*

   Simulation studies using finite elements proceed by discretizing space into a finite number of elements where the underlying physical variables of interest reside. Defining the field equations and their boundary conditions on these elements, followed by formulation of the system of equations (using Ritz method or Galerkin method of weighted residuals) will yield a linear system of equations of the form $[A] = \lambda[B]$ that can be solved iteratively.

For a given domain, a careful analysis of discretization errors is required to not compromise the validity of the numerical solution. Measurements with probes conducted on simpler geometries make it possible to test the degree of similarity between simulated and measured results.

ii. Realistic head model and phantom model simulations involving TMS

Simulations involving analytical calculations of induced fields provide a wealth of information that can be used to improve TMS based experiments and hence make the experiments more robust. We intend to demonstrate how finite element based TMS simulations can aid experimenters in making more conclusive derivations from their acquired data. The basis of this exercise lies on the rudimentary but critical definition of the threshold value of the conditioning TMS stimulation intensity. Our objective is to be able to predict the threshold values correctly from simulations and then define our stimulation intensities based on the calculated threshold values. The motivation behind this approach comes from the knowledge that threshold values cannot necessarily be calculated in every scenario. For example, how to calculate motor threshold on a paralyzed cat? Or how to calculate phosphene threshold of the visual cortex of an animal? It would therefore be more convenient to have one parameter that can be used to quantify different kinds of thresholds. This quantization parameter would be the electric field profile and magnitude induced on human cortex at threshold intensities. Once the E-field that elicits threshold values for the animals are defined, the conditioning stimulation intensities that will be used in in-vivo experiments, targeted in the following section, could be quantified. The final goal is to become confident about the use of simulations in experimental studies, by using them in phantom and animal studies, so that the practice can be extended to be used

seamlessly during human experiment studies, which would elucidate safety parameters and quality of data collected from human subjects.

iii. *Study the effect of a well-known TMS paradigm on the functional characteristics of large population of neurons over a large cortical region of interest.*

The goal of this study would be to use the knowledge of simulated current densities in experiment protocols involving in-vivo neurophysiology to determine the effect of the induced currents in neuronal populations over a large region of interest. Since TMS induces current over a large area of the cortex, such a study would help us in understanding how a population of neurons with different performance indices (such as orientation selectivity, state-dependency, etc.), in a relatively larger area of interest than the area encompassed by single electrodes used in acute experiments, are affected by the TMS. This goal consists of two parts:

(a) Study the effect of a selected TMS paradigm on the region of the cortex consisting of neuronal populations with similar functional characteristics

(b) Study the effect of selected TMS paradigms on the region of the cortex consisting of neuronal populations with diverse and selective functional characteristics

1.3 Thesis organization

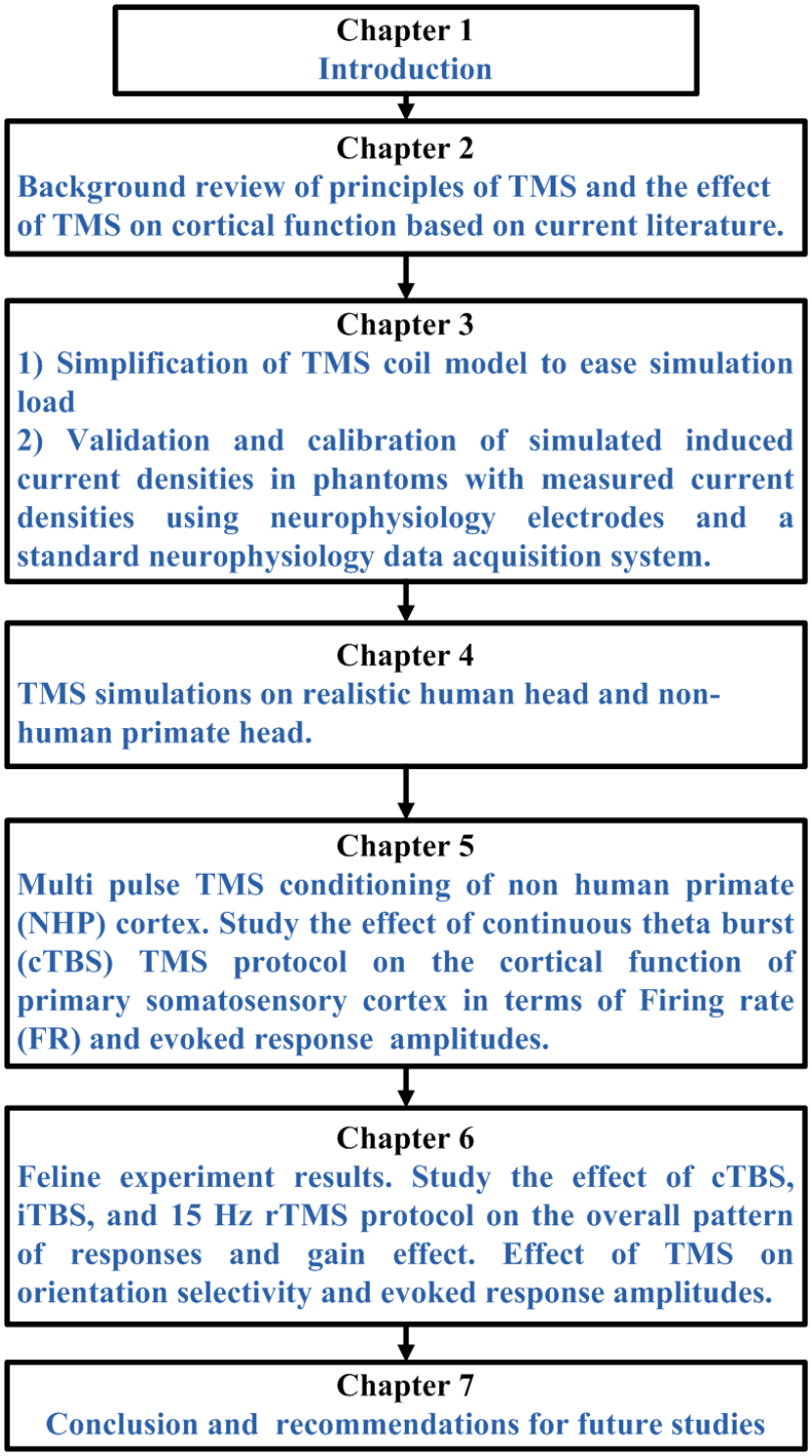

Figure 1-1. Dissertation outline.

Chapter 2 Background

2.1 Evolution of transcranial magnetic stimulation (TMS)

Since the first successful demonstration of non-invasive neuronal stimulation using magnetic fields (Barker et al., 1985a; Barker et al., 1985b), transcranial magnetic stimulation has been the preferred mode of neuronal/neural stimulation compared to not just invasive stimulation methods but other non-invasive stimulation methods too (e.g. transcranial electric stimulation and transcranial direct current stimulation). Transcranial electric stimulation (TES) involves the application of high intensity current pulses to the cortex via electrodes placed on the scalp. It has the distinct disadvantage that the application of such high intensity current (to enable the current to pass through the almost non-conductive skull barrier) results in patient discomfort due to pain. TMS scores over TES in that it does not transmit energy directly to the cortex in the form of electric current, but in the form of magnetic fields which face little or no attenuation at the skull barrier. Other painless variants of TES have come into existence over the years. These include transcranial direct current stimulation (tDCS), transcranial alternating current stimulation (tACS) and transcranial random noise stimulation (tRNS). However, the above mentioned stimulation methods need to be administered for long periods of time (20-30 minutes for tDCS), compared to TMS (40 s continuous theta burst protocol), for significant effects. tDCS, for instance, has been shown to have almost no effect on other neurophysiological measures apart from motor evoked potentials (Horvath et al., 2015). Motor evoked potentials (MEPs), as demonstrated by Merton and Morton

(1980), are electrical signals recorded from neural tissue or muscle following activation of motor cortex using electrical stimulation. The activation of the motor cortex can also be achieved magnetically using transcranial magnetic stimulation. The most common method of recording MEPs is by recording twitch of the active muscles by the use of surface electrodes placed over the active muscles. Until better protocols and experiment designs are introduced, understanding the underlying mechanisms of new methods to improve their efficiency faces a stiff challenge. In the meanwhile, TMS continues to push the boundaries of duration of effects of non-invasive stimulation.

2.2 Operation of a TMS stimulator

A commercial magnetic stimulator consists of five major components (Pascual-Leone, 2002)

1. The charging unit
2. The energy storage unit
3. The discharge circuit
4. The stimulating coil
5. The control unit

Figure 2-1 shows a Magstim Rapid TMS stimulator (Magstim, Whitland-Dyfed, UK with its major components labeled accordingly. The charging wires and their corresponding booster modules, together, make up the charging and energy storage unit. The main unit forms the discharge circuit while the figure-of-eight coil is the stimulating coil. The computer console is the digital control unit.

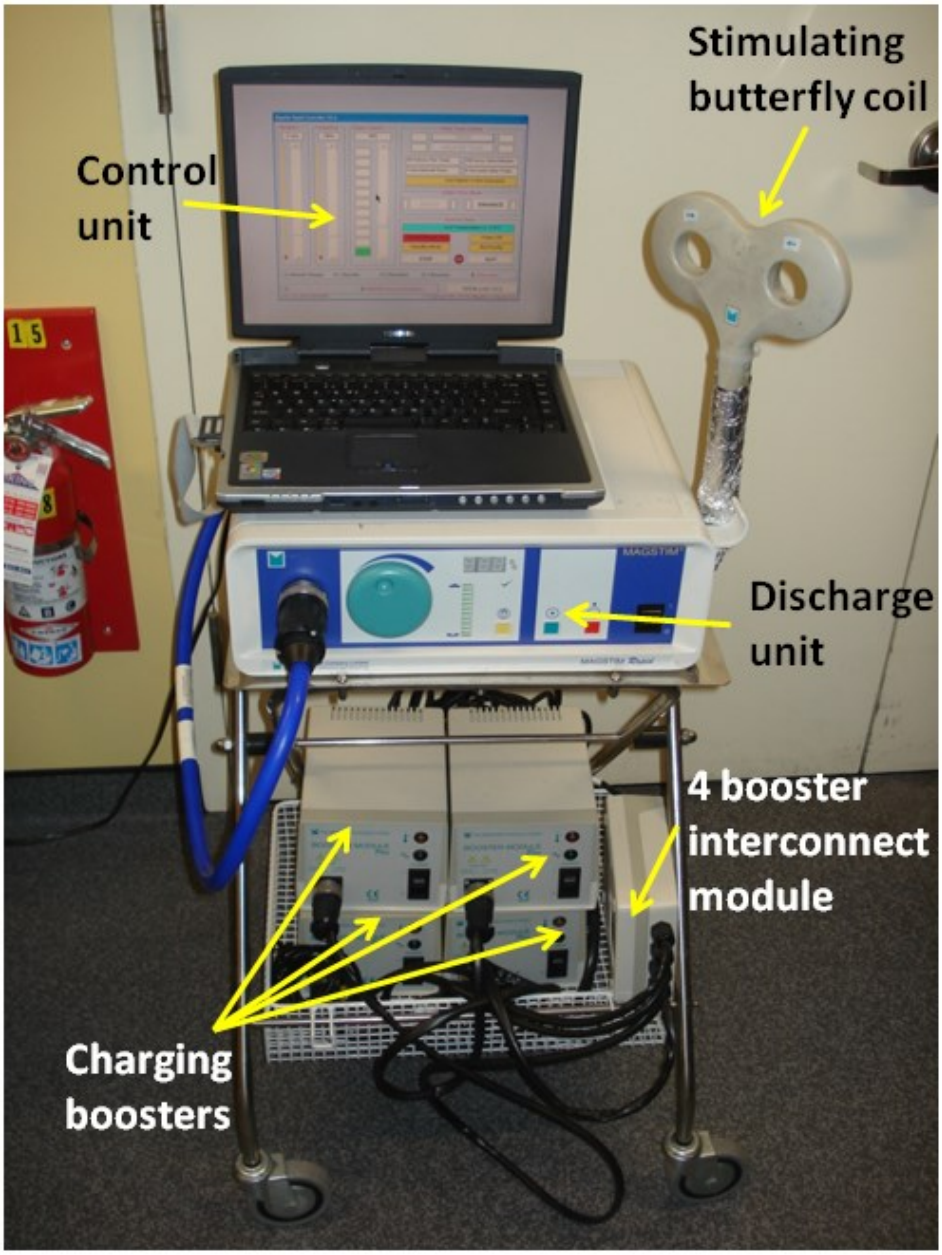

Figure 2-1. TMS equipment with labels showing the different parts of a TMS stimulator.

The TMS stimulator is an important device component in any TMS study and therefore, it is beneficial to understand the electronic principles underlying the operation of a TMS module. In addition to providing us knowledge about the operational modes of the TMS equipment, the investigation will also be able to shed light on the relevant signals at play during TMS stimulation

and the properties of these signals. Hence, the following segment deals with the mode of operation of a TMS circuit that lead to the final current discharge through a coil to produce the all-important magnetic field.

Circuit model of TMS stimulator

TMS pulse waveforms can be broadly categorized into four basic types: monophasic, biphasic, polyphasic, half sine and full sine (Pascual-Leone, 2002). The biphasic simulator is better than a monophosic stimulator due to its superior recharge rate, thereby making it conducive to deliver high frequency repetitive transcranial magnetic stimulation (rTMS) protocols. After being discharged, leading to the generation of a TMS pulse, the faster the storage capacitor of the TMS module gets recharged to it maximum energy storage capacity, the faster it will be able to deliver the following TMS pulse after the preceding TMS pulse. The biphasic simulator is also better than polyphasic stimulator in terms of comparatively less heat generation from energy dissipation. Each TMS pulse delivery results in the generation of certain amount energy in the form of heat (in addition to sound, observed in the form of a "click"). If sufficient time is not allowed between subsequent pulses, as is the case of rTMS protocols, the generated heat is not allowed to effectively dissipate to the surrounding air. This results in continuous increase in the temperature of the TMS stimulating coil. TMS modules are equipped with a threshold temperature lock mechanism, to protect against coil overheating. When the temperature of the stimulating coil reaches the factory-set threshold temperature value (40 °C), the protection circuits disable the equipment and TMS delivery stops. A biphasic stimulator, resulting in less heat dissipation per pulse of TMS compared to a polyphasic stimulator, allows more TMS pulses to be delivered, before the temperature of the stimulating coil reaches the threshold temperature value of the TMS module. The Magstim Rapid

stimulator intended for our studies generates a biphasic TMS pulse. The mode of operation of an equivalent circuit model of the TMS equipment that produces such a pulse is elucidated by Katayama and Iramina (2009). The equivalent circuit model of TMS equipment is shown in Figure 2-2 (a). The first mode of operation of a TMS module is called the charge mode in which switch SW1 closes thereby allowing the voltage source DC to charge the capacitor C. When the capacitor C is fully charged, switch SW1 opens and SW2 closes which results in the discharge of the stored capacitive energy within the rL circuit. This mode is called the oscillation mode and results in a decaying polyphasic curve. If the timing of the oscillatory mode is controlled in such a way (by controlling the time for which switch SW2 remains open), one can obtain one cycle of a decaying sinusoid or, as we know it, a biphasic stimulating current curve. The oscillatory mode is the TMS delivery mode through the coil. after the TMS discharge is complete, switch S2 open and switch S3 closes to complete the discharge of the energy stored in the coil (in some stimulators, a part of this discharge energy is used to recharge the capacitor C, resulting in faster recharge of the capacitor.). Based on the knowledge of operation of the circuit, we developed an ideal operational TMS module on Simulink 7.7 working in conjunction with MATLAB (Mathworks, Natick-MA, U.S.A.). Figure 2-3 shows the diagram of the equivalent circuit model designed on Simulink, based on the principle of operation discussed in Figure 2-2. It is to be noted that the circuit presented in Figure 2-3 appears more complex than the circuit presented in Figure 2-2 because Figure 2-3 includes additional components like pulse generators (to control the timing of the opening and closing of switches), blocks to export signals to MATLAB workspace (in order to view and verify the signals flowing through the circuit at different points in the circuit), mathematical operator blocks (to perform operations on the signals in order to obtain and compare properties of the generated signal by comparing it with those reported in literature, especially those concerning the

rate of change of current flowing the stimulating coil, the coil voltage, etc.) and blocks which display the generated signals for quick viewing). Although the above mentioned blocks are not presented in the circuit model presented in Figure 2-2, the circuit diagrams presented in Figure 2-2 and Figure 2-3 are effectively the same. The electrical parameters of the TMS equipment, obtained from (Guizhi et al., 2005; Weyh et al., 2005) and Magstim equipment datasheet, are provided in Table 2-I. The DC source chosen to charge the capacitor is rated between 400 V to 3 kV (Wagner et al., 2007). For our circuit model, we assigned a value of 3 kV.

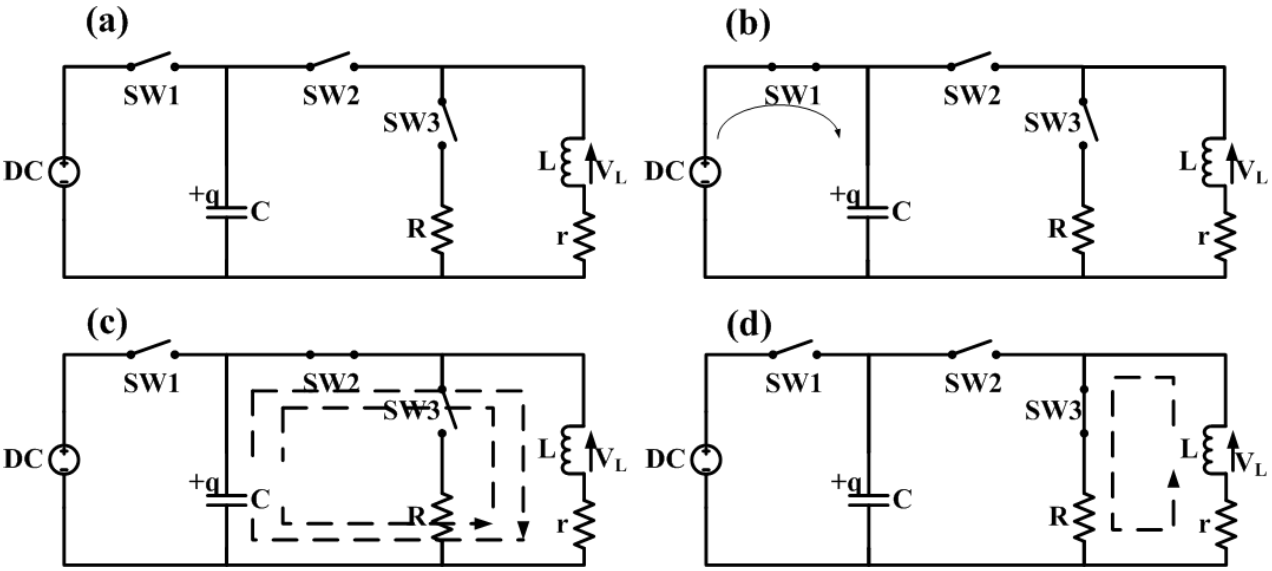

Figure 2-2. (a) Equivalent circuit model of a TMS equipment. (b) Charge mode of the TMS equipment. (c) Oscillation mode. (d) Discharge mode (Katayama and Iramina, 2009).

Table 2-I Numeric values of various components of a transcranial magnetic stimulator module

Capacitance (C)	Coil inductance (L)	Coil resistance (r)	Series resistance (R)
150 µF	15 µH	8 mΩ	500 Ω

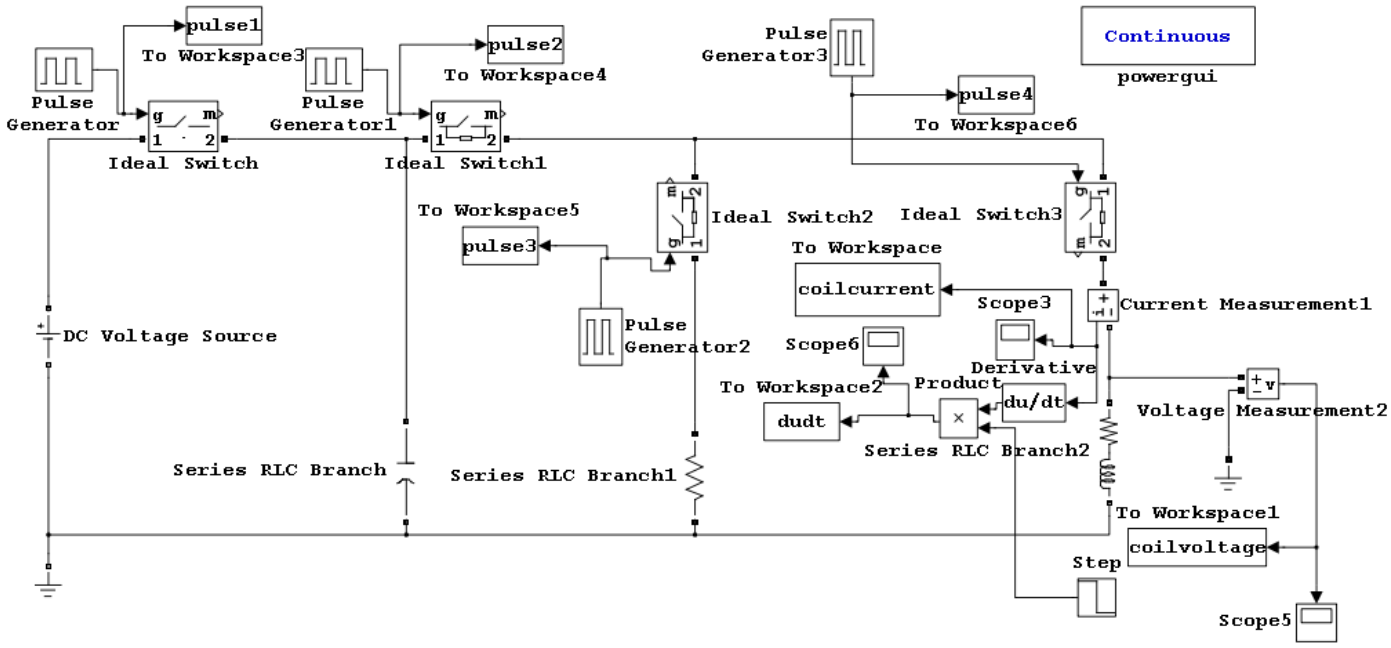

Figure 2-3. MATLAB Simulink model to simulate the operation of the TMS circuit presented in Figure 2-2.

At the initial state of the system, 'Ideal Switch' is closed and the capacitor gets charged. After a delay of 100 µs, 'Ideal Switch1' and 'Ideal Switch3' close to form the RLC circuit which results in the production of the damped oscillatory sinusoidal current pulse in the coil (represented by the inductor in series with a small resistance R1). The 100 µs delay also appears in the current and voltage waveforms of the coil. Finally, 'Ideal Switch1' opens followed by closing of 'Ideal Switch2', while 'Ideal Switch3' remains closed to trigger the discharge mode. The synchronized clocking sequence of the thyristor switches based on the timing diagram of the switches is shown in Figure 2-4 results in the production of the a decaying polyphasic (biphasic) current pulse shown in Figure 2-5.

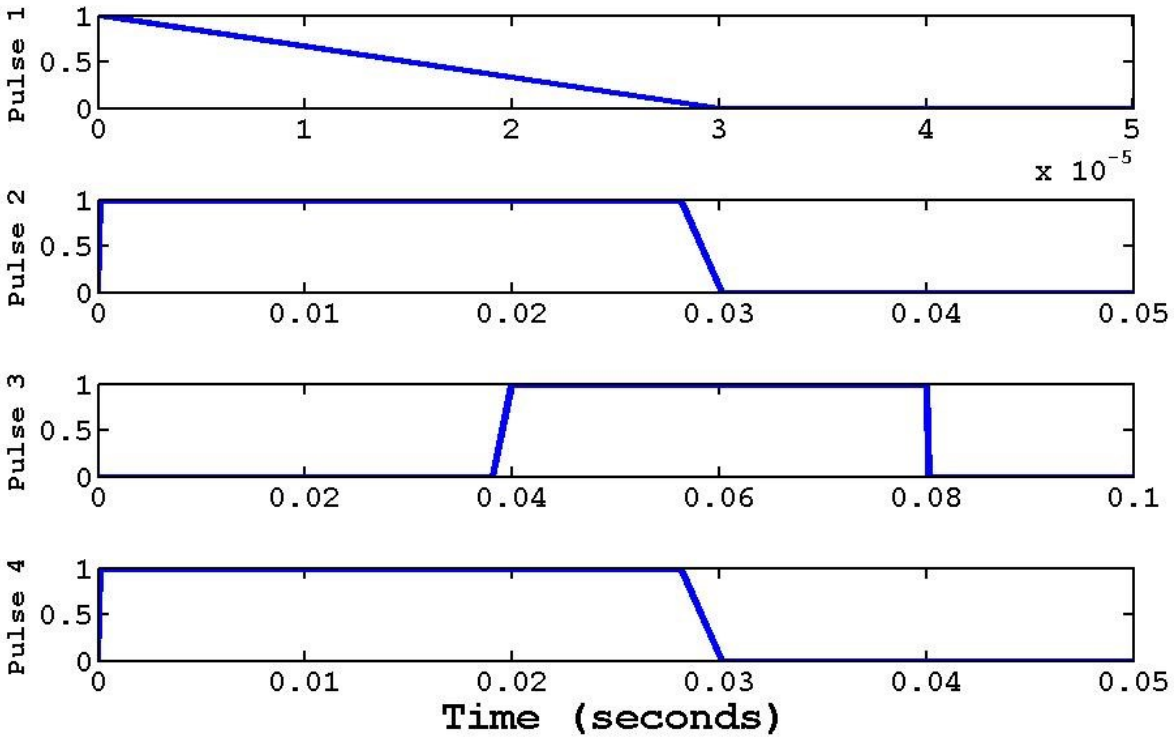

Figure 2-4. Timing diagram of thyristor switches.

On a broader perspective, the TMS stimulator circuit is a simple parallel RLC circuit. The behavior of this circuit is governed by two important parameters: the damping ratio, ζ and the Q-factor or quality factor (Basso, 2012)

$$\zeta = \frac{r}{2}\sqrt{\frac{C}{L}} \tag{2.1}$$

$$Q = \frac{1}{2\zeta} \tag{2.2}$$

Based on the values provided in Table 2-I, the computed value of the damping ratio, ζ is 0.013 and the Q-factor is 39.52

The system, based on the damping factor, can be classified as follows,

a) Overdamped – if $\zeta > 1$

b) Underdamped - if $\zeta < 1$

c) Critically damped - if $\zeta = 1$

Hence, we conclude that a TMS system operates in the low loss (indicated by the high Q-factor) underdamped condition with high amount of ringing. The response of the system follows a decaying exponential with oscillations. This behavior can be observed in Figure 2-5

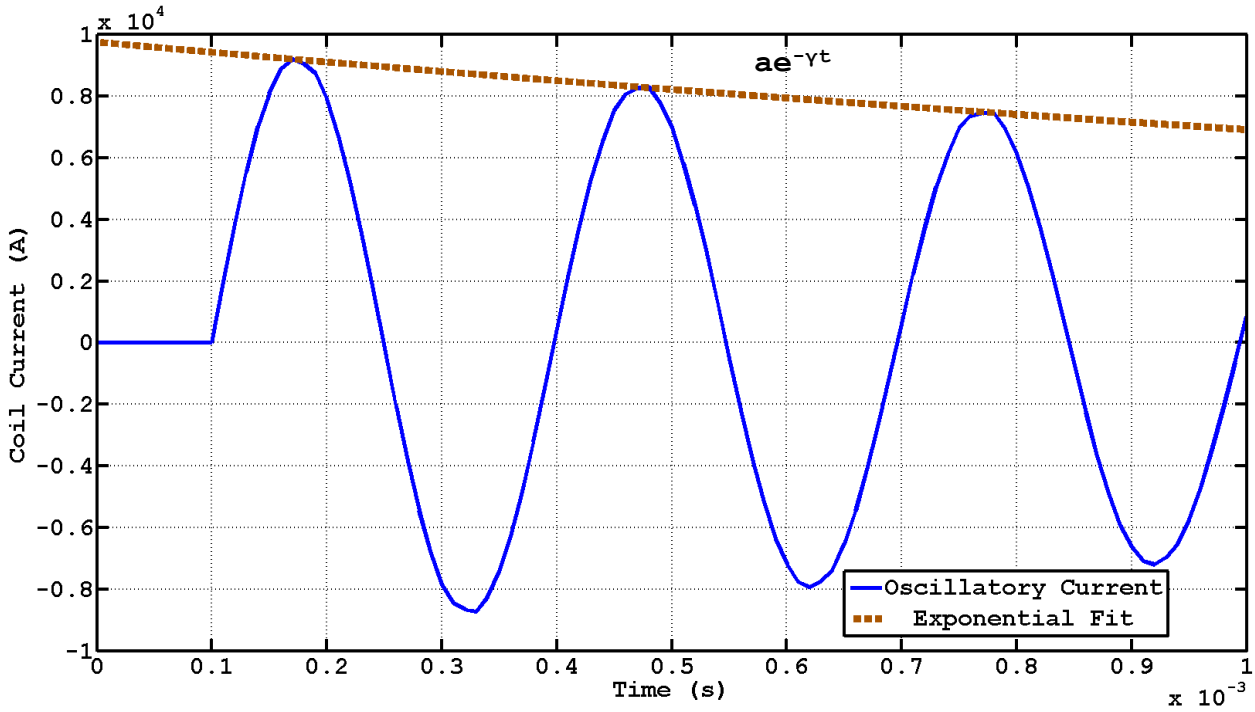

Figure 2-5. Polyphasic oscillatory coil current generated by the TMS stimulator depicting an exponential decay.

Another important parameter of an RLC circuit is the resonance frequency f_R , given by

$$f_R = \frac{1}{2\pi\sqrt{LC}} = 3.34\ kHz \tag{2.3}$$

The decay constant of the oscillating sinusoid is given by,

$$\gamma = \frac{r}{2L} = 266.67\ \mathrm{s}^{-1} \tag{2.4}$$

For the parameter values provided in Table 2-I, we calculated the resonant frequency (f_0) to be 3.355 kHz. A Fast Fourier Transform (FFT) analysis of the current waveform clearly depicts maximum power at 3.35 kHz (Figure 2-6)

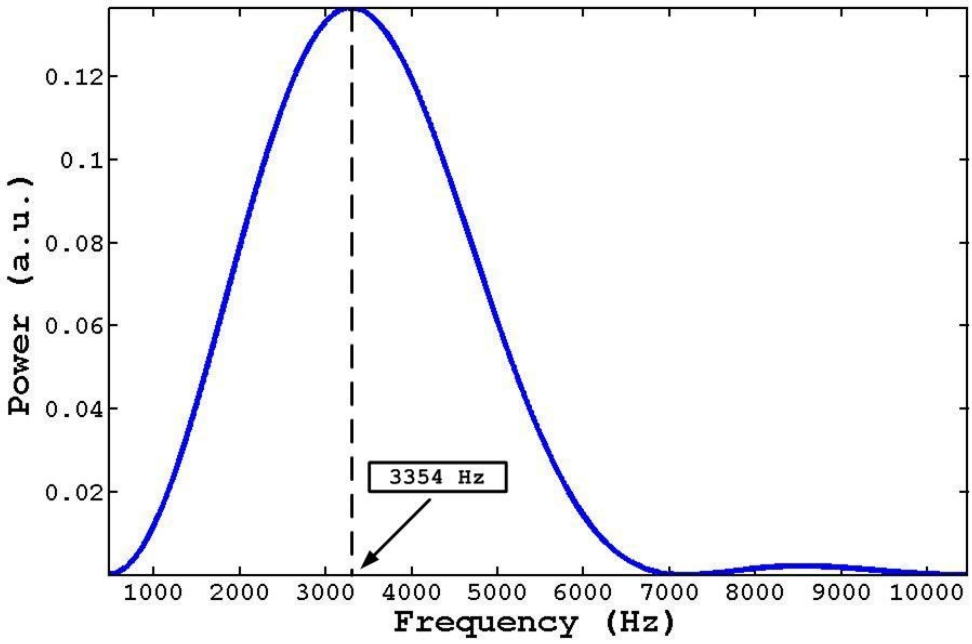

Figure 2-6. Operating frequency of the TMS pulse.

The TMS simulation was then curtailed to a time limit of 400 μs in order to restrict the generation of multiple cycles constituting a polyphasic current pulse thereby restricting the simulation to generate only one complete cycle of the polyphasic pulse which results in a single cycle of a biphasic current pulse, which is the signal that we intend to study. The simulation time had to be restricted because otherwise the circuit would continue operating till the specified simulation time limit is reached and continue producing multiple cycles constituting the polyphasic pulse. For a 3kV supply, the amplitude of the current that can flow through the coil is 9238 A. The maximum rate of change of current is 2×10^8 A/s. The maximum energy and power dissipated through the coil are 3620 J and 13.9 MW, respectively. The relevant figures are shown in Figure 2-7.

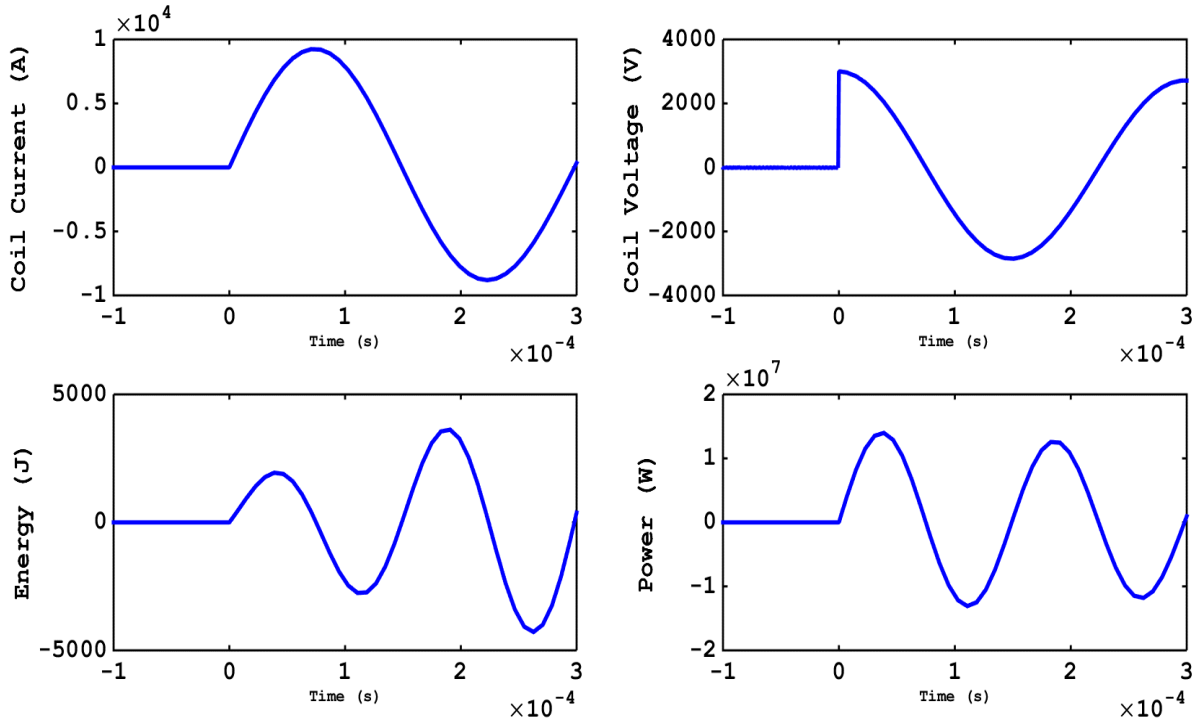

Figure 2-7. Characteristics of the stimulating TMS pulse.

2.3 Electromagnetic principles governing TMS

"Great things are done by a series of small things brought together"

The above quote by master Dutch artist Vincent Van Gogh captures the essence of the trail of events that led to the development of modern day application of electromagnetism, one of which is found in medicine in the form of transcranial magnetic stimulation (TMS). The complex mechanism of TMS has its humble beginning in the small twitch of a magnetic needle observed by Danish physicist Hans Christian Oersted. According to Oersted's experiment (Oersted, 1820), it was deduced that a current-carrying conductor produces a magnetic field in its vicinity. Numerous experiments later it was agreed upon that any current-carrying conductor, and example

of which is shown in Figure 2-8, can be assumed to be formed of a large number of small current carrying elements. The magnetic field $\mathbf{d}\vec{\mathbf{B}}$ produced by such a small element $\mathbf{d}\vec{l}$ of the current-carrying conductor carrying as current **i** at any point **P** in the region around it, having a position vector $\vec{\mathbf{r}}$ relative to the element depends on the following four factors:

(a) $\mathbf{dB} \propto \mathbf{i}$

(b) $\mathbf{dB} \propto \mathbf{dl}$

(c) $\mathbf{dB} \propto \boldsymbol{sin(\theta)}$

(d) $\mathbf{dB} \propto \mathbf{1/r^2}$

where θ is the angle between the length of the element and the line joining the element to the point P.

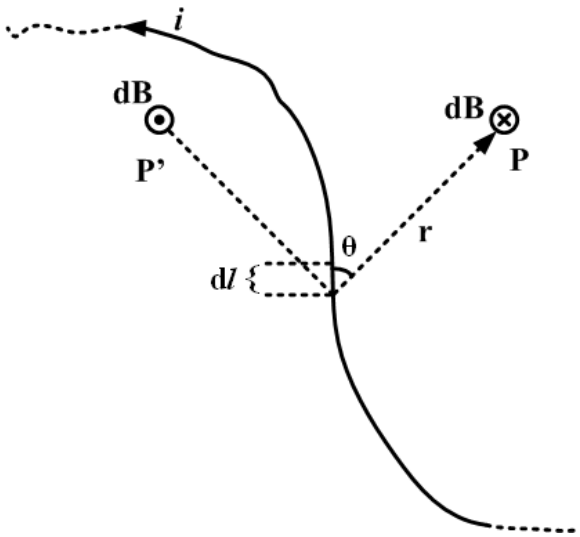

Figure 2-8. Biot-Savart law relating the magnetic field dB produced at any point P due to a current i flowing in an element dl and related spatially by a position vector r and an angle θ.

Based on the medium in which the conductor is placed, the constant of proportionality is found to be $(\mu_r * \mu_0)/4\pi$; where μ_r is the relative permeability of the medium and μ_0 is the permeability of free space. Hence magnetic field by the current carrying conductor element is given by

$$dB = \frac{\mu_r \mu_0}{4\pi} \frac{i\, dl \sin(\theta)}{r^2} \tag{2.5}$$

which in vector form translates to,

$$d\vec{B} = \frac{\mu_r \mu_0}{4\pi} \frac{i\left(\vec{dl} \times \vec{r}\right)}{\left|\vec{r}\right|^3} \tag{2.6}$$

In the SI system of units, $\mu_0 = 4\pi \times 10^{-7}$ H/m

This relation established in Equation (2.6) is called Biot-Savart's Law.

2.3.1 Direction of the magnetic field produced by a current carrying conductor

The direction of the magnetic field produced by a current carrying conductor can be determined by using any of the following two rules:

(a) Right hand palm rule

If we stretch out the palm of our right hand such that the thumb and the fingers are mutually perpendicular; and if now the thumb points in the direction of the current ***i*** in the conductor and fingers towards the point **P** at which the direction of the magnetic field is to be determined, the perpendicular drawn on the palm in the upward direction gives the direction of the magnetic field at that point.

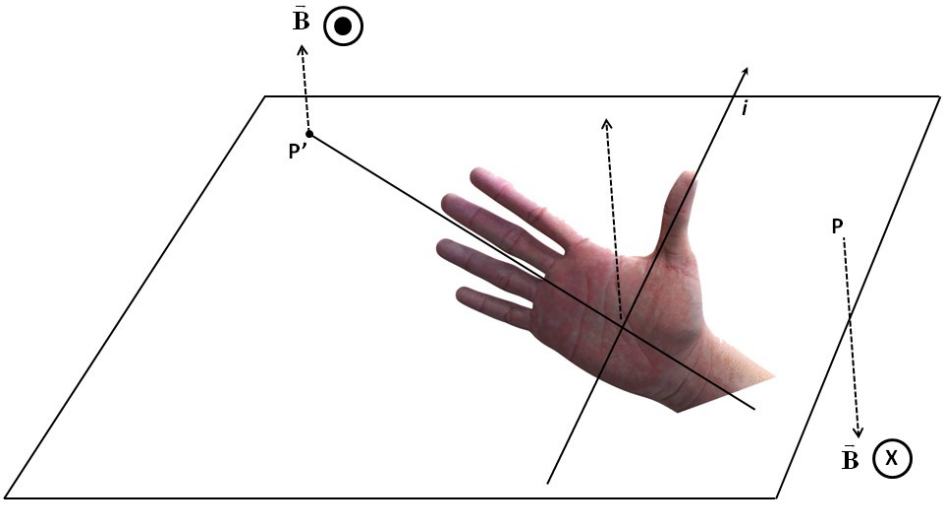

Figure 2-9. Schematic of right hand palm rule which is used to determine the direction of the magnetic field at any point P or P' when the conductor carrying a current *i* is positioned along the direction pointed by the thumb.

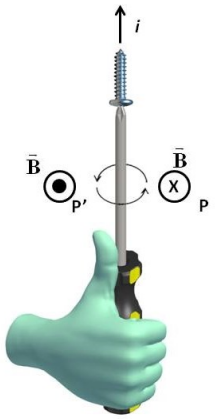

Figure 2-10. Schematic demonstrating the use of Maxwell's right hand screw rule to determine the direction of the magnetic field at any point p or P' around a conductor carrying a current *i* in the direction of the thumb or the direction in which the screw advances.

(b) Maxwell's right hand screw rule

If while rotating a screw by a screw driver, the screw advances along the direction of current in the conductor, then the direction of rotation of the thumb of our right hand gives the direction of magnetic lines of forces around the current carrying conductor.

In Figure 2-9 and Figure 2-10, the point **P** (or **P'**) and the current carrying conductor lies in the plane of the paper. If we apply any of the above two rules, the magnetic field at point **P** will be perpendicular to the plane of the paper and directed downwards shown by the cross (x) but at the point **P'** lying on the opposite side of the conductor , it will be vertically upwards, shown by the dot (.)

2.3.2 Magnetic field along the axis of a circular current-carrying coil

If we consider a circular coil of radius ***a***, carrying a current ***i*** flowing in anticlockwise direction, and placed with its plane perpendicular to the plane of paper, we can calculate the magnetic field at a point **P** lying along the axis of the coil at a distance ***x*** from its center. The problem description is shown in Figure 2-11

A small current element ***ab*** of length ***dl*** and carrying a current ***i*** is located at the top of the coil. This current carrying element is perpendicular to the plane of paper and the current in it is directed upwards. If ***r*** is the distance of this element from the point **P**, then according to Biot-Savart's law explained earlier, the magnetic field dB produced by this current-carrying element at the point **P**, is given by,

$$dB = \frac{\mu_r \mu_0}{4\pi} \frac{i\, dl \sin(\theta)}{r^2} \tag{2.7}$$

Here, μ_r will be equal to unity, since relative permeability of free space to itself is unity. θ is the angle between the current element and the line joining the element to the point **P**. Since element ***ab*** is perpendicular to the plane of paper and line **EP** lies in the plane of the paper, hence $\theta = 90^0$.

Thus Equation (2.7) yields,

$$dB = \frac{\mu_0}{4\pi} \frac{i\, dl}{r^2} \tag{2.8}$$

In accordance with right hand palm rule, the field **dB** will lie on the plane of paper and perpendicular to the line **EP** in the upward direction, as shown in Figure 2-11. This elemental field dB can be resolved into two components, dBsin(ϕ) and dBcos(ϕ), parallel and perpendicular to the axis of the coil, respectively.

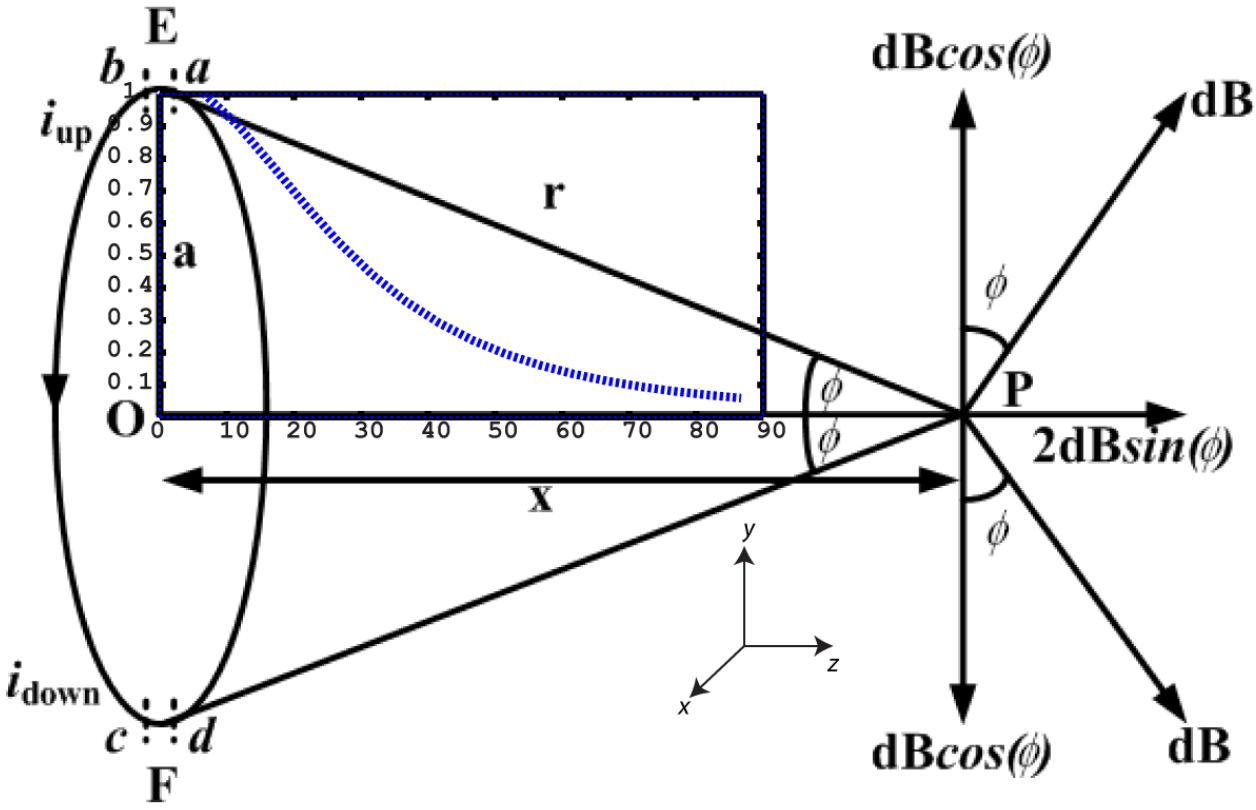

Figure 2-11. Magnetic field strength along the axis passing through the center of a current carrying coil located at a finite distance from the coil. The normalized magnetic field decay plot (shown in the form of the dashed blue curve) is shown for reference loop of diameter 36.2 mm carrying a current of 3000 A. The x-axis represents the values of x from 7 mm to 87 mm in steps of 5 mm. The y-axis is the normalized magnetic field amplitude.

If we consider another current element ***cd*** of the same length ***dl***, situated diametrically opposite to the element ***ab*** at the point **F**, then the current element ***cd*** is also perpendicular to the plane of paper but with a current directed downwards. The magnitude of the field produced by this element will also be equal to **dB**, but directed exactly in the opposite sense as shown in Figure 2-11. This field can again be resolved into two components dBcos(ϕ) and dBsin(ϕ), along and perpendicular to the axis of the coil, respectively. It becomes evident from the figure that the components of the two fields perpendicular to the axis of the coil will end up canceling each other

due to destructive interference, whereas the components of the two fields parallel to the axis of the coil will add up due to constructive interference. Thus, effectively, the contribution of each current element to the resultant magnetic field along the axis of the coil is equal to dBsin(ϕ). The current carrying coil can be considered to be composed of multiple such current carrying elements, the resultant field along the axis of which can be given by

$$B = \int dB\sin(\phi) = \int \frac{\mu_0}{4\pi}\frac{i\,dl}{r^2}\frac{a}{r} = \frac{\mu_0}{4\pi}\frac{i\,a}{r^3}\int dl = \frac{\mu_0}{4\pi}\frac{i\,a}{r^3}(2\pi a) = \frac{\mu_0}{2}\frac{i\,a^2}{r^3} \tag{2.9}$$

$$\therefore\ B = \frac{\mu_0}{2}\frac{i\,a^2}{\left(a^2+x^2\right)^{3/2}} \qquad \left(\because\ r^2 = a^2 + x^2\right) \tag{2.10}$$

A visual description of the magnetic field generated in a single loop circular coil is shown in Figure 2-12 (a). A butterfly coil, or as it is also known as a figure-of-eight coil consists of two single loop coils carrying currents in opposite direction. The field distribution for a butterfly coil is shown in Figure 2-12 (b).

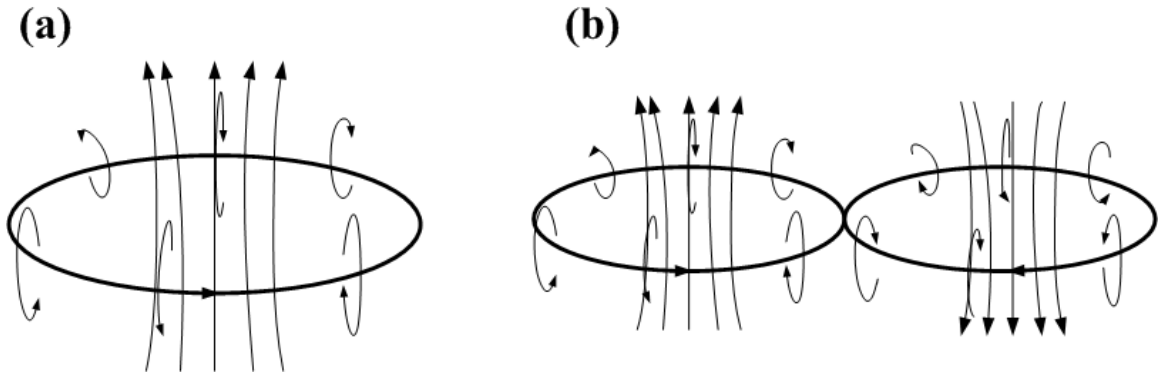

Figure 2-12. Magnetic field distribution for (a) a single loop circular coil and, (b) a butterfly coil.

If we ignore the phases of the magnetic fields and just project the absolute value of the magnetic fields on a plane parallel to the face of the coils and placed a finite distance under them, the magnetic field distribution would be as shown in Figure 2-13

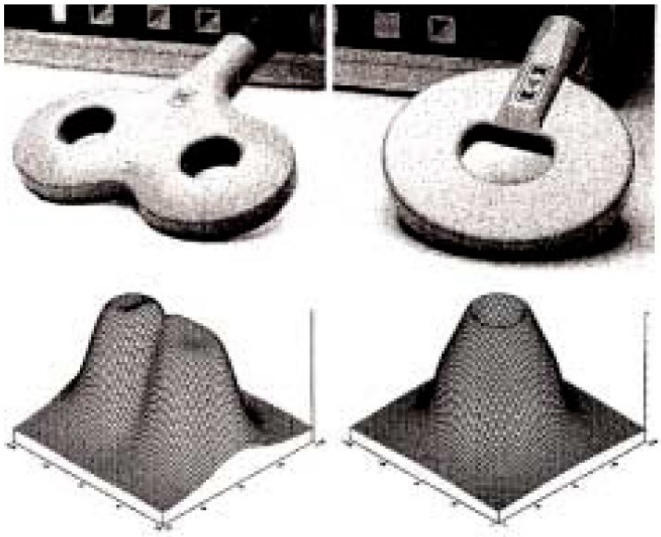

Figure 2-13. Absolute magnetic fields generated by two types of TMS coils. To the left is standard butterfly coil and to the right is a circular coil (Gershon, 2003).

While Oersted discovered that when an electric current is passed through a conductor, a magnetic field is produced around it; Michael Faraday discovered its complementary effect in 1831 (Day, 1999). Faraday is credited with the discovery of production of electric current by a magnetic field, through the phenomenon of electromagnetic induction. Based on his experiments, shown in Figure 2-14, he observed that whenever there was relative motion between a circular loop connected to a sensitive galvanometer and a bar magnet in the vicinity, either via motion of the coil or the magnet or both, there was a momentary deflection in galvanometer, which persisted till the relative motion persisted. The deflection indicated that an electric current flowed in the loop due to the relative motion between the magnet and the coil. In the absence of relative motion between the magnet and the loop of wire, a definite amount of magnetic flux is linked with the latter. However, when the magnet starts coming closer to the loop or starts moving away from the loop due to relative motion, the magnetic flux linked with the loop starts increasing or decreasing, respectively. This is due to the fact that the concentration of the magnetic lines of force is higher near the poles of the magnet.

Hence, it follows that the magnetic flux linked with the loop of wire starts increasing or decreasing as the loop of wire and the magnet begin to come close to each other or begin to move away from each other.

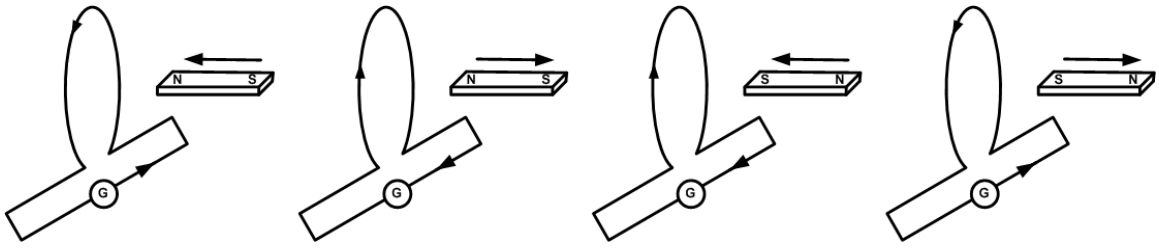

Figure 2-14. Schematic of Faraday's experiment to depict the induction of current in a conducting loop due to relative motion between a bar magnet and the loop.

Thus, the production of electro-motive force (e.m.f.) in the loop due to relative motion between the loop and the magnet is, in fact, due to the change taking place in the magnetic flux associated with the loop. When the relative motion stops, the change in magnetic flux becomes zero, and hence the e.m.f. also becomes the zero. If the loop or coil is in open circuit mode, induced e.m.f. due to relative motion will still be produced, but current will not flow in the loop. It was also observed that higher the speed of the relative motion between the coil and the magnet, the higher was the e.m.f. induced. If $\mathbf{d\varphi}$ is the change in the magnetic flux in a small interval of time **dt**, then the induced e.m.f. produced in the circuit is

$$\mathbf{e.m.f._{induced}} = -\frac{\mathbf{d\varphi}}{\mathbf{dt}} \tag{2.11}$$

The appearance of the negative sign is corroborated by Lenz's law. The law provides a simple method to determine the direction of induced current in a closed circuit and is based on the law of conservation of energy (Schmitt, 2002). According to Lenz's law, the induced current produced in a closed circuit always flows in such a direction that it always opposes the cause due to which it itself has been produced. Faraday's experiments confirmed this law. In his experiments, the

induced current in the loop was produced due to the motion of the magnet towards or away from the loop. It was observed that when the north pole of the magnet was brought closer to the loop, the direction of the current induced in the loop was such that the face of the loop towards the magnet behaved as a north pole i.e. it tended to repel the magnet coming towards itself i.e. it opposed the motion of the magnet which was the cause of the generation of the induced current. Similarly, when the north pole of the magnet was moved away from the loop or the south pole of the magnet was brought closer to the loop, the direction of the current induced in the loop was such that the face of the loop towards the magnet behaved as a south pole i.e. in every case, the current in the loop flows in such a direction that it opposes the motion of the magnet. Due to the fact that in each case the induced current opposes the motion of the magnet, some mechanical work needs to be done on the system to move the magnet against this opposing force. According to the law of conservation of energy, this work is obtained in the coil in the form of heat energy. If the motion of the magnet relative to the current loop is faster, the rate of doing work increases which results in increased production of heat energy in the coil i.e. the induced current will be higher. If the induced current was not to oppose the motion of the magnet, then we reach a scenario where we could get electrical energy continuously without doing any work, which is not possible. James Clerk Maxwell presented Faraday's law of electromagnetic induction shown in equation (2.11) in an integral form as

$$\oint \mathbf{E}.\mathbf{dl} = -\frac{\mathbf{d}}{\mathbf{dt}} \int_{\mathbf{S}} \mathbf{B(t)}.\mathbf{dS} \tag{2.12}$$

where $\oint$ represents the line integral and $\int_S$ represents the surface integral. By applying Stoke's theorem to equation (2.12), Oliver Heaviside, in 1892, converted the integral form of Maxwell-Faraday equation to a simpler differential form

$$\nabla \times \mathbf{E} = -\frac{\partial}{\partial \mathbf{t}} \mathbf{B}(\mathbf{t}) \tag{2.13}$$

where ∇ is Hamilton's operator (Heaviside, 2011) defined as

$$\nabla = \mathbf{i}\frac{d}{dx} + \mathbf{j}\frac{d}{dy} + \mathbf{k}\frac{d}{dz} \tag{2.14}$$

The induced current density $\mathbf{J}$ can then be calculated from Ohm's law

$$\mathbf{J} = \sigma \mathbf{E} \tag{2.15}$$

where σ is the conductivity of the conducting medium.

Extending the laws of electromagnetic induction to the case of the double loop butterfly coil described in Figure 2-12 (b), we can deduce that if a conducting plane is under the coil, as shown in Figure 2-15, the cause of induction on the conducting plate would be the upward directed magnetic field (for the left loop carrying an anti-clockwise current) and the downward directed magnetic field (for the right loop carrying a clockwise current). Based on Lenz's law, the effect should be such that it would oppose these causes and thus, the resulting induction should be in such a way that the magnetic field lines produced by those current profiles should be directed downward (under the left loop) and upward (under the right loop). The effected magnetic field lines are shown by the dotted line ending in hollow arrows in Figure 2-16

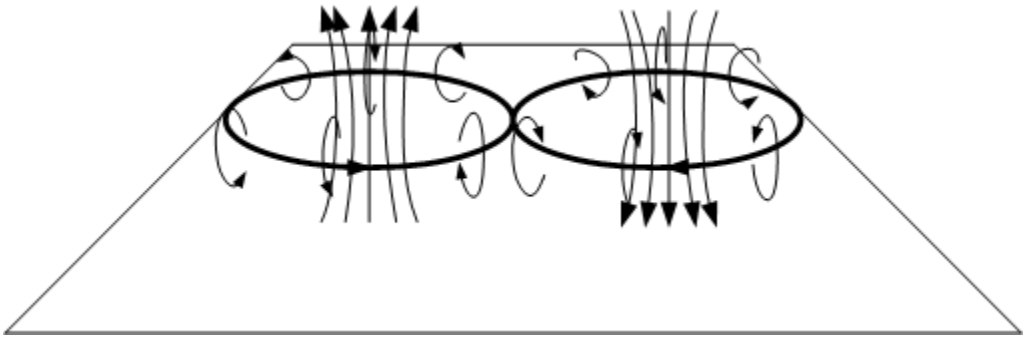

Figure 2-15. Magnetic field lines produced by a single turn butterfly coil with a conducting plane placed parallel to its face at a finite distance from it.

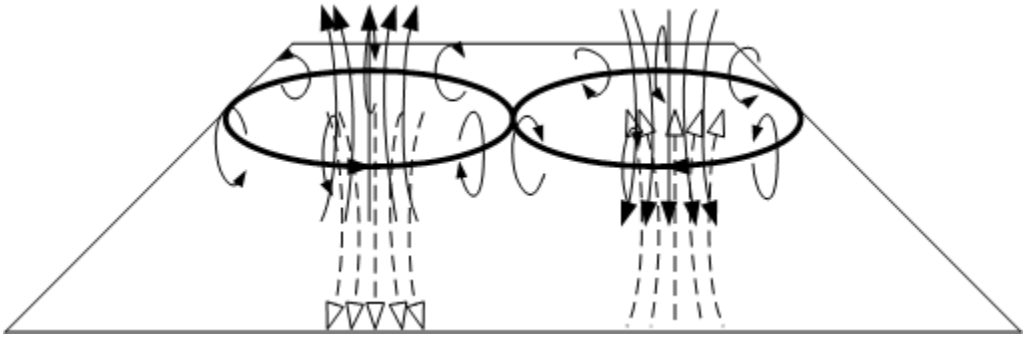

Figure 2-16. Application of Lenz's law to define the relationship between the cause (magnetic field produced by the loops of the coil) and the effect (magnetic field that will be produced due to the induced current on the conducting plane).

Application of the right hand palm rule or Maxwell's right hand screw rule enables us to then backtrack to the current profiles that would be able to produce these effected magnetic fields. Thus, an induced current loop with a clockwise current direction (under the left loop) and an induced current loop with an anti-clockwise current direction (under the right loop) would result in the desired effect. The induced current profiles on the conducting plane have been shown as dotted circles with the current directions on them represented by the hollow arrows.

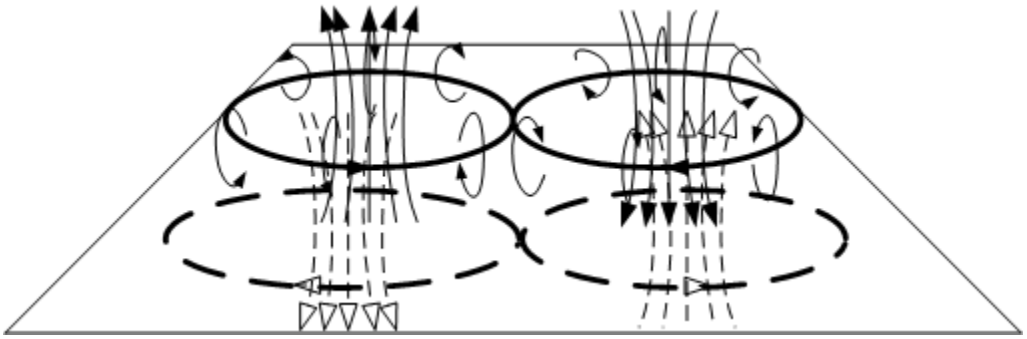

Figure 2-17. Profile of the induced current on the conducting plane that would support the effect needed for applied cause.

The induced electric field (or equivalently current) profiles produced by the two types of coils we have discussed so far have been shown in Figure 2-18

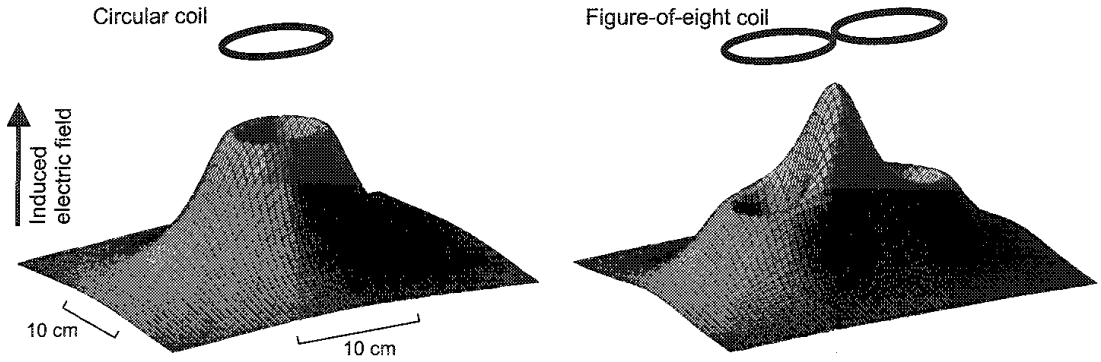

Figure 2-18. Induced field profiles on a plane under a circular coil and a butterfly coil (Ilmoniemi et al., 1999).

2.4 Coil geometries and their relevance

TMS essentially started with a circular discharge coil but as the applications and thereby, the demands of power and focality increased, new coil designs started appearing on the scene. One of the most important coil designs, that were an offshoot of the extensive research into developing more effective coils, was the butterfly coil (also referred to as the figure-of-eight (FOE) coil). The

difference in focality of the induced fields between the a circular and FOE coil can be clearly seen in Figure 2-18, where a circular loop generates an entire circular region of maxima underneath its edges compared to a much focal maxima peak that is generated by a FOE coil under the closest proximity of the current loops. Thus, a circular coil could be stimulating multiple regions of a brain simultaneously, whereas a FOE coil could be used to stimulate specific brain areas owing to its higher focality (Pascual-Leone, 2002). Numerical analyses of various coil geometries have been carried out to develop novel coil systems. In their work , Guizhi et al. (2005) presented a numerical analysis of not only how the focality of a FOE coil is better than that of a circular coil, they also analyzed how different arrangements of the coil elements and loops can have a bearing on increasing the focality of induction. However, the FOE coil also suffers from a disadvantage that in addition to a maximal peak at its center, it produces two additional side peaks which also tend to have relatively high magnitudes. This would not be of concern if the coil were to be used on smaller structures, but on relatively larger structures (comparable to the size of the coil), the two side peaks may result in secondary stimulation (Pascual-Leone, 2002). In order to address this issue, first a clover-leaf coil design was developed by Roth et al. (1994b) which resulted in a highly focal field distribution at the center of the coil. However, even though the peak induction site now resulted from the positive interference of fields of effectively two FOE coils and hence should have twice the peak amplitude value of a FOE coil, due to increased number of loops (four loops compared to the double loops of an FOE coil), the resulting inductance of the coil was 35 μH (more than two times the inductance value a FOE coil), the current that could flow through a clover-leaf coil for the same supply voltage would be much lower than what could flow through a FOE coil for the same supply voltage. Thus, the resultant effect was the amplitude of induction was more or less the same as that of an FOE coil. The cloverleaf design was flowed by a “slinky”

coil design which was developed by Chunye et al. (1995). It consisted of an additional circular loop mounted orthogonally to the plane of the FOE coil and located at the center of the FOE coil, with the normal to its face parallel to the plane of the FOE coil. With this coil design, Chunye et al. (1995) were able suppress the side peaks of the FOE coil but the focality of the central peak also suffered due a broader attenuation profile of the induced field on either side of the central peak. The most interesting development in coil design was proposed by Kai-Hsiung and Durand (2001), who developed a differential coil. The coil consisted of two wing units placed center coincident but mutually perpendicular to each other. In addition to these windings, there was a circular bottom unit at the center of the butterfly coil unit that would be used for stimulation. The butterfly units produced opposing direction fields, thereby restricting the spread of the induced fields while the circular unit served to enhance the induced fields at the site of excitation. The differential coil had more focality than its FOE counterpart, but again suffered from the amplitude issue that plagued the cloverleaf design. Another method of increasing focality of induced fields is by introducing a field guide in the form a shield plate (Dong-Hun et al., 2006). The shield plate could reportedly increase focality by 50 % and also prevent exposure of other parts of the brain to TMS. The shield plate acts as an additional conducting medium between the coil and the target, and by Faraday's law of induction and Lenz's law, produces a compensatory magnetic field around the flies of the coil, except for the center where it has a cut-out region to allow field lines to pass through uninhibited. In their work, Guizhi et al. (2005) included a discussion pertinent to novel set of coil designs referring them as multichannel coils which not only had better focality than both the conventional circular coil and the FOE coil (albeit again with a compromised peak amplitude induction value), but they also had the ability to stimulate multiple brain regions simultaneously, in a controlled way as opposed to a circular coil. Multichannel elements have great potential of

eliminating the use of two or three coil systems that are used simultaneously for some TMS studies, especially those involving paired pulse TMS studies (a type of TMS protocol explained in following sections). Multichannel coil analysis using numerical methods including finite element and boundary element methods have been proposed in the works of (Han et al., 2004; Lee et al., 2007; Ruohonen et al., 1999; Wang et al., 2005).

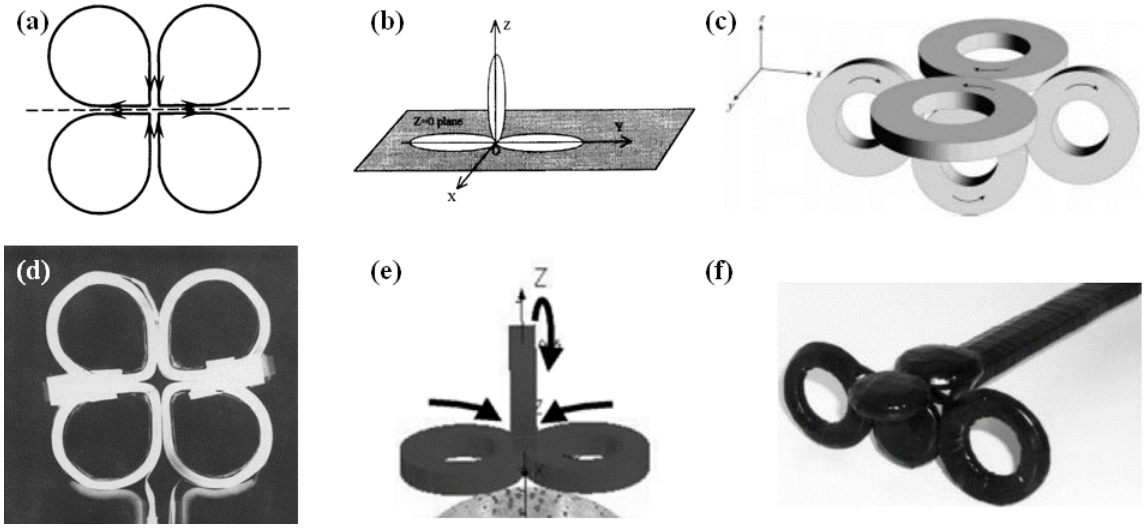

Figure 2-19. Design concept of (a) clover leaf coil (Roth et al., 1994b), (b) slinky coil (Chunye et al., 1995) and, (c) differential coil (Kai-Hsiung and Durand, 2001) along with images of tested (d) clover leaf coil (Roth et al., 1994b), (e) slinky coil (Kim et al., 2004) and, (f) differential coil (Kai-Hsiung and Durand, 2001).

With almost all the coil designs discussed so far, increase in focality has always existed with its conjoined twin: decrease in induction amplitude. One of the ways to increase the induced field amplitude is by increasing the strength of the inducing magnetic field amplitude.

The electric field induced in a conductor (e.g. gray matter) placed in a magnetic field B are related to each other by Maxwell's equation

$$\nabla \times \mathbf{E} = -\frac{\partial}{\partial \mathbf{t}} \mathbf{B}(\mathbf{t}) \tag{2.16}$$

The magnetic field B along the axis of a one of the circular current-carrying loops of the butterfly coil placed in air is

$$B = \frac{\mu_0 N}{2} \frac{i(t) a^2}{\left(a^2 + x^2\right)^{3/2}} \tan^{-1}\left(\frac{a}{x}\right) \tag{2.17}$$

or, in vector notation,

$$\vec{\mathbf{B}} = \frac{\mu_0 N}{2} \frac{i(t) a^2}{\left(a^2 + x^2\right)^{3/2}} \hat{\mathbf{k}} \tag{2.18}$$

where $\mathbf{N}$ is the number of turns of the coil loop, $\boldsymbol{\mu_0}$ is the relative permeability of free space, $\mathbf{i(t)}$ is the current in the coil, $\mathbf{a}$ is the radius of the coil loop and $\mathbf{x}$ is distance of a point on the gray matter in line with center of the coil along the axis of the coil.

Inserting (3.23) in (3.22) gives

$$\nabla \times \boldsymbol{E} = -\frac{\partial}{\partial t}\left(\frac{\mu_0 N}{2} \frac{i(t) a^2}{\left(a^2 + x^2\right)^{3/2}}\right) \tag{2.19}$$

If we do not intend to increase the size of the coil loop and the distance of the observation point at which the electric field E needs to be calculated,

$$\Rightarrow |\nabla \times \mathbf{E}| \propto -N \frac{\partial}{\partial t}(i(t)) \tag{2.20}$$

Thus, if we intend to increase the induced field strength, we can either do it by increasing the number of turns in the coil loop or by increasing the rate of change of current in the coil or both. In order to increase the rate of change of current in the coil, we simply need to increase the amplitude of the current flowing through the coil because the timing of the thyristor switches

restricts the time period of the current pulse to a constant value. Therefore, for a constant time period, the coil current with higher amplitude will have a higher rate of change of current compared to a lower amplitude coil current.

An increase in current amplitude would result in more Ohmic losses which would lead to coil heating. Increase in the number of turns would result in an overall increase in material cost and dimension of the coil. Addition of an iron core (Epstein and Davey, 2002) or a ferromagnetic core to the coil can achieve the desired result without an increase in the rate of change of current flowing through the coil or the number of turns in the coil. A ferromagnetic core, on account of its high magnetic permeability, intensifies the inducing magnetic field, in turn resulting in higher amplitude of induction. Even a modification to multichannel systems such as in which each constituent coil is driven by an independent circuit can produce high intensity stimulation at multiple selected brain regions simultaneously. As the intensity of the induced field increase, the penetrative depth of the field in the cortex also increases. Fifty different coil geometries have been modeled and studied by Deng et al. (2013) to investigate the depth-focality trade-off associated with TMS coils.

2.5 Effect of induced currents on neurons and neuronal activation

When TMS results in the induction of an electric field (generally of much higher amplitude than conventional neuronal or neural ionic currents), these strong fields are capable of influencing the flow of ions, in the medium in which they are induced, in accordance with the direction of their own field lines. Figuratively, if extracellular and intracellular ionic currents can be compared to a small waterfall, a hit by a TMS induced field could be compared to a huge tidal wave. Although

the waterfall would exist, the droplets of water in the waterfall would tend to be carried in the direction of the wave due to sheer force of the flow. Now if the wave were to fall on the waterfall from the sky above (as much of a stretch of imagination as it may sound), the general direction of the water droplets in the waterfall would not suffer a change of direction, because both the waterfall and the wave are flowing in the same direction, from above to ground level. It is only when these droplets are made to change their own original direction of flow that a spatial gradient in flow will come into existence. This spatial gradient is what could potentially cause, in neurons and nerves, stimulation. Revisiting the above allegory in neuronal terms, different scenarios of the flow relationship between the induced field and neuronal ionic current are presented in Figure 2-20

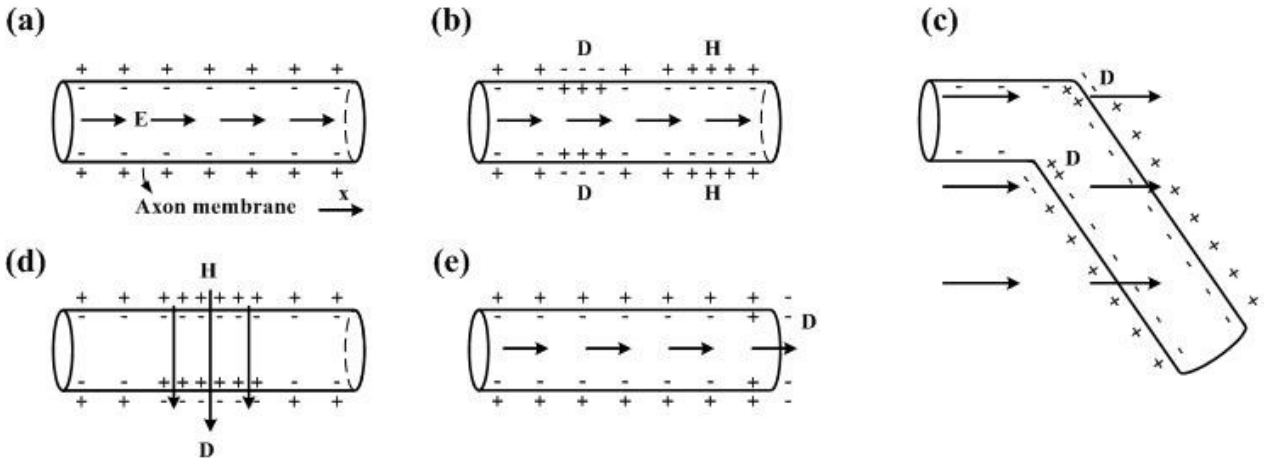

Figure 2-20. Diagrammatic representation of how an induced field in the extracellular fluid space can activate neurons. The arrows represent the direction of the external E field. In (a) the uniform E field is along the length of the axon. (b) Gradient activation due to non-uniform E field. (c) A bent axon is in the presence of the external E field resulting in gradient activation. (d) Transverse activation of the axon. (e) Gradient activation resulting from axon termination (reproduced from (Ruohonen, 1998)). D and H represent the points of depolarization and hyperpolarisation, respectively.

Ionic components within the axon and outside the axon are in equilibrium across the cell membrane and are in a state of homeostasis. Whenever this equilibrium is disrupted, it results in the generation of an action potential. In Figure 2-20 (a) the uniform external field, E, is along the length of the

axon and hence does not result in any ionic imbalance across the cell membrane. Therefore, there is no activation. In Figure 2-20 (b), there is a gradient activation because the ionic balance is disrupted due to the presence of a non-uniform E field. Conventionally, a flow of current out of the membrane (positive charge within the axon and negative charge outside the axon) results in depolarization (D) whereas a flow of current in to the membrane (negative charge within the axon and positive charge outside the axon) results in hyperpolarisation (H). In Figure 2-20 (c), the gradient activation is not due to a non-uniform e-field but due to a spatial gradient that is introduced along the direction of the uniform field because of a bend in the axon. Figure 2-20 (d) presents a scenario for transverse activation of the axon due to the mutually perpendicular direction the axon and the external field. In Figure 2-20 (e), gradient activation occurs due to an abrupt termination of the axon in the presence of an external field.

2.6 TMS protocols in current usage

TMS protocols can be classified based upon the number of TMS pulses administered before an observation of its effects. Different types of TMS are single pulse TMS, paired pulse TMS (ppTMS) and repetitive TMS (rTMS). As reported by Mishra et al. (2011) in their review, single pulse TMS involves the discharge of a single magnetic pulse at a given time. When a number of TMS pulses of the same intensity are delivered at regular intervals repeatedly to a discrete brain area, that type of TMS is called repetitive TMS or rTMS. Paired pulse TMS involves the pairing of a subthreshold stimulus with a suprathreshold stimulus with an inter-stimulus interval of 1-4 ms or 5-30 ms. Repeated paired pulse TMS (rppTMS) involves the delivery of paired pulse TMS at very low frequency (2 Hz). In their review, Kobayashi and Pascual-Leone (2003) discuss the

applications of different types of TMS that have been described above. Single pulse TMS is used to diagnose a wide variety of disorders arising from neurological diseases. Additionally, single pulse TMS studies are helpful in determining the spatio-temporal spread of TMS, with the temporal scale extending only a few milliseconds after TMS. rTMS finds applications in therapeutic use like in the treatment of depression and rehabilitation from stroke. ppTMS finds usage in the examination of intracortical inhibitory and facilitatory mechanisms as well as the examination of interhemispheric interactions. rTMS can be further classified depending upon the periodicity of the pulses in the train. If the train of pulses is such that one pulse is delivered every second, it is called 1 Hz rTMS. Similarly there are studies which report rTMS protocols extending to 50 Hz rTMS (Benninger et al., 2012). There could be other additional periodicities that could be included within the train. For example, short bursts of high frequency stimulation (50-100 Hz) are repeated at 5 Hz, 10 Hz and 20 Hz and are called theta, alpha and beta burst TMS (De Ridder et al., 2007). Theta burst TMS delivered at specific intervals yield continuous theta burst TMS, intermittent theta burst TMS and intermediate theta burst stimulation (Huang et al., 2005).

With the longer duration effects of rTMS protocols, another set of classification came into existence, based on the manner of administration of TMS. These are referred to as "***online"*** and "***offline"*** TMS. According to Bolognini and Ro (2010), in "online" TMS, subjects perform a particular task and at a particular point of time just before or during the performance of the task, a train of TMS pulses is administered to a specific area of the brain. During "offline" TMS, a specific area of interest is stimulated with rTMS pulses, a few minutes before the performance of a task.

Just like periodicity of pulses play an important role in determining the effects of TMS, the intensity of the TMS stimulation pulses also plays an important role in affecting neuronal processing. Most TMS studies base the intensity of stimulation as a percentage of resting or active

motor thresholds. The choice of motor threshold (MT) is due to the fact that this is the only parameter that results in a visible deterministic effect (twitch of targeted muscle). Motor threshold also represents a measure of the membrane excitability of pyramidal neurons (Pascual-Leone et al., 1998b). Previously, resting motor threshold (RMT) was obtained by delivering single pulse of TMS to the motor cortex and observing the response of the targeted muscle, stimulated cortically by the TMS pulse, on the contralateral side, when the target muscle is in a relaxed state before and immediately prior to the application of the TMS pulse. The target muscle for motor threshold experiments is the first dorsal interosseous (FDI) muscle. Similarly, active motor threshold (AMT) is obtained by delivering TMS to the motor cortex and observing the response of the FDI muscle on the contralateral side, when the FDI muscle is in a state of voluntary contraction before and just prior to the application of the TMS pulse. The observation of the response of the FDI muscle can be achieved in two ways; the first is by observing the muscle twitch visually and the second is by recording the muscle response using electromyography (EMG) surface electrodes. If observation of muscle twitch is used to determine the MT, then it is defined as the lowest setting of the stimulator output at which ≥ 5 out of 10 stimuli result in observable movement of the index finger (Westin et al., 2014). If EMG is used to define MT, then a reliable response of the muscle is defined as a motor evoked potential (MEP) of 50-100 μV (for RMT) or 200-300 μV (for AMT) occurring in 50 % of 10 to 20 consecutive trials (Rothwell et al., 1999). TMS studies generally use TMS intensities defined as a percentage of RMT or AMT. When TMS is delivered at less than 100 % RMT or 100 % AMT, it is called subthreshold stimulation and if the stimulation intensity exceeds 100 % RMT or 100 % AMT, it is called suprathreshold stimulation. Komssi et al. (2004) demonstrated that stimulus intensity as low as 60 % of RMT was sufficient to evoke measurable potentials (in the form of MEPs) and there was a non-linear relationship between brain response

and intensity of TMS stimulation. The MEP amplitudes and the global mean field amplitude (a measure used by the authors to quantify brain response) showed a non-linear relationship with respect to stimulus intensity. The intensity of TMS stimulus varied from 60 % and 80 % RMT (subthreshold stimulus) to 100 % and 120 % RMT (suprathreshold stimulus). The non-linearity in response-stimulus relationship has been also detailed in the work of Hanakawa et al. (2009). Garry and Thomson (2009) showed that short interval intracortical inhibition, a measure used to quantify intracortical inhibitory processes, was significantly affected at suprathreshold intensities but not at subthreshold intensities. We, therefore, understand that choice of TMS stimulation intensity (subthreshold or suprathreshold) can have significantly differing effect on brain response.

Duration of TMS trains, which indirectly governs the number of TMS pulses used for conditioning, has an effect on the duration of the effects of TMS after conditioning too. Huang et al. (2005) showed that continuous theta burst stimulation delivered to the left motor cortex for twenty seconds (amounting to 300 pulses) resulted in an decrease in motor evoked potential amplitude (MEP) of left M1 for 20 minutes after TMS and forty seconds conditioning amounting to 600 pulses) resulted in a decrease in MEP amplitude for up to 60 minutes after TMS. In another study, Peinemann et al. (2004) found that thirty seconds conditioning of the primary motor cortex with 5 Hz rTMS (resulting in 150 pulses) resulted in no significant change in MEP amplitude of the contralateral muscle but when the number of pulses used for conditioning were increased to 900, the MEP amplitude of the contralateral target muscle was increased significantly for between 5-20 minutes post TMS. This duration increased 30 minutes when the number of pulses was increased to 1800.

2.7 Single pulse TMS and induced currents

Maxwell-Faraday equation can be used to obtain the electric field induced in a conducting medium when the conducting medium is influenced by the magnetic field produced by a TMS coil placed in the vicinity of the conducting medium. Some popular methods to obtain the solution of the differential equations involve using finite difference algorithm (Roth et al., 1994a), finite element method (Chen and Mogul, 2009; Opitz et al., 2011; Thielscher et al., 2011; Windhoff et al., 2011) and boundary element method (Lee et al., 2007; Salinas et al., 2009). Early simulations of induced currents were either based on non-homogenous phantom models ,with individual layers possessing homogenous properties (Krasteva et al., 2002) or approximate head models (Wagner et al., 2004b). Opitz et al. (2011) considered anisotropy of the brain while solving for induced fields using finite element method.

2.8 Evoked potentials (EPs)

One of the most effective ways to understand cortical functionality is by stimulating a part of the cortex and studying the unit firing and recruitment patterns. Invasive stimulation of the cortex had been in existence since the 1960s when Bindman et al. (1964) reported that when extremely low values of current (0.25 A/mm^2 square pulse waveform of duration 200 μs) are applied to the rat cortex via surface electrodes (in the form of two fine needles inserted beneath the skin), the currents had the capability of influencing spontaneous activity and the evoked response of neurons (recorded from the pia or gray matter) for hours following just minutes of stimulation. Non-invasive stimulation had been in existence for ages before this but it was only in the early 1980s

that Merton and Morton (1980) developed a non-invasive method to stimulate two areas of the human cortex using the method of transcranial electrical stimulation (TES). This was followed by magnetic stimulation of the brain (Barker et al., 1985a; Barker et al., 1985b). EPs therefore, can be summarized as recordings of the neuronal system's electrical response to the stimulation of specific sensory pathways. Study of such EPs can provide invaluable information relative to the functional integrity of pathways within the neuronal system. Some of the most commonly encountered EPs in TMS studies are motor evoked potentials (MEPs), visual evoked potentials (VEPs) and somatosensory evoked potentials (SEPs).

Every evoked response, resulting from the stimulation of the auditory, motor, visual or somatosensory cortex, is constituted of a series of waves of opposite polarities. As per convention, the negative polarity waves are represented by the alphabet N whereas the positive polarity waves are represented by the alphabet P. In addition to the alphabetical representation, the temporal information of the polarity is also included in the form of latency of a polarity from the stimulation point. This temporal information is denoted as a subscript next to the alphabetical representation. Therefore, P_{100} represents the positive peak which appears 100 milliseconds after the application of the stimulus. Similarly, N_{75} represents a negative peak which appears 75 milliseconds after the application of the stimulus. Each of these positive and negative peaks can have their sources in different parts of the unit cortex. For instance, in visual evoked potentials, the N_{75} wave is caused by foveal stimulation and has its origin in area 17 of the visual cortex, whereas P_{100} has its source in area 19 and N_{145} in area 18 (Pal, 2001). All these positive and negative peaks collaborate to yield a waveform which is the response of the cortical unit characteristic to that particular stimulus. In other words, the generated waveform is the evoked response of the particular region of the brain, elicited by the given stimulus. Every evoked response is characterized by some major parameters

like its amplitude (most negative potential to most positive potential), latency (time of occurrence of the first negative or positive polarity) and duration (time from the occurrence of the first negative of positive polarity, to the time of occurrence of the last negative of positive polarity). The typical evoked response recorded using scalp EEG electrodes from the primary visual cortex area V1 of humans to a checkerboard visual stimulus is shown in Figure 2-21 with the N_{75} and P_{100} peaks labeled accordingly.

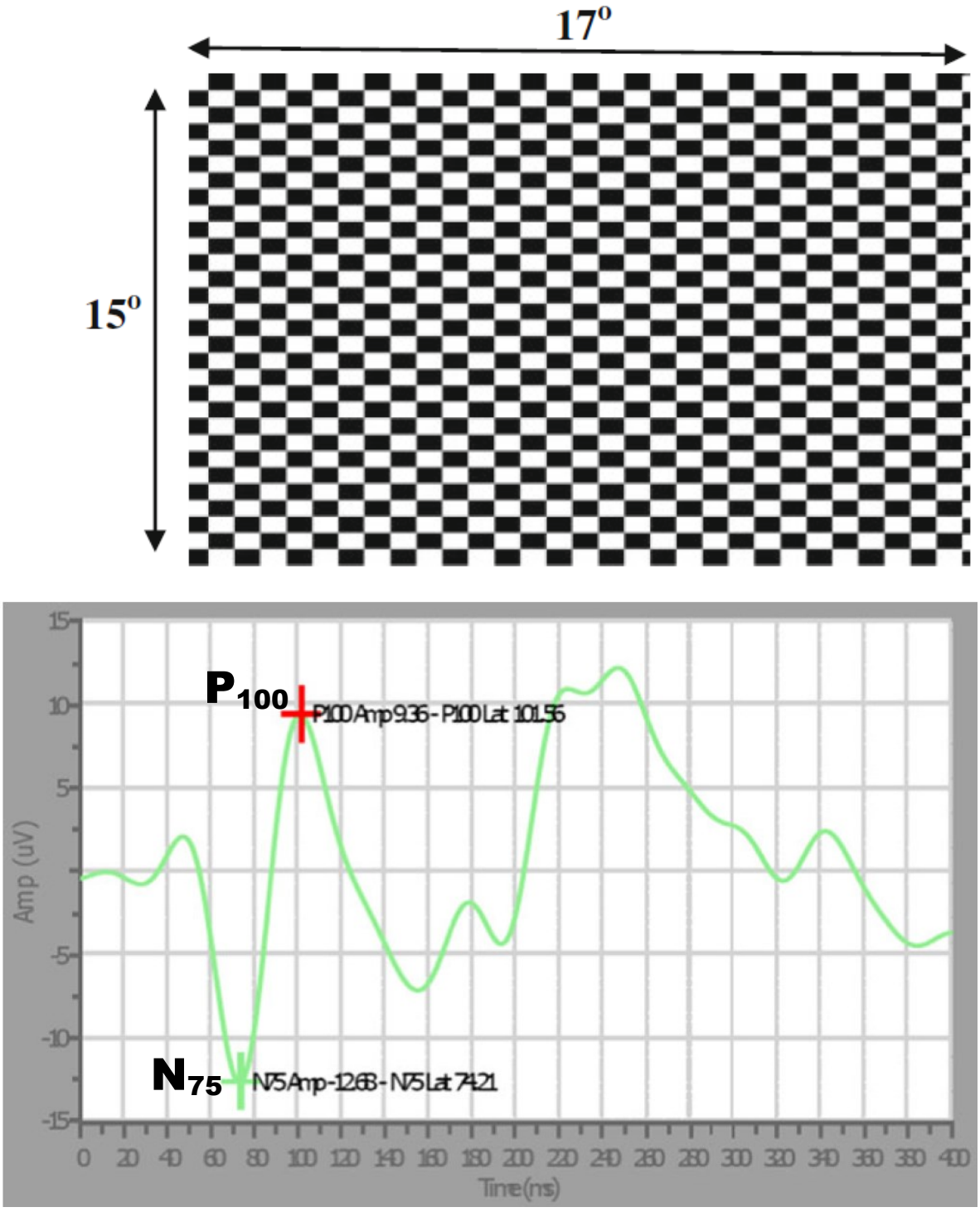

Figure 2-21. Standard full field checkerboard pattern (top row) visual stimulus and the corresponding cortical response obtained from area V1 of humans (bottom row) reported by Yadav et al. (2012).

The effect of different TMS paradigms on evoked responses has provided great insight in to the mechanisms underlying their behavior and connectivity within the cortex. It is interesting to observe how a particular TMS paradigm can effect a cortical region depending on the site of its delivery, the intensity of TMS pulses used and the periodicity of the pulses (in case of rTMS paradigms). For instance, delivery of 1 Hz rTMS to the motor cortex resulted in a decrease in MEP amplitude elicited from the contra lateral whereas delivery of TMS to the primary visual cortex had no effect on the contra lateral MEP amplitude (Casula et al., 2014). A similar study shows the effect of delivery of another suppressive paradigm, called continuous theta burst (cTBS), to one location and its effect on the responses of another location. cTBS produces similar effects as low frequency 1 Hz TMS and due to its shorter delivery time (for same number of pulses as a 1 Hz protocol), it improves patient comfort and has been propagated to replace 1 Hz rTMS (Brückner et al., 2013).

In vivo single pulse TMS studies are helpful in generating input-output curves which provide a measure of excitatory feedback to corticospinal efferent output which may be glutamatergically mediated (Pascual-Leone et al., 1998b). Single pulse TMS studies have been conducted to study the functional connectivity between the visual cortex and somatosensory cortex. Kupers et al. (2006) demonstrated that application of TMS to the occipital cortex (stimulating the visual cortex) could result in tactile sensations on the tongue (having its projection on the somatosensory cortex). Zangaladze et al. (1999) showed how the application TMS to the visual cortex disturbed the successful identification of grating orientation of a plastic grating employing the use of tactile perception. A similar study involving motor cortex and somatosensory cortex has been conducted by Ishikawa et al. (2007) who demonstrate, among other results, how application of cTBS to the motor cortex results in increase in excitability of the ipsilateral somatosensory cortex.

Another aspect to TMS related studies is the variability associated with the effects of TMS. As discussed by Brückner et al. (2013), cTBS is a suppressive paradigm like 1 Hz rTMS. Therefore, application of cTBS to a cortical area (for example left S1) is expected to suppress left S1 activity, the effect of which should be perceived on the contralateral observation side (right hand median nerve). But what about the effect of this TMS on the non-stimulated right S1 and its corresponding effect on the left hand median nerve? Seyal et al. (1995) demonstrated that suppression of ipsilateral sensorimotor cortex resulted in facilitation of the contralateral unstimulated sensorimotor. The mechanism of reciprocal gating was supposed to be behind this hemispheric "rivalry", where particular region on one hemisphere tends to oppose the activity of its homologue in the opposite hemisphere. Interestingly though, Ishikawa et al. (2007) showed that application of suppressive cTBS paradigm to one side of the somatosensory cortex resulted in decreased activity of the ipsilateral observation side too, which challenged the hemispheric rivalry theory. Blankenburg et al. (2008) also showed that application of 10 Hz rTMS to the right parietal cortex (a high frequency rTMS paradigm which increases cortical activity) resulted in increased activity of the contralateral (unstimulated) S1, especially in the presence of electrical stimulation of the ipsilateral median nerve. The final straw that broke the proverbial "hemispheric rivalry theory" camel's back was the work of Eshel et al. (2010) who studied responses from both the stimulated and non-stimulated somatosensory cortex simultaneously, using the similar TMS parameters as Seyal et al. (1995). They showed that excitation of the ipsilateral cortex was accompanied by an excitation in the non-stimulated contralateral homologue too.

A summary of selected TMS studies on relevant parameters (for ease of comparison) has been presented in the table below.

2.9 Conclusion

TMS is fast gaining popularity due to its non-invasive property. However it is still a relatively new technique for stimulation, but one that has tremendous potential. Due to its relatively preliminary stage of development, much of the understanding of the relevant concepts has followed applications. Most studies pertaining to TMS are compartmentalized into either single pulse numerical studies or cortical response studies due to the strong independent nature of these two study domains. More information and insight about the intricate mechanisms of TMS can be obtained if efforts are made to merge these two tributaries. It is then that we can possibly start to grasp the three most important facets of TMS: What, How and Why.

Table 2-II TMS studies pertinent to its effects on evoked responses (cell color key provided at the end of the table)

SN #	Study	Species	Paradigm	Cortical area	Detection method	Observation region w.r.t. TMS delivery region	TMS intensity	No. of pulses	Duration of interventions	After effects	Duration of after effects
1	Casula et al. (2014)	Humans	1 Hz rTMS	M1	surface EMG electrodes	contraleteral	90 % RMT	1200	1200 s	MEP amplitude	nearly 300 s
				V1				1200		MEP amplitude	nearly 300 s
2	Maeda et al. (2000b)	Humans	1 Hz rTMS	M1	surface electrodes	contralateral	90 % RMT	240	4 minutes	MEP amplitude	130 s
3	Siebner et al. (1999)	Humans	1 Hz rTMS	M1	surface electrodes	contralateral	90 % RMT	1800	30 minutes	MT*	20th minute
4	Schambra et al. (2003)	Humans	1 Hz rTMS	M1	surface EMG electrodes	contralateral unstimulated M1 or ipsilateral limb	115 % RMT	1800	30 minutes	MEP amplitude	15 minutes
5	Filipović et al. (2010)	Humans	1 Hz rTMS	M1	surface EMG electrodes	contralateral	Just below AMT (typically 90% of RMT)	(600*3blocks) perday *4 days	32 minutes per day * 4 days	MEP amplitude, RMT, AMT	24 hours
6	Veniero et al. (2013)	Humans	1 Hz rTMS	M1	surface EMG electrodes	contralateral	70 % RMT	(300*3blocks)	17 minutes	MEP amplitude	nearly 8 minutes
				Pre Motor Cortex						MEP amplitude	
7	Todd et al. (2006)	Humans	2 Hz rTMS	M1	surface EMG electrodes	contraleteral	70 % AMT	600	10 minutes with breaks	MEP amplitude	
										RMT	
							80 % AMT			MEP amplitude	30 minutes
										RMT	
							90 % AMT			Variable MEP amplitude	
										RMT	
8	Peinemann et al. (2004)	Humans	5 Hz rTMS	M1	surface EMG electrodes	contraleteral	90% RMT	150	30 s	MEP amplitude	
								900		MEP amplitude	between 5 -20 minutes
								1800	470 s (12 trains of 150 stimuli each with 10 s inter train interval)	MEP amplitude	30 mins
9	Quartarone et al. (2005)	Humans	5 Hz rTMS	M1	surface EMG electrodes	contraleteral	90% RMT	1500	780 s (5 trains of 300 stimuli each with 120 s inter train interval)	MEP amplitude	2 minute blocks
										AMT and RMT	2 minute blocks
							90% AMT			MEP amplitude	2 minute blocks
										AMT and RMT	2 minute blocks
10	Ragert et al. (2004)	Humans	5 Hz rTMS	S1	Scalp electrodes	contralateral hand (ipsilateral SI side as TMS)	90% RMT	2500	590 s including breaks for first 1250 followed by 45 minute break and then 590s for second 1250	First SEP amplitude	1hr + 200secs
										Second SEP amplitude	1hr + 200secs
						ipsilateral hand (contralteral SI side as TMS)	90% RMT			First SEP amplitude	1hr + 200secs
										Second SEP amplitude	1hr + 200secs
11	Todd et al. (2006)	Humans	6 Hz rTMS	M1	surface EMG electrodes	contraleteral	70 % AMT	600	10 minutes with breaks	MEP amplitude	
										RMT	
							80 % AMT			MEP amplitude	
										RMT	
							90 % AMT			Variable MEP amplitude	
										RMT	
12	Maeda et al. (2000b)	Humans	10 Hz rTMS	M1	surface electrodes	contralateral	90 % RMT	240	240 s	MEP amplitude	130 s

Table 2-II continued

13	Blankenburg et al. (2008)	Humans	10 Hz rTMS	S1	fMRI Bold	Contralteral S1 or ipsilateral hand					
14	Huang et al. (2005)	Humans	15 Hz rTMS	M1	surface electrodes	ispilateral	80% AMT	300	20 s	MEP amplitude	
15	Wu et al. (2000)	Humans	15 Hz rTMS	M1	surface electrodes	ipsilateral	120% RMT	30	2 s	MEP amplitude	30 s
16	http://www.benthamscience.com/open/toneurj/articles/V001/20TONEURJ.pdf	Cats	15 Hz rTMS	V1	surface scalp electrodes	ispilateral	50 % MSO	90	6 15 hz trains with inter train interval of 5 secs	delta	not mentioned
										theta	not mentioned
17	Maeda et al. (2000a)	Humans	15 Hz rTMS	M1	surface electrodes	ispilateral	90% RMT	240	4 trains of 60 pulses with inter train interval of 56 secs; total time is 4 minutes	MEP amplitude	
18	Maeda et al. (2000b)	Humans	20 Hz rTMS	M1	surface electrodes	contralateral	90 % RMT	240	240	MEP amplitude	130 s
19	Huang et al. (2005)	Humans	cTBS	left M1	surface electrodes	ipsilateral	80% AMT	300	20 s	MEP amplitude	20 min
								600	40 s	MEP amplitude	60 min
20	Ishikawa et al. (2007)	Humans	cTBS	left M1	surface electrodes	ipsilateral	80% AMT	600	40 s	MEP amplitude	42 min
				left S1	surface electrodes					MEP amplitude	
				left M1	surface scalp electrodes					SEP amplitude	53 min
				left S1	surface scalp electrodes					SEP amplitude	13 min
21	Katayama et al. (2010)	Humans	cTBS	left S1	surface electrodes	ipsilateral	80% AMT	600	40 s	MEP amplitude	
	Katayama et al. (2010)	Humans	cTBS	left S1	surface scalp electrodes	ipsilateral	80% AMT	600	40 s	SEP amplitude	
22	Zapallow et al. (2012)	Humans	cTBS	left/right S1	surface scalp electrodes	ipsilateral	80% RMT	600	40 s	SEP amplitude	12-16 mins, 30 mins
23	Benali et al. (2011)	Rats	cTBS	corpus callosum	tungsten electrode in layer 4	NA	25-29% MSO	600x5	regular paradigms repeated over 15 minute intervals	SEP amplitude (both first and second)	
24	Volz et al. (2013)	Rats	cTBS	corpus callosum		NA	25-29% MSO	600, 1200,	like above, regular paradigms repeated over 15 minute intervals	Spiking activity	
25	Katayama et al. (2010)	Humans	iTBS	left S1	surface scalp electrodes	ipsilateral	80% AMT	600	regular paradigm repeated over 15 minute intervals	MEP amplitude	
										SEP amplitude	15 min and 30 min after TMS
26	Benali et al. (2011)	Rats	iTBS	corpus callosum	tungsten electrode in layer 4	NA	25-29% MSO	600x5	regular paradigm repeated over 15 minute intervals	SEP amplitude (first)	
										SEP amplitude (second)	
27	Di Lazzaro et al. (2008)	Humans	iTBS	Right M1	surface electrodes	ipsilateral	80% AMT	600	regular paradigms repeated over 15 minute intervals	MEP amplitude	

Key	
	increase
	Decrease
	no effect

Chapter 3 TMS and Induction

Preface

This chapter addresses the purely engineering aspect of transcranial magnetic stimulation (TMS). Hence, neurophysiology is not considered for discussions in this chapter. The rationale behind this approach is that before we try to understand “why” TMS affects neurophysiology, we need to understand “ how ”, indeed, does it affect neurophysiology. The underlying reasons are the electric fields (E-fields) that are induced on the cortex due to a time varying magnetic field produced by a stimulating coil placed near cortex. These E-fields result in induced currents on the cortex that change the ionic concentration outside the neurons, thereby disturbing the neuronal equilibrium established between ions across the neuronal membrane. Although simulations have been used to determine the profiles of these currents induced in a given medium, they have not been validated experimentally. In order to establish the trust quotient in not only the simulated studies done so far, but also the studies that will be conducted in the future, we aim to validate the simulated fields induced by a single pulse of TMS (the induced E-fields or, conversely, induced current densities) in a conducting medium of our choice (0.9 % NaCl saline solution). This was done by comparing the fields induced in saline, obtained from FEM simulations, with actual measurements of induced fields in the same

medium. The same phantom models were used to obtain simulated induced fields and measured induced fields.

Validating and Calibrating a simulated finite element model of transcranial magnetic stimulation (TMS) by measuring the electric field induced by a single pulse TMS

Ajay Venkateswaran, Niladri Mohanty, Mirza A Baig, Frederic Lesage, Amir Shmuel

Keywords: magnetic coil (MC), transcranial magnetic stimulation (TMS), finite element model (FEM), induced current density, figure-of-eight (FOE) coil, multi electrode array (MEA)

Acknowledgements:

This work was supported by a grant from the Natural Sciences and Engineering Research Council of Canada and the Canadian Institute of Health Research (**CHRP 385962-10**).

3.1 Abstract

Transcranial magnetic stimulation induces high magnitude electric fields on the cortex, which can modify cortical activity. Special probes and elaborate data acquisition schemes need to be used to measure these fields in vitro or in vivo. Alternatively, numerical analysis methods can provide a measure of these fields. However, the electric field magnitudes and profiles obtained through numerical analyses need to be validated with measurements. TMS induces primary and secondary fields in the vicinity of the stimulating coil. Here we introduce a method by which the electric fields induced in a conducting volume, simulated using numerical analysis involving finite element models, can be validated with experimental measurements. Electric fields induced in two saline based conducting volumes (phantoms), one smaller than the span of the stimulating coil and the other extending beyond the span of the stimulating coil, were simulated using finite element

analysis. The induced electric fields were also measured in two corresponding phantom models, using a generic data acquisition system in conjunction with regular neurophysiology probes in the same conducting volumes. The induced electric field profiles and magnitudes obtained from simulations were compared to results obtained from measurements. The results of the volumetric field distribution from the larger phantom (simulating an infinite half-plane) showed high correlation (Correlation Coefficient = 0.97) while the correlation values for the smaller phantom were low (Correlation Coefficient = 0.103). We hypothesize that the difference in field distribution between the larger phantom and smaller phantom arose from the role of the secondary fields in the cumulative field distribution in the two phantom models. We expect that finite element method provides an approximate solution of the total E-field calculations (Salinas et al., 2009), with the total simulated E-field calculation including the primary and secondary fields. We hypothesize that the measurements provide estimations of only primary induced fields. This interpretation is consistent with the high correlation between measured and simulated estimations of the fields in the larger phantom (where secondary fields are expected to be negligible). We further hypothesize that the smaller phantom resulted in secondary fields which the measurements were not, but simulations were able to estimate, resulting in low correlation between the measured and simulated field estimations. In conclusion, the results of simulated field distributions from the larger phantom, which were validated experimentally, provide a fair degree of confidence in the ability of simulations to predict induced field values correctly. However, additional work needs to be done to validate the field profiles in smaller conducting volumes. Achieving acceptable consistency of simulated results with measured results will enable us to extend our work to in-vivo experiments.

.

3.2 Introduction

The essence of magnetic stimulation lies in its non-invasive property. This said, however, the same property is also acting as a hindrance in learning more about the manner in which transcranial magnetic stimulation (TMS) affects neurons. Current literature displays contradicting observations making it difficult to generalize the effects of TMS. For instance, the delivery of continuous theta burst (cTBS) TMS pulses, a form of high frequency repetitive TMS (rTMS) protocol delivered in short bursts (Huang et al., 2005), has been shown to produce different neuronal effects. In some studies, continuous theta burst (cTBS) applied to the motor cortex suppressed motor evoked potentials (MEP) amplitudes (Huang et al., 2005; Ishikawa et al., 2007). In contrast, Benali et al. (2011) reported an increase in the fundamental (response to the first stimulus from a train of three closely spaced (temporally) stimuli) somatosensory evoked potential (SEPs) P_1N_1 amplitudes and MEP amplitudes, respectively, following cTBS conditioning. Huang et al. (2005) also reported that 15 Hz rTMS conditioning of the motor cortex had no effect on MEP amplitudes obtained from the contralateral hand whereas Wu et al. (2000) reported an increase in MEP amplitude after 15 Hz rTMS conditioning of the motor cortex. Conditioning of primary motor cortex (M1) in humans with 1 Hz rTMS resulted in a reduction in MEP amplitude in some studies (Casula et al., 2014; Maeda et al., 2000b) whereas in other studies 1 Hz rTMS did not demonstrate any effect on MEP amplitude (Filipović et al., 2010; Veniero et al., 2013). To resolve these contradictions and gain confidence about the effects of TMS, quantification and calibration of what is induced on the cortex in the first place is required. A major factor in determining the effect of TMS on neuronal

responses in a region is the electric field or current density that is induced by TMS in that region of the cortex. While much work has been done to use simulations for investigating the spatial distribution of the induced fields (Guizhi et al., 2005; Salinas et al., 2007) and their effects on the neurons (Abdeen and Stuchly, 1994), the validation of simulations of the induced electric fields has unfortunately not been explored to great degrees. A major impediment in this regard has been the inability of data acquisition systems (DAQs) to record the high amplitude TMS pulses, owing to their low dynamic ranges. The result of this limitation is that the pre-amplifiers of the DAQs, which process the measured signals, saturate which results in clipping of the measured signals, leading to a flat profile beyond the saturation value on the final recorded signal. This clipping results in faulty profile of the signals and measures obtained from such signals cannot be trusted.

Understanding the mechanisms of action of TMS has been the subject of active research. In TMS, current flowing through the stimulating coil produces a time varying magnetic field in its vicinity which induces a primary electric field (E-field) in the space surrounding the TMS coil. When a conductive medium (a volume conductor or a human head) is exposed to this induced E-field, charges accumulate at surfaces with different electrical conductivities creating a secondary E-field (Salinas et al., 2009). The nomenclature of primary and secondary E-fields should not be confused with similar nomenclature used in EEG/MEG studies where primary fields are associated with primary currents (which is due to neuronal conduction arising from action potentials, post synaptic potentials, etc. and is due to active conduction within the neuron) and secondary fields associated with secondary currents (which is due to volume conduction of the neuronal currents in the brain and results from passive conduction in the cortical medium). Thus, in TMS the source of the primary E-field is the current flowing in the stimulating coil and hence is a property of the coil whereas the source of the secondary E-field is charge accumulated at conductivity (media)

boundaries. The spatial distribution of E-fields induced in a conducting medium due to TMS pulses has been evaluated in phantoms (Salinas et al., 2009; Tay et al., 1989; Yunokuchi and Cohen, 1991), animal models ((Lisanby et al., 2001; Tay et al., 1989)), human model simulations (Opitz et al., 2011; Salinas et al., 2009; Thielscher et al., 2011) and, in a human epileptic patient with one intracranial electrode (Wagner et al., 2004a). The work by Wagner et al. (2004a) was a landmark study because they demonstrated a method for recording cortical current density induced due to a TMS pulse in a live human patient suffering from epilepsy. However, the induced current values were never compared to corresponding numerical simulations. Animal model studies performed to date suffer from the same limitation. The human model simulations had the opposite drawback because the studies were based on numerical solutions but did not have any validation from in vivo measurements. The electric fields induced in a medium due to a given magnetic coil (MC) have been reported in other studies (Cohen et al., 1990; Maccabee et al., 1990). The phantom model studies mentioned above suffered from limitations of the probes used to calculate the induced current. They used loaded probes with separation between the two wires of the probe extending to the range of millimeters. In addition, the probe was effectively a single electrode recording, and the lack of multi contact measurements increases the probability of reducing the accuracy of the measurements. Furthermore, the probes and data acquisition systems used in these studies were designed to specifically estimate the TMS induced E-fields from a matrix of potentials (magnitudes of which may scale to the order of few V) recorded by the electrodes in the conducting medium. This aspect reduced the sensitivity of the system to neuronal responses (the magnitudes of which are of the order of μV). In fact, all the measured induced electric fields reported in the studies above were calculated based either on mathematical models or by the use of pickup-coils/loaded probes/linear probes. Numerical methods provide ideal solutions whereas measurements provide

real-world data subject to noise. Measurements are also subject to some inherent variability depending on the manner in which the measurements were acquired (probe type, data acquisition system characteristics, etc.). A pickup coil can be used estimate the spatial distribution of the fields but it cannot provide absolute values of the induced fields for the reason that measurements depend its intrinsic characteristics such as the inductance of a the loop (which by itself is a function of the loop area and geometry of the loop) and on the manner in which the signals are acquired (differential vs. single ended). These tend to change the magnitude of the measured signals, thereby changing the measured current. Therefore, there is a need to develop a modular approach which can link ideal simulated solutions to measured data, and more importantly, define, calibrate and validate models based on experimental data. This will allow us to trust future simulated results and correctly interpret empirical observations.

Our study is motivated by the need to bridge the gap between simulated and experimental TMS domains, in order to enable us to understand how TMS affects neuronal behavior. The induced fields have been previously evaluated and validated in air (Salinas et al., 2007). However, no literature is available that exhaustively shows a large scale evaluation and validation of simulated induced fields in a conducting medium in the vicinity of a TMS coil, combining numerical modeling and experimental validation. Validating simulations of the induced fields and current density using a realistic head model should ideally be done in the intact brain, which is a conducting volume. However, before proceeding to validating simulations in the complex intact brain, it is desirable to test the concept in a controlled, simple environment. Here we present simulations of the fields induced by single pulse TMS in a conducting volume. We then evaluate these simulations by measurements using a neurophysiology recording system which can simultaneously record changes in neuronal responses to TMS too. The potential problems

associated with such a study and the potential developments that can be made to address the problems are discussed.

3.3 Materials and Methods

3.3.1 Phantom descriptions and measurement schemes

A "large" volume conductor (Maccabee et al., 1990) was used in order to avoid the effect of proximity of boundary conditions in simulations so that we could obtain more reliable current density profiles. The large volume conductor was used as a phantom model to test the closeness of measurement results with corresponding simulated results. All simulations in this study were performed on the finite element platform of CST EM Studio Low Frequency (LF) frequency domain solver (Computer Simulation Technology AG, Darmstadt, Germany). These low frequency electromagnetic fields range from 0 Hz to 100 kHz. The large volume conductor constituted of a rectangular phantom measuring 510 mm in length (l) and 255 mm in width (w) and 310 mm in height (h) (Figure 3-1). The uniform thickness ($t_{phantom}$) of the glass walls shown in Figure 3-1 (a) was measured at 3 mm. In this experimental setup, the figure-of-eight (FOE) coil was held parallel to the face of the phantom. There was no rotation in the coil either relative to the transverse, longitudinal or vertical axis of the phantom. The effective face of the coil was placed at a distance of 10 mm from the face of the phantom. The center of the coil was positioned 90 mm lower than the top edge of the phantom tank (a constraint based on the depth to which our multi electrode array (MEA) could go before the DAQ connectors came precariously close to touching the surface of saline in the tank). This experiment setup was used to obtain the current densities on defined planes while moving deeper into the conducting volume (0.9 % saline solution) along the

vertical axis of the phantom, over a large region of interest. Each plane of measurements consisted of 21 points parallel to the face of the coil (at a sampling resolution of 10 mm) from where signals were recorded. Similarly measurements were conducted at 13 different points (at a resolution of 6 mm) normal to and away from the face of the coil. Nine such planes (with 10 mm separating adjacent planes) were used to record our measurements from resulting in a 21×13×9 matrix of induced field potentials. The plane definition is shown in Figure 3-1(b). The depths traversed are shown in Figure 3-1 (c).

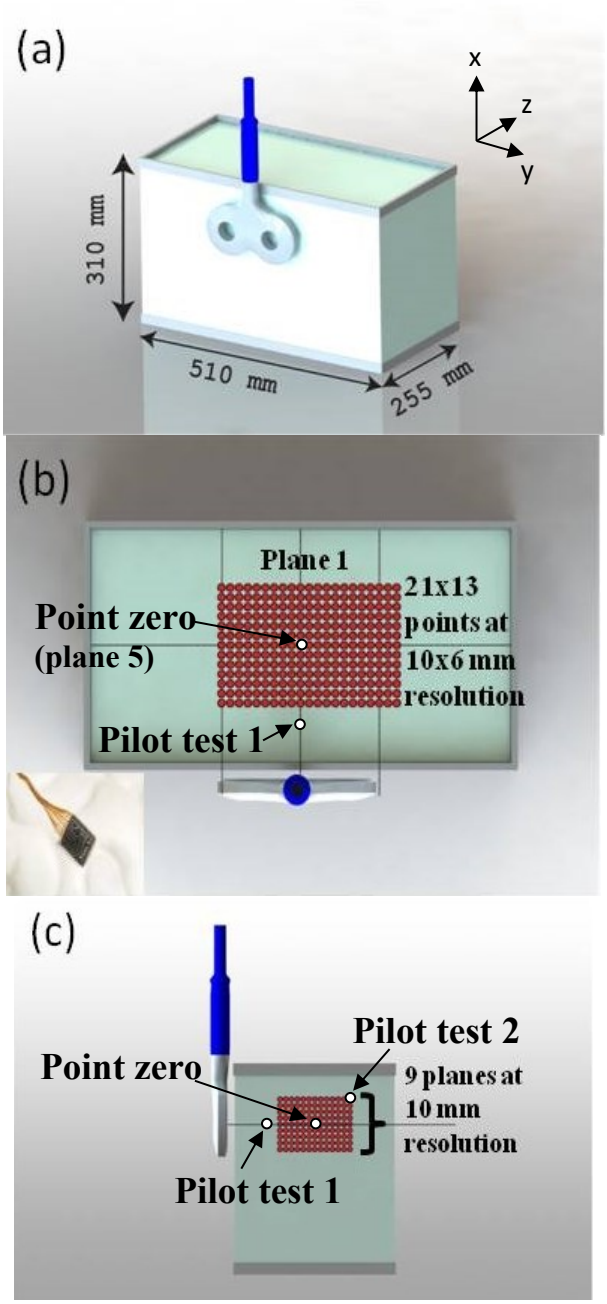

Figure 3-1. Simulation and experimental setup plan to calibrate induced current densities at different points in a medium within a large volume. (a) An isometric view of the setup plan. (b) Top view of the setup plan with outlined data acquisition positions (marked by the red dots) forming a region of interest (denoted by the rectangular grid formed by the red dots). The axes passing through the center of the coil, the outer perimeters of the coil and center of the square cross-section of the phantom are shown by the vertical and horizontal dotted black lines forming crosshairs. (c) Translation of the MEA along the depth of the phantom to obtain 8 additional planes (9 including the first plane defined in (b)).

In another setup, our objective was to study the effect of edge reflections (reported in the work of Salinas et al. (2009)) and gauge the extent to which such reflections can impact the validation of fields induced by TMS obtained from simulations with those obtained through measurements. In order to achieve that, a "small" volume conductor (Maccabee et al., 1990) was used which constituted of a cuboidal phantom filled with saline Figure 3-2 (a). The reflections come into existence as soon as volume being influenced by TMS starts approaching the size of the of the TMS coil, as explained by Salinas et al. (2009) based on the work by Tofts (1990). Our phantom in (Figure 3-2) is smaller than the wingspan of the butterfly coil and thus, ensures that we would obtain strong reflections from the phantom edges.

Our phantom was filled with saline up to a height (*h'*) of 180 mm. The inner volume of the phantom had a tapering trapezoidal base (Figure 3-2 (c)). This may result in asymmetric reflection from the bottom surface of the phantom, especially considering the small volume of induction and hence needed to be included in the 3D model. In this experimental setup, the figure-of-eight (FOE) coil was held parallel to the face of the phantom. There was no rotation in the coil either relative to the transverse, longitudinal or vertical axis of the phantom. The effective face of the coil (which is the one facing the phantom) was positioned at a distance of 10 mm from the face of the phantom. This experimental setup was used to obtain the current densities on a defined plane at different depths of saline along the vertical axis of the phantom. Each plane of measurements consisted of 21 points parallel to the face of the coil (at a sampling resolution of 3 mm) from where signals were recorded. Similarly measurements were conducted at 9 different points (at a resolution of 3 mm) normal to and away from the face of the coil. Seventeen such planes (with 3 mm separating adjacent planes)

were used (Figure 3-2 (c)) to record our measurements resulting in a 21×9×17 matrix of induced field potentials. A non-symmetrical data acquisition strategy was chosen for the small volume phantom. The relatively high resolution of data points which required manual positioning of the array using micro-manipulators was the governing factor in our choice. The small volume had a square cross section. Since the coil was positioned along the midline of the square cross section, the fields on either side of the midline would be symmetric. Hence, we obtained measurements on one half section with a small extension of the recordings on the other half.

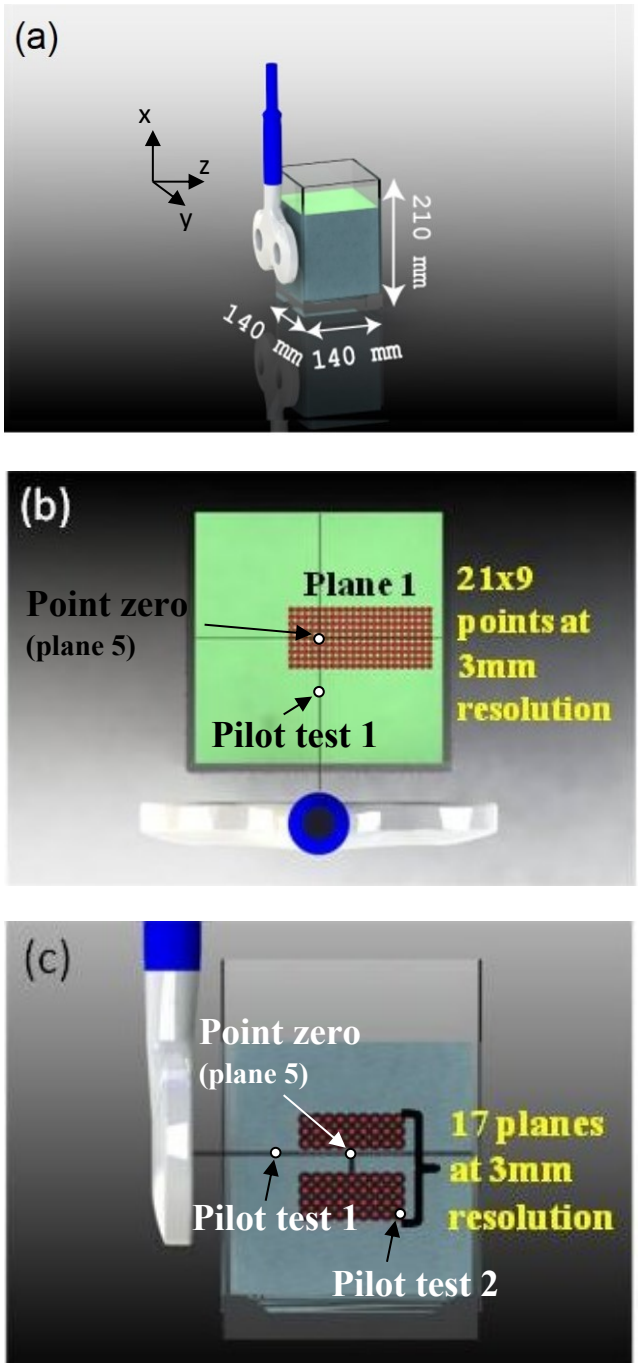

Figure 3-2. Simulation and experimental setup plan to calibrate induced current densities at different points in a medium within a small volume. (a) An isometric view of the setup plan. (b) Top view of the setup plan with outlined data acquisition positions (marked by the red dots) forming a region of interest (denoted by the rectangular grid formed by the red dots together) named Plane 1. The axes passing through the center of the coil and center of the phantom are shown by the vertical and horizontal dotted black lines forming a crosshair. (c) Translation of the MEA along the depth of the phantom to obtain 16 additional planes (17 including the first plane defined in (b)).

Dielectric constant (63), conductivity (1.45 S/m) and density (1004.6 kg/m^3) of normal saline were obtained from Stogryn (1971), (1989) and Maidment (1993), respectively.

Two pilot experiments were conducted in order to choose the optimum TMS pulse intensity for small and large volumes. For the first pilot experiment, the array was brought in line with center of the coil and equidistant from the lateral walls of the phantom (point zero). Figure 3-1 and Figure 3-2 show the point zero, pilot test1 and pilot test 2 points in each setup. The minimum distance between the coil and array is 91.5 mm in the large volume and 58 mm in the small volume. In order to be conservative, pilot test 1 was conducted to measure the strength of the induced fields at a distance of 68.5 mm from the coil in the large volume and 35 mm from the coil in the small volume. Similarly, the maximum distance between the coil and array is 113.56 mm in the large volume and 61.18 mm in the small volume. Pilot test 2 was conducted to measure the strength of the induced fields at a distance of 113.56 mm from the coil in the large volume and 61.18 mm from the coil in the small volume. The pilot test points for the large and small volumes are shown in Figure 3-1and Figure 3-2, respectively. Hence, if we chose our intensity (near the saturation limit) based on the distances mentioned above, the signal would neither saturate, nor overly decay (because TMS induced fields decay rapidly as the square root of distance from the surface closest to the stimulating coil (Pascual-Leone, 2002)) during the course of the planar recording paths.

3.3.2 Recording electrode

A planar Utah multi-electrode array (MEA; Blackrock Microsystems, Salt Lake City-UT, U.S.A) was used for the electrophysiological recordings (Figure 3-3). The array was suspended in the saline medium at different positions to acquire current flow in the medium (in terms of potential

variations) from those specific locations. At any given position, the array was positioned parallel to the face of the coil with the electrodes on the array (projecting perpendicularly from the base package of the array) facing the coil: the array was always parallel to the plane of the FOE coil and the electrodes on the array were oriented parallel to the normal of the face of the coil, oriented towards the face of the coil. The array is MRI and TMS compatible and hence did not show any induction when subjected to TMS field while being suspended in air with the connector package shielded with aluminum foil. The entire setup was protected from stray electromagnetic fields, arising from the electronic devices present in the experiment room, by enclosing it in a Faraday cage. The array behaves as an eddy current probe (Salinas et al., 2007, 2009) and records the primary induced field.

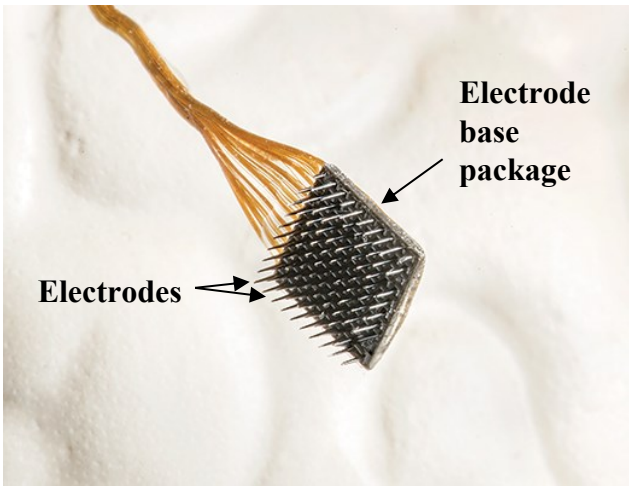

Figure 3-3. The multi electrode array (MEA; Blackrock Microsystems) used for all measurements. The picture shows 96 electrodes (arranged in a 10 × 10 grid, one electrode at each corner being inactive) spaced 400 µm apart. Each electrode shaft is 1 mm long. The connectors are made of gold wiring.

3.3.3 Measurement setup

The measurement setup to record the induced current densities in the small and large volumes is shown in Figure 3-4 (a). The setup was assembled on a stereotaxic frame with micro-manipulators to adjust the position of the array. Since the array package was flexible due to its long wire bundle, a special plastic holder was designed to secure it from bending. In order to further secure the array, the connector package was sewn to the adapter with nylon threads (to prevent array movement when the DAQ tethers were attached or moved during position change) and packed with Surgifoam (Ferrosan, Søborg, Denmark) along the entire length of the connecting wire bundle followed by securing the Surgifoam with insulation tape. For localization of the array in the phantom, we used laser diode pointers in conjunction with grids marked on the phantom with a permanent marker, at a resolution of 10 mm (using a ruler), to mark the reference position of the array (position zero) in saline. One of the laser pointers was also used to align the center of the FOE coil to position zero, as shown in Figure 3-4 (b) and (c). Hence, after a re-attachment of the tethers, the array could be moved to the reference position marked by the laser grid and then moved relative to the reference position. All the ferromagnetic components of the experiment setup were then wrapped in aluminum foil to provide adequate shielding from stray TMS fields. In addition to this, the entire setup was placed within a Faraday cage to avoid electromagnetic contamination from other electrical devices present in the experiment room.

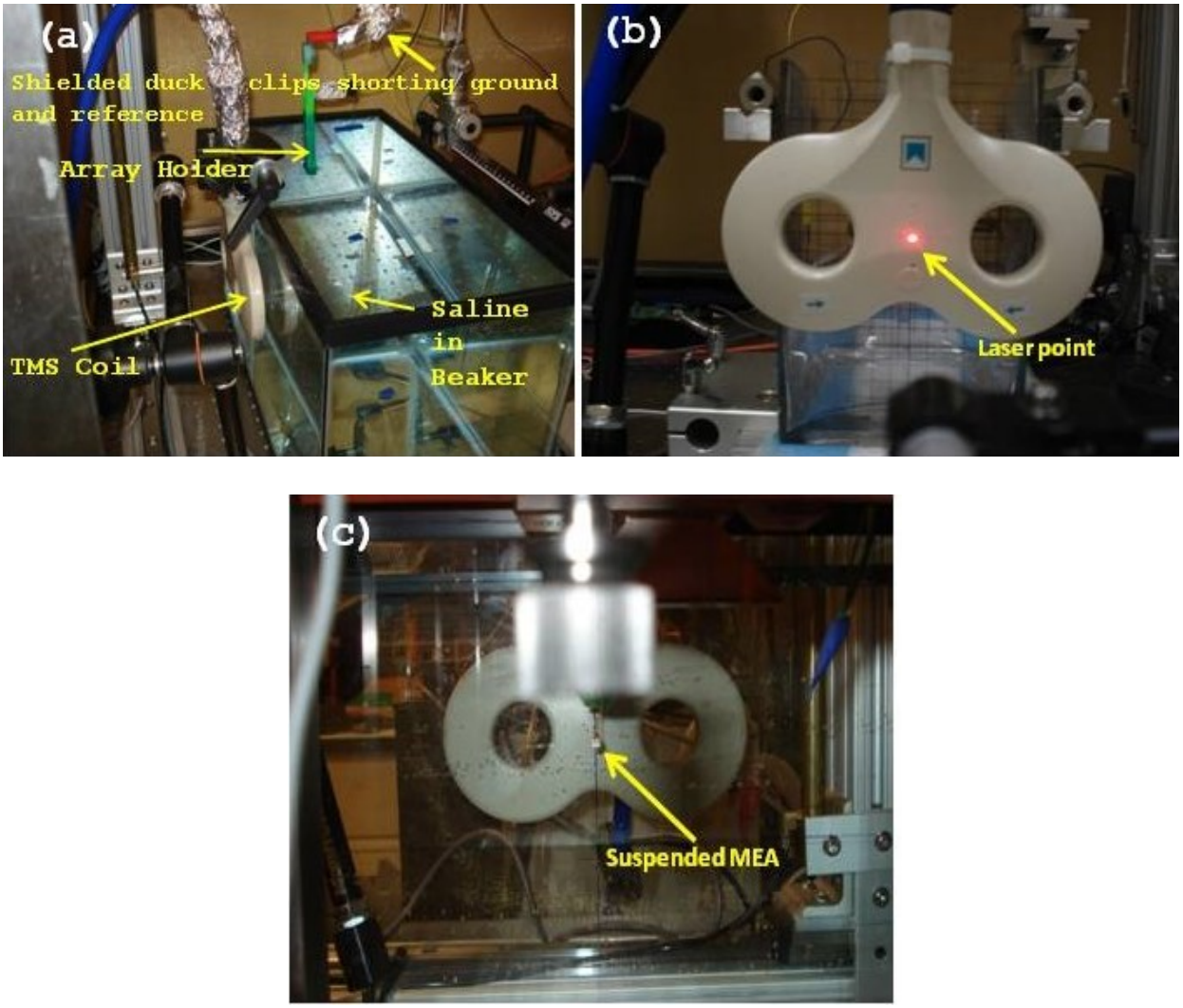

Figure 3-4. Setup to measure current density in the large volume. (a) Complete setup with proper shielding of all parts and the Faraday cage used for global shielding from electromagnetic interferences. (b) Localization of the center of the coil with the MEA suspended in the phantom using laser pointers. The electrode lies behind the coil, in line with the laser point and the center of the coil. (c) Localization of the center of the coil with the MEA suspended in the phantom using laser pointers. The laser pointer lies behind the coil, in line with the MEA and the center of the coil.

3.3.4 Transcranial magentic stimulation (TMS) and delivery protocol

TMS pulses were delivered using a Magstim Rapid TMS stimulator (Magstim, Whitland, UK), producing a biphasic waveform, through a 70 mm butterfly coil, also known as a figure-of-eight (FOE) coil.

3.3.5 Data acquisition

In order to optimize dataset size and facilitate analysis, we used 32 out of the available 96 electrodes on the MEA for recording data. The electrophysiology data were acquired on a Digital Lynx® SX module (Neuralynx, Bozeman, MT, U.S.A.), at a sampling rate of 32 KHz. The Digital Lynx was chosen due to its distinct advantages of having a substantially large dynamic range (± 132 mV) which prevents saturation of the signals at relatively low TMS stimulus intensities. The Magstim TMS module was controlled by external triggers generated by a National Instruments board operated by a custom made Labview module on the backbone of the software supplied by National Instruments. The trigger pulses were recorded on Labview at 10 KHz. The Digital Lynx system and Labview module were synchronized by a TTL pulse generated by Digital Lynx and recorded by the Labview module.

3.3.6 Theory

Measured data

Most work concerning TMS is with regard to the neuronal responses to the currents induced in the cortex due to TMS. However, to investigate the mechanisms underlying TMS, it is mandatory to measure the induced E-fields in the medium due to TMS. Electrophysiological electrode recording reflects the induced E-field in the form of potential. A grid of measurement points along with a reference point can provide a map of the differential current density which can be measured between any point on the grid and the reference point. Wagner. et al. (2004a) had proposed a method to calculate the differential current density in 1-dimension. Our extension of the method (assuming no displacement current) to 2-dimension plane is

$$\vec{J}_i = \sigma \vec{E} = \sigma\left(-\nabla V\right) = -\sigma\left(\nabla V\right) = -\sigma\left(\frac{V_i - V_{ref}}{d}\hat{d}\right) \tag{3.1}$$

where, $\vec{J}_i$ is the differential current density between i^{th} position and the reference position in A/m^2, V_i is the potential recorded by the i^{th} position electrode in Volt, V_{ref} is the potential recorded by the reference position electrode in Volt, d is the magnitude of displacement between the i^{th} position and the reference position (chosen as the center of the conducting plane) of the MEA, $\hat{d}$ is the unit vector in the direction of displacement and σ is the homogenous conductivity of the medium in S/m. (assumed to be homogenous and isotropic for our study). Since we assumed a homogenous conductive medium, (3.1) is valid because the term $(V_i - V_{ref})/d$ is a good approximation of the gradient of potential at that point. Additionally, the assumption of the medium being isotropic implies that there is no polarization. The schematic for our calculations is shown in Figure 3-5. Obtaining the current density of each point over the entire grid profile provides the differential current density map over our region of interest. The differential current density also holds an advantage in that all common mode signals including analog ground of the DAQ and panel ground of the electrophysiology signal acquisition board, which are common to all recording positions, get eliminated. Therefore, we end up with a more reliable current density map that can be compared to simulations. Simulations will give us electric fields and current densities with respect to ideal grounds and infinity. Therefore, a differential current density of simulated results too will avoid these common mode signals for comparison with measured profile. Hence, we end up comparing equivalent profiles.

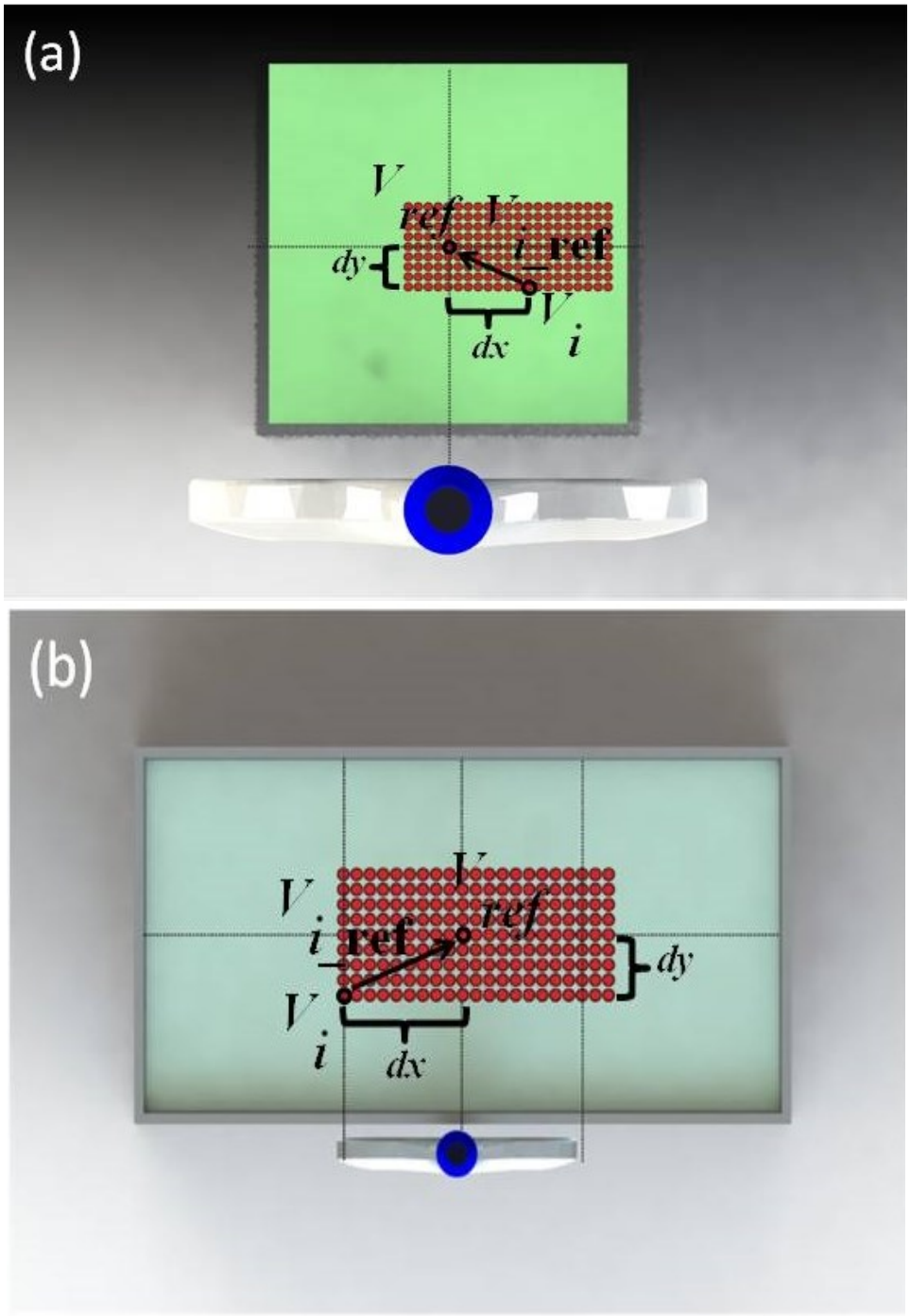

Figure 3-5. (a) Location definitions on plane for the small volume measurements. (b) Location definitions on plane for the large volume measurements and simulations. The reference point is in the middle of each conducting volume, in line with the axis passing the center of the coil. dx and dy represent the displacements of any given i^{th} position from the reference point. The potentials at the reference points and the i^{th} location have been marked as V_{ref} and V_i, respectively and the gradient vector between these points has been marked by V_{i_ref}, the direction of which is given by the arrow.

The potential amplitudes V_i and V_{ref} that are recorded during measurement translate to the following,

$$V_i = V_{i0} - V_{analoggnd} - V_{panelgnd} - V_{baseline}^{noise} \; ; \; V_{ref} = V_{ref0} - V_{analoggnd} - V_{panelgnd} - V_{baseline}^{noise} \tag{3.2}$$

where, V_{i0} is the absolute potential of the i^{th} location, V_{ref0} is the absolute potential of the reference location, $V_{analoggnd}$ is the potential of the analog ground of the data acquisition system, $V_{panelgnd}$ is the potential of the ground on the digital reference selection (DRS) board receiving the signals from the electrodes and transferring them to the DAQ, and $V_{baseline}^{noise}$ is the baseline noise associated with the recording setup. $V_{analoggnd}$, $V_{panelgnd}$ and $V_{baseline}^{noise}$ form a common mode signal and can vary depending upon multiple factors such as recording setup, type of data acquisition system used to record the signals, the type of electrodes used, etc. Hence it is close to impossible to generalize this common mode signal to different scenarios. We therefore used differential signals.

$$V_{ref\_i} = V_i - V_{ref} \tag{3.3}$$

Where,

$$\begin{aligned} V_i &= \left(V_{i0} - V_{analoggnd} - V_{panelgnd} - V_{baseline}^{noise}\right) \;\; \&, \\ V_{ref} &= \left(V_{ref\,0} - V_{analoggnd} - V_{panelgnd} - V_{baseline}^{noise}\right) \end{aligned} \tag{3.4}$$

Thus, when Equation (3.4) is inserted in Equation (3.3), Equation (3.3) eliminates the common mode signals. The displacement between the i^{th} location and the reference location is given by,

$$\vec{d}_{ref\_i} = \left(-dx\right)\hat{i} + \left(dy\right)\hat{j} \tag{3.5}$$

$$\vec{E} = -\nabla V \tag{3.6}$$

$$\vec{E}_{ref\_i} = -\nabla V_{ref\_i} = -\left(\frac{V_{ref\_i}}{-dx}\hat{i} + \frac{V_{ref\_i}}{dy}\hat{j}\right) \tag{3.7}$$

Resolving $\vec{E}_{i\_ref}$ along the *x* and *y* axes yields,

$$\vec{E}_{ref\_i} = \vec{E}^{x}_{ref\_i} + \vec{E}^{y}_{ref\_i} = \left(\frac{V_{ref\_i}}{dx}\hat{i} - \frac{V_{ref\_i}}{dy}\hat{j} \right) = \left(\frac{V_{ref\_i}}{dx}\hat{i} + \frac{V_{i\_ref}}{dy}\hat{j} \right) \tag{3.8}$$

Where $\vec{E}^{x}_{ref\_i}$ and $\vec{E}^{y}_{ref\_i}$ are components of the vector $\vec{E}_{ref\_i}$ along the *x* and y axes, respectively.

The current density associated with this electric field is given by Ohm's law as,

$$\vec{J}_{ref\_i} = \sigma\, \vec{E}_{ref\_i} = \sigma \left(\vec{E}^{x}_{ref\_i} + \vec{E}^{y}_{ref\_i} \right) = \sigma \left(\frac{V_{ref\_i}}{dx}\hat{i} + \frac{V_{i\_ref}}{dy}\hat{j} \right) \tag{3.9}$$

$$\left| \vec{J}_{i\_ref} \right|_{measured} = \sqrt{\left(\sigma \frac{V_{ref\_i}}{dx} \right)^2 + \left(\sigma \frac{V_{i\_ref}}{dy} \right)^2} \tag{3.10}$$

Simulated data

Finite element model simulations yield idealized results by solving Maxwell's equations in the simulation domain. The solutions are based on assumptions of boundary conditions (Dirichlet, Neumann, radiation or absorbing) and global references. CST EM Studio Low Frequency domain solver used Dirichlet boundary conditions or fixed boundary conditions (since such a boundary condition specifies scalar values that a solution needs to converge to along the boundary of the domain) to solve boundary value problems. The potentials that can result from simulations, therefore, tend to be free of common mode artifacts. However, they also suffer from the assumption that the global references that are used to calculate such potentials are with respect to pure ground located at infinity. A feature of simulations is that one need not obtain the potential at different points in order to calculate the induced fields. Simulations can directly output the induced field profiles (induced E-fields or conversely, induced current density). With measurements, this is not

possible because the fundamental recording entity is in the form of potential, which needs to be used to perform further calculations to obtain the induced fields. As mentioned earlier, simulated field values are based on references which assume ideal ground located at infinity. The best method, therefore, to remove the effect of this assumption from simulations is by using differential signals in simulated data too. This ensures that we compare differential profile maps of measured and simulated data, with measured differential profiles devoid of common mode signals and simulated data devoid of the effect of ideal ground assumption. Hence, we would end up comparing equivalent profiles.

$$\vec{J}_i = \vec{J}_{ix}^{real} + \vec{J}_{ix}^{imaginary} + \vec{J}_{iy}^{real} + \vec{J}_{iy}^{imaginary} + \vec{J}_{iz}^{real} + \vec{J}_{iz}^{imaginary} \tag{3.11}$$

$$\vec{J}_{ref} = \vec{J}_{refx}^{real} + \vec{J}_{refx}^{imaginary} + \vec{J}_{refy}^{real} + \vec{J}_{refy}^{imaginary} + \vec{J}_{refz}^{real} + \vec{J}_{refz}^{imaginary} \tag{3.12}$$

where, $\vec{J}_i$ and $\vec{J}_{ref}$ are the ideal (with reference to ground at located at infinity) and absolute current densities, obtained with respect to ideal grounds located at infinity, for the i^{th} and the reference locations. For our simulations, frequency dependent characteristic of permittivity of saline was not taken into account (achieved by setting the loss tangent to zero value). Complex permittivity of saline was, therefore, replaced by only the real part of the complex permittivity. Since the imaginary part of permittivity was ignored, the imaginary components of current densities shown in Equations (3.11) and (3.12) would be zero. The imaginary components have been included in equations for correct representation of formula. Since our region of interest extends in x-y plane, ignoring the z component of the fields yields,

$$\vec{J}_i = \vec{J}_{ix}^{real} + \vec{J}_{ix}^{imaginary} + \vec{J}_{iy}^{real} + \vec{J}_{iy}^{imaginary} \tag{3.13}$$

$$\vec{J}_{ref} = \vec{J}_{refx}^{real} + \vec{J}_{refx}^{imaginary} + \vec{J}_{refy}^{real} + \vec{J}_{refy}^{imaginary} \tag{3.14}$$

$$\vec{J}_{ref\_i} = \vec{J}_i - \vec{J}_{ref} \tag{3.15}$$

$$\begin{aligned} \vec{J}_{ref\_i} = &\left(\vec{J}_{ix}^{real} + \vec{J}_{ix}^{imaginary} + \vec{J}_{iy}^{real} + \vec{J}_{iy}^{imaginary}\right) - \\ &\left(\vec{J}_{refx}^{real} + \vec{J}_{refx}^{imaginary} + \vec{J}_{refy}^{real} + \vec{J}_{refy}^{imaginary}\right) \end{aligned} \tag{3.16}$$

$$\begin{aligned} \Rightarrow \vec{J}_{ref\_i} = &\left\{\left(\vec{J}_{ix}^{real} - \vec{J}_{refx}^{real}\right) + \left(\vec{J}_{ix}^{imaginary} - \vec{J}_{refx}^{imaginary}\right)\right\} + \\ &\left\{\left(\vec{J}_{iy}^{real} - \vec{J}_{refy}^{real}\right) + \left(\vec{J}_{iy}^{imaginary} - \vec{J}_{refy}^{imaginary}\right)\right\} \end{aligned} \tag{3.17}$$

$$\Rightarrow \vec{J}_{ref\_i} = \sigma\left[\begin{array}{l} \left\{\left(\vec{E}_{ix}^{real} - \vec{E}_{refx}^{real}\right) + \left(\vec{E}_{ix}^{imaginary} - \vec{E}_{refx}^{imaginary}\right)\right\} + \\ \left\{\left(\vec{E}_{iy}^{real} - \vec{E}_{refy}^{real}\right) + \left(\vec{E}_{iy}^{imaginary} - \vec{E}_{refy}^{imaginary}\right)\right\} \end{array}\right] \tag{3.18}$$

Since imaginary component is zero,

$$\vec{J}_{ref\_i} = \sigma\left\{\left(\vec{E}_{ix}^{real} - \vec{E}_{refx}^{real}\right)\right\} + \left\{\left(\vec{E}_{iy}^{real} - \vec{E}_{refy}^{real}\right)\right\} \tag{3.19}$$

$$\left|\vec{J}_{ref\_i}\right|_{simulated} = \sigma\left|\vec{E}_{ref\_i}^{x} + \vec{E}_{ref\_i}^{y}\right| \tag{3.20}$$

The overall differential current density map over the entire region of interest can then be obtained by collecting the current densities obtained for individual points and arranging them in a matrix (refer equation (3.21)). In Equation (3.21) point numbered 7 is used as the reference position such that $\mathbf{7} \subseteq \mathbf{n}$ where n is the total number of points defining the region of interest. The differential current density maps obtained from measurement and simulation could then be compared and analyzed to see the difference/similarity between simulated and measured induced current density maps.

$$J_{measured} = \begin{bmatrix} | & | & & | \\ | & | & & | \\ | & | & \sqrt{\left(\sigma\frac{V_{7\_7}}{dx}\right)^2 + \left(\sigma\frac{V_{7\_7}}{dy}\right)^2} & | \\ | & | & | & | \\ \sqrt{\left(\sigma\frac{V_{7\_1}}{dx}\right)^2 + \left(\sigma\frac{V_{1\_7}}{dy}\right)^2} & \sqrt{\left(\sigma\frac{V_{7\_2}}{dx}\right)^2 + \left(\sigma\frac{V_{2\_7}}{dy}\right)^2} & -- & \sqrt{\left(\sigma\frac{V_{7\_j}}{dx}\right)^2 + \left(\sigma\frac{V_{j\_7}}{dy}\right)^2} \end{bmatrix} \quad \sqrt{\left(\sigma\frac{V_{7\_n}}{dx}\right)^2 + \left(\sigma\frac{V_{n\_7}}{dy}\right)^2}$$

and,

$$J_{simulated} = \begin{bmatrix} | & | & | & | & |\bar{J}_{7\_n}| \\ | & | & | & | & | \\ | & | & |\bar{J}_{7\_7}| & | & | \\ | & | & | & | & | \\ |\bar{J}_{7\_1}| & |\bar{J}_{7\_2}| & -- & |\bar{J}_{7\_(j-1)}| & |\bar{J}_{7\_j}| \end{bmatrix} \tag{3.21}$$

3.3.7 Data Analysis

Electrophysiology signals corresponding to five TMS pulses in a trial were averaged to obtain a single averaged electrophysiology signal for that particular TMS trial. There were two distinct analyses that were performed on the recorded data depending upon whether it was a pilot experiment or recording the potentials over a desired region of interest.

In the case of pilot experiments, the goal was to first determine the intensity of TMS at which the induced current in the saline medium (in which the recording electrode array was submerged)

caused the DAQ pre-amplifier to saturate. In order to achieve this, we varied TMS intensity starting with 1 % of maximum stimulator output (MSO) and increasing in steps of 1 % MSO till 15 % MSO intensity was reached. After this, TMS intensity was increased in steps of 5 % (20-50 % MSO) and 10 % (50-100 % MSO). Thus, 27 measurements were recorded at an inter-trial separation of 10 s, with the position of the MEA remaining constant. Each measurement consisted of 5 pulses at a given TMS intensity. The responses to the 5 pulses in each trial were averaged to obtain one averaged TMS induced pulse. Figure 3-6 (b) presents the voltage recorded across 32 channels of the Utah array for a specific TMS pulse intensity for the pilot position of the array in saline. The recorded potentials across the 32 channel grid were again averaged to obtain one average induced potential profile, for a given TMS intensity. Since the spatial distribution of the 32 electrodes did not exceed a few square millimeters, the induced field in such a small region is approximately constant due to which the potentials across all 32 electrodes could be assumed to be similar (as can also be observed in Figure 3-6 (b)). The average signal of 32 electrodes, therefore, did not differ much from the potential recorded by any individual electrode. In addition to that, there was an advantage that the averaged signal had higher signal-to-noise ratio (SNR) compared to a signal recorded from one electrode. Continuation of this process for all 27 conditions provided the entire range of induced triphasic (a biphasic current pulse in the coil induces a triphasic current in the induction medium due to Faraday's law of induction) current signals in saline over a wide range of TMS intensities. Close observation of the upper and lower limits of each of these pulses revealed the TMS intensities which cause the pre-amplifier to saturate (which in the case of our DAQ was ±131072 μV).

Additionally, each averaged (over 32 electrodes) potential signal per trial (within a one second window extending 0.5 s before the onset of TMS and 0.5 s from the onset TMS pulse) was

converted to the frequency domain by a Fast Fourier Transform (FFT). There, we clearly observe that the peak magnitude of the signal corresponded to 3.35 KHz. This value of frequency was used later to define the solution frequency for all of our simulations.

The measurements for the main experiment were conducted over the regions of interest (ROIs) defined in Figure 3-1 (a) and Figure 3-2 (b) for the large and small volume setups, respectively. Each trial represented a variation in the position of the MEA in the saline solution, with the TMS intensity remaining constant. The selection of constant TMS intensities for the individual small and large volume setups were based on the same set of pilot experiments performed on each setup separately. The reason to identify separate threshold intensities for small and large volumes arises from the fact that the sizes of the conducting volumes in the two setups are different. Therefore, the proximal edges of the planes of measurement defined for the small volume setup will be closer to the TMS coil compared to the edges of the planes of measurement defined for the large volume setup. The conducting medium and stimulating coil is the same for both setups. Therefore for a fixed intensity of TMS pulse, points closer to the stimulating coil will record higher values of induction. Due to this, the threshold TMS pulse intensity for the sets of planes for each setup may be different. For example, if we refer to Figure 3-7 (a), the midpoint (location of the point along the midline of the coil) on the proximal edge of the measurement plane in the small volume is at a distance of 68 mm (58 mm + 10 mm (distance of the coil from the phantom)) from the coil. We can refer to this midpoint as MIDPOINT_A. The equivalent midpoint on the proximal edge of the plane in the large volume (MIDPOINT_B in Figure 3-7 (b)) is at a distance of 101.5 mm (91.5 mm + 10 mm (distance of the coil from the phantom)) from the coil. If same intensity of TMS pulse is used for induction in the small and large volume setups (for example X % of MSO), MIDPOINT_A may measure a higher value of induction compared to MIDPOINT_B because

MIDPOINT_A is much closer to the coil than MIDPOINT_B. For a certain value of TMS stimulation intensity (Y % of MSO where Y>X), the induction at MIDPOINT_A may be of sufficient amplitude to saturate the pre-amplifier, while the induction at MIDPOINT_B may not be of sufficient amplitude to saturate the pre-amplifier. Of course, there may be a TMS pulse intensity, Z % of MSO (Z>Y>X), which may result in sufficiently high induction at both MIDPOINT_A and MIDPOINT_B to cause saturation of the pre-amplifier in both cases. For all the mentioned reasons, it is prudent to measure the threshold stimulation intensities of the two setups (small and large volumes) separately. The average magnitude of the induced current density signal (based on the theory discussed in the previous section) was obtained for each point on a specific plane and the current density profile across the entire plane was obtained. The cumulative results from individual planes were able to provide us the volumetric field distributions.

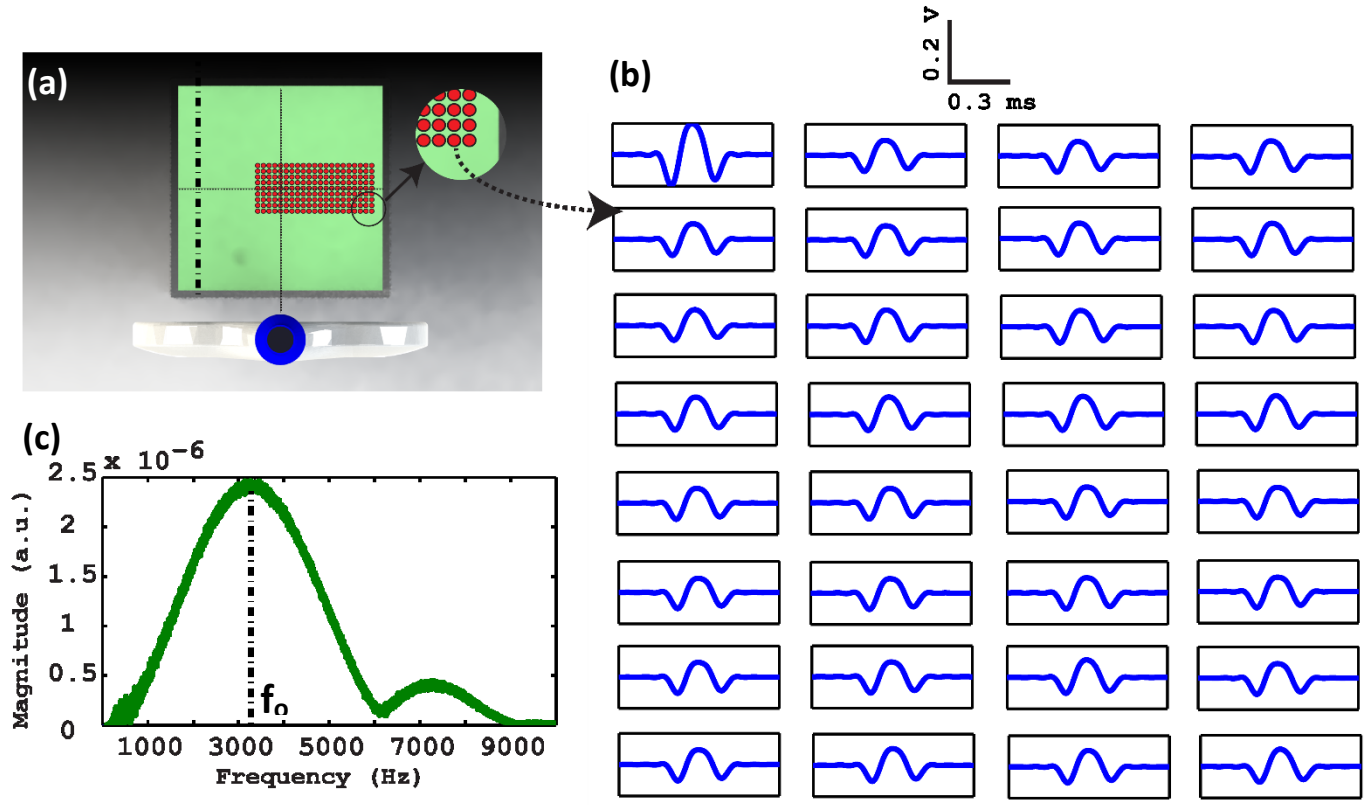

Figure 3-6. (a) ROI defined by the grid of recording locations (marked by the red dots) with a magnified image of the grid. At one such location in the grid (or one red dot) shown by the tail of the dotted curved arrow we get (b) which is a representation of the TMS induced current density spike in the form of a triphasic potential waveform recorded by each of the 32 electrodes at that particular red dot location. 32 such voltage profiles are obtained at each of the 189 red dot points (21x9) defining the ROI of each of the 17 planes. (c) FFT analysis of the averaged signal of all 32 electrodes (in a 1 s window; 0.5 s before the onset of the TMS pulse and 0.5 s from the onset of TMS pulse) to depict the operating frequency, f_0, of TMS corresponding to the peak magnitude of the signal. Note that while we present here the range of 0-10K Hz, the power extends asymptotically towards infinity.

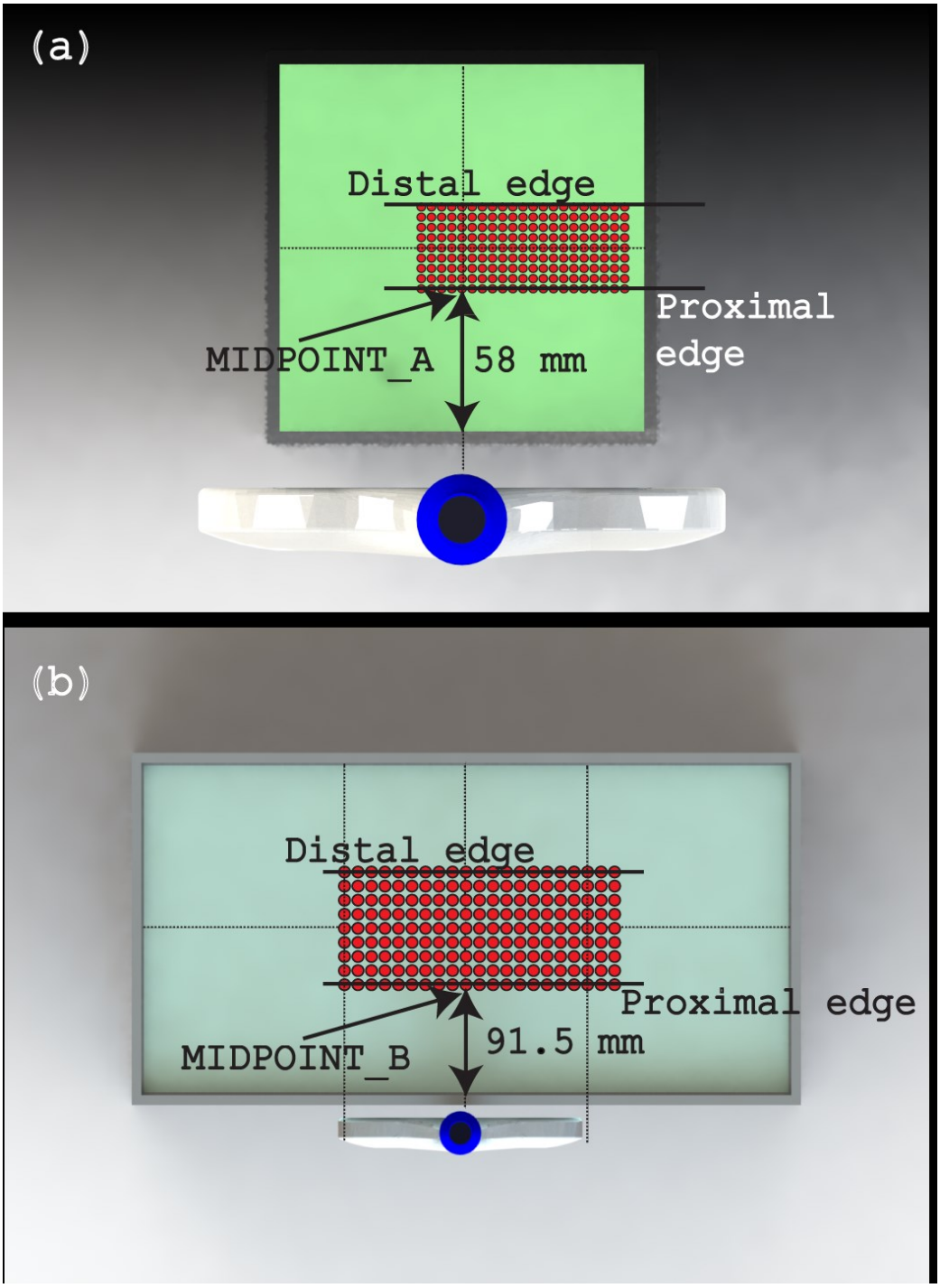

Figure 3-7. Comparison of distances of the measurement planes (ROIs) from the face of the coil in the case of (a) the small volume setup and, (b) the large voume setup.

3.3.8 Development of Single Turn FOE TMS Coil Model

Based on the FFT results obtained in the previous section, each biphasic current pulse was defined to have a pulse frequency of 3.35 KHz and correspondingly, a time period of 300 μs.

Simulations to simplify the realistic butterfly coil geometry

TMS Coil

The effect of TMS is dependent on the geometry of the coil that is used for stimulation. We have considered a 70 mm figure-of-eight coil for our study. The major advantage with this kind of coil over some other coil shape, for example a circular coil, is its increased focality and penetration power (Guizhi et al., 2005; Pascual-Leone, 2002). Since the stimulating coil is an integral part of TMS, a model that is as close to the real coil in shape, size and profile is vital for simulating the TMS process. Simpler coil designs can then be designed based upon the results obtained from the actual coil model.

We based the design of the coil for our simulation on a real 70 mm butterfly coil provided by Magstim. X-ray images of the actual butterfly coil, shown in Figure 3-9 (a), were used to create a three dimensional realistic butterfly coil model on SolidWorks (Dassault Systèmes, Vélizy-Villacoublay, France,). An important aspect in the development of the coil model was not to get carried away with model complications as that in turn would only lead to large simulation time, as demonstrated later in the current section. The developed model was healed numerous times in order to eliminate overlapping and intersecting triangles, rough edges and material discontinuity (which is important in order to eliminate reflections and losses which in turn have a huge bearing on the performance of a device). The final realistic TMS coil model is shown in Figure 3-8 (b). The developed coil model was then exported to CST EM Studio (Computer Simulation

Technology AG, Darmstadt, Germany) Low Frequency module in a stereolithographic (STL) format for simulating the fields induced due to a current in the modeled coil. STL is a 3-D computer aided design (CAD) file format in which the STL volumes (or objects) are primarily a collection of triangular surface element mesh, which means that STL objects only define the surface geometry of a 3-D object. One cannot assign material properties to these volumes.

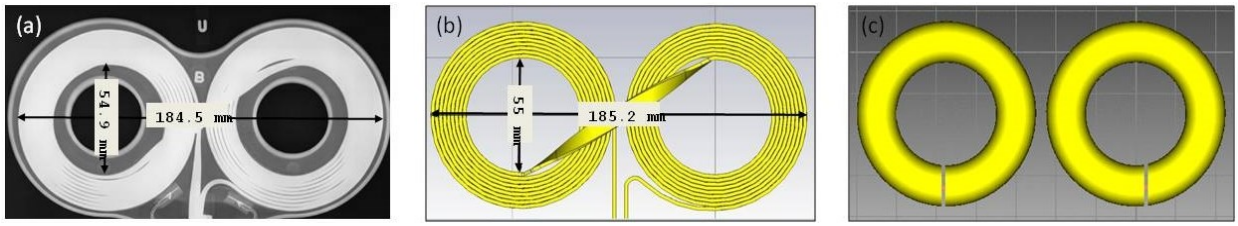

Figure 3-8. (a) Acquired X-ray image of a Magstim 70 mm butterfly coil. (b) An exact 3D model of the Magstim 70 mm butterfly coil. (c) A simplified single turn rendition of the exact 70 mm butterfly coil.

The electric field (**E**) induced in a conductor (e.g. gray matter) placed in a time varying magnetic field (**B**) are related to each other by Maxwell's equation

$$\nabla \times \mathbf{E} = -\frac{\partial}{\partial t}\mathbf{B}(\mathbf{t}) \tag{3.22}$$

The magnetic field B along the axis of one of the circular current-carrying loops of the butterfly coil placed in air is

$$\vec{\mathbf{B}} = \frac{\mu_0 N}{2}\frac{i(t)a^2}{\left(a^2+x^2\right)^{3/2}}\hat{\boldsymbol{k}} \tag{3.23}$$

where N is the number of turns of the coil loop, μ_0 is the relative permeability of free space, $i(t)$ is the current in the coil, a is the radius of the coil loop and x is distance of a point along the axis of a one of the circular current-carrying loops of the butterfly coil.

Inserting (3.23) in (3.22) gives

$$\nabla \times \boldsymbol{E} = -\frac{\partial}{\partial t}\left(\frac{\mu_0 N}{2} \frac{i(t)a^2}{\left(a^2 + x^2\right)^{3/2}} \hat{\boldsymbol{k}} \right) \tag{3.24}$$

If two different coil loops of same radius a are chosen such that the first coil loop consists of N_1 turns and the second consists of N_2 turns, with the same current **i(t)** flowing through them, then the induced electric field due to these two coil loops at a distance **x** along their central axes will be related to each other by

$$\frac{|\boldsymbol{E}_1|}{|\boldsymbol{E}_2|} = \frac{|\boldsymbol{B}_1|}{|\boldsymbol{B}_2|} = \frac{N_1}{N_2} = \mathrm{k} \tag{3.25}$$

Based on Equation (3.25), we have been able to establish a relationship between the induced E-field magnitude (or magnetic field strength magnitude) and the number of turns in the coil. The constant **k** is also known as the *turns ratio* (similar to the terminology used in case of transformer windings).

The location at which the induced E-field magnitude needs to be taken into consideration is different from the location at which the magnetic field strength needs to be considered. For example, if we intend to compare the maxima of E-field magnitudes in equation (3.25), we would have to obtain the induced field values at a point which lies directly under the closest point between the two circular loops. This is because the induced field magnitude is maximum under the closest point between the two circular loops (refer Figure 3-9 (a)) as opposed to calculation of the maxima of the magnetic field strength magnitudes, which have their maxima under the axes passing through the center of each loop (refer Figure 3-9 (b)). The magnetic field strength directly under

the closest point between the two circular loops (where the induced E field magnitude has maximum magnitude) is effectively zero.

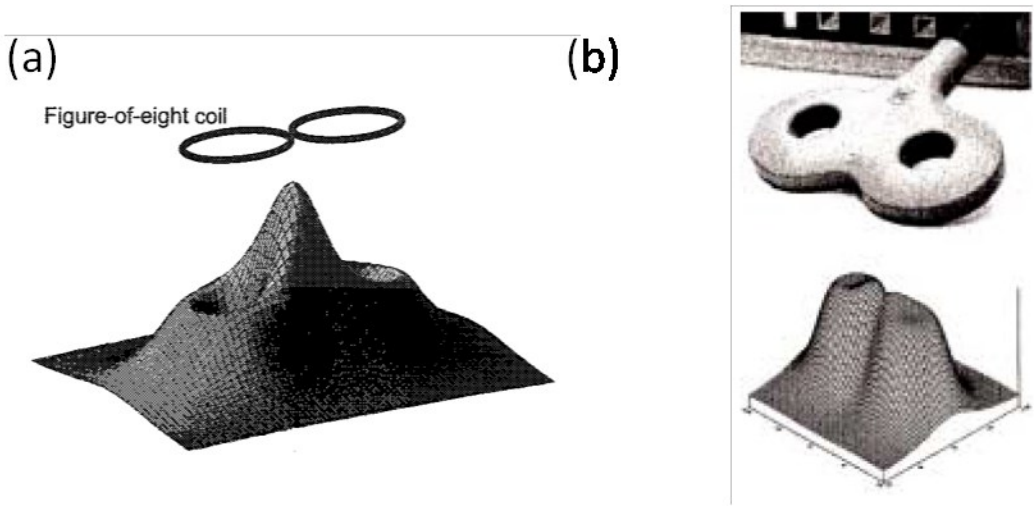

Figure 3-9. Representation of (a) Induced field profile on a plane under a butterfly (or FOE) coil (Ilmoniemi et al., 1999) and, (b) magnetic field profile produced by a butterfly (or FOE) coil (Gershon, 2003).

According to Kammer et al. (2001), the maximum energy of Magstim Rapid (Biphasic) System is,

$$\Delta E = 252 \text{ J} \tag{3.26}$$

We used ΔE instead of the conventional symbol E for energy in order to differentiate it from the symbolic representation of induced electric field, which has been used in equations preceding equation 3.28. This energy is stored in the capacitors, the equation for which is given by:

$$\Delta E = \frac{1}{2} C (\Delta V)^2 \tag{3.27}$$

where C is the capacitance of the capacitor in Farad and ΔV is the potential difference across its plates measured in Volt. Again, we used ΔV instead of the conventional symbol V for potential difference in order to differentiate it from the SI unit of potential difference, Volt (V).

At 100 % MSO, the maximum operating voltage of Magstim Rapid is (Magstim):

$$\Delta V = 1.67 \text{ kV} \tag{3.28}$$

Substituting (3.28) and (3.30) in (3.29), we get:

$$C = \frac{2E}{(\Delta V)^2} = (2 \times 252)/1670^2 = 180 \ \mu \text{F} \tag{3.29}$$

This energy, from the capacitors, is then discharged through the stimulating coil, which is an inductor (***L***).

If the maximum current that can flow through the coil is (***I***), then the energy stored (and later dissipated) by the coil is given by:

$$E = \frac{1}{2} L I^2 \tag{3.30}$$

Where ***L*** is the inductance of the coil in Henry and ***I*** is the current through the coil in Ampere.

From the specification sheet for Magstim Rapid stimulator datasheet (1990), we infer that the average inductance of a Double 70 mm coil is:

$$L = 16.35 \ \mu \text{H} \tag{3.31}$$

Substituting (3.28) and (3.33) in (3.32), we get:

$$I = \sqrt{\frac{2E}{L}} = \sqrt{\frac{2 \times 252}{16.35 \times 10^{-6}}} = 5552 \text{ A} \tag{3.32}$$

Equating (3.29) and (3.32), we get:

$$\frac{1}{2}C(\Delta V)^2 = \frac{1}{2}LI^2 \tag{3.33}$$

$$I = \Delta V \sqrt{\frac{C}{L}} = \Delta V \sqrt{\frac{180 \times 10^{-6}}{16.35 \times 10^{-6}}} = 3.32\, \Delta V \tag{3.34}$$

Equation (3.34) that shows we could vary either current flowing through the coil or potential difference across the capacitor to arrive at the same value of stimulation, provided the constant factor is taken into consideration. We chose to use current to define our stimulation parameter.

Therefore, as an example, if we consider 43 % MSO on a Magstim Rapid System discharging magnetic flux through a 70 mm double coil, we refer to a coil current of:

$$I = 3.32 \times 0.43 \times 1670 = 2384 \text{ A} \tag{3.35}$$

Equipped with this information, simulation was performed, with a sinusoidal driving current, with a time period of 300 μs and amplitude 2384 A varying at the rate of 10^8 A/s. CST EM Studio has been used for static and low frequency applications such as estimation of via-plate capacitances (Zhang et al., 2009); in the computation of capacitance matrix, electrostatic potential, electric field strength and flux density of spherical capacitors (Virjoghe et al., 2008) and, in improving the output voltage of planar insulating core transformers (PICTs) by optimizing flux compensation capacitor values (Kang et al., 2011). The following step involved the development of the simulation domain for the estimation of induced E-fields in conducting volumes due to a single

pulse of TMS discharged by a stimulating coil placed in its vicinity. We used a solved example, *team7 tet.cst* (which is provided with the CST EM studio software installation package) as a reference project model. The reference project model consisted of a current carrying coil operationally similar to a TMS coil, enabling us to develop the stimulating coil model to be used in our FEM TMS model. A good starting point of comparison, between the realistic TMS coil model (shown in Figure 3-8 (b)) and the single turn coil model (shown in Figure 3-8 (c)) was to compare the number of tetrahedral elements that are needed to discretize the two coils. The volume occupied by the realistic TMS coil was 229.66 mm × 185.34 mm × 24.50 mm (along x, y and z axes) and correspondingly, the volume occupied by the single turn TMS coil was 90 mm × 185 mm × 20 mm. When the same default settings were used to generate the tetrahedral mesh for the two coils, the realistic coil was discretized into 21,575 second order tetrahedral elements and the single turn coil was discretized into 18,492 elements. The mesh obtained for both coil models using default mesh generator settings is shown in Figure 3-10. The default mesh generator creates tetrahedral elements using the triangular surfaces defining the STL model of the coils, without discretizing the triangular surfaces further. Next we defined a problem in which we would like to compare the magnetic field strength profiles obtained from the realistic coil and the single turn coil for comparison with that presented in Figure 3-9 (b). In order to proceed, we needed to define a bounding box for the problem and apply necessary boundary conditions. From Figure 3-10 and the volume description of the coils, we could anticipate that a bigger bounding box would be needed to encapsulate the realistic TMS coil model compared to the single turn model. We defined a bounding box extending uniformly by 50 mm in both directions (+ve and -ve) along x, y and z axes with respect to the coil geometries. Thus, the bounding box volume for the realistic TMS coil was 329.66 mm × 285.34 mm × 124.50 mm (along x, y and z axes) and correspondingly, the

volume occupied by the single turn TMS coil was 190 mm × 285 mm × 120 mm. Using the same default mesh generation settings as those used to discretize the individual coils, we proceeded to discretize the coil and the bounding box. The realistic coil along with its bounding box resulted in 36,557 tetrahedral elements (21,575 elements for the coil and 14,982 elements for the bounding box) and the single turn coil along with its bounding box resulted in 32,942 elements (18,492 elements for the coil and 14,450 elements for the bounding box). We thus reduced the number of tetrahedral elements for our problem definition by (36,557 – 32,942 = 3,615) elements. Dirichlet boundary conditions were defined for the problem domain by defining the bounding box walls as perfect electric conductors (PEC). The PEC condition forces the tangential component of the electric fields and the normal component of the magnetic field at these walls to zero. The choice of PEC boundary condition over perfect magnetic conductor (PMC) was done keeping in mind that in all subsequent simulations following the current set of simulations, we would be interested in simulating the fields on only one side of the coil (bottom face) because we would be placing an object facing only one side of the coil. Hence, the magnetic fields on the opposite side (the top side) of the coil could be ignored, which could be forced to zero by the assigned PEC layer. The solution frequency was set to 3.35 kHz (based on the result obtained in Figure 3-6 (c)) and desired level of accuracy (defined by the residual value in terms of the Eigen system's relative residual) was set to $1x10^{-4}$. The single turn coil model simulation solved the problem to the desired level of accuracy in 7 s (residual value of 8.54×10^{-5} in 16 iteration steps) whereas the realistic coil model simulation setup could not converge to even an accuracy value of $1x10^{-2}$ after two and a half days, at which point it was decided to stop the simulation. The completion of the single turn coil simulation to the desired level of accuracy enabled us to infer that the bounding was large enough to obtain a reliable solution, because the bounding box extended the same length (50 mm) in both

directions along all three axes for both coil models. It could also be inferred that since the same default mesh generation settings were used for both simulations, the minimum edge length of each tetrahedral element in the bounding boxes of the two simulations would be the same. Therefore, the meshing of the bounding box was not a problem, since the meshing of the bounding box using the same edge length parameters of tetrahedral elements as those used for the realistic simulation resulted in a reliable simulation. That left only the meshing of the realistic coil model as a potential problem. Therefore, it was decided to vary the number of tetrahedral elements in the realistic coil, while keeping the number of tetrahedral elements in the bounding box the same. The realistic coil model was designed using a strip of wire (with a cross sectional area of 5 mm × 0.8 mm = 4 mm^2) coiled in multiple concentric turns but with different radii for the turns. The single turn coil consisted of only one turn of wire of circular cross section (cross section area 314.15 mm^2). The large difference in the cross sectional areas of the realistic coil strip and single turn coil suggested that the same edge length of the tetrahedral elements to mesh both, the realistic coil and single turn coil, may be the problem because the strip in the realistic coil model may not have a sufficient number of elements (and hence sufficient number of nodes) defining its structure. Therefore, the minimum edge length of the tetrahedral elements defining the strip would need to be reduced which meant that a denser meshing would be needed for the realistic coil. The number of tetrahedral elements for the coil was increased in steps (all the while noticing the speed of simulation and the accuracy value of the simulations) till the 1,555,384 tetrahedral elements defining the realistic coil (leading to a total of 1,570,366 elements for the problem domain including the bounding box) resulted in a simulation that achieved a level of accuracy (residual of 2.53×10^{-4} in 2001 iterative steps) close to the desired level of accuracy (residual of 1×10^{-4}) in 6 hours and 14 minutes. The single turn coil therefore reduced computation time considerably from

nearly 18 hours to 7 s and it achieved this by substantially reducing memory and processor requirements (owing to lesser number of tetrahedral elements defining the problem domain; 32,942 elements vs. 1,570,366 elements, a reduction of nearly 98 % in the number of tetrahedral elements).

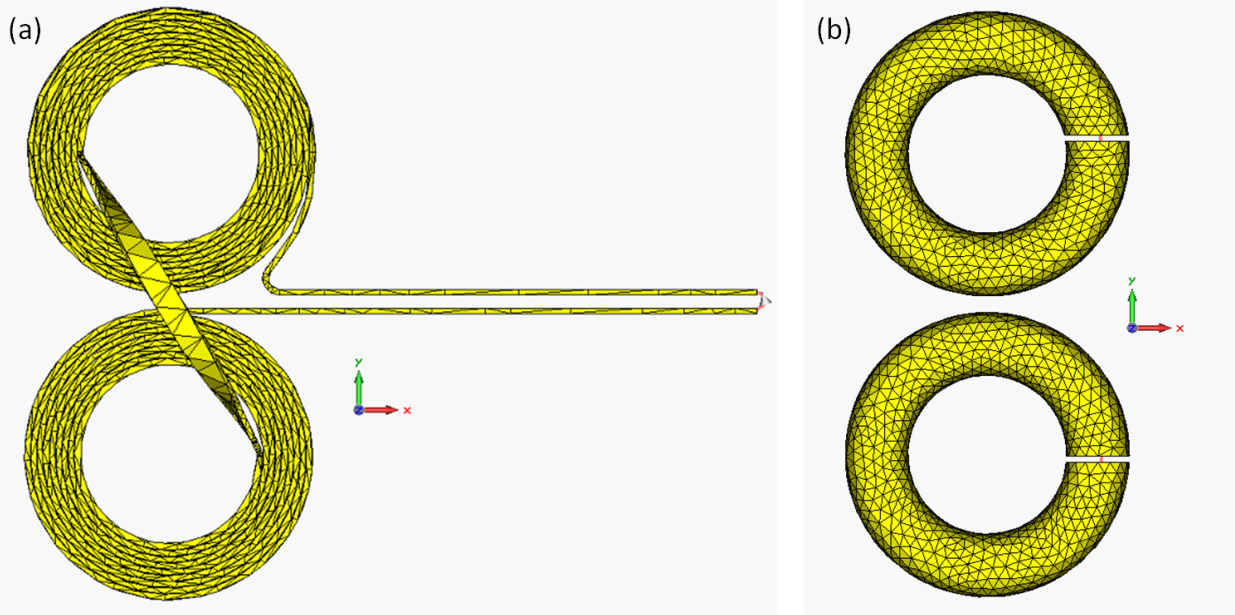

Figure 3-10. Mesh generated using default settings on CST EM studio for (a) realistic coil model and, (b) single turn coil model.

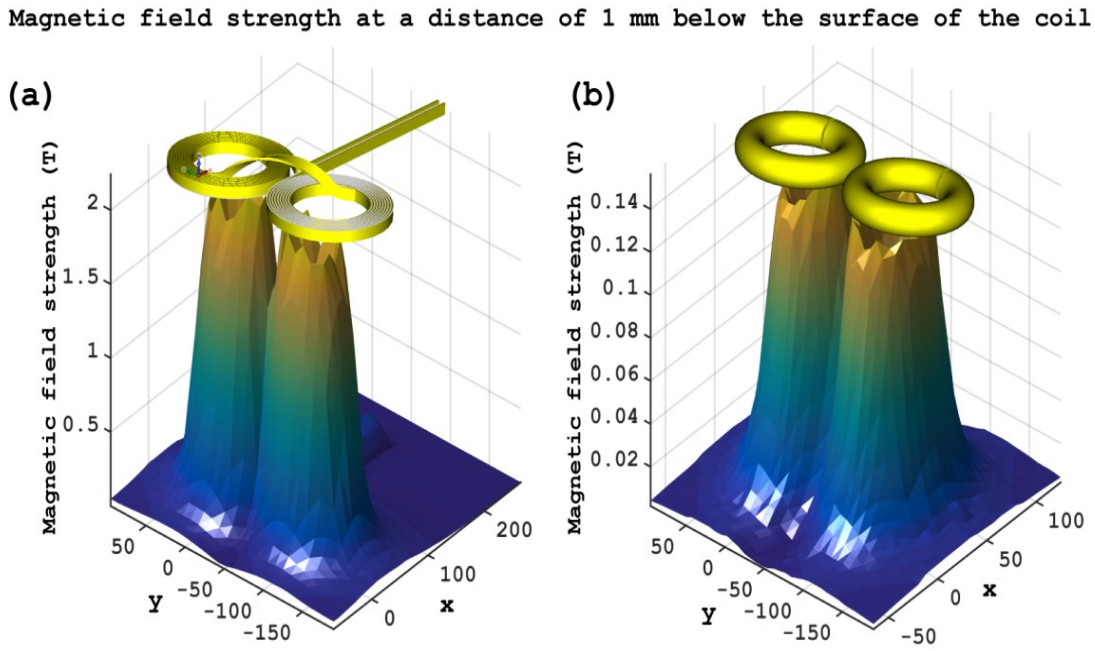

Figure 3-11. Simulated magnetic field strength (B) at a distance of 1 mm from (a) the realistic coil and, (b) single turn coil. Maximum deliverable sinusoidal current of amplitude 5552 A and time period 300 µs flows through the TMS coils.

Figure 3-11 presents the magnetic field strength simulated for the realistic and single turn coils, at a distance of 1 mm from the coils. The profiles of magnetic fields are comparable to that obtained from literature and presented in Figure 3-9 (b). A closer look at the magnetic field strength magnitudes however reveals that for the same amount of current (5552 A) flowing through both coils, the realistic coil generated a peak field magnitude of 2.24 T (reported peak magnetic field of Magstim's double 70 mm coil is 2.2 T (Hovey and Jalinous, 2006)) whereas the single turn coil produces a peak field magnitude of 0.156 T. Substituting the peak field magnitude values in equation 3.25 yields the scalar k as,

$$k = \frac{|\boldsymbol{B_1}|}{|\boldsymbol{B_2}|} = \frac{2.24}{0.156} = 14.35 \tag{3.36}$$

The electric field E is related to the magnetic field strength B according to Equation (3.22). Figure 3-12 shows the electric field induced in a conducting volume (in our case, saline) is placed 10 mm below the coil, the electric field that is induced in it due the magnetic field produced by the coils. The profiles of the induced E-fields match the one that is presented in Figure 3-9 (a). For the same value of coil current (5552 A) the realistic TMS coil results in a peak induced electric field amplitude of 498 V/m and the single turn TMS coil induced a peak electric field of strength 34.9 V/m. It can be noted that the realistic coil's induced electric field amplitude is related to the electric field amplitude of the single turn coil by a factor of 14.27 , which is almost the same as the turns ratio **k**, because the induced E-field is related to magnetic field strength by Equation (3.22).

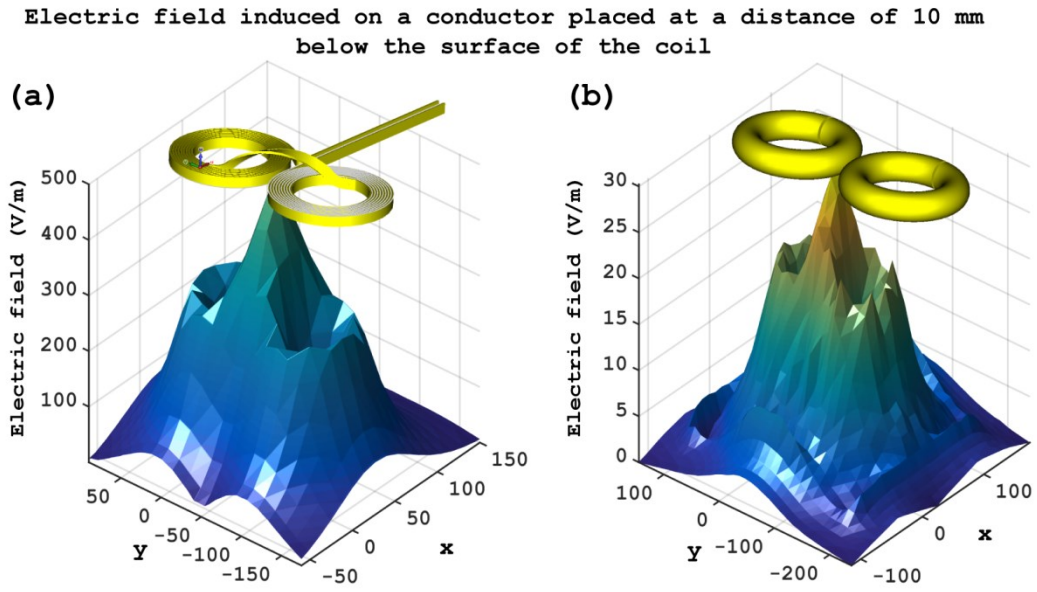

Figure 3-12. Simulated electric field (E) induced on a conducting plane (saline) placed at a distance of 10 mm below (a) the realistic coil and, (b) single turn coil. Maximum deliverable sinusoidal current of amplitude 5552 A and time period 300 μs flows through the TMS coils.

According to Equation 3.25,

$$\mathrm{k} = \frac{N_1}{N_2} \tag{3.37}$$

A fractional value for turns ratio in Equation 3.25 (such as that resulting from Equation 3.26) makes little sense. So the turns ratio was rounded off to an upper value of 15. The turns ratio in Equation 3.36 could also be computed theoretically (as opposed to being determined empirically as shown above) but since the coil is not a simple spiral but a helical spiral with each turn having a different radius, the calculation of turns ratio based on theoretical equations could become complicated.

Equation (3.23) also reveals that the magnetic field B along the axis of one of the circular current-carrying loops of the butterfly coil placed in air is related to the current flowing in the coil as follows,

$$\boldsymbol{B} \propto i \tag{3.38}$$

which means that in order to increase the magnetic field strength produced by the coil, one should increase the current flowing through the coil. This implies that if we intend our single turn coil to produce the same magnitude of magnetic field strength as the realistic coil (2.24 T), it can be achieved by driving a current of amplitude,

$$\frac{i_1}{i_2} = \frac{|\boldsymbol{B_1}|}{|\boldsymbol{B_2}|} \tag{3.39}$$

$$or\ i_1 = \frac{|\boldsymbol{B_1}|}{|\boldsymbol{B_2}|} \times i_2 = \mathrm{k}\ \times i_2 = 15\ \times 5552\ \mathrm{A}$$

$$=>\ i_1 = 83280\ \mathrm{A}$$

When the current amplitude in the single turn coil is increased from 5552 A to 83280 A, the peak magnetic field strength increases to 2.26 T (refer Figure 3-13 (a)) from 0.156 T (refer Figure 3-11 (b)) and the peak induced electric field strength increases to 502 V/m (refer Figure 3-13 (b)) from 34.9 V/m (refer Figure 3-12 (b)). The close match of the field profiles and the peak values of magnetic field strength and the induced electric field strength of the single turn coil (when a coil current of 83280 A flows through its coils) to the corresponding values obtained for the realistic coil (when 5552 A flows through its coils) demonstrates that the single turn coil model can mimic the performance of the realistic coil very closely.

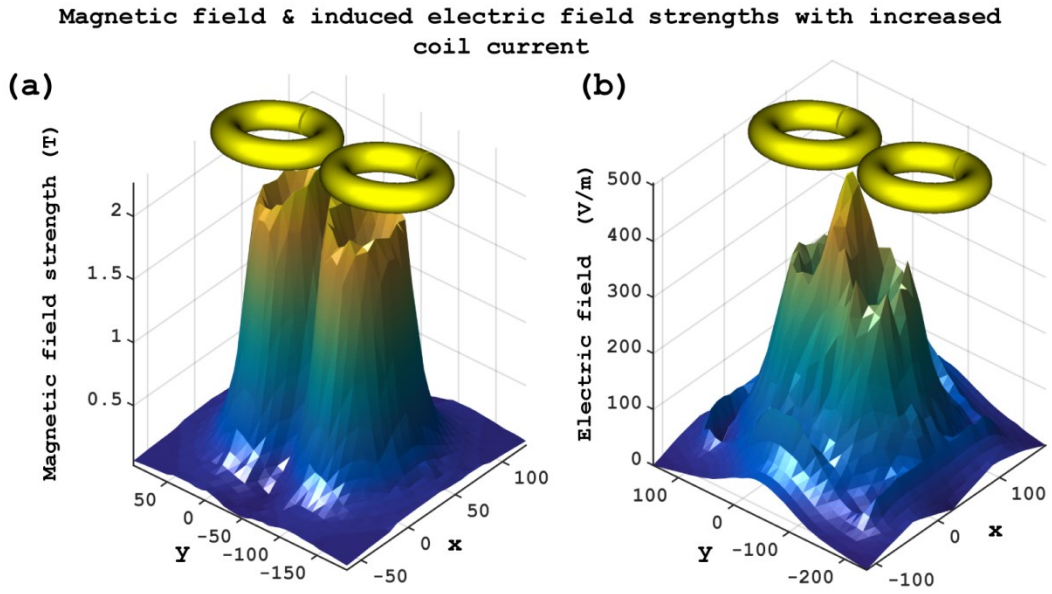

Figure 3-13. (a) Simulated magnetic field strength (B) at a distance of 1 mm from the single turn coil and, (b) Simulated electric field (E) induced on a conducting plane (saline) placed at a distance of 10 mm below the coil , when the coil current amplitude is increased from 5552 A to 83280 A.

3.3.9 Validation of the simple coil model for FEM simulations by comparing it with real TMS coil data

Having obtained the simplified single turn FOE TMS coil model, it was pertinent to make sure that the behavior of the simulated coil followed that of the real 70 mm FOE TMS coil. In order to validate this, we conducted a measurement to obtain the magnetic field strength along the axis of one of the loops of the TMS coil. The resultant magnetic field at the center of the TMS coil would be effectively zero due to the interaction of opposite direction magnetic fields arising from opposite current directions in the two loops of the TMS coil. Therefore, magnetic field strength decay at the center of either loop (where the magnetic field strengths would be maximal) was sought. Figure 3-14 (a) through (c) show the experimental setup to measure the magnetic field decay. Figure 3-14 (a) shows the alignment of the centers of the pickup coil and one of the loops of the TMS coil. The first measurement was made with the pickup coil at a distance of 7 mm from the face of the coil (Figure 3-14 (b)) and we translated along the axial center of the loop, away from the coil, in the direction shown by the yellow arrow in Figure 3-14 (c). Measurements of magnetic field strengths were taken in steps of 5 mm advancements away from the face of the coil. The resultant induced voltage magnitudes were then normalized (since we would like to compare the decay rates of the induced voltage and not the magnitudes of the induced voltages) with respect to the induced voltage at the closest point (at a distance of 7 mm from the coil face) and the induced voltage (hence magnetic field strength) decay plot was obtained. After the measured results were obtained, we simulated the magnetic field for the measurement setup. CST EM studio Low Frequency (LF) frequency domain solver was not capable of conducting simulations with Neumann boundary conditions or open boundary conditions. Real measurements are made in open boundary conditions. Therefore, it was essential to test if Dirichlet boundary conditions (which are

assumed in CST EM studio Low Frequency (LF) frequency domain solver simulations) would have a bearing on the results in the absence of Neumann or open boundary condition assumptions. As discussed in section 3.3.8, PEC Dirichlet boundary conditions were used for the simulations. It was also important to identify if the bounding box size of the simulation setup would affect the simulated results or not. The bounding box could play an important role in defining the number of tetrahedral that would be involved in the solution process and hence, would govern simulation time and computer memory requirements. This was achieved by simulating the magnetic field produced by the coil in different sized bounding boxes (an irregular bounding box with different projections along x, y and z directions followed by constant 500 mm, 1000 mm and 2000 mm extensions along all directions from the coil). The magnetic field strengths at the same points were calculated and normalized, as mentioned in the measurement scheme. Figure 3-14 (d) shows that the sizes of bounding boxes have no effect on the decay profiles as profiles of all bounding boxes follow each other closely. Additionally, the closeness of the decay profiles of all simulated magnetic field strengths compared to the measured field strength proves that the use of Dirichlet boundary condition does not affect the decay profile.

Simulation of the magnetic field strength achieved two purposes,

1. The effect of boundary conditions on the simulated results, and
2. The effect of the bounding box on the simulated results

The measured data shows a deviation from the simulated result at distances > 62 mm. This is hypothesized to be due to the low sensitivity of the balanced probe to the magnetic fields at such distances. In order to address this issue, we recommend performing the validation at a higher value

of TMS stimulator output (approximately 10-15 % MSO). The higher value of stimulator output would mean stronger magnetic field strength at distances > 62 mm which the balanced probe could be capable of measuring correctly.

The closeness of results obtained from the measurement and simulation, strengthened our confidence in the correctness of our simulation of the coil.

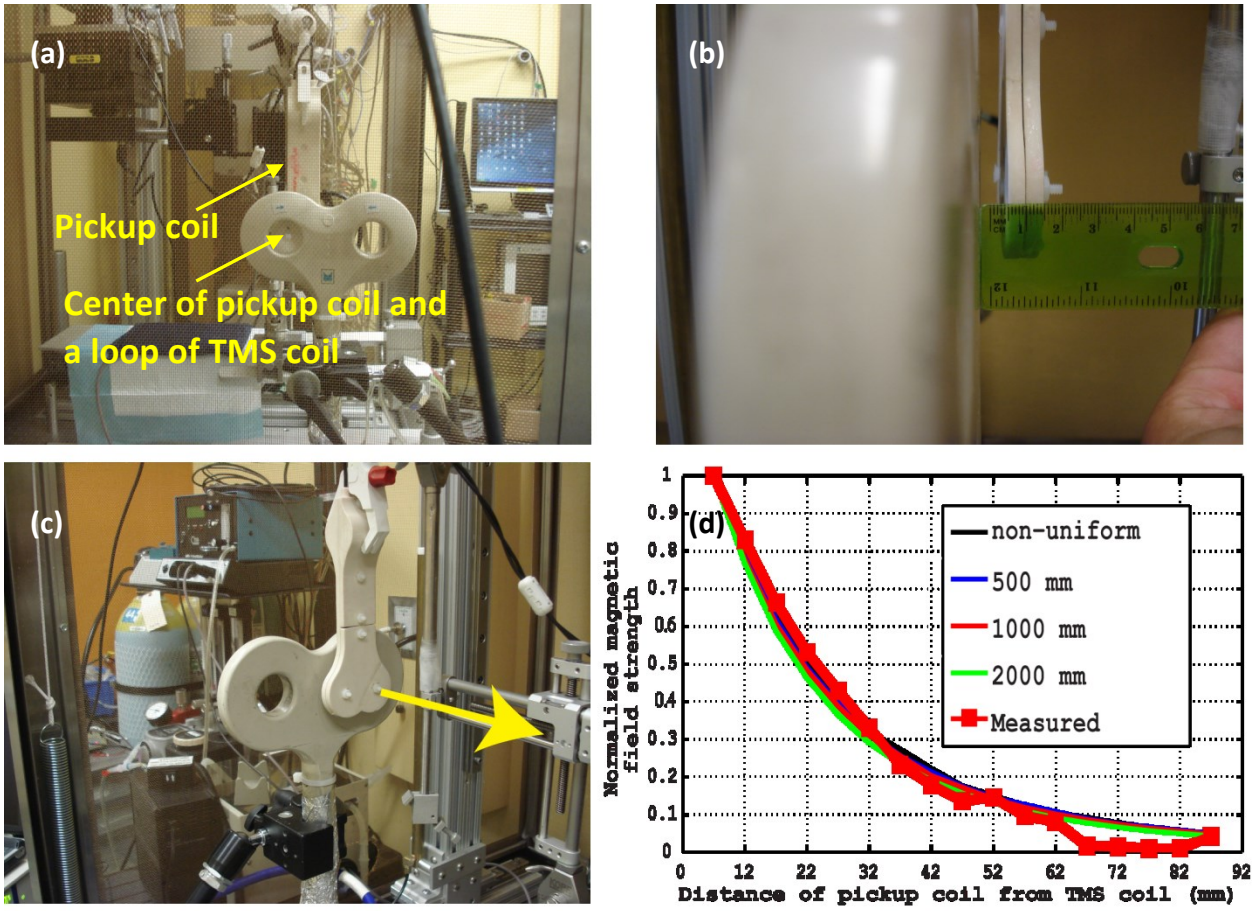

Figure 3-14. Images of the measurement setup that was used to validate the designed single turn butterfly coil. (a) The setup consisting of a balanced probe which acts as a pickup coil to detect the TMS pulse generated magnetic field. The center of one wing of the TMS coil and the center of the pickup coil were aligned. (b) The distance measured between the first recording position of the pickup coil and the face of the TMS coil. (c) Translation of the pickup coil away from the TMS coil along the yellow arrow. (d) Comparison between the results obtained from the measurements and those obtained using different sizes of bounding boxes for simulations with the simplified single turn TMS coil.

3.4 Results

3.4.1 Pilot experiments with small and large volumes

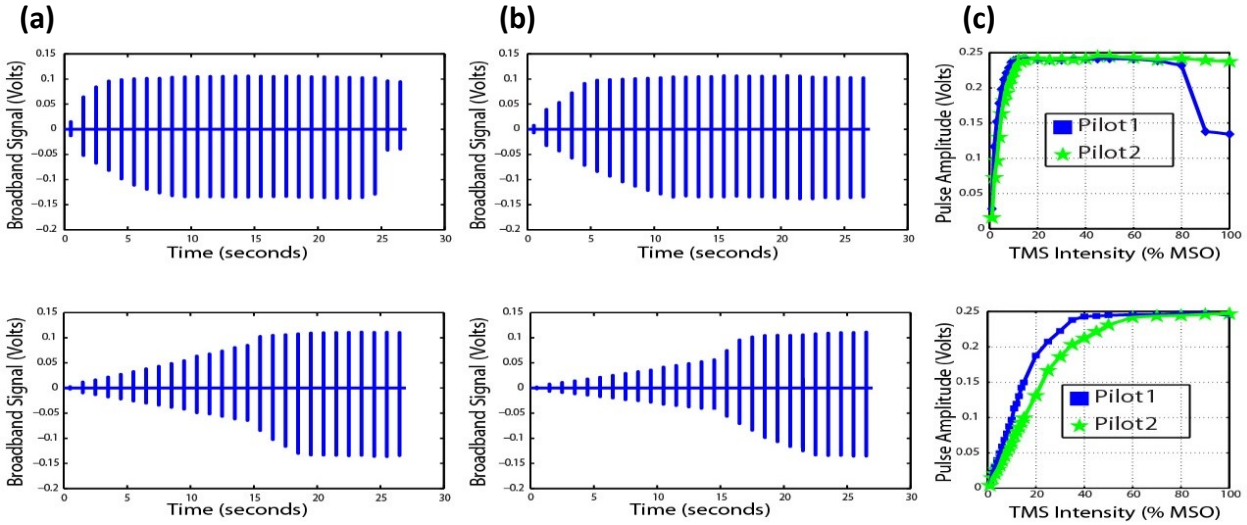

Figure 3-15. (a) Timecourse of average TMS induced potential spikes at different TMS intensities (1 % MSO to 100 % MSO) for Pilot experiment 1. (b) Timecourse of average TMS induced potential spikes at 27 different TMS intensities for Pilot experiment 2. (c) Peak-to-peak amplitudes of TMS induced potential spikes as a function of different TMS intensities for both Pilot 1 and Pilot 2 experiments. These results guide the choice of the optimal TMS intensity for the small volume current density measurements.

From Figure 3-15 (a) and Figure 3-15 (c), Pilot experiment 1 shows that the triphasic signals saturate by the time the TMS intensity reaches 6 % MSO while 1 % MSO elicits erratic pulses. Hence, if we chose 5 % intensity for our experiments, we should expect to obtain a discernible current density profile. This was verified with Pilot Experiment 2, results of which are shown in Figure 3-15 (b) and Figure 3-15 (c). From Pilot Experiment 2 we see that the pulses saturate at a higher intensity of 10 % MSO while a defined triphasic pulse is also obtained at 5 % MSO. Hence, our choice of 5 % MSO for the small volume measurement setup was justified. A similar analysis was conducted for the large volume. Thus, 11 % MSO intensity was used in the large volume setup while 5 % MSO intensity was used for the small volume setup.

3.4.2 Complete ROI experiment results

Each simulation took less than four minutes. Figure 3-16 (a) shows the grid defining the ROI on a plane in the large volume conductor. The induced current density profiles for every plane, such as the one shown in Figure 3-16 (a) were extracted. Figure 3-16 (b) shows the current density profile on the ROI obtained by measuring the induced potential. Figure 3-16 (c) is a magnified image of the current density distribution shown in Figure 3-16 (b), while Figure 3-16 (d) is the equivalent current density profile of the same ROI obtained through FEM simulation. Figure 3-17 (a) to Figure 3-17 (d) are the equivalent plots of Figure 3-16 (a) to Figure 3-16 (d), for the small volume.

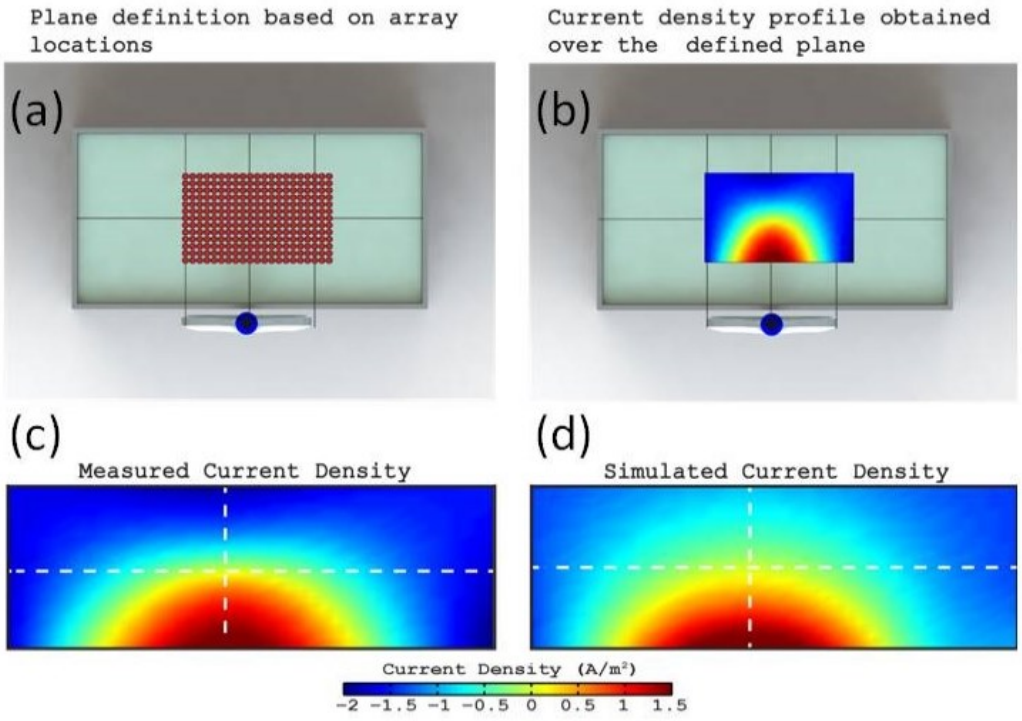

Figure 3-16. (a) Plane definition for the large volume. (b) Measured current density over the plane. (c) Magnified image of the measured current density on the plane. (d) Simulated current density of the same plane. The color bar at the bottom represents the current density magnitudes for both (c) and (d).

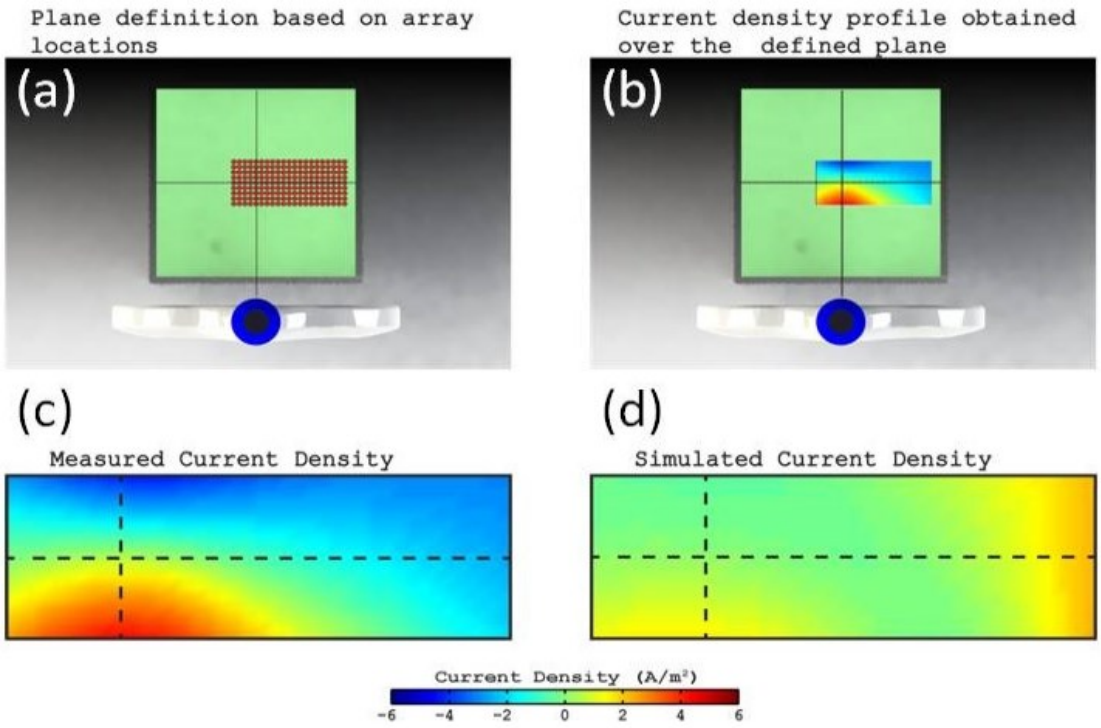

Figure 3-17. (a) Plane definition of the small volume. (b) Measured current density over the plane. (c) Magnified image of the measured current density on the plane. (d) Simulated current density of the same plane. The color bar at the bottom represents the common current density magnitudes for both (c) and (d).

It can be observed that the simulated and measured current density profiles for the large volume are similar but the observation is different for the small volume. The simulated current density shows a strong field distribution near the edge of the phantom (which can be seen on the right side of Figure 3-17 (d)). These fields near the edge are not present in the measurement results (as seen in Figure 3-17 (c)).

Once we obtained the current density profiles from both measurements and simulations for individual planes, we plotted the simulated current density as a function of the measured current density. Figure 3-18 (a) shows the relationship between the simulated and measured current densities existing on each of the nine planes obtained from the large volume, in the form of scatter plots. In order to test the linearity of the relationship between measured data and simulated data,

we chose not to use simple linear regression because we present the simulated data (response) as a function of the measured data (predictor) and since we assume errors in both simulated data and measured data. The dotted red line in each scatter plot represents the orthogonal linear regression fit that was obtained for the distribution while the dotted black line represents the unity slope and zero intercept line, forming a reference line (denoting the relationship that would exist between simulated and measured current density, if they were identical). The slope and y-intercept obtained from the orthogonal fit applied to the distribution on each plane as a function of the plane number, is shown in Figure 3-18 (b). Similarly the correlation coefficient of the distribution obtained from each plane is plotted in Figure 3-18 (c). The data from all ROIs were then combined together (separately for simulated and measured current densities) to obtain a volumetric ROI.

The volumetric distribution of simulated current density was then projected as a function of the volumetric measured current densities to obtain the volumetric relationship, as shown in Figure 3-18 (d). Similar to the individual planar distributions, the dotted red line represents the orthogonal fit that was obtained for the volumetric distribution. Volumetric correlation coefficient was 0.97 (Figure 3-18d). Similarly, Figure 3-19 (a) to (d) are the equivalent plots of Figure 3-18 (a) to (d), for the small volume except for the difference that Figure 3-19 (a) shows the relationship between the simulated and measured current densities existing on each of the sixteen (out of a total of seventeen) planes in the form of scatter plots. All corresponding analyses are also projected to sixteen planes instead of the nine that were acquired from the large volume.

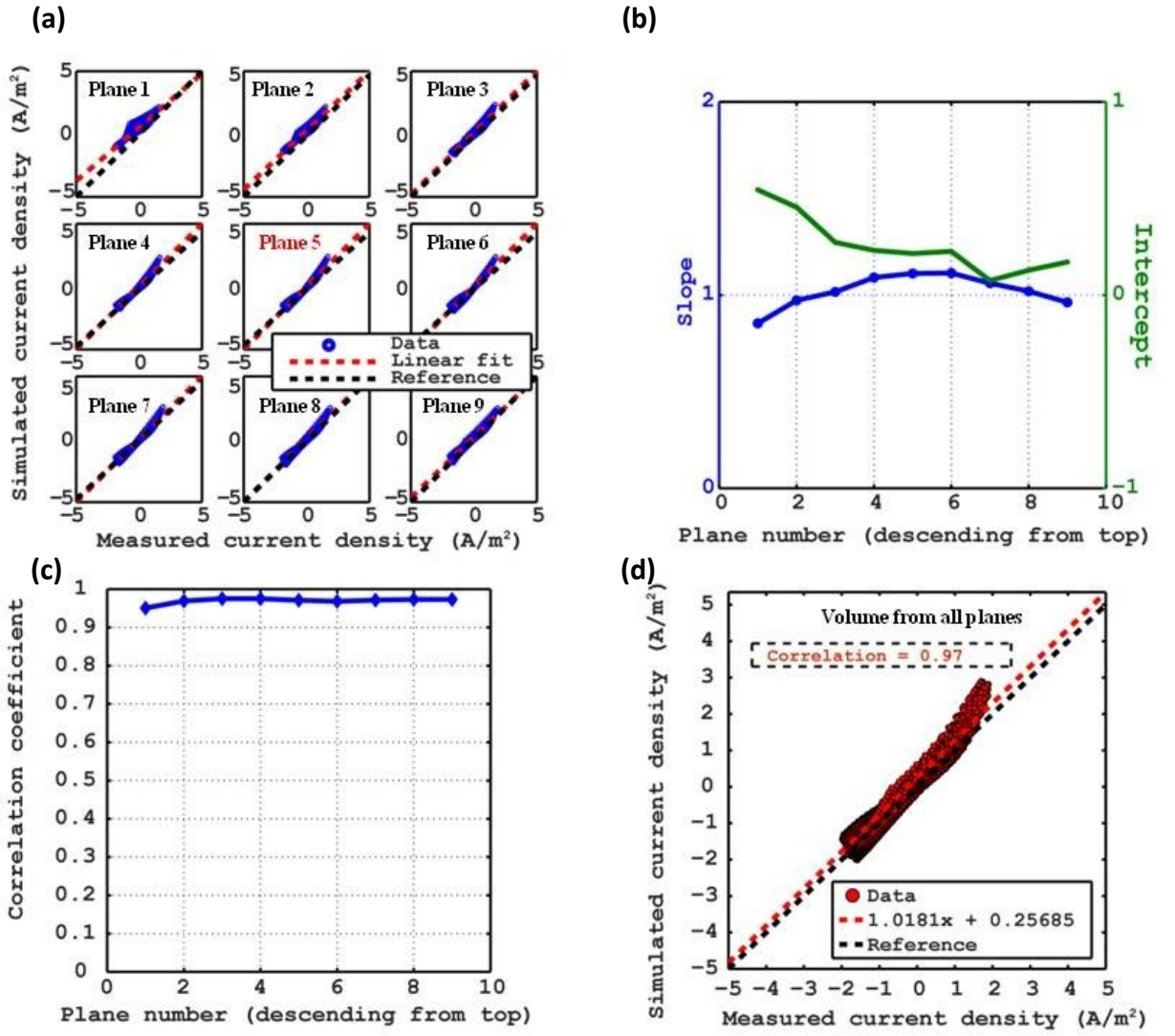

Figure 3-18. Analysis of current density induced in a large volume by a single pulse of TMS. (a) Scatter plots showing the relationship between simulated current density magnitudes and measured current density magnitudes at each point in the defined ROIs, plane by plane. Each plane was obtained by moving the ROI (simulation) or MEA (measurement) deeper into the saline volume. 9 off the 17 recorded planes are shown here. Plane 5 is the ROI that lies in line with the central axis of the TMS coil. (b) Slope (blue curve) and Y intercept (green curve) of the orthogonal fit applied to each scatter plot, as a function of the plane number. It shows how the relationship between the simulated and measured data changes as we go deeper into the saline volume. (c) Correlation obtained from the scatter plots as a function of plane number. (d) Total volume characteristic scatter plot obtained by combining all the planes together for the simulated and measured datasets, separately, and projecting the relationship between them through one scatter plot.

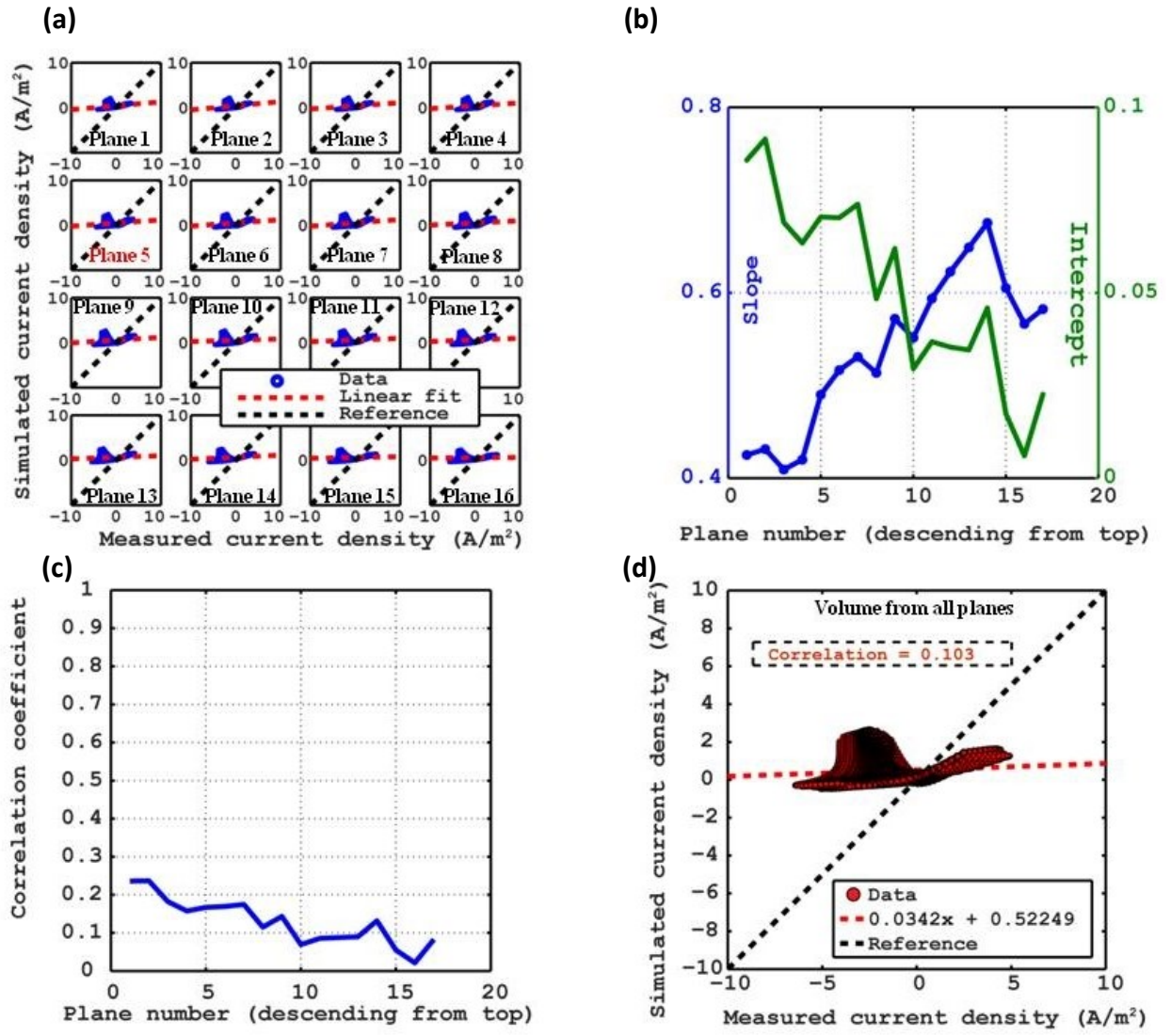

Figure 3-19. Analysis of current density induced in a small volume by a single pulse of TMS. (a) Scatter plots showing the relationship between simulated current density magnitudes and measured current density magnitudes at each point in the defined ROIs, plane by plane. Each plane was obtained by moving the ROI (simulation) or MEA (measurement) 3 mm deeper into the saline volume. 16 off the 17 recorded planes are shown here. Plane 5 is the ROI that lies in line with the central axis of the TMS coil. (b) Slope (blue curve) and Y intercept (green curve) of the orthogonal fit applied to each scatter plot, as a function of the plane number. It shows how the relationship between the simulated and measured data changes as we go deeper into the saline volume. (c) Correlation obtained from the scatter plots as a function of plane number. (d) Total volume characteristic scatter plot obtained by combining all the planes together for the simulated and measured datasets, separately, and projecting the relationship between them through one scatter plot.

3.5 Discussion

3.5.1 Significance of E-field calculations to TMS studies

Accurate estimations of total E-fields are especially needed when TMS is used for clinical applications (Salinas et al., 2009). Most clinical applications of TMS involve conditioning of targeted cortical regions with a train of TMS pulses (referred to as repetitive transcranial magnetic stimulation or simply rTMS). Correct estimate of total induced E-fields will provide better per-pulse dose approximations for such clinical studies. This, in turn, will allow clinicians to monitor patient progress and/or treatment effectiveness over time. Another important aspect that accurate dosage information provides, according to Salinas et al. (2009), is that they are beneficial when comparing treatments across patient groups (e.g. control vs. impaired) because they are a more reliable measure than for example using TMS stimulator output settings which are subject to variability depending upon the stimulator/coil parameters. For this reason, TMS conditioning is conducted using a generic measure called resting motor threshold (RMT) and not TMS stimulator intensity, because E-field magnitude required to achieve RMT is a stable measure but the TMS intensity that may be used to achieve RMT is subject to inter-individual variability associated with difference in the different segments of the human head, for example, difference in scalp thickness. Indeed, Julkunen et al. (2012) demonstrated that for TMS applications, the induced field is a more stable measure than percentage of maximum stimulator output intensity. In addition to improving the efficiency of clinical studies, accurate E-field estimates will also contribute to safety protocols associated with TMS studies.

3.5.2 Relevance of simulations and measurements in saline phantom

$$\nabla \times \boldsymbol{E} = -\frac{\partial}{\partial t}\boldsymbol{B}(t)$$

In equation 3.22 (re-introduced above), the magnitude of the induced E-field on a conductor is proportional to the magnitude of the magnetic field strength due to which induction occurs. Let us consider the first case, of TMS being performed on a five segment head model consisting of scalp, skull, CSF, gray matter (GM) and white matter (WM). If we denote the conductivities of each segment such that conductivity of (scalp = σ_{scalp}, skull= σ_{skull}, CSF= σ_{CSF}, gray matter = σ_{GM} and, white matter = σ_{WM}), then based on the conductivity values $\sigma_{CSF} > \sigma_{scalp} > \sigma_{GM} > \sigma_{WM} > \sigma_{skull}$. If the stimulating coil produces a peak magnetic field of strength B, the magnetic field will induce an E-field of strength E'_{scalp} on the scalp. E'_{scalp} in turn results in a magnetic field B_{scalp}, which is 180 degrees out of phase with B, Thus, the resultant magnetic field reaching the next interior layer from scalp, i.e., the skull is going to be

$$B'_{skull} = B - B_{scalp} \tag{3.41}$$

B'_{skull}, results in an induced E-field on the skull, E'_{skull} (which is negligible because of the extremely low conductivity of bone). This E'_{skull} will result in its own associated magnetic field strength, B_{skull}. This process continues as we move from one layer to another such that fields reaching the CSF and GM layers are

$$B'_{CSF} = B - B_{scalp} - B_{skull} \tag{3.42}$$

$$B'_{GM} = B - B_{scalp} - B_{skull} - B_{CSF} \tag{3.43}$$

Now, let us consider a second case where the scalp and skull segments are absent and the magnetic field produced by the coil interacts with the CSF layer first. Then the magnetic field resulting in induction on the CSF layer will be

$$B''_{CSF} = B \tag{3.44}$$

Based on Equations (3.42), (3.43) and (3.44),

$$B''_{CSF} > B'_{CSF} > B'_{GM} \tag{3.45}$$

Therefore,

$$E''_{CSF} > E'_{CSF} > E'_{GM} \tag{3.46}$$

If we use an electrode and data acquisition system to measure the electric field strengths based on the methodology provided in this study, higher magnitudes of potential will be recorded by the electrode for E''_{CSF} (since $V = \mathbf{E}.\mathbf{dl}$, where V is the potential difference, E is the electric field strength and dl is the distance between the points where the potential difference is being measured) compared to the potential recorded for E'_{GM}. So, if our measurement setup is capable of measuring the higher amplitude of potentials associated with E''_{CSF} (without any clipping of the signals resulting from saturation of the pre-amplifiers as discussed in the Introduction section), then it is plausible that the setup will be capable of measuring the relatively lower amplitude potentials associated with E'_{GM}. The second case is reflective of our phantom experiment with saline (since CSF and saline have been assumed to have same conductivity). Hence, if we are able to get a

reliable measure of the induced E-field in saline in the phantom experiment, we could possibly get a reliable measure of the induced E-field on the cortex (or GM) when we proceed to validate the simulations on realistic head geometries using in- vivo measurements. To this end, the phantom experiments demonstrate that our measurement setup and methodology can support simple validation using simplified in-vivo measurements.

The phantom experiments reflect a homogeneous layer model whereas in-vivo experiments will reflect a heterogeneous model consisting of different layers including scalp, skull, CSF, gray matter and white matter (considering the basic 5 layer model of a head as a starting point). Therefore, in terms of layers, the phantom is less complex (it is a simplification) relative to the real situation encountered in head geometries. The phantom does not completely guarantee precision in the real world situation but helps in validating and calibrating the measurement setup that may be used for in-vivo studies involving more complex geometries. In conclusion, the phantom validation does not fully present a 'sufficient' test for validating real world complex geometries, but it is a 'necessary' test towards such validation.

3.5.3 Simulations and measurements in small and large volumes

The 2-D Utah array (consisting of a 10 x 10 grid of electrodes) that was used to measure the E-fields is similar to the 2-D eddy current probe that was used in (Salinas et al., 2007, 2009). This kind of probe, based on the work of Epstein et al. (1990), can be used to measure E-fields when the electric and magnetic fields have only transverse components which vary along the direction normal to both fields. We incorporated this method of measurement in our experiment where the direction of motion of the probe is mutually perpendicular to the transverse components of the electric and magnetic fields in the saline volume. The notable attribute with such E-field

measurement method, as demonstrated by (Salinas et al., 2007, 2009), is that using the Utah array we can expect to measure only the primary component of the induced field (a dipole probe rotated in 3-D space shown in their study is capable of measuring the total electric field which is a combination of the primary and secondary E-fields).

From Figure 3-17 (d), we observe that the first hurdle that was faced in the small volume simulations was that the E-fields near the closer edge (the right side in Figure 3-17 (d)) is visibly dominant on the right side of the image in the simulated E-fields. We hypothesize that the reason for this phenomenon is E-fields caused by the edges of the phantom. These E-fields appear in the form of visible bumps (refer Figure 3-19 (a) and Figure 3-19 (d)) on the scatter plot, that is otherwise more linear. We hypothesize that these strong E-fields near the edges of the beaker arise due to secondary current sources which result from charge accumulation at boundaries where conductivity changes from one medium to another. Our hypothesis is supported by observations made by Salinas et al. (2009) who demonstrated that similar E-fields coming from the edges of the phantom (representing the saline-glass boundary) are secondary fields.

These secondary fields are associated with charge accumulation at surfaces with different electrical conductivities. We hypothesize that they do not appear in the measurement where, as discussed in the preceding paragraph, only the primary E-field component can be measured. Although there is no direct evidence that the FEM software package we used (CST) considers secondary E-fields and secondary currents, the company that produces this software states that it does. FEM simulations in general do calculate the total E-field in the conducting volume (Hanus et al., 2005; Salinas et al., 2009; Wagner et al., 2004b), which includes the primary and the secondary fields and hence displays the effect of the secondary E-fields in the simulation results.

Our comparison shows findings consistent with a scenario in which the measured data shown in Figure 3-17 (c) does not measure the secondary E-fields, and the simulated data shown in Figure 3-17 (d) measures the total E-field, including the primary and secondary fields. The effect of such out of phase secondary E-fields is that they can hypothetically cause a destructive interference with the primary fields. Additionally, the presence of these secondary E-fields in simulations changes the induced field profile (compared to E-field profile obtained from the measurements, hypothesized to not include contributions of secondary current) thereby reducing the linear relationship between the simulated and measured result. We hypothesize that such effects underlie the lower values of slope of this linear relationship in Figure 3-19 (b) and poor correlations in Figure 3-19 (c). To support our hypothesis that secondary currents in the simulations, but not in our measurements, underlie the mismatch, future experiments can avoid the mismatch by measuring with a probe that is capable of detecting secondary currents. Within this current thesis, this hypothesis can be supported (although not proven) by comparing the measured and simulated E-fields in a setup where secondary E-fields could be expected to be negligible. In order to address this question, the large volume setup experiment serves as a calibrating experiment. According to Salinas et al. (2009), secondary currents come into existence when the size of the conducting volume approaches the size of the TMS coil. For clarity, we can assume that the face of the stimulating coil is defined by dimensions along the x and y- axes (refer Figure 3-1 and Figure 3-2). Let us also assume that the stimulating coil is placed close to a conducting volume. If the dimensions of the conducting volume along either x or y-axis becomes equal to or smaller than the corresponding dimension of the stimulating coil, secondary current sources will come into existence. In contrast, if we take a conducting volume much larger than the coil, secondary currents will be negligible. The large volume is similar to the large saline tanks which were used in the

works of (Durand et al., 1992; Kobayashia et al., 1997) and were used to simulate a semi-infinite medium to reduce the effect of secondary currents arising from accumulation of charge at conductivity boundaries. We expect that in such scenario, the total E-field calculated from FEM simulation should predominantly represent primary E-fields (since secondary fields are expected to be negligible) and should correlate well with the measured E-field. Our hypothesis is supported but not proven by Figure 3-16 (d), which shows E-field that can be expected from primary E-field, with no clear deformation of the shape by E-fields that cannot be accounted for by the primary E-field in the FEM simulation.

The effect of the hypothetical absence of the secondary fields on the relationship between simulated and measured current densities is supported (but not proven) by Figure 3-18 (a) and Figure 3-18 (d), where no bump can be noticed as the one observed in corresponding results of the small volume. The relationship appears to have a strong linear characteristic demonstrated by closeness of the slope and correlation coefficient to unity, as shown in Figure 3-18 (b) and (d). These results are consistent with (but do not prove) a scenario in which the simulated results now almost entirely represent the primary E-field due to the almost negligible secondary E-fields. The minor changes in slope as we move from one plane to another as seen in Figure 3-18 (b) are possibly caused by reflections coming from the top and bottom layer conductivity jumps, resulting in small secondary fields from saline-to-air and saline-to-glass, respectively. However, the size of the conducting volume ensures that these hypothetical reflections are minimal. Overall, the results from the large volume experiment resemble the simulation results.

Our overall evaluation of the existence of secondary current in our simulations and measurements is as follows: (1) there is no direct evidence in our measurements for a secondary current. (2) There

is no evidence that the simulation is not wrong. (3) Strictly based on our data, one cannot make full proof conclusion about which method, simulation or measured data, is correct. (4) Based on the fact that electromagnetic induction is a fundamental part of electromagnetism, information from the company that produces CST, indirect information from the literature, and indirect evidence from our data (discussed above, in this section), we hypothesize (but do not prove) that our simulations consider secondary E-fields and secondary currents, whereas our measurements cannot measure them.

The following details support statement (4).

A. CST (or any other electromagnetic simulator) solves full range of Maxwell's equations. Our understanding is that CST does simulate the secondary fields as it is part of the fundamental Faraday's equations (induction). Faraday's law of electromagnetic induction is one of the fundamental equations in Maxwell's equations. Indeed, the 'CST EM studio low frequency' simulation module, which we used for our TMS simulations, takes secondary electromagnetic entities into consideration (https://www.cst.com/~/media/cst/products/cst-em-studio/cst_ems_low.pdf).

B. We verified the simulations first by comparing the results of the magnetic field and induced E-field profiles obtained from our simulations with their corresponding profiles and peak field values available in the literature. This has been discussed in detail in Section 3.3.8. For the comparison of induced E-field profiles between simulated E-fields and the E-field distribution available in the literature, a conducting volume (saline) was placed under the coil. Once this was achieved and we were reasonably confident about the simulations, the simulation problem model was just modified by replacing the conducting volume mentioned above with the

phantom model (which again contained saline in a glass phantom). Therefore, the conducting volume (saline) profile changed from a thin sheet to the geometric distribution of the cavity of the phantom (because saline occupies the inner cavity of the phantom).

C. Since our study is the first to use CST EM studio for TMS simulations, we verified the conformity of the induced E-fields in a conducting medium by simulating identical setups using 'Maxwell' (Ansoft Corporation) and 'CST EM Studio' (the software package we used). Maxwell has been used for TMS related studies by Wagner et al. (2004b). The results obtained from Maxwell and CST were identical.

3.5.4 Effect of electrodes on measured field distribution

The Utah array we used is MRI compatible. Even the components of the array which were under the direct influence of the TMS magnetic field, were non-magnetic (electrode contacts which were made of platinum and the lead interconnects which were made of gold). Due to this, the distortion (caused by the array) of the stimulating magnetic field from TMS, can be considered negligible.

von Ellenrieder et al. (2012) aimed to quantify the perturbation due to the presence of a measuring depth electrode on the intracranial electric potential distribution. They showed that the perturbation on the measured electric potential, caused by the electrode, is negligible if the source of electric activity is located more than approximately 1 mm away from the electrode. In their work, von Ellenrieder et al. (2012) used a model of a needle-like electrode with multiple contacts along its length. The electrode had a shank length of 25 mm with 5 contact points separated by 5 mm. The exposed contact lengths were variable (to simulate different impedances) and had values of 0.5 mm, 1 mm, 2 mm or 3 mm. Such electrodes are similar to the electrodes on the Utah array except for two differences. The first difference is that the electrode shank model used in the study of von

Ellenrieder et al. (2012) had multiple contacts whereas an electrode shank on the Utah array had one contact. The second difference is that the contact length on a Utah array electrode is of the order of 60 ± 40 μm (which is much smaller than the contact lengths on the multi-contact electrode model used by von Ellenrieder et al. (2012) and hence provides much smaller area of perturbation). The study also demonstrated that the field distributions are not very sensitive to electrode contact impedances; hence, neither low nor high impedance electrodes would alter the field distributions appreciably. The study also concludes that the measurements of the electrode's contacts would depend on the electrode only if the source of electrical activity is located within 1 or 2 mm of the electrode (the effect at a distance of 2 mm being less prominent as the size of the contact decreases). It can be observed that the perturbation appears to decrease with decreasing size of contact lengths. Hence, if the electrode involved in our study (with an electrode contact length of 60 ± 40 μm compared to 0.5 mm, 1 mm, 2 mm or 3 mm contact lengths used in the study by von Ellenrieder et al. (2012)), were to be used by Ellenrieder et al. (2012), the minimum distance for an electrode to be able to perturb the field distribution can be expected to be 1 mm (which represents worst case scenario).

Effect on Primary E-fields

The source of the primary E-field is the current flowing in the stimulating coil and hence is a property of the coil. In our phantom experiments the stimulating coil, which is the source of the primary E-field, is always located at a distance of more than 1 mm from the electrodes. The minimum distance between the coil and the electrodes in the small volume is 58 mm + 5 mm (thickness of the glass wall) + 10 mm (distance between the phantom and the coil) which amounts to 73 mm (refer Figure 3-20 (a)). Similarly, in the large volume, the minimum distance of the coil

from the electrodes is 88.5 mm + 3 mm + 10 mm = 101.5 mm (refer Figure 3-20 (b)). At such large distances, the effect of the electrodes on the primary E-field can be neglected.

If the electrodes are used to perform in-vivo measurements to calculate the E-fields on the cortex, they would have to be implanted in GM. Under such circumstances, based on the average thicknesses of the different segments of the human head volume (Adeloye et al., 1975; Awada et al., 1998; Makris et al., 2008; Wagner et al., 2004a), the electrodes would be at a distance of more than 7.1 mm (average thickness of skull) + 5 mm (average thickness of scalp) which amounts to nearly 12.1 mm from the coil (if the coil is placed in contact with the scalp), which is more than 1 mm. Hence, even in the case of in-vivo measurements, the electrodes can be assumed to have negligible effect on the primary E-field.

Effect on secondary E-fields

Although the Utah array is not suited to record the secondary E-field (a dipole probe is needed to achieve the measurement of the total E-field which includes the primary and secondary E-fields), it is important to identify whether or not the presence of the Utah array will influence the secondary E-field. Heller and van Hulsteyn (1992) demonstrated that the maximum of the secondary induced E-field occurs on the boundaries where conductivities show discontinuity. If we take the example of our phantom experiments, the jump in conductivities takes place near the edges of the phantom (where the medium switches from saline to glass) or at the top surface which is open to air (where the medium switches from saline to air). These boundaries have been indicated with red lines in Figure 3-20. A redistribution of the maximal E-fields then takes place within the entire conducting volume. These maximal E-fields behave as current sources (or sources of electrical field). In our experiments, the electrodes are never closer than 22 mm to such a source of electrical activity (the

distance between rightmost positions of the electrodes and the saline/phantom boundary marked in red in Figure 3-20 (a)). Therefore, for our phantom experiments, the effect of electrodes on the secondary E-field can be neglected.

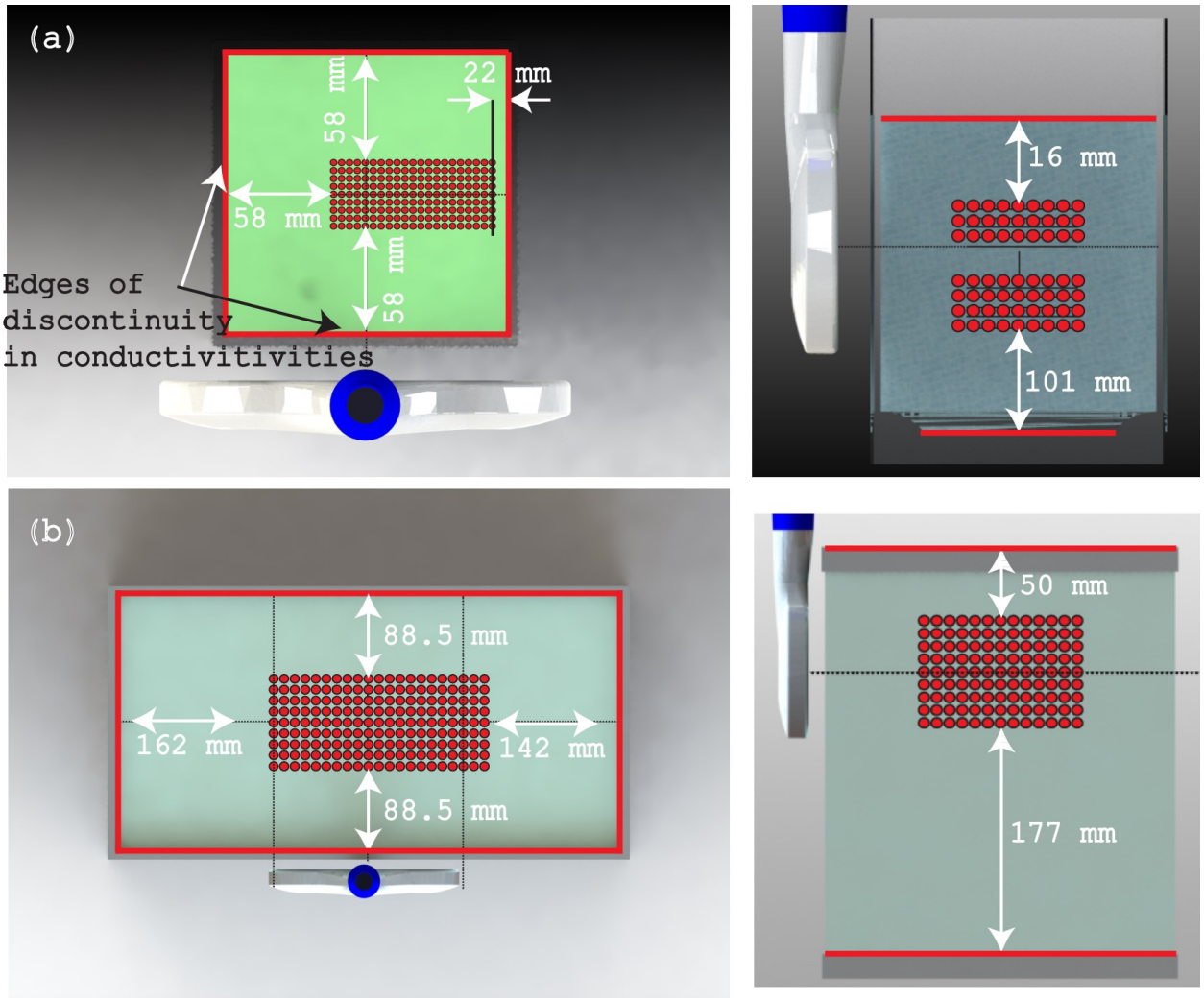

Figure 3-20. Distance of electrode positions from boundaries where conductivity jumps from one value to another (represented by the solid red lines) in the case of (a) the small volume and, (b) the large volume.

The situation may be more challenging when the measurements are obtained from the cortex of subjects in in-vivo experiments. The electrodes of the Utah array used for phantom experiments

have a shank length of 1 mm (with the exposed electrode surface located at the distal tip of the shank). Revisiting the concept that maximum of the induced E-field occurs on the boundaries where conductivities jump in values; this maximal E-field induction will take place at the boundary between CSF and GM, as shown by the green contour in Figure 3-21. Again, 1 mm distance between the E-field profile and electrode location may be sufficient to negate the effect of electrodes on the measured potential but the challenging part will be the adequate implantation of the Utah array on the cortex such that the electrodes are implanted normal to the cortex. Any deviation will result in the electrodes being implanted at a depth lesser than 1 mm and under such circumstances, the effect of electrodes will be difficult to negate. Even if a perfect implant is achieved, the base package (from which all the electrodes project out as shown in Figure 3-3) of the Utah array will rest on the cortical surface. This in turn will distort the secondary E-field distribution on the cortex because it will disrupt the CSF volume (and hence the CSF-GM boundary) at the location of implant.

Hence, based on the above discussion, it can be expected that in-vivo measurements will be able to provide a reliable measure of only the primary E-field and not the secondary E-field.

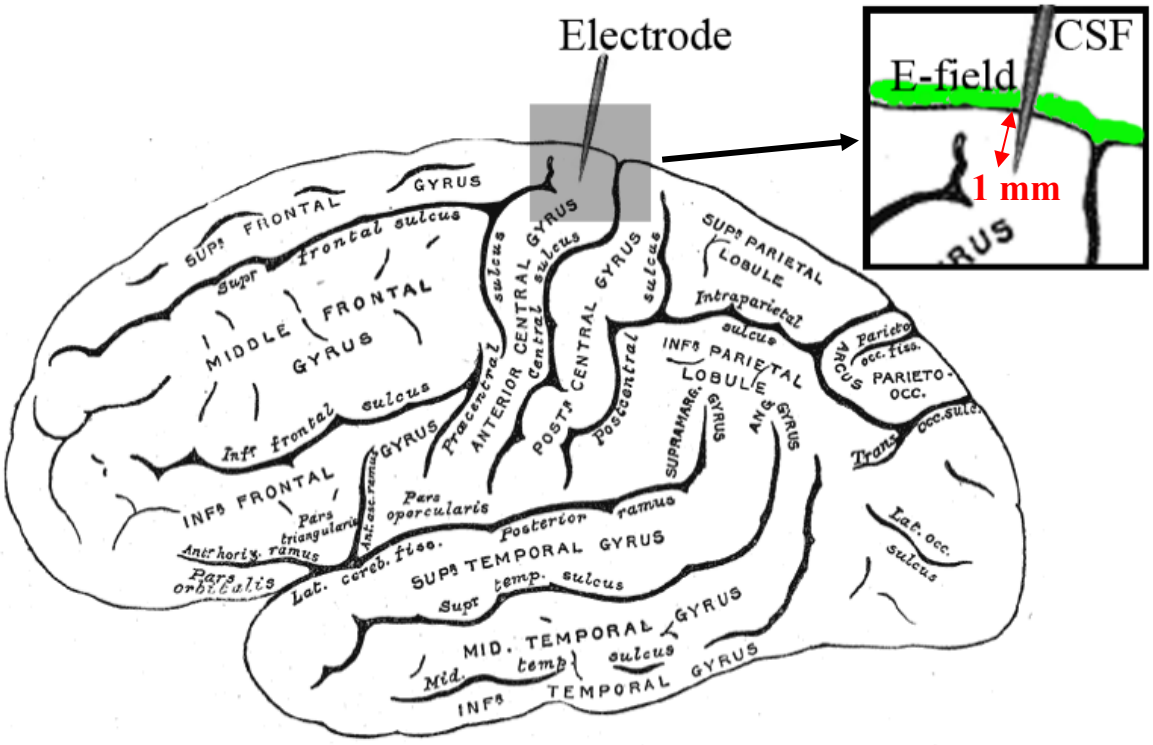

Figure 3-21. Distance of electrode implanted on the cortex (GM) with respect to maximal induced E-field (represented by the solid green contour) which occurs at the boundary between the cortex and cerebrospinal fluid (CSF).

3.5.5 Future validation experiments: dipole probe

The measured values of current densities are consistent with a measure of the primary induced E-field. We were able to validate the simulated E-field values with measured E-field values only in the large volume (where secondary E-fields are expected to be negligible) but we were unable to validate it in the small volume in which secondary E-fields are expected to play a significant role.

Although validation of simulated E-fields in the large volume increases our confidence in our simulation methodology, further validation of the induced E-fields in a small volume is required

in order to verify the capability of simulations to efficiently and accurately model the total induced E-fields. For future validation experiments, it would be beneficial to use the dipole probe (which measures the total E-field unlike the Utah array which records the primary E-field) referred to in the study by Salinas et al. (2009) and validate the simulated total E-fields with the measured total E-fields in the small volume. A single TMS pulse measurement can be performed with a dipole probe or by mimicking the dipole probe using the current Utah array. The Utah array can be rotated in x, y and z directions at each location to measure both transverse and longitudinal E-fields, similar to what was done by Salinas et al. (2009) with a dipole probe. Such a method of measurement will enable us to record the total E-field (which includes the primary and the secondary E-fields). The total E-field profiles from measurements can then be compared with the total E-field profiles obtained from simulations.

Further validation of induced E-fields on small volume conductors using a dipole probe will substantiate the confidence in TMS simulations. However, there are two potential problems that can arise when the fields are measured in-vivo. The first hurdle would be rotating the dipole probe in the cortex of a live subject to obtain all components of the induced E-field to calculate the total E-field induced on the cortex. This part of the experiment may not be feasible. Secondly, as discussed earlier, the total E-field that is measured may not be accurate due to the influence of the electrode array on the secondary E-fields.

In spite of the poor correlation between our simulations and data obtained from the small volume phantom, we were able to establish a certain degree of confidence in the legibility of simulated results based on the results obtained from the preliminary analysis of field profiles (magnetic and induced E-fields produced by the stimulating coil by comparing them with results available in

literature), the validation provided by the large volume experiment, and the information provided in the literature with respect to small volume. The key aspect that came to the forefront with this study is that the primary E-field component is a robust measure (since it depends on the stimulating coil) and can be measured correctly, whether the measurements are performed in phantom models or in-vivo. This is an interesting aspect because the primary component that is measured can be extracted from the total E-field that is provided by the simulations, in order to isolate the secondary E-field. The contribution of the secondary field to the total field distribution may become more important if tissue anomalies on the cortex (as in the case of stroke patients) or hematoma (sub-dermal or sub-dural) appear in patients because these infarcts add additional conductivity boundaries resulting in reorganization of secondary E-fields. This would result in a change in the total E-field compared to situation where there is no anomaly present. The impact of brain related anomalies on total E-fields induced on the cortex has been explored on approximate 3-D human head models for conditions pertaining to stroke (Wagner et al., 2006) or the presence of brain atrophy (Wagner et al., 2008).

3.5.6 Future simulations: frequency or time domain solvers?

Single frequency simulations, such as the one we performed for this thesis at the peak frequency of the response, do not take the constructive/destructive interference of responses at other frequencies into account. Therefore, simulated amplitudes, even at the peak of the temporal response, are inaccurate. In order to make the comparison between measured and simulated field distributions more consistent, improvements can be made on the simulations side too. With regard to FEM simulations, it would be judicious to perform a parametric analysis of the total induced E-fields over a range of frequencies from simulations which will be capable of providing the same

information as a time domain simulation. A time domain solver may also be an alternative solution to parametric frequency domain simulation. However, time domain solvers tend to be more time consuming than frequency domain solvers owing to the fact that solutions are obtained over a broadband range of frequencies. Fourier analysis implies that any time varying signal can be represented as a combination of multiple sine waves of differing amplitudes, frequencies and phases. With time domain simulations, we can analyze the behavior of the system over time. A frequency domain simulation helps us to analyze the behavior of the system in response to one of the sinusoids which the time-varying signal is composed of. A combination of the responses of the system to each of the sinusoids comprising the time varying signal will yield the same information as one time domain simulation of the signal. However, in practice, a signal may comprise of many component sinusoids and it may not be feasible to perform a frequency domain analysis for every sinusoid. A frequency domain simulation of selected frequencies may solve this problem, because instead of looking at every individual sinusoid, one can select a smaller number of sinusoids to investigate. A frequency domain solver performing such a parametric analysis has the flexibility of allowing few but optimum solution frequencies (for instance cutting out DC and close to DC frequencies and choosing only a small range of frequencies around the peak operating frequency of TMS). This reduces overall simulation time compared to time domain solvers. Additionally, since frequency domain analysis captures and describes well signals that are periodic over time, it can be beneficial to the analysis of E-field estimates associated with different types of rTMS protocols (which consist of periodic trains of stimulating pulses).

3.5.7 Significance of simulations

Simulations are non-invasive and therefore have an advantage that they are not influenced by any changes in tissue geometry or their conductive properties. Measurements tend to be invasive and hence may alter the tissue geometry (in the form of a blood clot, brain edema, or simple swelling due to incision). A certain degree of confidence in simulations was established in our current study. If the simulated results are validated in small volume conductor in future studies, simulated E-fields on realistic head geometries can be reliably assumed to provide accurate E-field measures.

The correct estimation of the total induced E-fields is, as discussed section 3.5.1, important to improving clinical application of TMS. Simulations appear well equipped to provide this information in a non-invasive manner. A good starting point to quantify dosage levels for TMS conditioning is by obtaining accurate and reliable E-field estimates at RMT because RMT is the generic measure that is used as a reference to establish TMS dosage levels.

Again, the far reaching advantages of simulations to yield total E-fields could include critical choices of stimulation intensities and dosage levels for TMS experiments, especially in patients suffering from stroke, brain lesions, infarcts or any other form of sharp and unnatural conductivity inhomogeneity. Indeed, such infarcts tend to change the distribution of the induced E-fields which arises from the intrinsic tendency of charges to accumulate more in regions of sudden changes in conductivity. Such occurrences may potentially lead to unwanted episodes such as induction of a seizure. Our study and future studies for validating simulations will, thereby, support safety measures required to conduct good TMS experiments which will yield more reliable results without having to compromise on patient safety and discomfort.

3.6 Conclusion

Our work demonstrates that a simple single turn coil model with a correct current factor can be used for simulations, thereby considerably reducing the number of tetrahedral elements in the problem domain mesh, thereby reducing the calculation nodes. This results in much faster computations and reduction in memory requirements and processor load of the computing platform. Hence, due to the use of this single turn coil model, FEM simulation methods become more practical.

Accurate estimation of total induced E-fields is important for future clinical studies involving TMS. Frequency domain FEM simulation results are capable of providing reliable description of the total E-fields that are induced in a conducting medium because they take secondary currents into account too, and are essentially non-invasive in nature (which means they do not alter the geometry or conductivity of the observation domain). This feature becomes more critical when we deal with volumes whose size is almost equal to the size of the coil span or is relatively smaller than the coil span (as in the case of spherical human head models, realistic human head models and animal head models e.g., non-human primates, cats, rats, etc.) because all these mentioned cases lead to the generation of secondary sources and secondary currents. In addition, the complex gyral and sulcal geometries result in sharp conductivity inhomogeneity resulting in additional secondary currents. FEM simulations, take all these factors into account and hence provide comprehensive information of induced currents, which allows a researcher to draw critical conclusions about TMS stimulation parameters (angle of coil, intensity of stimulation, target area

localization, etc.) in a very short time. This would enable a researcher to be more methodical and hence, obtain more accurate and reliable results from TMS related experiments.

3.7 Summary

Our work discusses the importance of accurate E-field estimates to TMS studies. FEM simulations are capable of providing such estimates and we attempted to validate TMS related simulations in phantom models. A fair degree of confidence was achieved in the simulation methodology and results, but complete confidence was not achieved due to the failure to obtain a good match between simulated and measured E-fields in a small volume conductor. Potential problems and suggestions to achieving the hypothesized validation of E-fields in the small volume conductor and eventually in in-vivo setups have been discussed.

Chapter 4 FEM TMS Simulations

Preface

Chapter 3 dealt with the validation of fields induced by TMS pulses in a conducting medium placed in the vicinity of a stimulating figure-of-eight (FOE) butterfly coil. Simulated induced field profiles were compared with measured field profiles in phantom model setups. Validation of induced E-fields was successful in the large volume phantom but not in the small phantom. Based on our partial validation and the report by (Hanus et al., 2005; Salinas et al., 2009; Wagner et al., 2004b) that FEM simulations calculate the total E-field in the conducting volume, we assume that the simulation-based estimation of the total E-fields in a conducting medium is reliable. A natural progression from the previous stage would involve application of simulated induced fields from realistic head geometries and estimate their effect on neuronal responses. Most electrophysiological (invasive) and behavioral (non-invasive) TMS studies involve the application of TMS pulses whose intensities are not defined as a percentage of maximum stimulator output (MSO) of the stimulator but rather as a percentage of motor thresholds (MT) of the subjects. This is because different individuals may require different intensity of TMS pulse to elicit neural activation. This in turn is likely to have two causes. Firstly, the excitability of cortex differs between subjects, due to normal variability (Gilio et al., 2003; Todd et al., 2009) and change in excitability with age (Shibuya et al., 2016). In addition, the head geometries can vary considerably. For instance, within humans, the thickness of the scalp

can vary depending on the subjects' age and hair growth pattern (Hori et al., 1972). Even if the thicknesses of all other segments of human head geometry (skull, cerebrospinal fluid, gray matter and white matter to name a few) are assumed to be the same across individuals, the differences in scalp thicknesses is sufficient to introduce a variable factor into measurements. The reason is the high conductivity of the scalp tissue (second highest after the conductivity of the cerebrospinal fluid), resulting in the induction of strong electric fields. These electric fields result in magnetic fields of their own, which are out of phase with the magnetic fields produced by the stimulating coil. Hence, the magnetic field reaching the next interior layer in the head geometry (the skull) will have a reduced magnitude of field strength (magnetic field produced by the coil minus magnetic field produced by the induced electric field on the scalp). This effect of back compensation continues through the different layers and if variability has been introduced by the first segment of the human head, this variability will be present in subsequent layers too. Thus, induction of electric field on the cortex will vary from one individual to another. For example, we consider that 50 % of maximum stimulator output TMS pulse intensity (creating a peak magnetic field strength of 1 T) results in an induction of an electric field strength on the cortex whose magnitude may be the threshold value for neural activation. A different individual, with thicker scalp will have more back compensation and therefore the magnitude of induced electric field on the cortex may be lower than threshold value

for neural activation. Last but not least, different geometries of the patterns of sulci and gyri cause variability of the induced currents too.

This paper aims to test the hypothesis that similar magnitudes of induced E-field strengths are sufficient to reach motor threshold (MT) across humans and non-human primates, due to the similarity in neural activation thresholds. In order to test our hypothesis, we estimate the E-field induced on the cortex of humans at motor threshold TMS pulse intensity using finite element model (FEM) simulation. The same magnitude of E-field strength is then induced on an analogous site in a FEM of a non-human primate (NHP) cortex by varying the current amplitude in the stimulating coil, thereby varying the stimulator output. The value of the stimulator output intensity obtained from the simulation is verified by performing in-vivo measurement of MT on three NHP subjects.

Estimating resting motor threshold in TMS from FEM simulations

Ajay Venkateswaran, Frederic Lesage, Amir Shmuel

Keywords: magnetic coil (MC), transcranial magnetic stimulation (TMS), finite element model (FEM), induced current density, figure-of-eight (FOE) coil, multi electrode array (MEA)

Acknowledgements:

This work was supported by a grant from the Natural Sciences and Engineering Research Council of Canada and the Canadian Institute of Health Research (**CHRP 385962-10**).

4.1 Abstract

Resting membrane potential (RMP) is the equilibrium potential established between the intracellular fluid (ICF) and extracellular fluid (ECF) across a cell membrane. Based on the concentration of Na+ and K+ ions in the ICF and ECF, Nernst equation establishes this equilibrium potential at –70 mV for mammals. When RMP of neuronal cell membranes is disrupted due to external factors (such as the induced electric field in the ECF due to transcranial magnetic stimulation (TMS)) which change the concentration of ions in the ECF, action potentials are generated. The objective of this study is to test the hypothesis that the magnitude of the induced electric field (E-field) required to achieve the resting-motor thresholds (RMT) in humans and primates are similar. Motor threshold is the generic parameter on which TMS conditioning dosage levels are based. We use the average RMT stimulator intensity in humans (44 % of maximum stimulator output (MSO)), available from the literature, to estimate the induced electric field on the motor cortex of humans, using finite element model (FEM) simulations on a spherical human head model and a realistic human head model based on image segmentation. 44 % MSO intensity

resulted in induced E-field of magnitude 176 V/m at the targeted motor cortex in the realistic head model and 74 V/m in the spherical human head model. We then used a segmented realistic non-human primate (NHP) head model and a spherical cat head model and changed the current amplitude in the stimulating coil model in order to induce 176 V/m on the motor cortex of the NHP and 74 V/m on the spherical cat head model cortical segment. 55.4 % MSO intensity resulted in 176 V/m on the realistic NHP motor cortex and 55 % MSO resulted in 74 V/m induction on the cat head cortical segment. 3 NHPs were then used to test the predicted RMT intensity of 55.4 % MSO. In-vivo measurement of RMT on these three NHPs resulted in an average RMT intensity of 51± 5.2 % (Mean ± SD) of MSO. We hypothesize that the reasonable difference between the RMT values in NHPs, estimated from simulations and that obtained from in-vivo measurements, is due to inaccuracies in the NHP FEM model due to errors associated with manual segmentation of the NHP head volume. Optimized segmentation techniques may be able to achieve a more accurate segmentation of the NHP head volume and possibly result in a better match between simulated and measured RMT stimulation intensities. The cat results have been presented as an alternative method that can be used to approximate the stimulator output for TMS conditioning in cat experiments. In conclusion, similar induced currents are required to reach the RMT in humans and primates. Our results support the estimation of RMT in conditions under which it cannot be measured, such as in experiments in paralyzed animals.

.

4.2 Introduction

Transcranial magnetic stimulation is a non-invasive technique which involves the application of time varying magnetic field pulses to the brain to alter cortical functionality. It involves induction of current in the cortex due to an externally applied magnetic field, based on Faraday's law of electromagnetic induction, followed by the subsequent effect of these currents on neuronal behavior.

TMS dosage levels are usually based on a certain measure of the intensity of stimulation, generally indicated as resting or active motor thresholds (RMT or AMT). Motor threshold (MT) is a parameter that can be measured by observing the twitch of the target muscle or by recording the responses of the target muscle using patch electrodes connected to a signal analyzer such as an oscilloscope. MT also represents a measure of the membrane excitability of pyramidal neurons (Pascual-Leone et al., 1998b) and provides insights into the efficacy of a chain of synapses from pre-synaptic cortical neurons to muscles (Kobayashi and Pascual-Leone, 2003). Hence, MT forms the reference parameter for the choice of stimulation intensities.

MT is established based on responses of target muscles, which in turn, depend on cortical responses (motor evoked potentials, MEPs) generated by the motor cortex neurons in response to TMS pulses. TMS induces electric fields (E-fields) in the extracellular fluid (ECF) region of the target cortex. Since MEPs involve the activation of cortical neurons, they would involve a disruption of the resting membrane potential (RMP) of the neurons, caused by the induced E-field.

Resting membrane potential of -70 mV is a fairly constant measure across mammals (Purves et al., 2001). Hence, the magnitude of induced E-field that can cause a disruption of the RMP is expected to be fairly constant across mammals.

Numerical methods have had a fair degree of success in calculating the induced current on different types of conducting media that are encountered in realistic head models. Numerical methods such as finite difference method (FDM), boundary element method (BEM) and finite element method (FEM) have the distinct advantage of being completely non-invasive techniques which do not mandate the presence of subjects for the analysis process. They can also be optimized to obtain fast and accurate estimations of fields induced in conducting media due to the impinging magnetic field pulses. In addition to this, numerical studies have the potential to decrease participant time during TMS experiments/treatments.

Three layer (Roth et al., 1994a; Roth et al., 1991) and four layer (Deng et al., 2013; Salinas et al., 2009) spherical and hemispherical shell models of a human head have been used to numerically estimate the currents induced in different segments of a human head due to the influence of a single pulse of TMS. In more recent studies, realistic human head models have been used for numerical estimation of the induced currents (Opitz et al., 2011; Thielscher et al., 2011) taking anisotropy of white matter into account too. However, animal models, which are extensively used for invasive TMS studies, have not been developed yet.

Here we test the hypothesis that similar magnitudes of E-field are required to reach RMT in humans and non-human primates (NHPs). We use FEM simulations to estimate E-fields induced in humans and NHP head models and demonstrate that the E-fields required to reach RMT in humans and primates are similar.

4.3 Materials and methods

4.3.1 Finite element model simulation on a realistic human head

Most TMS studies report the intensity of stimulation as a percentage of resting or active motor thresholds. The choice of motor threshold (MT) is due to the fact that this is the only parameter that results in a visible deterministic effect (twitch of targeted muscle). Motor threshold also represents a measure of the membrane excitability of pyramidal neurons (Pascual-Leone et al., 1998b) and provides insights into the efficacy of a chain of synapses from pre-synaptic cortical neurons to muscles (Kobayashi and Pascual-Leone, 2003) and hence forms the reference parameter for the choice of stimulation intensities. Previously, resting motor threshold (RMT) was obtained by delivering single pulse of TMS to the motor cortex and observing the response of the targeted muscle, stimulated cortically by the TMS pulse, on the contralateral side, when the target muscle is in a relaxed state before and immediately prior to the application of the TMS pulse. The target muscle for motor threshold experiments is the first dorsal interosseous (FDI) muscle. Similarly, active motor threshold (AMT) is obtained by delivering TMS to the motor cortex and observing the response of the FDI muscle on the contralateral side, when the FDI muscle is in a state of voluntary contraction before and just prior to the application of the TMS pulse. The observation of the response of the FDI muscle can be achieved in two ways; the first is by observing the muscle twitch visually and the second is by recording the muscle response using electromyography (EMG) surface electrodes. If observation of muscle twitch is used to determine the MT, then it is defined as the lowest setting of the stimulator output at which ≥ 5 out of 10 stimuli result in observable movement of the index finger (Westin et al., 2014). If EMG is used to define MT, then a reliable response of the muscle is defined as a motor evoked potential (MEP) of 50-100 μV (for RMT) or

200-300 μV (for AMT) occurring in 50 % of 10 to 20 consecutive trials (Rothwell et al., 1999). TMS studies generally use TMS intensities defined as a percentage of RMT or AMT. When TMS is delivered at less than 100 % RMT or 100 % AMT, it is called subthreshold stimulation and if the stimulation intensity exceeds 100 % RMT or 100 % AMT, it is called suprathreshold stimulation. Komssi et al. (2004) demonstrated that stimulus intensity as low as 60 % of RMT was sufficient to evoke measurable potentials (in the form of MEPs) and there was a non-linear relationship between brain response and intensity of TMS stimulation. The MEP amplitudes and the global mean field amplitude (a measured used by the authors to quantify brain response) showed a nonlinear relationship with respect to stimulus intensity. The intensity of TMS stimulus varied from 60 % and 80 % RMT (subthreshold stimulus) to 100 % and 120 % RMT (suprathreshold stimulus). The non-linearity in response-stimulus relationship has been also detailed in the work of Hanakawa et al. (2009). Garry and Thomson (2009) showed that short interval intracortical inhibition, a measure used to quantify intracortical inhibitory processes, was significantly affected at suprathreshold intensities but not at subthreshold intensities. More recently, Berger et al. (2011) demonstrated that 1 Hz repetitive transcranial magnetic stimulation (rTMS) delivered to the motor cortex at 40 % RMT resulted in significant reduction of motor evoked potential (MEP) amplitude whereas the same TMS protocol delivered to the motor cortex at 100 % RMT resulted in increased MEP amplitude. We, therefore, understand that choice of TMS stimulation intensity (subthreshold or suprathreshold) can have significantly differing effect on brain response. We also understand that the choice of stimulation intensity is measured in terms of RMT or AMT. RMT is measured in order to have a subject-specific reference of excitability. If experimenters use fixed percentage power of maximum stimulator output (MSO) on all subjects, some subjects, with higher excitability will be influenced more than others. Conversely, subjects

with lower excitability will be influenced less than others. This may result in inter-individual variability in the effects of TMS. For this reason, the investigation of RMT or AMT is important for TMS studies.

The average RMT of humans, when stimulated with a 70 mm butterfly coil by Magstim, is approximately 44 % maximum stimulator output (Gilio et al., 2003; Todd et al., 2009) but no literature is available with regard to the electric field that is induced on the motor cortex at RMT intensities. In their work, Julkunen et al. (2012) demonstrated that for removal of the effect of coil-to-cortex distance (CCD) from motor threshold measurements, the induced field is a more reliable measure than percentage of maximum stimulator output intensity. The quantification of the induced electric field at MT is an interesting point because neural activation threshold across not only humans but different species remains fairly constant due to the equilibrium potential (or resting membrane potential) that is established across cell membranes (Purves et al., 2001). When this equilibrium is disrupted by an induced electric field (in the extracellular space), an action potential is generated. Since the neural activation threshold is a stable measure, the electric field magnitude that can cause neural activation can be assumed to be a quantifiable measure.

With regard to humans, there is literature available with regard to average motor threshold stimulation intensities. No literature is available regarding the MT of non-human primates (NHPs). Gu and Corneil (2014) have reported that threshold for activation of neck muscles of three macaque monkeys (established by delivering TMS to the frontal cortex) was [45 %, 40 %, and 35 %] of maximum stimulation output (MSO). Similarly, no literature is available on either MT or phosphene threshold (PT) of felines (the PT is more relevant in feline experiments because feline models are predominantly used to study the effect of TMS on the visual cortex (Moliadze et al.,

2005; Moliadze et al., 2003) and in most feline experiments, the animal is paralyzed to prevent movement of the eyes).

The current study aims at determining the threshold induced electric field magnitude at average RMT in humans and to study whether using that value of electric field magnitude to predict the TMS stimulation intensity in other species is reliable.

4.3.2 Finite element model simulation on a realistic human head

Three dimensional volumes of different segments constituting a head volume (e.g. scalp, skull, cerebrospinal fluid, gray matter, white matter, etc.) were generated based on the information provided by MRI images obtained from the database of the Brain Imaging Center (BIC) at Montreal Neurological Institute (MNI). The MRI images in Medical Imaging NetCDF (MINC) format were exported to Brainsight® (Rogue Research, Montreal), which is a neuronavigation program that provides segmentation tools too. In subsequent sections, segment refers to each part of the head volume i.e. Scalp, skull, cerebrospinal fluid, gray matter or white matter. Therefore, there are 5 segments in our head models. Thresholding, based upon the brightness and contrast, was carried out for five different regions relevant to our study (scalp, skull, cerebrospinal fluid, gray matter and white matter). Corresponding to each segment of the human head, threshold intensity (brightness and contrast) was selected, through visible observation, for each MRI slice to highlight the selected segment in the MRI slices. Manual seeds were planted on each MRI slice by selecting the highlighted segment. The seed planted on each MRI slice was a selection of particular pixel intensity. The software then selected all pixels, corresponding to the intensity of the seed pixel, on the MRI slice. Repeating this process for each segment through all slices provided us with coordinates of the selected segments across the whole head volume. Manual segmentation

technique based on thresholding, such as the one being used for this study, is time consuming and does not provide accurate segmentation because it is prone to manual errors. More elaborate and automated non-linear registration (Collins and Evans, 1997; Collins et al., 1995), patch-based label fusion (Chakravarty et al., 2013; Coupé et al., 2011) and non-local segmentation (Eskildsen et al., 2012) techniques can provide faster and more accurate segmentation than manual segmentation. For the current study, the time required for manual segmentation was not a concern and compromise in accuracy of the realistic models was considered to be acceptable. If the results would prove to be satisfactory, segmentation techniques mentioned above could be implemented to arrive at more accurate description of head geometries.

Based on the coordinates of the five defined regions of interest (ROI's) obtained through the seeding procedure, individual stereolithographic (STL) surface meshes corresponding to each of the five mentioned segments, were generated from Brainsight (which provides a 3-D reconstruction tool from seeded regions of interest from a sequence of MRI slices). STL is a 3-D computer aided design (CAD) file format in which the STL volumes (or objects) are primarily a collection of triangular surface element mesh, which means that STL objects only define the surface geometry of a 3-D object. One cannot assign material properties to the volumes defined by these surfaces tessellated with small-area triangular elements. Each STL object was exported and saved. Once the individual segments were obtained, the post processing step involved model simplification to reduce the file sizes. If the individual STL files had been loaded on the electromagnetic simulation software, it would have led to RAM related issues on the computer due to the default dense triangulations defining the surfaces. In order to overcome this, the model was resampled (reduced triangulation). The segmented STL files obtained from Brainsight were exported to Magics (Materialise, Leuven, Belgium) where the triangulation was reduced. Each

segment was then checked for errors, smoothed and eventually, all the segments were imported into one file and arranged concentrically. After the alignment, Boolean operations were performed in order to eliminate any possibility of overlaps and intersections. The cumulative head model was then cleaned again and checked for overlap and intersection errors. This reduced the size of the STL files to be imported into the finite element analysis software platform from 800 MB to 5 MB. This lead to a minor variation in the geometry of the segments but resulted in a substantial decrease in memory requirements without affecting the residual values and thus the convergence. CST EM Studio Low Frequency (LF) frequency domain solver (Computer Simulation Technology AG, Darmstadt, Germany) was used to perform simulations using FEM. In CST EM Studio, the level of accuracy is defined by the residual value which is the ratio between the result of current iteration and the result of the preceding iteration. It is always presented as a relative measure of current value to previous iteration value and therefore, has no units.

The STL object file corresponding to each segment was imported to CST EM Studio Low Frequency (LF) frequency domain solver for simulating the induced E-fields using FEM. Each segment was again cleaned and healed using object healing tool on CST in order to make sure that all the nodes on the individual segments were clearly defined on the simulation platform following which the 3D surfaces were rendered into 3D volumes. Material characteristics based on the specifications provided in Table 4-I were assigned to the 3D volume segments. A summary of all the steps is shown in Figure 4-1.

Table 4-I Material properties of the five segments considered for simulation.

Segment	Relative Permittivity (ε_r)	Relative Permeability (μ_r)	Electric Conductivity (σ) (S/m)	Material Density (ρ) (kg/m^3)
White matter	120	1	0.126	1030
Gray Matter	120	1	0.276	1030
CSF	60	1	1.654	1010
Skull	80	1	0.01	1850
Scalp	120	1	0.465	1100

Material properties of each segment of a human head used in the FEM calculations are based on values reported by (Makris et al., 2008; Schimpf et al., 1998; Wagner. et al., 2004b)

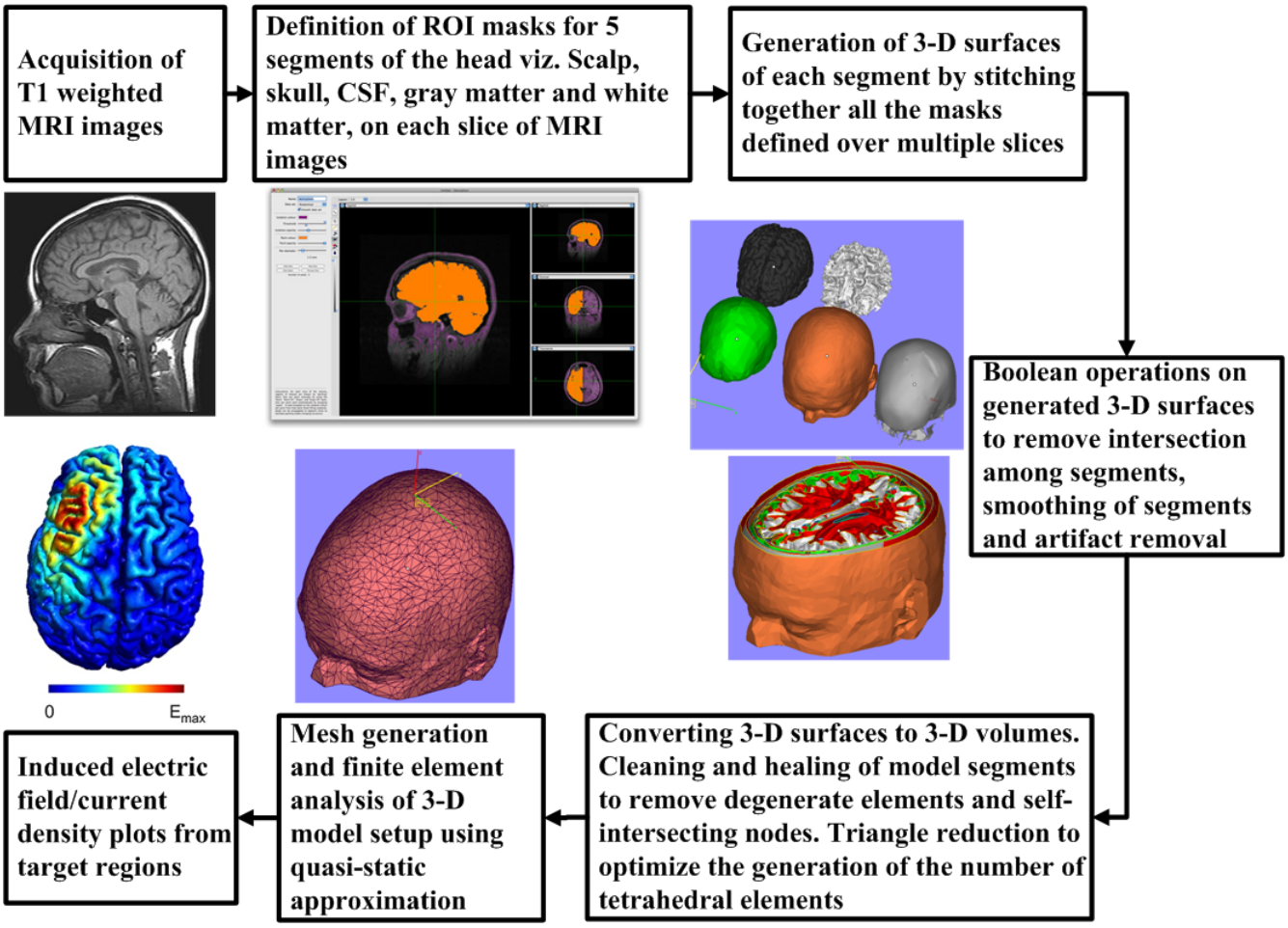

Figure 4-1. Flow-chart and pictographic representation of sequence of steps involved in obtaining simulated current density distribution in realistic 3D head models from MRI images. Reference image of induction of electric field, due to a given TMS pulse, on human cortex has been obtained from Opitz et al. (2015).

4.3.3 Electric field induced on the motor cortex at average motor threshold stimulation intensity

The averaged human head model, developed from the average human MRI images from BIC database, was used to quantify the induced electric field magnitude on the motor cortex when the TMS coil was oriented to replicate the orientation of the coil used to evaluate motor threshold in real experiments. The most optimal orientation of the coil occurs when the direction of the induced

current is perpendicular to the direction of the pre-central gyrus (Terao et al., 1998). This occurs with a 45° lateral diagonal coil orientation (refer Figure 4-2 (a) and (b)) roughly perpendicular to the central sulcus. Recently, Bashir et al. (2013) have demonstrated using neuro-navigation techniques in conjunction with TMS MEP recordings that this kind of coil orientation does not necessarily result in maximum MEP amplitude but for our study, we decided to conform to the classic 45° orientation. The 3-D model setup with a realistic FOE coil and its single turn equivalent for simulation using FEM is depicted in Figure 4-3. All the segments were meshed using second order tetrahedral elements and consisted of 2,500,000 elements. The desired accuracy was set to $1x10^{-3}$ residual value.

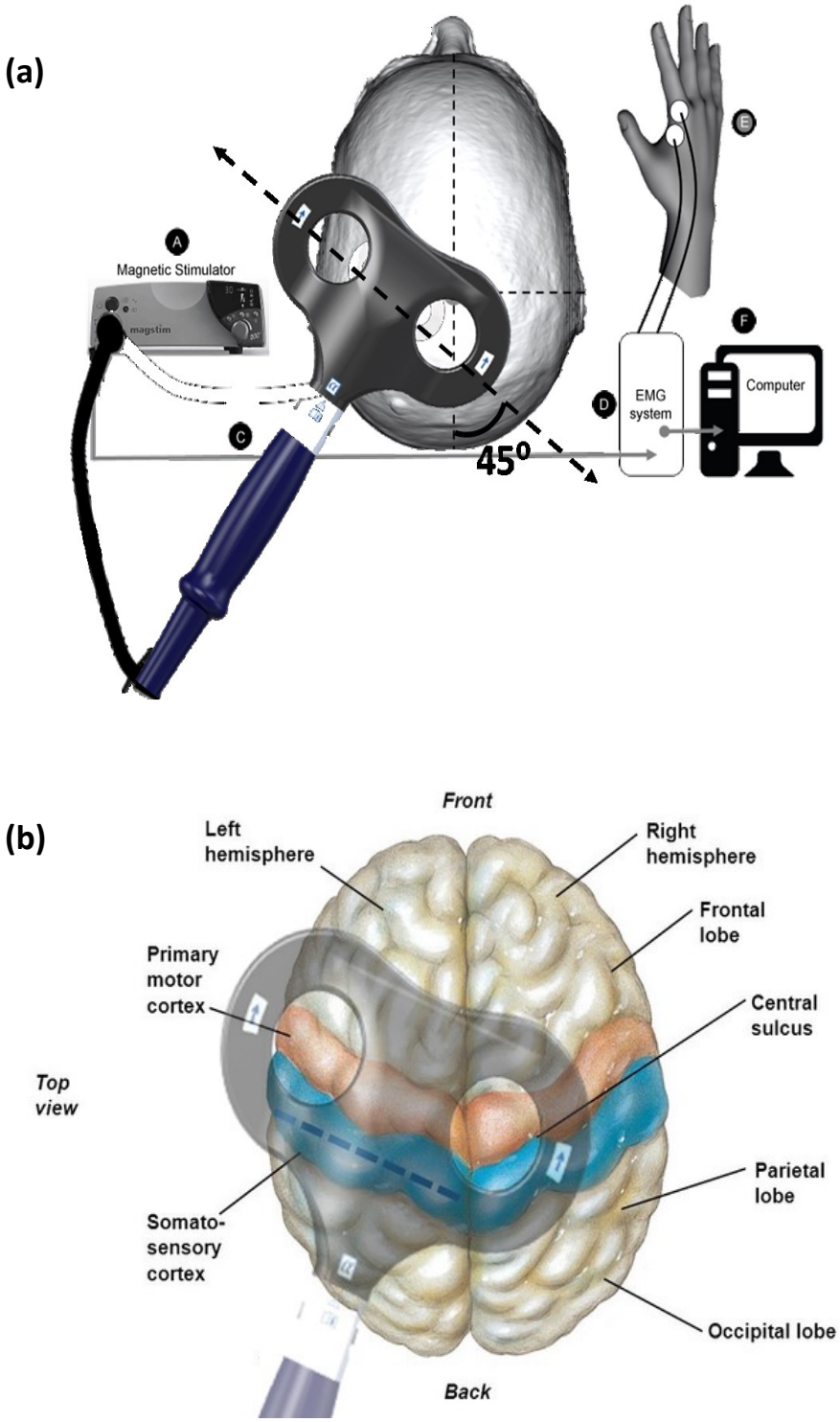

Figure 4-2. (a) Orientation of a figure-of-eight (FOE) or butterfly coil with respect to the human head. (b) Orientation of coil with respect to motor cortex in experiments targeted to elicit motor evoked potentials (MEPs) and determination of motor threshold (MT).

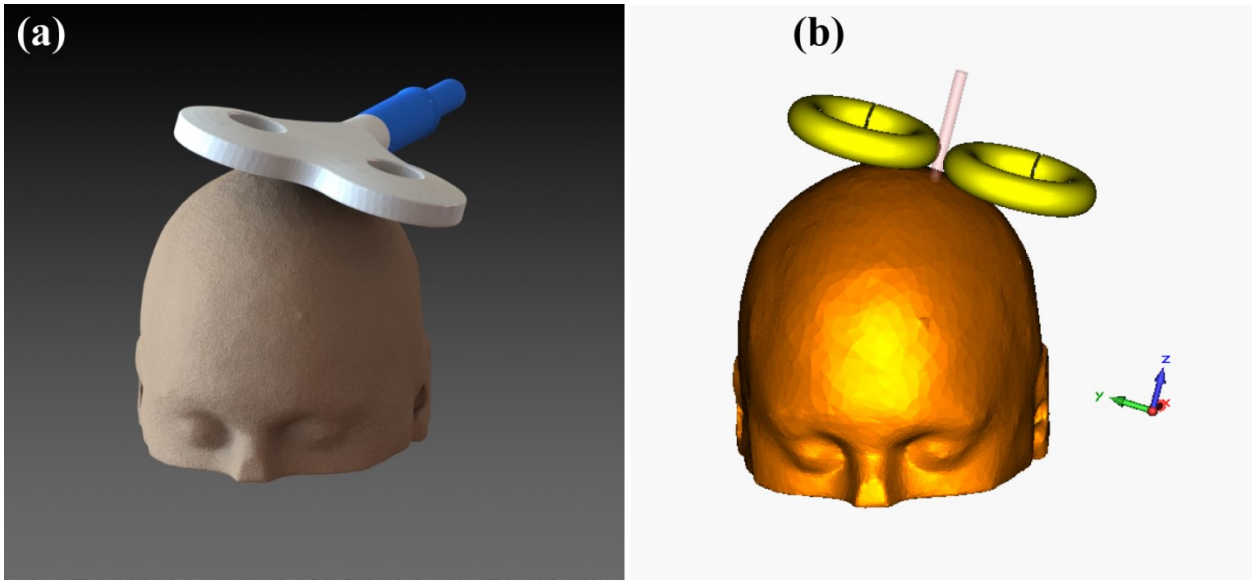

Figure 4-3. (a) Schematic depicting the optimum placement of the realistic coil relative to a human head (such that induced current on the motor cortex is directed perpendicular to the gyrus) to calculate resting motor threshold. (b) Equivalent finite element analysis model setup for determination of current induced on the motor cortex in humans at average motor threshold intensity (44 %) using a single loop model of the real TMS coil.

4.3.4 Finite element model simulation on a realistic NHP head

For the non-human primate model (3.2 kg macaque female), a close variant of the methodology used for the generation of the 3-D human head model, was used. T1-weighted images (MPRAGE, 0.5 mm × 0.5 mm × 0.5 mm, TR2300, 128 slices) of the NHP were used to develop four masks corresponding to scalp, bone, gray matter and white matter. The cerebrospinal fluid (CSF) is not easily identified in a T1 weighted image of an NHP. Since its location can be inferred by the empty space between the skull and gray matter, CSF volume was obtained indirectly by scaling up the gray matter segment and then performing a Boolean subtraction of the bone and gray matter from the ballooned segment. This provided the five required segments for the NHP head. The total volume occupied by the NHP brain was 37.531 cm^3 and the volume occupied by the head was 114.314 cm^3. An important point to be noted in this choice of segmentation technique is that it is

not possible to clearly distinguish between skull and CSF from a T1 weighted MRI image. Due to this, we may be underestimating the CSF volume thereby resulting in an underestimation of the induced electric field. The STL object files were then imported to CST EM Studio Low Frequency (LF) frequency domain solver for simulation of induced E-fields using FEM. As a first iteration, a stimulation intensity identical to the one used for human RMT measurement, was used (44 % MSO). This led to lower induced field on the cortex given that the size of an NHP head is smaller than that of an average human. Thus, for the second iteration, current in the coil was adjusted accordingly in order to match the induced field magnitude on human motor cortex (at 44 % MSO). The coil current was adjusted by increasing the amplitude of the stimulating current pulse. An increase in the amplitude of the pulse (while keeping the time period of the pulse constant) results in a faster rise time of the stimulating pulse. This results in an increase in the induced electromotive force (e.m.f.) since e.m.f. is directly proportional to the rate of change of current in the coil. As induced e.m.f. increases, the induced potentials increase and correspondingly, the induced electric field also increases. The 3D coil model was aligned as it would be for RMT measurement, targeting the motor cortex with the coil aligned at a distance of 10 mm from the scalp segment such that the induced current would flow perpendicular to the gyral length. The simulation setup is shown in Figure 4-4 (b). All the segments were meshed using second order tetrahedral elements with a total of 900,000 tetrahedral elements and the desired accuracy was set to $1x10^{-3}$ residual value.

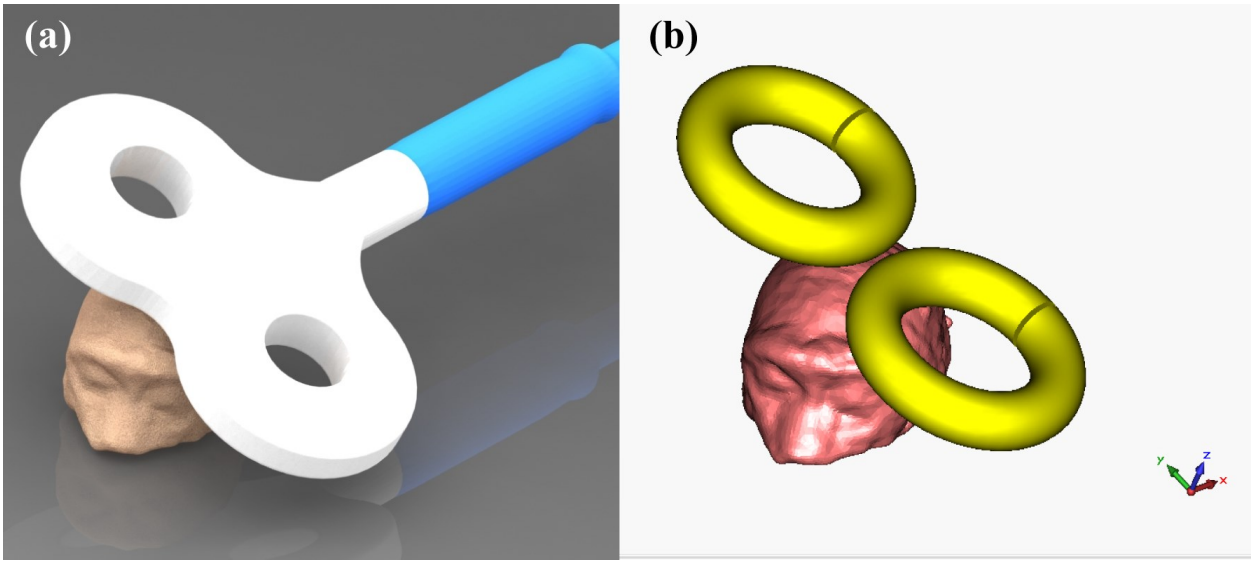

Figure 4-4. (a) Schematic depicting the optimum placement of the realistic coil relative to an NHP head (such that induced current on the motor cortex is directed perpendicular to the gyrus) to calculate resting motor threshold. (b) Equivalent finite element analysis model setup for determination of current induced on the motor cortex in NHPs using a single loop model of the real TMS coil.

4.3.5 Determination of motor threshold (MT) using in-vivo measurement in NHPs

Three NHPs, whose brain and head volumes were a close match to NHP used to develop the FEM model template, were selected for in-vivo measurement of MT. Adhesive liquid electrolyte gel surface patch electrodes (EL503, Biopac Systems Inc., Goleta-CA, U.S.) were attached to record signals from the FDI muscle of the animals (similar to the electrode placement in humans shown in Figure 4-2 (a)). The signals for MEPs from surface patch electrodes were amplified and filtered (DC-3 KHz) with a GRASS amplifier (Natus Neurology, Middleton-Wisconsin, U.S.A.). They were subsequently recorded on a custom-made LABVIEW (National Instruments, Austin-Texas, U.S.A.) program at a sampling rate of 10 KHz. Motor threshold was measured at rest (resting motor threshold or RMT). In order to elicit MEPs, the coil was approximately aligned rostro-

caudally, perpendicular to the central gyrus with the lower plane of the coil tangential to the local cortex. RMT was defined as the lowest intensity of TMS pulse, required to elicit MEPs of magnitude ≥ 50 μV in at least five out of ten trials.

4.3.6 FEM simulations using spherical head models

We performed an analysis of the induced currents on a spherical head model of a cat, all the while retaining the key aspects enforced on the model due to surgery (regional absence of scalp, bone, etc.) in order to improve our approximation. Our rationale and approach is explained in the following sections.

Choice of stimulation intensity for feline experiments

With paralyzed cats that we intended to use for in-vivo experiments, the procedure to ascertain MT (or PT) is rather difficult. Hence, we sought a different way to choose our stimulation intensity based on FEM simulation, instead of choosing a random TMS stimulus intensity. The simulation for one TMS pulse, delivered through a figure-of-eight coil, was conducted on 5 layered spherical shell head models, one each for humans and cats. The 5 layered spherical head model of humans was developed based on the combination of specifications provided in numerous studies (Adeloye et al., 1975; Awada et al., 1998; Makris et al., 2008; Wagner et al., 2004b). Similar to the proposed NHP cortex simulation, the underlying principle/logic was to use the induced E-field magnitude obtained for a TMS pulse of intensity equal to the average resting motor threshold (RMT) intensity of humans (44 % MSO) as reference and induce the same magnitude of E-field on the surface of the gray matter segment of the feline head model; by varying the current amplitude in the stimulating coil.

4.3.7 Induced field magnitude in a spherical human head model

The 5 layer sphere model of a human head was based on the combination of specifications provided in numerous studies (Adeloye et al., 1975; Awada et al., 1998; Makris et al., 2008; Wagner et al., 2004b). The diameter of the innermost sphere (representing WM) was set to 130 mm and the approximations for the thicknesses of skin-scalp, skull, CSF and GM were 5 mm, 7.1 mm, 3 mm, and 3 mm, respectively. The thickness of the skull was obtained by averaging the values reported by Adeloye et al. (1975). The radii of the spheres used to define WM, GM, CSF, Skull and Scalp are as follows:

$$R_1 = 65 \text{ mm}, R_2 = 68 \text{ mm}, R_3 = 71 \text{ mm}, R_4 = 78.1 \text{ mm and}, R_5 = 83.1 \text{ mm}$$

Based on the average stimulation intensity for MT in humans (44 %), we evaluated the strength of the induced electric field on the surface of the gray matter segment of the human spherical head model. For actual MT experiments in current practice, the insulated coil is held in contact with the scalp, with the “sweet spot” of the coil right above or close to the target area (in case of determination of MT, the target area is the motor cortex).

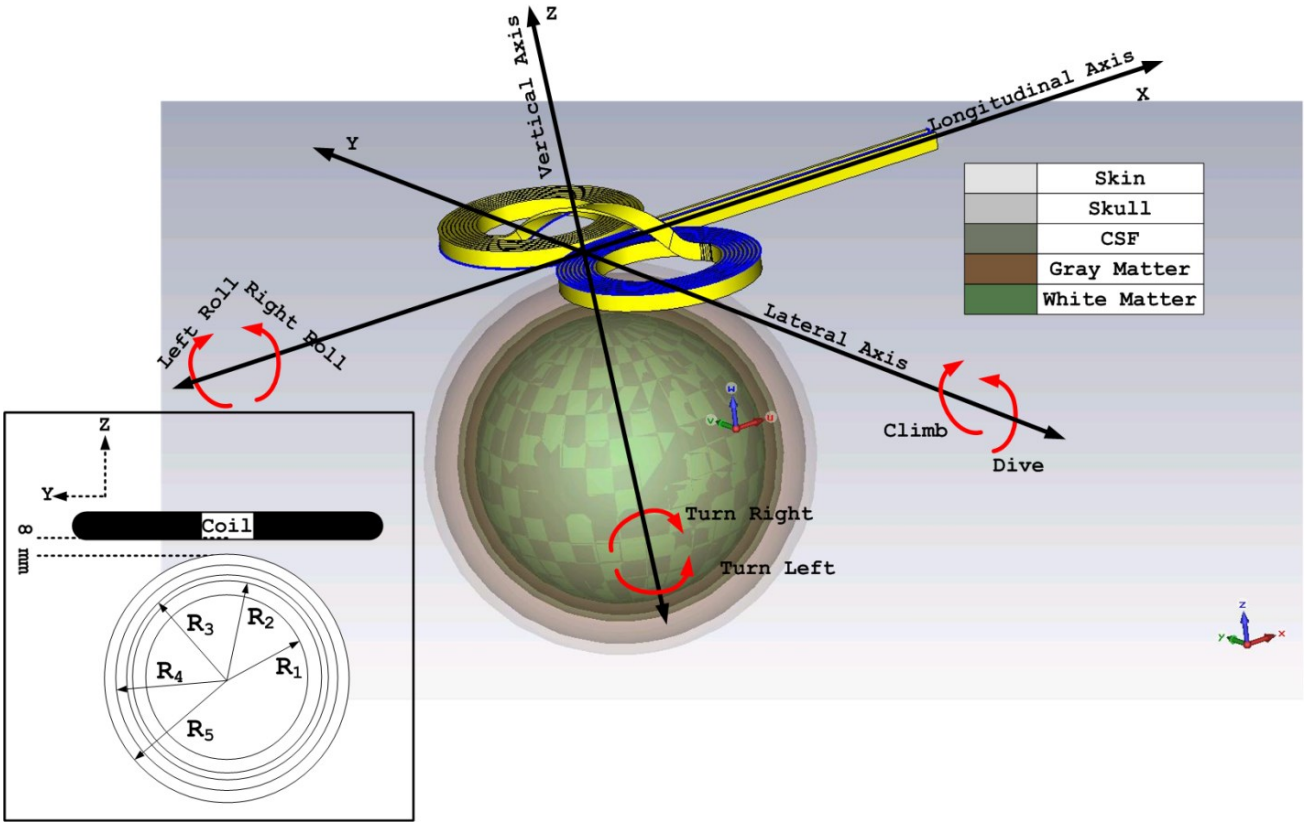

Figure 4-5. Simulation setup on spherical human head model that was used to evaluate and optimize the simplistic TMS coil model which could replicates the effects of a realistic TMS coil model shown in the image.

The sweet spot (or the most effective spot for neural activation (MESNA)) lies approximately midway (21 mm from the center of the coil as opposed to 22.5 mm) between the axis passing through the center of the coil along with the centers of the two windings (central transverse axis) and the outer fly of the coil parallel to the central transverse axis. This also corresponds to a (-) mark on the actual Magstim FOE coil shown in Figure 4-7 (a). The MESNA was a fascinating site since we were particularly interested in the effects of TMS on neuronal responses and not on the direct induction of electric field on the cortex. Abdeen and Stuchly (1994) have previously shown that the spatial derivative of the induced electric field is common to the activation function of both straight and bent neurons, with the difference that the activation function of bent neurons consists

of an additional component of the induced electric field itself (due to which it is easier to stimulate bent neurons that straight neurons). This view is also supported by Rothwell (1993). With the aid of the explanation provided by Pascual-Leone (2002), our deduction, that the spatial derivative of the induced E-field would be maximum right around the MESNA mark, was further strengthened. Hence, the site with maximum probability of activation would be around the MESNA mark and not right beneath the center of the coil. In fact, this offset in the stimulation point using TMS has been reported in previous work (Herwig et al., 2002). However, the offset is not exactly equivalent to the position of the MESNA since the average reported offset is around 10 mm. In order to be conservative in our approach, we decided to use an offset that was nearly midway between the MESNA and the offset reported by (Herwig et al., 2002). In our simulation setup, the target site is ¾ distance from the center of the coil to the MESNA, resulting in an offset of 15.75 mm. The target site is right above the target region, i.e., above the center of the spherical shell model and we have retained a finite distance of 1 mm between the scalp and the coil in order to compensate for the insulation casing of the coil. The simulation setup consisted of 300,000 second order tetrahedral elements and the desired accuracy was set to $1x10^{-3}$ residual value.

4.3.8 Spherical cat head model

For the spherical head model of a cat, we assumed that the thicknesses of the GM, CSF and scalp would remain the same as that of humans. The only things that would vary are the volume (hence radius, since we intend to use a spherical volume, where the volume of a sphere is given by $Volume = {}^{4}/_{3}\ \pi r^{3}$, r being the radius of the sphere) of the white matter segment and the thickness of the skull. Based on the Cuvier's fraction of brain-to-body weight ratio (n.d.), we calculated that the volume of WM in a human head is 47 times the volume of WM in a cat head.

Hence, the radius of the WM segment for the cat head volume would be reduced in factor by cubic root of 47. Hence the WM diameter for a cat was calculated to be 36 mm, from ear to ear. The thickness of the skull was obtained from the MRI images provided in the work by (Kim and Kim, 2011) and was averaged to a value of 2 mm. The thicknesses of the segments for the cat head model were, thus, defined: Scalp - 5 mm (obtained during feline experiments performed in our laboratory), skull – 1.3 mm (average skull thickness obtained from Kim and Kim (2011)) , CSF – 2 mm (Klarica et al., 2006) and GM – 1.5 mm (average thickness of GM obtained from Kim and Kim (2011)). The radii of the spheres used to define WM, GM, CSF, Skull and Scalp are as follows: $r_1 = 18$ mm, $r_2 = 21$ mm, $r_3 = 24$ mm, $r_4 = 26$ mm and, $r_5 = 31$ mm

We intended to use the stimulation intensity based on the induced E-field amplitude in feline experiment in which the scalp would be removed and the cortex would be exposed for optical imaging and subsequent implantation of a neurophysiology electrode array by creating a circular opening (approximately 18 mm in diameter), centered on the midline at Horsley-Clark coordinate A4) on the skull.. In order to replicate the experimental setup the scalp segment was ignored and an 18 mm circular window was created on the skull. The simulation setup consisted of 430,000 second order tetrahedral elements and the desired accuracy was set to $1x10^{-3}$ residual value.

4.4 Results

4.4.1 FEM simulation on a realistic human and NHP heads

We simulated field induction at the operating frequency of TMS, 3.324 kHz. The simulation was performed on an 8 GB RAM, 3.00 GHz Core 2 Duo processor computing platform and it took 20

minutes for the FEM solver to converge to a solution for realistic human head model (residual of $1.35x10^{-3}$ in 30 iterative steps) and about 5 minutes for the realistic NHP model (residual of $9.75x10^{-4}$ in 46 iterative steps). For pulse intensity value of 44 % maximum stimulator output reported for motor threshold in humans, we obtain an average electric field of magnitude 176 V/m at the target location on the motor cortex (the spread of the range is from 143-215 V/m). This is shown in Figure 4-6 (a), where the intersection of the pointer (perpendicular to the plane of the coil) and the cortex defined the required field magnitudes. For the same value of stimulation intensity, the field induced at the motor cortex of NHPs was nearly 125 V/m (the spread ranged from 113-135 V/m) as shown in Figure 4-6 (b). The reduction in induced field strength, for the same TMS pulse intensity, is in accordance with observations made in other studies (Valero-Cabré et al., 2005; Weissman et al., 1992). The stimulation intensity was then increased to 50 % MSO in a second iteration. This resulted in an E-field profile of magnitude 158 V/m shown in Figure 4-6 (c) at the target motor cortex of the NHP model. The iterations were continued till a simulated intensity of 55.4 % MSO resulted in an induction of 176 V/m E-field magnitude on the NHP motor cortex.

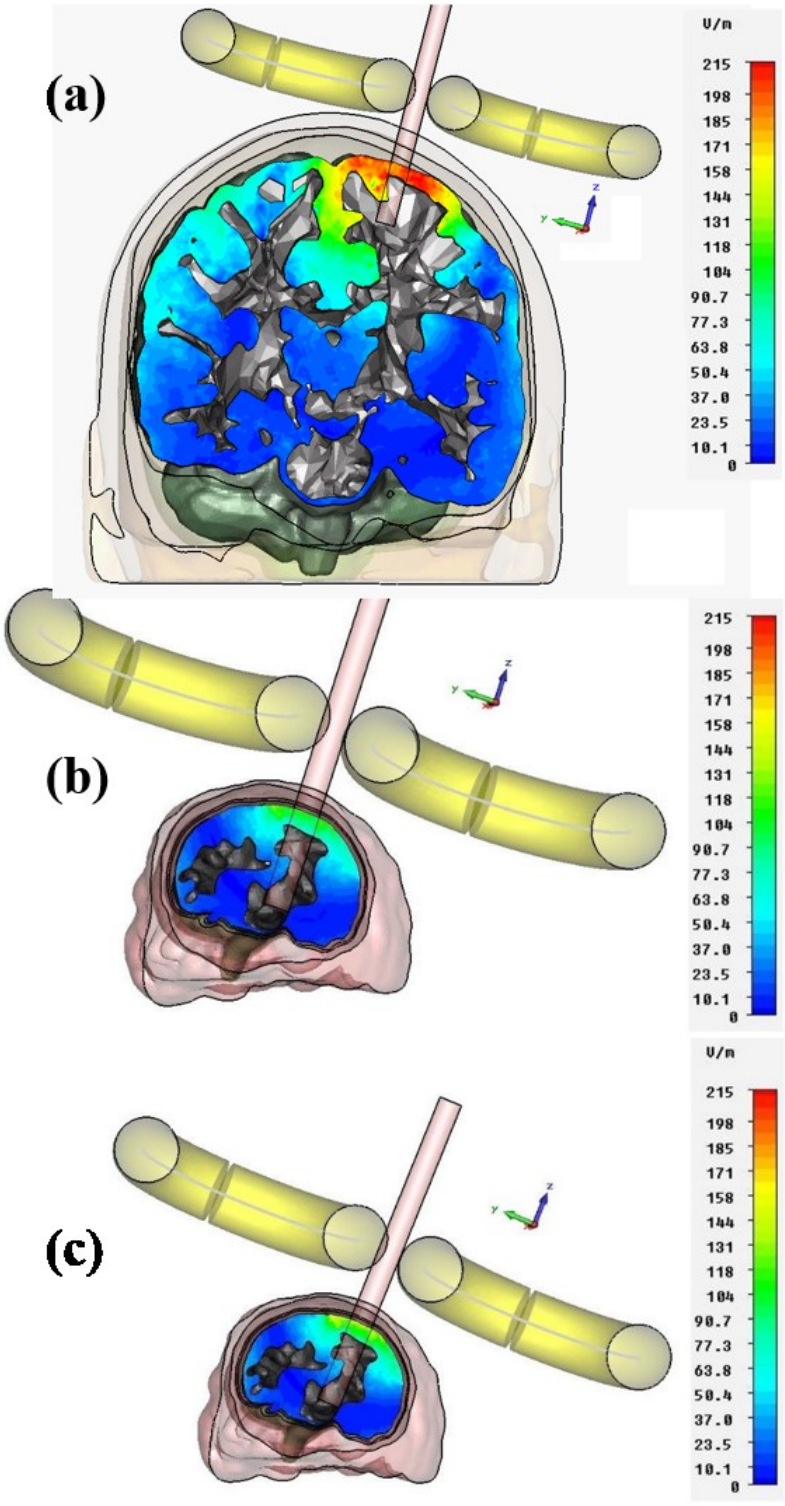

Figure 4-6. Profile of induced electric field on the motor cortices of (a) human head at 44 % MSO. (b) NHP head at 44 % MSO and, (c) NHP head at 50 % MSO. A guide pointer, perpendicular to the plane of the coil, was used in the models to localize the targeted motor cortices on both human and NHP head models.

4.4.2 Motor threshold (MT) values from in-vivo experiments

In-vivo measurement of MT from three anesthetized NHPs provided us a mean value of 51± 5.2 % (Mean ± SD) of MSO.

4.4.3 FEM simulation on a spherical human and cat head models

For the spherical models, it took about 2 minutes for the FEM solver to converge to a solution for spherical human head model (residual value of 8.75×10^{-4} in 12 iteration steps) and about 3 minutes for the spherical feline head model (residual value of 6.49×10^{-4} in 32 iteration steps). The region on the cortical segment of the spherical shell model lying directly under the target site of the coil is our region of interest (ROI) in the plot and it is represented by a white circular patch in Figure 4-7 (b). The average strength of the E-field induced in our ROI was determined to be nearly 74 V/m. In Figure 4-7 (c), we see that the average induction on a spherical cat cortex at the previously defined ROI is nearly 57 V/m (70 % of induction obtained at the ROI during MT in spherical human head volume in Figure 4-7 (b)). We increased the stimulation intensity for the spherical cat head simulation accordingly till the E-field estimate at the selected ROI reached 75.6 V/m Figure 4-7 (d). The stimulation intensity required to achieve this was 55 % MSO.

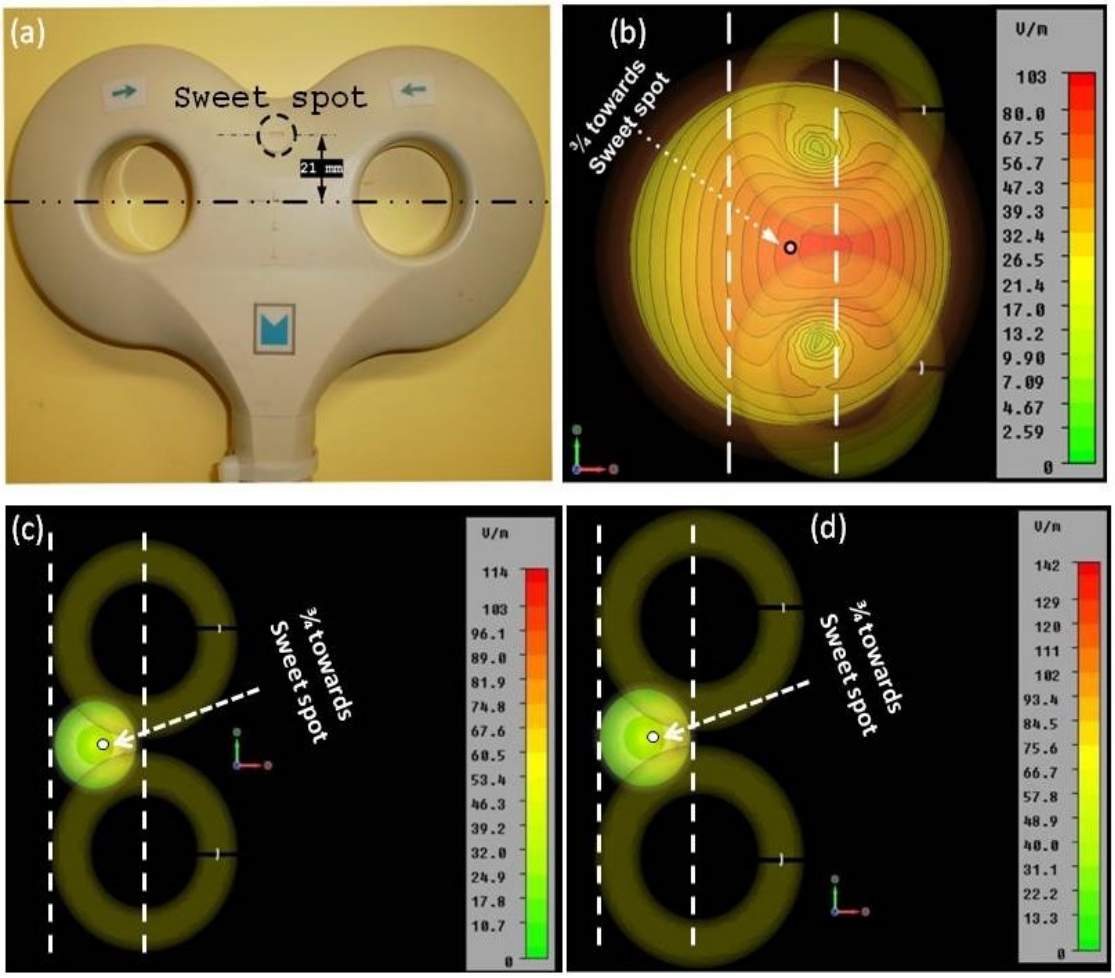

Figure 4-7. Comparison between spherical human head model and an equivalent spherical cat head model. (a) Electric field induced on the surface of gray matter in a spherical human head model for average motor threshold intensity (44 % MSO) for humans. (b) Electric field induced on the surface of gray matter in a spherical cat head model at 43 % MSO intensity. (c) Electric field induced on the surface of gray matter at ¾ distance towards the "sweet spot" from the center of the coil, in a spherical cat head model at 43 % MSO intensity. (d) Electric field induced on the surface of gray matter at ¾ distance towards the "sweet spot" from the center of the coil, in a spherical cat head model at 55 % MSO intensity.

4.5 Discussion

4.5.1 Finite element simulation on realistic human head model

The E-field magnitude values of neural activation for humans using TES is in the range of 45-112 V/m using a 0.05 ms pulse width, while the E-field magnitude ranges between 30-130 V/m when it is obtained using TMS (Won Hee et al., 2015). The average magnitude of the electric field induced on the human motor cortex for RMT using TMS from our simulations yields a value of around 176 V/m. We report a higher measure of induced E-field magnitude obtained from realistic head model simulation compared to what has been reported in literature but the reason for this difference in E-field magnitudes becomes clearer when we find the sources of the reported E-field magnitude values of neural activation for humans in the work of Won Hee et al. (2015). For instance, the work of Komssi et al. (2007) reports E-field magnitudes in the range of 33-44 V/m at the excitation threshold of the motor cortex. Such low values of induced E-field magnitude at MT may appear much smaller than the values we obtained from our simulation (176 V/m). However, a closer inspection reveals the source of this discrepancy. The first major difference is that Komssi et al. (2007) use a monophasic stimulator to estimate MT whereas the source of average MT intensity (44 % MSO) that we used for our study comes from the work of Gilio et al. (2003) who used a biphasic stimulator to estimate MT. In their work, Komssi et al. (2007) report that this difference in stimulating coil current property was significant because with a monophasic current even 20 % of MT stimulation intensity is sufficient to evoke measurable brain responses but with a biphasic current 60 % of MT intensity (nearly three times that for monophasic stimulation) is necessary to evoke measurable brain responses. Secondly, Komssi et al. (2007) use a different measure to classify MT using EEG (based on measurable brain responses) rather than

the classically accepted method of using EMG (based on measuring the activation of the FDI muscle). This is an important difference because MT based on measurable brain responses recorded by EEG represent neural threshold at the cortical level but these brain responses may not result in descending volleys (traveling down the cortico-spinal tract to the peripheral nerves) of sufficient strength to stimulate peripheral nerves, thereby, not satisfying the RMT constraint (50 μV peak-to-peak amplitude in at least 50 % of successive trials) (Kobayashi and Pascual-Leone, 2003) or to elicit a visible twitch of the FDI muscle. (Komssi et al., 2007) have themselves not validated the measurable brain response and the corresponding activation of peripheral nerves. Therefore, it may be possible that Komssi et al. (2007) have reported a range of induced field strength that is sufficient for cortical activation but not peripheral nerve activation. Based on these two differences, the higher value of induced E-field magnitude obtained from our simulation may be plausible. Additionally, no work exists with regard to estimation of electric field induced on the cortex at MT stimulus intensity using realistic head geometry in simulations.

Two additional studies (Epstein et al., 1990; Rudiak and Marg, 1994) referenced by Won Hee et al. (2015) with regard to E-field magnitude at MT intensities in humans may be different from the value reported from our simulation because both aforementioned studies do not report cortical E-field magnitude values. In their work, MT test was performed (by visual observation of twitch of the index finger which was already in tensed state which means they were performing active motor threshold (AMT) measurement). AMT threshold intensities tend to be lower than RMT threshold intensities (used in our study for our simulation) because the target muscle is already in a pre-innervated state before TMS is delivered to the cortex; a point used in the work of Thielscher and Kammer (2002). Therefore the strength of descending volleys, to activate the peripheral nerves at an already heightened state of activation, can be lower than those required for activating the

peripheral nerve at rest (in RMT measurement). Secondly, the E-field magnitudes were measured in air using a pickup coil, at different TMS intensities. The intensity of the stimulator output at which MT was observed was then matched with the corresponding E-field magnitude in air for that intensity of stimulator output. Therefore, not only were cortical E-field magnitude values absent, even the reported E-field magnitudes would be considered to be lower due to the fact that they were matched for AMT and not RMT values. If RMT values had been matched, the E-field magnitudes should be expected to be higher.

Another source of induced E-field magnitude in the work of Won Hee et al. (2015) comes from Thielscher and Kammer (2002). There again, a monophasic stimulator (Magstim 200) was used to estimate electric field intensity magnitude at AMT (not RMT). As explained above, both factors can lead to a lower estimation of induced E-field strength compared to electric field intensity magnitudes at RMT using a biphasic stimulator (which is what we report in our study).

4.5.2 Finite element simulation on realistic NHP head model

No report is available in the literature with regard to induced E-field magnitude on NHP cortex at MT stimulation intensity. However, Won Hee et al. (2015) have reported the neural activation threshold E-field magnitude (using transcranial electric stimulation (TES) excitation, not TMS) corresponding to MT is 45 ± 7 V/m. However, it is to be noted that the threshold value of neural stimulation in TES appears to be dependent on the size of the pulse width (the same parameter estimated using a 0.2 ms pulse width, as opposed to 0.05 ms pulse width mentioned earlier, yielded an E-field value of 29 V/m) and is a completely different method of cortical stimulation. Based on the discussion in the preceding section, a difference in stimulating coil current property (monophasic vs. biphasic) can result in a difference in MT values by a factor of three. Therefore,

a difference in stimulation methods altogether (TES vs TMS) may result in a substantial difference in E-field magnitude values corresponding to MT.

The experimental mean value of MT using TMS stimulation from the three anesthetized NHPs was 51± 5.2 % (Mean ± SD) of MSO. This value is close to what we find from our simulation results (55.4 % MSO, to induce a field of similar magnitude on an NHP cortex as we would see on a human motor cortex at its RMT of 44 % MSO). Based on our FEM simulations, a stimulation intensity of 55.4 % MSO would have resulted in an induction of 176 V/m E-field magnitude on the NHP motor cortex. The difference in the expected MT intensity value (from simulations) and measured MT intensity on the NHP cortex may be due to the fact that during manual segmentation of the NHP head volume, we may have over-estimated the CSF segment (which was obtained indirectly via Boolean operation). This may result in higher magnitude of induced E-field on the CSF segment. A higher magnitude of E-field could have resulted in higher values of magnetic field strength associated with the induced E-fields. A higher magnitude of magnetic field strength may have resulted in higher back compensation from the CSF segment (since the magnetic field associated with the induced E-field on the CSF layer will be out of phase with the magnetic field produced by the stimulating coil). This effect could have led to lower value of magnetic field strength reaching the interior gray matter segment (because magnetic field strength reaching gray matter = Magnetic field strength produced by the coil – (magnetic field strength of E-field induced on scalp + magnetic field strength of E-field induced on skull (nearly zero) + magnetic field strength of E-field induced on CSF)), thereby resulting in lower value of induced E-field magnitude on the surface of the gray matter segment. A more accurate segmentation method for NHP head volumes may be able to overcome this problem resulting in E-field magnitudes closer to that in humans.

4.5.3 Finite element simulation on spherical head model of humans

The maximum value of the induced E-field magnitude obtained on the cortex at RMT stimulation intensity of 44 % MSO in the spherical human head model was nearly 100 V/m (value of the E-field magnitude lying under the central crossover windings of the stimulating coil in Figure 4-7 (b)). This value is lower than the E-field estimate obtained from realistic head model. An explanation for this is provided in the following section.

4.5.4 Comparison between FEM simulation on realistic human head model and spherical human head model

The maximum value of the induced E-field magnitude obtained on the cortex at RMT stimulation intensity of 44 % MSO in the realistic human head model was 176 V/m (refer Figure 4-6 (a)) whereas the maximum value of the induced E-field magnitude obtained on the cortex at RMT stimulation intensity of 44 % MSO in the spherical human head model was nearly 100 V/m (value of the E-field magnitude lying under the central crossover windings of the stimulating coil in Figure 4-7 (b)). A lower value of maximum E-field magnitude in the spherical head model, compared to the realistic head model, may be due to the fact that we used a basic spherical segmented head model for our simulations without accounting for anisotropies and non-linearity. With regard to MEG and EEG studies, Hamalainen and Sarvas (1989) demonstrated the inaccuracy associated with the basic spherical layered head model in the estimation of fields arising from neuronal current, compared to realistic head models. This is due to the fact that a single sphere model does not capture the true geometric detail of some regions of the head. This results in over-simplification of the geometry in these regions resulting in erroneous estimations of fields in these regions. This prompted Huang et al. (1999) to investigate the approximation of the head volumes

as a combination of spheres rather than a single spherical volume. They presented a sensor-weighted overlapping sphere head model for MEG problems, which fitted the return currents of a realistic head model with multiple overlapping spheres on a sensor-by-sensor basis. Figure 4-8 shows the difference between head volume estimations using single sphere model and overlapping spheres model. The computational requirement was almost the same as that for single sphere models and the accuracy was similar to estimations obtained using BEM (which has higher computational requirement compared single sphere model estimations) on realistic head volumes. John et al. (2001) presented a three dimensional interpolation method which had nearly identical accuracy as BEM and had better performance than the sensor-weighted method. Their method was based on using the sensor-weighted method to define the head geometry and fitting pre-computed estimated fields from a similar grid of sensor locations using BEM in conjunction with constant Galerkin or Linear Galerkin error control methods. Finally, Vatta et al. (2010) demonstrated that estimation of fields in EEG studies on realistic head models using finite difference method (FDM) and BEM was more accurate than estimation of fields using sensor-weighted spherical model. Thielscher and Kammer (2002) discuss in their work how sphere models of the human head can be used for TMS studies but also mention an important drawback. They allude to the fact that although sphere models of the head can provide estimation of field distributions, they fail to provide information about the site and size of the stimulated cortex. The realistic head geometry consists of gyral and sulcal convolutions which results in charge accumulation at these regions. This could result in high induction at these locations resulting in activation of those regions. The sphere volume, on account of being of uniform curvature, does not consist of such convolutions and hence, may not reflect activation at the corresponding regions. Salinas et al. (2009) also demonstrated that the size and geometry of the volume conductor is very important to estimation

of fields induced by TMS. The inclusion of gyral and sulcal convolutiuons enables realistic head models to provide more accurate estimations of induced fields than estimations obtained using simple spherical head models.

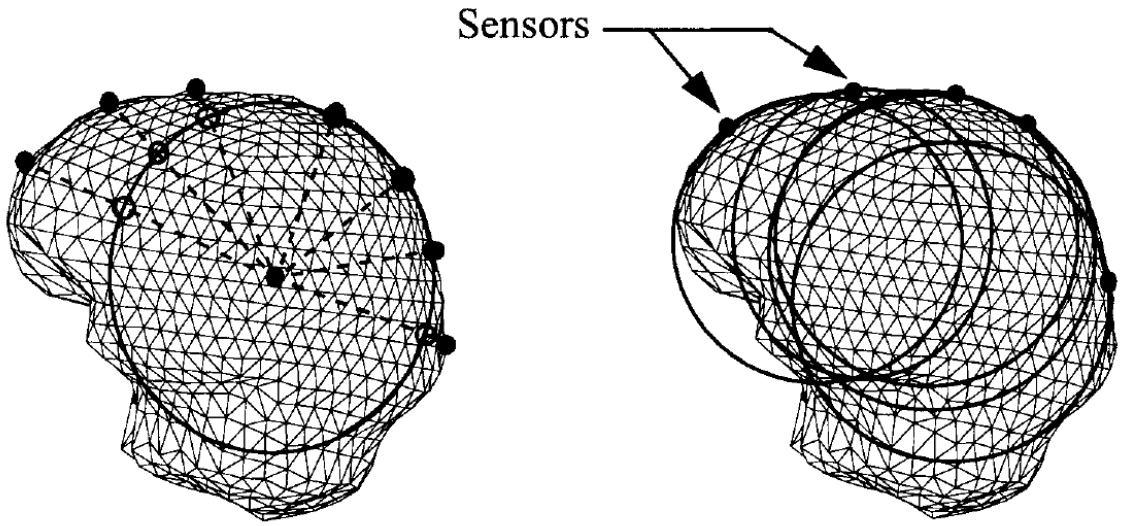

Figure 4-8. Difference between approximations of a head model using single sphere head model (left) and sensor-weighted overlapping sphere head model (right) (John et al., 2001).

4.5.5 Finite element simulation on spherical head model of cats

Based on the E-field magnitude obtained in the spherical human head model (100 V/m), we estimated that a stimulation intensity of 55 % MSO would be sufficient to induce the same strength of E-field magnitude on the target region of the cat cortex.

4.6 Conclusion

According to Benali et al. (2011), 30 % MSO at 10 mm distance from a human head induces 130 V/m in the human brain. From our simulations, we find that 44 % MSO induces average electric field strength of 176 V/m on a human motor cortex and 125 V/m on the NHP motor cortex. This means that for the same stimulation intensity of 44 % MSO, the induced electric field magnitude on a NHP motor cortex is 28.9 % lower than the strength of the electric field magnitude induced on a human motor cortex. Similarly, for the same stimulation intensity, we observe from the spherical cat and human head models that the induced electric field magnitude on a feline cortex is 30 % lower than the strength of the electric field magnitude induced on a human cortex. Based on the work of Weissman et al. (1992) which compares induced field strength based on brain size, Benali et al. (2011) concluded that the induced electric field magnitude in a rat brain is 37 % of the strength of electric field magnitude induced in a human brain. The reduction in induced electric field strength for both NHP and feline models compared to that in a human cortex follows the observation in the work of Weissman et al. (1992) in the sense that the smaller the brain weight (analogously, the brain volume) compared to the weight of a human brain, the more is the reduction in the induced field strength for the same stimulation intensity, using the same coil. This is due to the fact that for a given 70 mm butterfly coil producing a fixed number of magnetic lines of force, the number of lines of force passing through the conducting volume (in this case the brain) is higher in a human brain, lesser in a monkey brain and far lesser in a rat brain (since volume of human brain > volume of NHP brain > volume of feline brain > volume of rat brain). Thus, we conclude that, for same stimulation module and coil size, compared to humans, higher stimulation intensities are required to elicit measurable motor responses from small animals. It may therefore,

be more beneficial to use stimulating coil of comparable size to the NHP and feline heads since it will lead to more effective lines of force influencing the conducting media, thereby leading to more induction for a given pulse intensity. For the same distance of a conducting volume from the coil, the smaller size of the coils (which would mean a reduction in the loop diameter) would also improve the focality of stimulating coil (compared to a bigger diameter human coil) as demonstrated in the work of Cohen and Cuffin (1991). Thus, the RMT threshold value of stimulation (in terms of stimulator intensity) can be decreased further and it may be possible to conduct TMS conditioning at lower values of stimulation intensities of the stimulating module.

RMP of -70 mV is a fairly constant measure across mammals (Purves et al., 2001). We hypothesized that since RMP is constant across mammals, the magnitude of the induced electric field (E-field) due to TMS required to disrupt RMP to achieve the resting-motor thresholds (RMT) in humans and primates are also similar. According to our study, the induced E-field magnitude at 44 % MSO, required to elicit RMT in humans, is 176 V/m. FEM simulation of an NHP FEM model estimated that 55.4 % MSO was required to induce 176 V/m on NHP motor cortex. In-vivo measurement of RMT from three anesthetized NHPs demonstrated that 51 ± 5.2 % (Mean ± SD) of MSO was sufficient to achieve RMT. Our findings support the hypothesis that similar magnitudes of induced E-fields are required for reaching RMT in humans and non-human primates.

4.7 Summary

Method of performing numerical analysis to calculate current induced by TMS on the cortex of NHP using finite element analysis was presented for the first time. A method to estimate induced

E-fields induced on cortex, when accurate head models are not available, was also demonstrated. We demonstrate how simulations can be used before actual measurement of RMT (in the case of NHPs) to identify the stimulation intensity that would be needed to achieve RMT from NHPs. We tested our hypothesis that since RMT is a generic measure driven by disruption of RMP, achieving RMT requires similar levels of induced E-fields in humans and primates.

A fairly good match was obtained between RMT estimated from FEM simulations and those obtained in-vivo. Our study demonstrates the potential of FEM-based simulations to predict RMT across subjects in a pre-analysis session, before conducting clinical or behavioral experiments with them. Such analyses can help in quantifying the effects of TMS during experiments because a good, reliable and consistent baseline value of TMS intensity removes a lot of errors that may find their way into the recordings owing to wrong placement of the coil and/or usage of wrong TMS stimulation intensity. Since every subject head size and geometry may vary, it is important to perform such simulations for individual subjects. Such a study has the potential to elucidate future experimental/clinical results and may lead to development of safer and more robust TMS stimulation paradigms.

Chapter 5 rTMS and ERPs

Preface

While the previous chapter gives us an idea about the spread of the induced current in a medium from one TMS pulse, we would like to look at what this induced current is capable of doing. More interestingly, how would a train of TMS pulses, each of which induces the same current, affect neuronal responses? The induced current profile would be the same for each of the TMS pulses in the train but an additional component is added in terms of periodicity of the pulses. The periodic properties of a train can result in wide range neuronal effects over varying durations. In this chapter, we investigate effects of a particular train of TMS pulses on neuronal responses. The goal of this study, involving a non-human primate model, is to observe the neuronal responses of populations of neurons having similar response properties over a large region of interest, and identify the effect of TMS on their function.

Effects of continuous theta burst transcranial magnetic stimulation on neuronal processing in the primate's somatosensory cortex

Ajay Venkateswaran, Sebastien Thomas, Mirza A Baig, Pascal Kropf, Amir Shmuel

Keywords: transcranial magnetic stimulation (TMS), continuous theta burst (cTBS), finite element model (FEM), multi electrode array (MEA), somatosensory evoked potential (SEP)

Acknowledgements

This work was supported by a grant from the Natural Sciences and Engineering Research Council of Canada and the Canadian Institute of Health Research (**CHRP 385962-10**).

5.1 Abstract

Continuous theta burst (cTBS) is a transcranial magnetic stimulation paradigm which has been known to reduce cortical excitability in rat and human models. Here we aimed to investigate the effect of cTBS on evoked responses in the primary somatosensory cortex of the macaque non-human primate (NHP). We studied the effect of continuous theta burst (cTBS) protocol on neuronal processing in the primary somatosensory cortex of NHPs, in response to median nerve stimulation. To this end, we quantified the relationship between changes in somatosensory evoked potential (SEP) amplitude, local-field potentials (LFP) and firing rates of neuronal populations. Although cTBS suppressed SEP amplitude for an average of ~40 minutes, the spatial pattern of the responses remained approximately unchanged. Namely, TMS induced a linear suppressive gain effect, which was proportional to the SEP response before cTBS TMS. Spontaneous multi-unit activity (MUA) increased, and spontaneous local field potential (LFP) band limited magnitude

(BLM) remained unaltered. Our findings suggest that cTBS reduces the capacity of cortical neurons to respond synchronously to a short, potent sensory stimulus, possibly by suppression of cortical excitabilty.

5.2 Introduction

Transcranial magnetic stimulation (TMS) involves the application of time-pulsed magnetic fields to cortical tissue by means of a coil located near the head. Until recently, noninvasive brain stimulation using TMS has been used mainly for investigating the relationship between brain and behavior. However, recent efforts have demonstrated therapeutic effects of TMS in the recovery and rehabilitation from stroke (Ernst, 1990; Khedr et al., 2009; Koski et al., 2004; Maulden et al., 2005; Mayo et al., 1999; Nakayama H, 1994 Apr; Takeuchi et al., 2005), depression (Fitzgerald et al., 2003; John et al., 2007; M.S. George, 1995 Oct 2; Mosimann et al., 2002; Pascual-Leone et al., 1996) and other psychiatric and neurological disorders. Repetitive TMS (rTMS) can decrease or increase cortical excitability beyond the period of stimulation. Such changes can last for minutes or hours, and are likely to be capable of inducing long-term plasticity, i.e. changes in brain function (De Gennaro et al., 2008; Gersner et al., 2011; Siebner, 2010; Vlachos et al., 2012). Therefore, TMS provides excellent potential for clinical applications. However, the application of TMS in rehabilitation from stroke, depression and other conditions has been hindered by lack of tools for predicting TMS effect on cortical tissue, and lack of understanding of its mechanism of action.

Transcranial magnetic stimulation (TMS) represents a non-invasive way to stimulate muscles, nerves and brain cells (Barker et al., 1985b; Cooke and Bliss, 2006; Wagner et al., 2007). In short, a rapid current discharge in a coil creates a magnetic field that, in turn, induces an electric field.

Neurons under the influence of this induced electric field can then be stimulated (Pascual-Leone et al., 2002) provided the induced fields are strong enough to disrupt the resting membrane potential of the neurons. TMS is being used in some treatments for depression, pain syndromes and epilepsy (Cooke and Bliss, 2006; Pascual-Leone et al., 1998a). Despite a growing use of this technique in both clinical and research environments, the effects of TMS on the brain cannot always be accurately predicted. It varies with the area studied and the stimulation paradigm used (Fitzgerald et al., 2006). It also varies with the neuronal state of the stimulated area (Allen et al., 2007; Pasley et al., 2009). In certain cases it gives rise to completely opposite modulation effects for unknown reasons (Wang et al., 1996).

TMS research in humans has been appropriately regulated by parsimony rules and safety guidelines (Rossi et al., 2009a). While these guidelines are providing a safety canvas for the clinical use and research with humans, animal models have become a valued environment for pursuing research where the range of possible stimulation paradigms is wider and where more invasive procedures can be performed to better understand TMS. Substantial work on TMS has been performed over the recent years in feline models and their visual system (Allen et al., 2007; Aydin-Abidin et al., 2006; Aydin-Abidin et al., 2008; Moliadze et al., 2005; Moliadze et al., 2003; Valero-Cabre et al., 2007).

As for rodents, performing TMS studies is somewhat challenging, mainly because of the size ratio between the rat's head and the commercially available coils, giving poor spatial specificity in the area stimulated by TMS (Luft et al., 2001; Rotenberg et al., 2010). Still, these difficulties can be overcome, either by careful placement of coils, resulting in more focality at the cost of depth of penetration (Deng et al., 2013) or by designing new coil geometries (Guizhi et al., 2005) . A lot is

known about the effects of TMS on visual systems (Moliadze et al., 2005; Moliadze et al., 2003) based on experiments in felines. They were invasive and recorded from a limited region in the form of single unit activity. However, little is known about the effects of TMS on the somatosensory cortex. Recent studies on the effect of TMS on the rat somatosensory cortex are heavily weighted in favor of changes in protein distributions brought about by TBS to the corpus callosum (Benali et al., 2011; Volz et al., 2013) . The uniqueness of our study lay in performing invasive studies on a species closer to humans and over a large region of interest and a large pool of neurons, to be applicable to humans.

Using the well-known primary somatosensory cortex in NHPs (Shoham and Grinvald, 2001), we sought to investigate the effects cTBS TMS stimulation on this cortical entity. To this end, we recorded neuro-sensory responses in the NHP cortex by using multi-channel extracellular electrodes, positioned in the middle of the magnetic field induced by a figure-of-eight coil. Analysis of neurophysiology signals obtained from our multi-channel probes revealed that cTBS stimulation significantly reduced the peak-to-peak evoked potentials amplitude, an effect that lasted for an average of 40 minutes. There was no significant and consistent change in band limited magnitude of spontaneous activity in the different EEG bands. .

5.3 Materials and Methods

5.3.1 Animals and anesthesia

Anatomical MRI images of the animals were acquired first (T1-weighted images (MPRAGE, 0.5 mm × 0.5 mm × 0.5 mm, TR2300, 128 slices). The images were exported to neuronavigation

software Brainsight (Rogue Research, Montreal) to register the obtained brain volume with an average macaque brain template based on the best manual correlation between the locations of the anterior and posterior commissures. Once the registration was complete, a 3D volume of the scalp, bone (skull) and curvilinear brain were recreated so that the area of the bone lying above the region of interest, forelimb representation on primary somatosensory cortex (S1FL), could be localized. Twenty four hours prior to the scheduled experiment time, the animal was deprived (from food) in order to prevent vomiting during/after intubation. On the day of experiment glycopyrrolate (0.05 mg/kg) was administered, in order to stabilize heart rate and decrease bronchial secretions. The animal was initially given an anesthesia cocktail of ketamine (15 mg/kg) and diazepam (1 mg/kg). It was then placed on a heating pad to prevent hypothermia, and intubated with a tracheal tube. The animal was then ventilated with a mixture of 2 % Isoflurane in combination with 70 % nitrous oxide and 30 % oxygen. End tidal carbon dioxide (Et-CO_2) concentration was maintained in the range of 30-40 mm of Hg. A pulse-oximeter was clipped to the tongue of the animal to observe the animals' heart rate (HR) and blood oxygen saturation in the form of saturation of peripheral oxygen (SPO2). A rectal probe was inserted to monitor the body temperature (maintained at T=37.6^{o} C). A catheter was inserted to the saphenous vein of each hindlimb. These catheters were used to perfuse the animal with 5 % Dextrose in Lactated Ringer's solution at an infusion rate of 6ml/kg/hr. A urinary catheter, connected to a collection bag, was also inserted into the urethra of the animal. The animal was then placed on the stereotaxic frame in sphinx position. Once on the stereotaxic frame, the animal was anesthetized with a mixture of isoflurane along with a combination medical air (or oxygen, if required) and nitrous oxide (80/20 %). Buprenorphine (analgesic; dosage 0.01mg/kg), glycopyrrolate (secretion reducing agent; dosage 0.05mg/kg) and dexamethazone (anti-inflammatory; dosage 0.5mg/kg) were administered to the animal.

Administration of buprenorphine and glycopyrrolate was repeated every 7 hours whereas dexamethazone was administered once every 24 hours. Animal physiology was monitored every 10 minutes. The head of the animal was registered with its own 3D head volume model on Brainsight based on 3D anatomical landmarks. The region of interest and the corresponding scalp area were marked. Xylocaine 2 % was administered along the intended incision. A pinch reflex was done to measure the depth of anesthesia before we proceeded to make an incision. Two bone screws were inserted for EEG acquisition and for reference for the neurophysiological recordings, one on each side of Bregma. They made contact with the dura mater, but did not penetrate it. We then performed craniotomy of a 15 mm × 15 mm square region of the skull, from 5.0 mm Anterior to 10 mm Posterior relative to Bregma, and 15 mm to 30 mm lateral to the midline, to engulf the expected forelimb representation. The drill temperature was kept low by periodically dipping it into cold saline, in order to avoid burns on the underlying cortex. Mannitol (2 g/Kg) was administered IV slowly over 20 minutes prior to duratomy, in order to prevent brain edema. Following the duratomy, an electrocorticography (ECoG) array was placed over the exposed cortex and evoked responses to median nerve stimulation were recorded and analyzed to localize the region of activation (Figure 5-1 (a)). Once the target region was confirmed using ECoG array, a multi-electrode array was implanted at the site of activation. The array was secured by rooting the electrode lead cables to the bone with QuickSil (WPI, Sarasota, FL) and the array and the exposed cortex were covered with a thin film of wet Surgifoam (Ferrosan, Søborg, Denmark) to keep the cortex wet (Figure 5-1 (b)). The dura was flapped back over this thin film of Surgifoam followed by a replacement of the previously drilled out square piece of bone (skull) over the dura to cover the 15 mm × 15 mm hole.

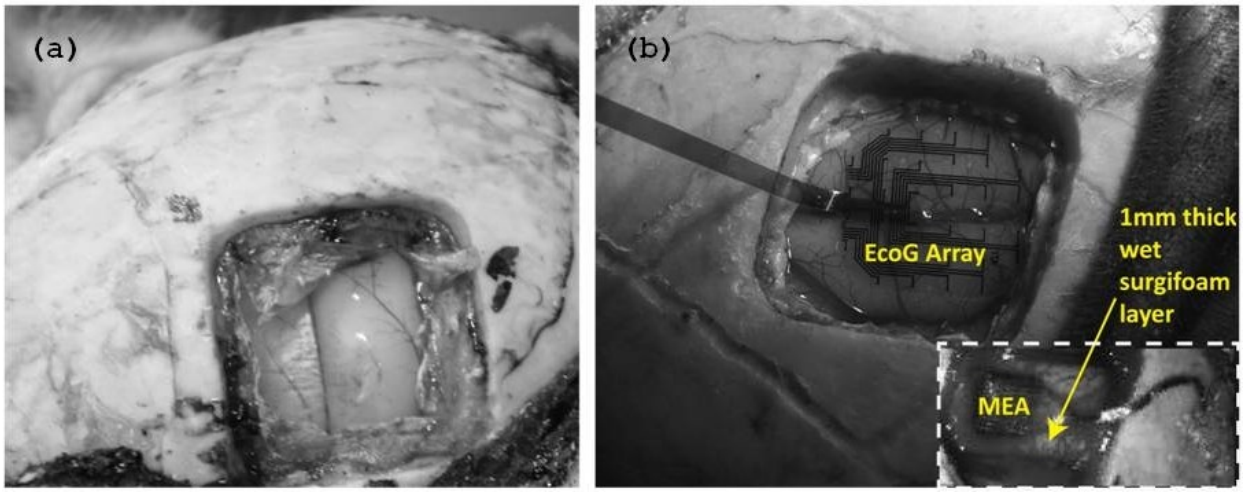

Figure 5-1. (a) Surgical procedure on NHP to expose primary somatosensory cortex. (b) Placement of ECoG surface array on the exposed cortex, to localize responses to median nerve stimulation.

5.3.2 Neurophysiology

A planar Utah multi-electrode array (MEA; Blackrock Microsystems, Salt Lake City, UT) was used for the electrophysiological recordings. The array consisted of 96 operational electrodes and four non-operational electrodes (one on each corner) arranged in a 10×10 grid. Each electrode had a shank length of 1 mm (penetrating depth) and the inter-electrode distance on the grid was 400 µm. Thus, the average recording area of the electrode grid was ~13 mm^2. We recorded neurophysiology from 64 functional electrodes. Even though we did not record from the all 96 electrodes, we still ended up recording from ~13 mm^2 area, due to the equal distribution of these 64 electrodes over the array map.

5.3.3 Electrical stimulation paradigm

The fore limbs of the animal were shaved, scrubbed and received gentle coat of Ten20 conducting gel. Cup electrodes for median nerve stimulation were then placed and held in place by wrapping

them to the arm with elastic band. Median nerve stimulation of forelimbs was achieved with the aid of a bipolar electrical stimulator (A365, WPI, Sarasota, FL). The stimulator drove current through the two cup electrodes (cathode proximal) and stimulated the median nerve near the wrist. Threshold of the response to electrical stimulation of the median nerve was ascertained based on visible twitch of the thumb. The electrical stimulation amperage value for the experiment was then set to 1.5 times the threshold amperage value.

5.3.4 Transcranial Magnetic Stimulation

TMS was delivered to the cortex using a Magstim Rapid TMS stimulator, producing a biphasic waveform, through a 70 mm butterfly coil. The coil used for our study is shown in Figure 4-4 (a).

High frequency continuous theta burst protocol was delivered to the primary somatosensory area (S1) at the site corresponding to the forelimb representation on the homunculus. A single train of 40 s duration consisting of 600 pulses (three 50 Hz pulses repeated at 5 Hz intervals) (Huang et al., 2005) at 90 % RMT was delivered after 21 (trials) minutes of pre-TMS recording. Neuronal parameters obtained from recordings for 21 minutes before the application of TMS were used as baseline measures.

5.3.5 Motor Threshold

Adhesive liquid electrolyte gel surface patch electrodes (EL503, Biopac Systems Inc., Goleta-CA, U.S.) were attached to record signals from the first dorsal interosseous (FDI) muscle of the animals. The signals for motor evoked potentials (MEPs) from surface patch electrodes were amplified and filtered (DC-3 KHz) with a GRASS amplifier (Natus Neurology, Middleton-Wisconsin, U.S.A.). They were subsequently recorded on a custom-made LABVIEW (National Instruments, Austin-

Texas, U.S.A.) program at a sampling rate of 10 KHz. Motor threshold was measured at rest (resting motor threshold or RMT). In order to elicit MEPs, the stimulating coil was aligned rostro-caudally, approximately perpendicular to the central gyrus with the lower plane of the coil tangential to the local cortex (Figure 4-4 (b)). RMT was defined as the lowest intensity of TMS pulse, required to elicit motor evoked potentials (MEPs) of magnitude ≥ 50 μV in at least five out of ten trials (Rothwell et al., 1999). Average MT of the three anesthetized NHPs was 51± 5.2 % (Mean ± SD) of maximum stimulator output (MSO). TMS pulses for somatosensory conditioning were delivered at 90 % RMT.

5.3.6 Experimental paradigm and data analysis

Neuronal data and other physiological parameters were acquired at 24,414 Hz and 10000 Hz on a Tucker Davis Technology data acquisition system, respectively. For somatosensory evoked response amplitude analysis, both data groups were down-sampled to 2000 Hz. Figure 5-2 (a) depicts a trial definition of our experimental paradigm. Each trial consisted of 25 s pre-stimulation spontaneous activity recording, 10 s of stimulation period (5 stimuli of duration 1 ms each, repeated at 0.5 Hz) followed by 25 s of post-stimulation spontaneous activity recording. The inter stimulus interval frequency of 0.5 Hz ensures recovery from inhibition which may arise if two stimulus pulses are temporally very close to each other. Each of the three aforementioned segments provided us recordings of LFP (specifically somatosensory evoked potentials or SEPs). The trials were repeated every 60 s. The three time segments corresponding to pre-stimulation, stimulation and post stimulation activity are depicted in blue, green and pink, respectively. Each trial, therefore, represented cortical activity over a complete minute. A complete TMS experiment consisted of 111 trials (thereby making it of 111 minutes duration) with 21 (trials) minutes baseline

activity, 40 s cTBS conditioning between the 21st and 22nd trials followed by 90 (trials) minutes of post TMS activity.

A typical recording of one such trial is shown in Figure 5-2 (c). For clarity, we've shown only a 35 s window in which we can see the evoked responses (top subplot) to electrical stimulation of the median nerve (bottom subplot). The high signal to noise ratio enables us to clearly see the five evoked responses to the five electrical stimulation triggers. A magnified time window depiction in Figure 5-2 (d) shows the latency between the application of the electrical stimulation and the onset of the somatosensory response. For analysis of SEPs we averaged the responses to five stimuli in a 10 s period to one evoked response. The peak-to-peak response amplitudes of the trial averaged evoked responses were calculated as shown in Figure 5-2 (d). For multi-unit activity analysis, the raw neuronal data acquired at 24,414 Hz was down-sampled to 20000 Hz. Multi-unit activity in each trial was determined by using a band-pass between 300 Hz to 3000 Hz and detecting the spikes in the filtered signal that reached three standard deviations above the average baseline filtered signal prior to TMS conditioning.

For time-course analysis we re-sampled the 111 time points (each time point representing one trial) to 37 time points by averaging 3 consecutive trials together.

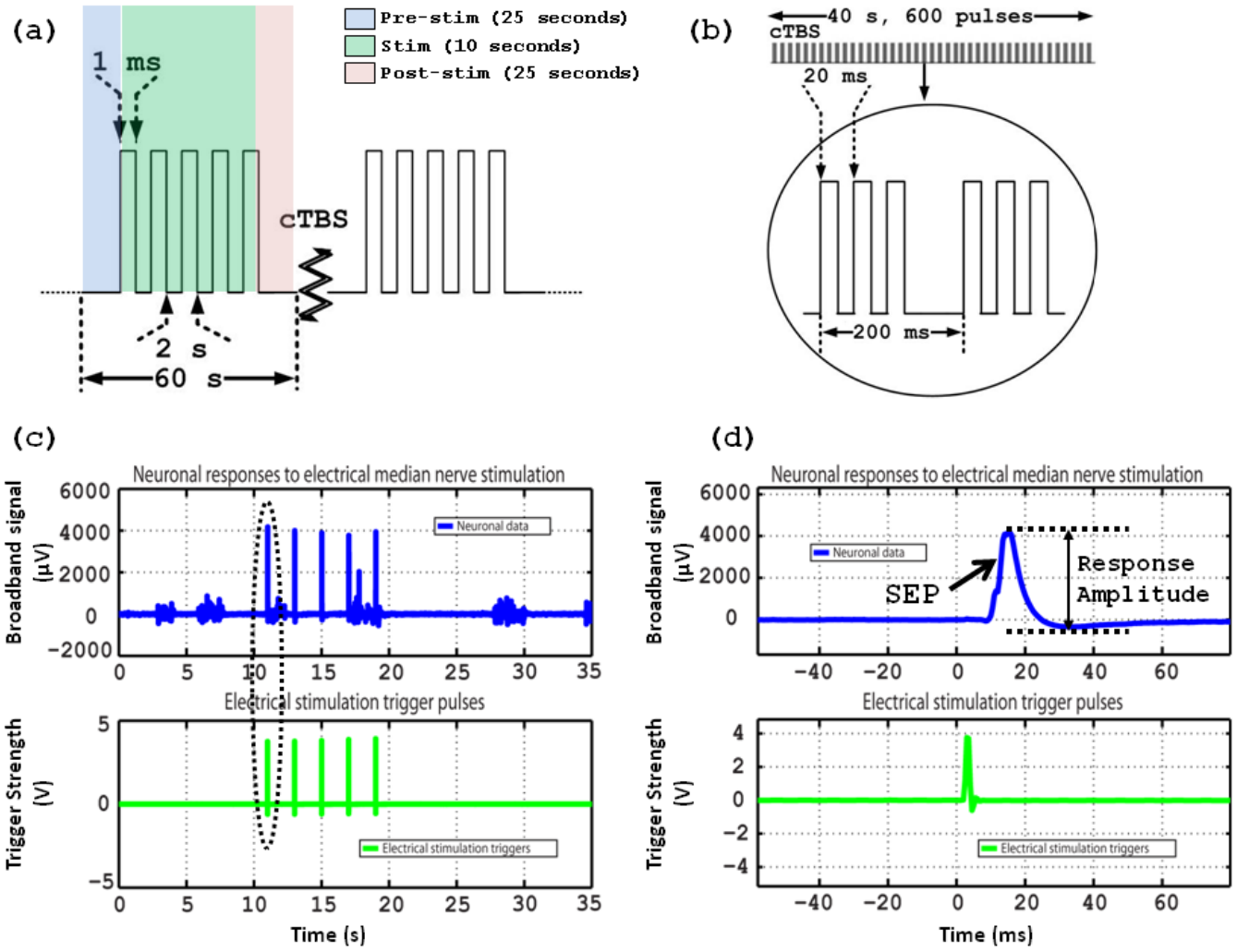

Figure 5-2. (a) Definition of one trial of median nerve stimulation depicting 25 s of pre-stimulus baseline spontaneous activity, 10 s of stimulation including 5 median nerve stimulus pulses delivered at 0.5 Hz, followed by 25 s of post-stimulation activity. (b) Timing diagram of a 40 s continuous theta burst pulse train consisting of 600 pulses (three 50 Hz pulses repeated at 5 Hz intervals). (c) Broadband neuronal recording depicting the responses evoked due to median nerve stimulation which was delivered based on the trigger pulses. (d) Temporally magnified image of somatosensory evoked potential due to median nerve stimulation delivered at the trigger pulse. The panel also shows the peak-to-peak response amplitude used for our analysis.

5.4 Results

5.4.1 Analysis of evoked responses

In order to investigate the effect of cTBS on cortical function, we looked at the cumulative effect of cTBS over the entire recording region. This was done by quantifying the SEP amplitudes recorded by each of the 64 electrodes before and after cTBS conditioning. To achieve this, it was essential to obtain a time-course of response amplitudes relative to the response amplitudes right before the delivery of cTBS. In order to check our observations, we plotted the response amplitudes of 64 electrodes 3.5 minutes and 8.5 minutes after the application of cTBS as a function of their respective response amplitudes 1.5 minutes before cTBS. The three scatter plots in Figure 5-3 depict this relationship between pre- and post TMS activity obtained from three different primates' cortices.

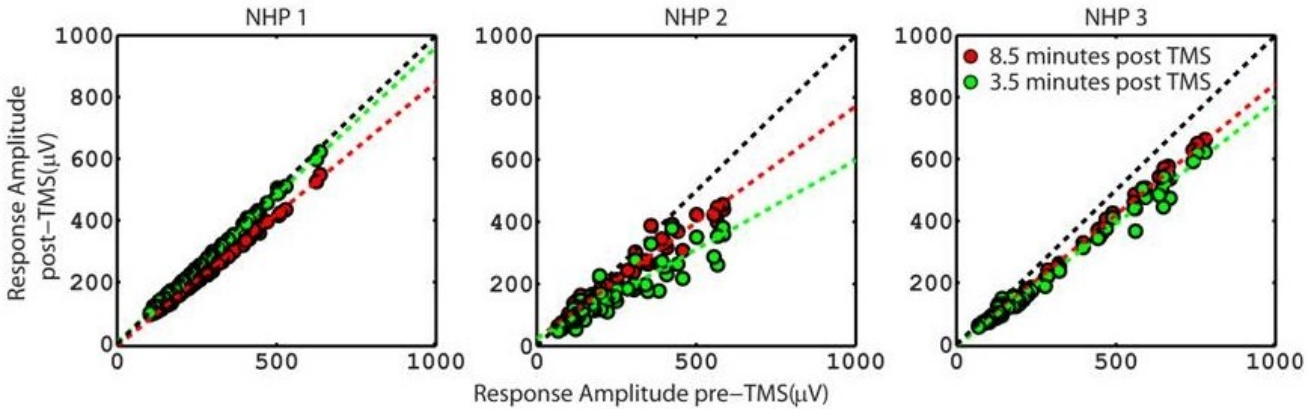

Figure 5-3. Effect of cTBS on evoked response amplitudes recorded over 64 electrodes 3.5minutes and 8.5 minutes after cTBS conditioning. The dotted black 45 degree inclination lines on each plot represent the unity slope. The dotted green and red lines represent the orthogonal regression fit to response amplitude distribution over 64 electrodes 3.5 minutes and 8.5 minutes after cTBS conditioning, respectively, for the three NHPs under study.

In order to test the possible linear relationship between the pre- and post-TMS responses, we chose not to use simple linear regression because we present and analyze the post-TMS measure as a function of the pre-TMS measure and both parameters are subject to measurement errors (arising from background noise). Therefore, we assume errors in both pre- and post-TMS measurements. Orthogonal regression fits this scenario better than linear regression, which assumes that one of the two variables is given with no errors. In each of the three plots in Figure 5-3, linear fits of the response pattern is shown by the dotted green and red lines. The unity slope reference line is depicted by black dotted line. We then calculated the slopes and y-intercepts of the linear fit of responses from individual trials and plotted them as a function of the averaged responses over the 3 trials preceding cTBS. This allowed us to obtain the time-courses of these two parameters (Figure 5-4). In addition, we estimated to which extent the pattern of responses from the 64 electrodes in each averaged trial was linear with the baseline response averaged over the 3 trials preceding the administration of cTBS. To this end, we computed correlation coefficients, presented as a function of time in Figure 5-5.

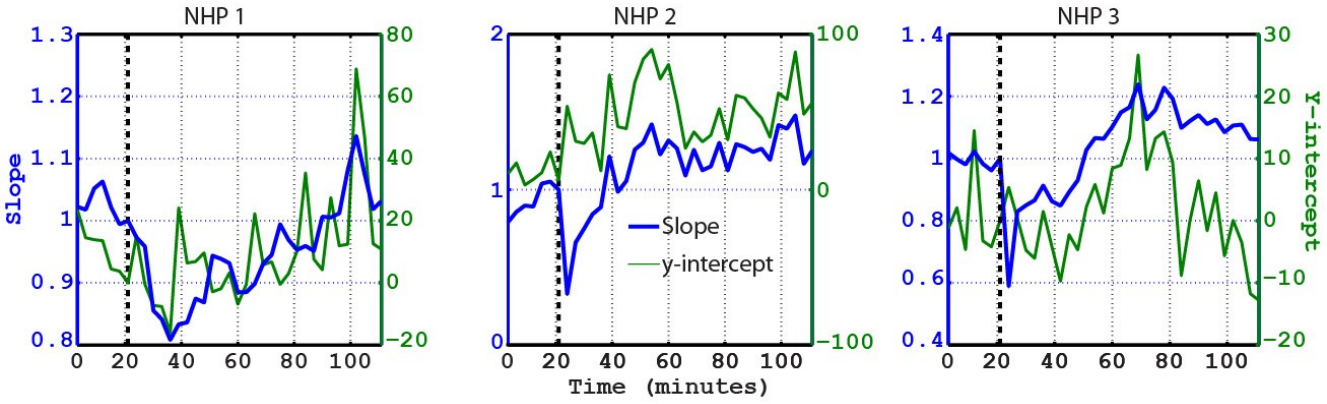

Figure 5-4. Time-course of the slope and y-intercept of orthogonal regression fit to the response amplitude distribution over 64 electrodes at each time point with respect to pre-TMS response amplitude distribution over the same 64 electrodes right before cTBS conditioning. Three plots are shown, one for each of the three NHPs under study.

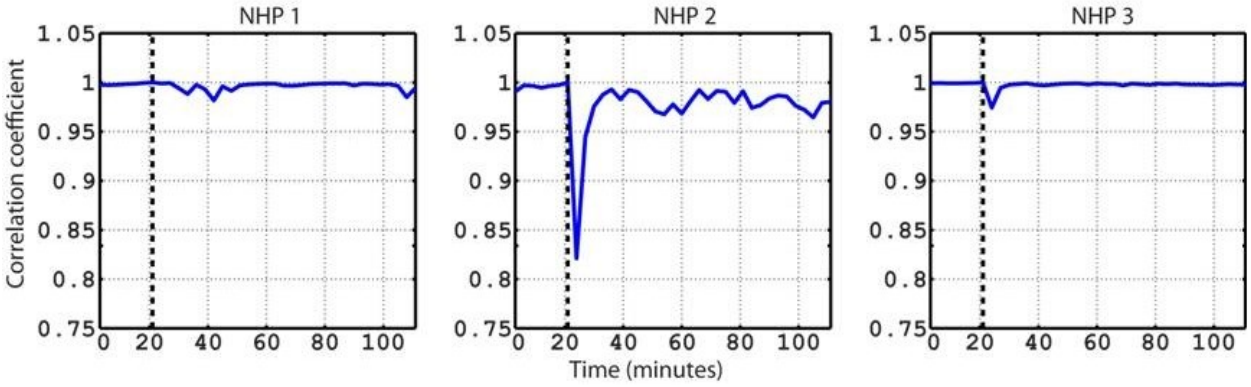

Figure 5-5. Time-course of the correlation coefficient of response amplitude distribution over 64 electrodes at each time point with respect to pre-TMS response amplitude distribution over the same 64 electrodes right before cTBS conditioning.

5.4.2 Multi-unit activity

In order to identify the effect of TMS on action potentials, we quantified the multiunit activity (MUA) of the population of neurons. A temporal window extending 500 ms on either side of the median nerve stimulus was formed based on the number of spikes obtained in 10 millisecond bins. The MUA within this 1 s window was averaged over all electrodes, trial by trial. Figure 5-7 shows the spiking activity obtained from the three animals with the green horizontal dotted line showing the position in time where cTBS was delivered.

The stimulation period was divided into two epochs; 9.0 s prior to median nerve stimulation (pre-stimulus spontaneous activity period) and 1.8 s post median nerve stimulation (post-stimulus evoked activity period). From Figure 5-2 (d) we observe that an SEP component reaches culmination around 40 ms. Thus, 100 ms data on either side of the stimulus were rejected (to remove SEP component on the post stimulation side). From each trial, we extracted 9 s of spontaneous activity (recorded from before the first stimulus of every trial) and (1.8*5) = 9 s of

inter-stimulus activity. To illustrate this, we refer to the schematic of the trial definition presented in Figure 5-6., where the pre- and post-stimulation spontaneous activity regions are demarcated. This way, we intended to isolate the "pure" pre-stimulus spontaneous activity (unadulterated by any immediately preceding signal effect) and inter stimulus spontaneous activity (referred to as post-stimulus spontaneous activity). Each trial gave us one pure spontaneous activity epoch and five post-stimulus spontaneous activity epochs.

.

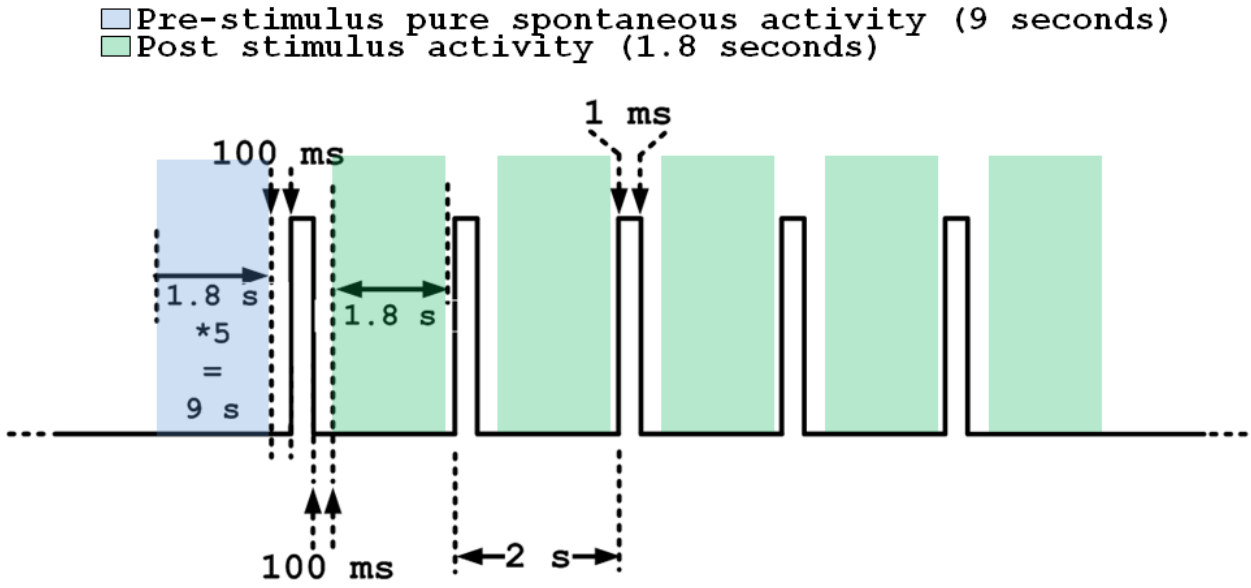

Figure 5-6. Schematic of sampled pre-stimulation and post stimulus spontaneous activities. 9 s activity before the first stimulus of a trial (represented by the light blue boxed region) corresponds to pure pre-stimulus spontaneous activity whereas 1.8 s activity after every stimulus in a trial (represented by the light green boxed regions) corresponds to post-stimulus spontaneous activity.

Analyses were performed on each of the five post-stimulus epochs and the results were averaged to obtain one averaged post-stimulus measure per trial. Similarly, the 9 s pre-stimulus spontaneous activity epoch was split into five 1.8 s sub-epochs and analyses were performed on these 5 sub-epochs individually and the results were averaged to obtain one 1.8 s pre-stimulus spontaneous

activity measure. We therefore, computed measures over 1.8 s of data, preceding and following median nerve stimulation. In order to substantiate the absence of short-latency afferent inhibition (response of one stimulus altering the response of a following stimulus in two temporally close stimuli), we reported the average firing rate time courses in the average 1.8 s period of pre-stimulus spontaneous activity and 1.8 s period of post stimulation activity following a median nerve stimulation (refer Figure 5-8). The two timecourses shown in Figure 5-8 are identical which indicates that the inter-stimulus interval of 0.5 Hz was sufficient to avoid short-latency afferent inhibition.

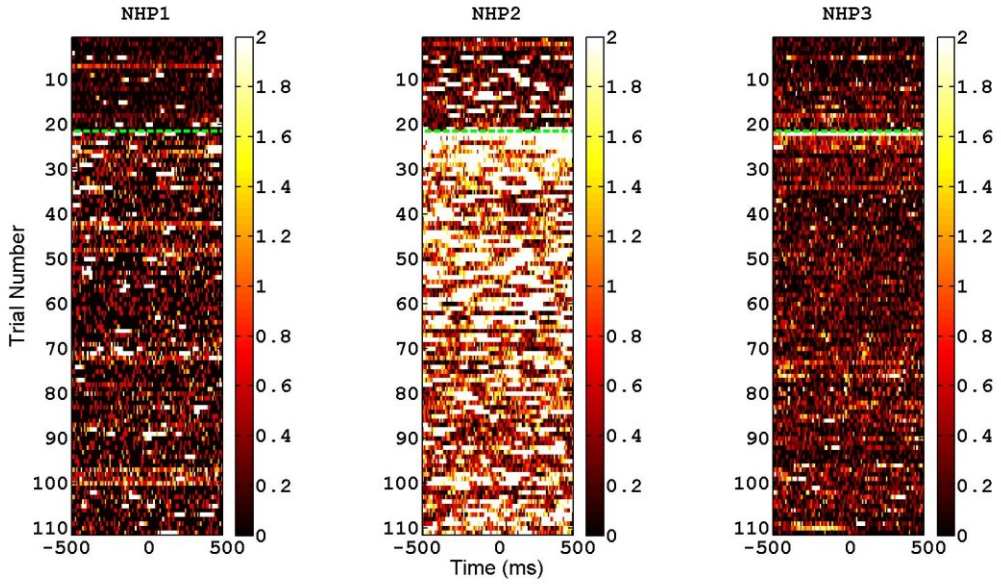

Figure 5-7. Multiunit activity presented in 1 s time courses with the median nerve stimulus presented at time (t=0) for the three NHPs under study. Each pixel represents the number of spikes recorded within a 10 ms bin. The green horizontal lines delineate pre-TMS spiking activity from post-TMS spiking activity. The 1 s time-courses are presented as a function of trial number along the vertical axis.

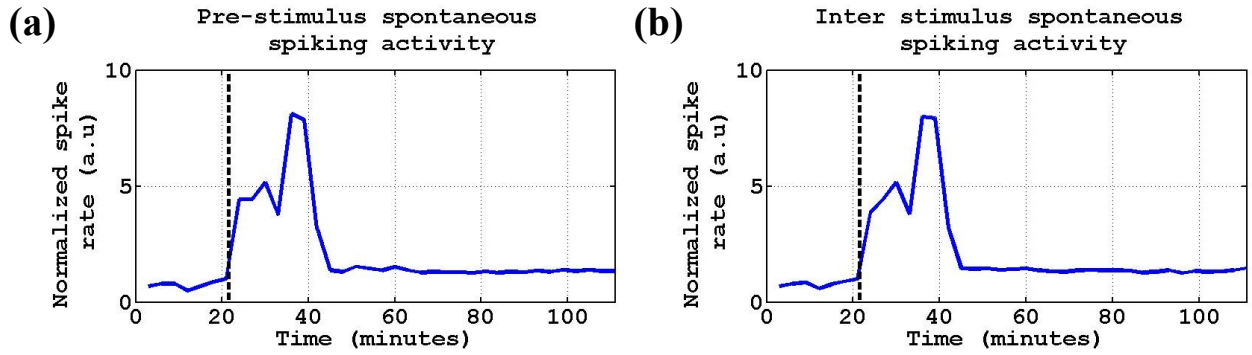

Figure 5-8. Separation of average spontaneous spiking activity time courses obtained (a) 1.8 s before the first median nerve stimulus (off a train of 5 in a trial) and, (b) 1.8 s after a median nerve stimulus (following the removal of 100 ms evoked potential component right after a stimulus). Each plot has been normalized with respect to the average spike rate in the trial right before TMS (at time =21 minutes).

5.4.3 Band limited magnitude analysis

The band limited magnitude (BLM) of the pre-stimulus epoch was determined by computing the BLM of each 1.8 s sub-epoch of the pre-stimulus spontaneous activity and averaging the results to obtain one averaged 1.8 s pre-stimulus BLM measure. The BLM activity was categorized into six bands; (a) Delta band (1-4 Hz), (b) Theta band (5-8 Hz), (c) Alpha band (8-12 Hz), (d) Beta band (15-30 Hz), (e) Low Gamma band (30-57 Hz) and (f) High Gamma band (63-150 Hz). The discrete fast Fourier transform (DFFT) of the neuronal signals was computed using a fast Fourier transform (FFT) algorithm. The magnitudes of the resulting signals at each frequency was estimated. Magnitudes corresponding to the frequency bands described above were averaged to obtain the average BLM corresponding to each band. The relationship between response magnitudes of the first stimulus of every trial and BLM bands in the 1.8 s spontaneous activity region was studied. We observed that spontaneous EEG BLM band activities remained fairly unaffected by cTBS. We proceeded to compare the average response amplitude at each time point with the corresponding BLM of each band. A comparison between response amplitude and band limited activity,

represented in Figure 5-10, demonstrated that the correlation of response amplitude is relatively low and inconsistent with all bands corresponding to spontaneous activity.

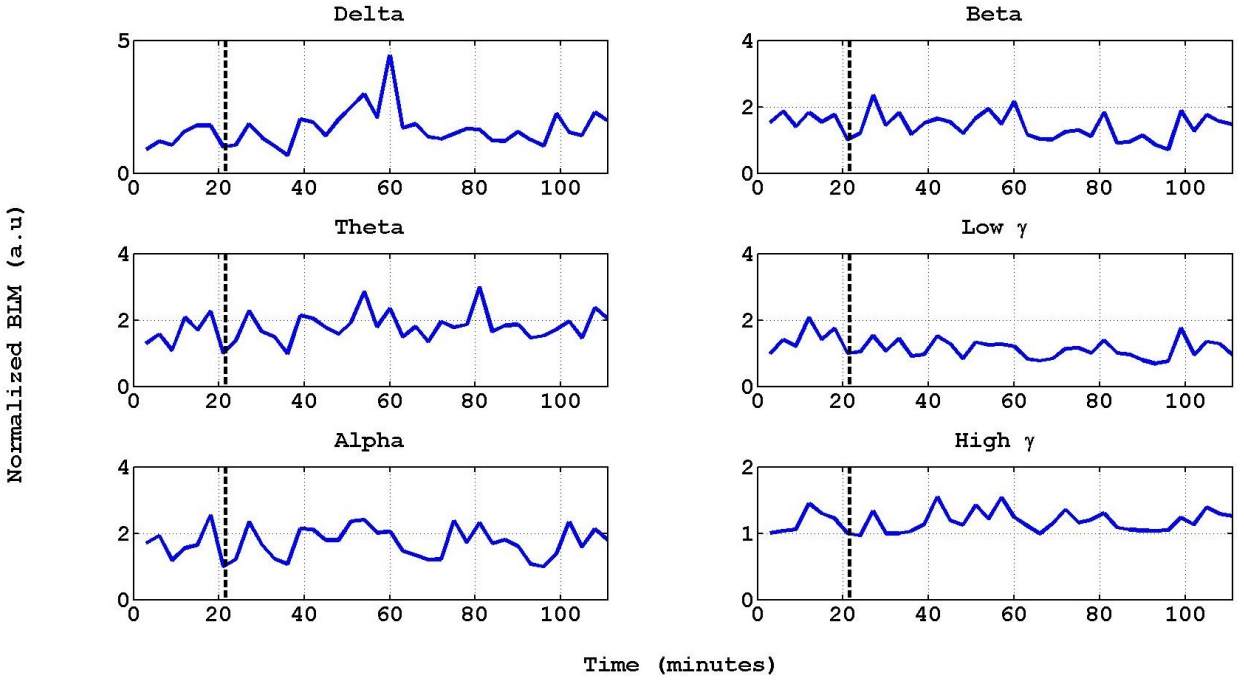

Figure 5-9. Local field potential band limited magnitude time courses of pre-stimulus spontaneous activity. The average band activity was obtained from the broadband signal extracted 1.8 s before the arrival of the first stimulus of each trial. The individual plots present Delta band (1-4 Hz), Theta band (5-8 Hz), Alpha band (8-12 Hz), Beta band (15-30 Hz), Low Gamma band (30-57 Hz) and High Gamma band (63-150 Hz) BLM time courses. In each panel the cTBS delivery is represented by the vertical black dotted line. Each plot has been normalized with respect to the average BLM in the trial right before TMS (at time =21 minutes).

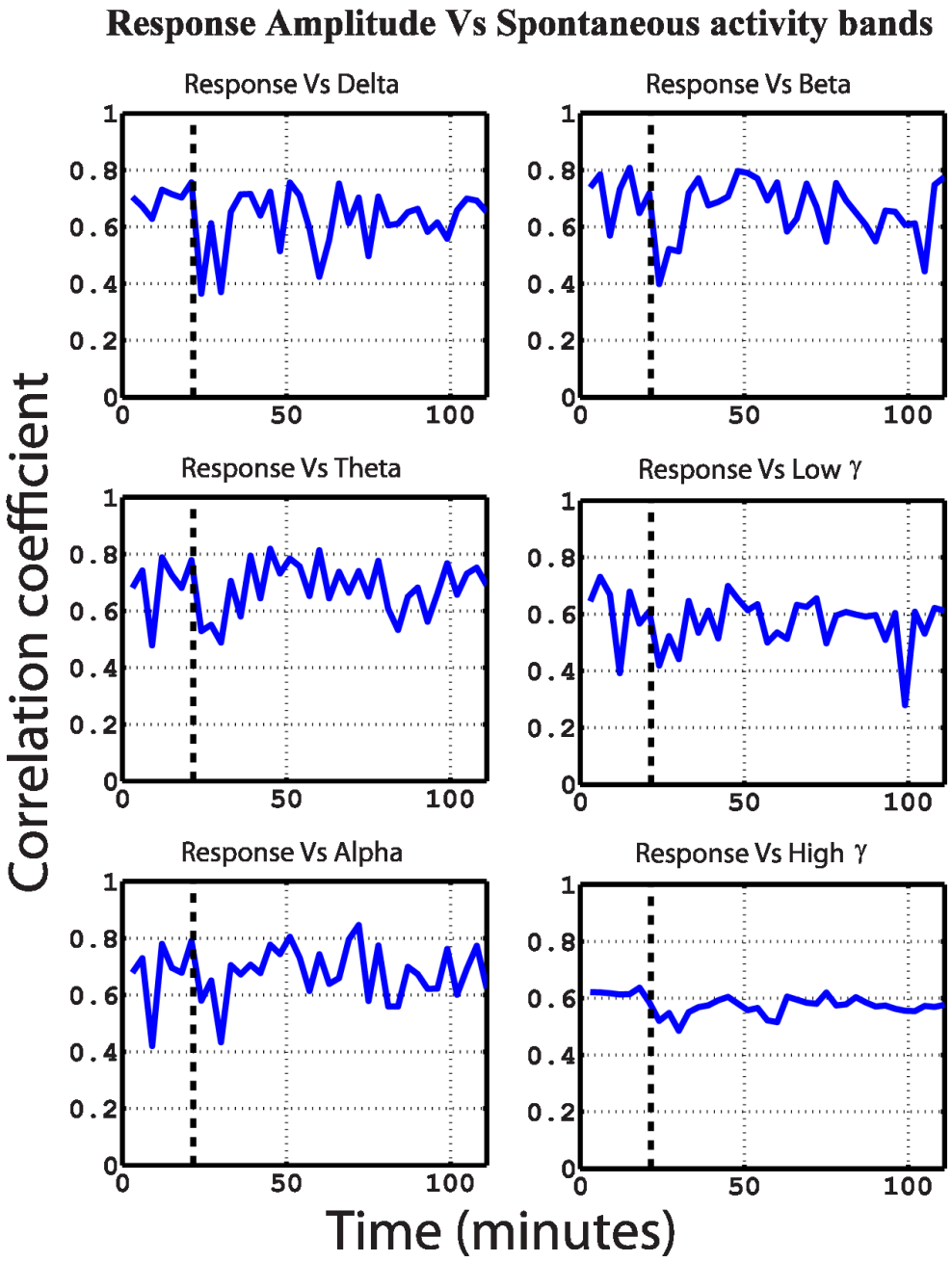

Figure 5-10. Correlation of response amplitude with average Delta (1-4 Hz), Theta (5-8 Hz), Alpha (8-12 Hz), Beta (15-30 Hz), Low γ 30-57 Hz) and High γ (63-150 Hz) band activity.

5.5 Discussion

5.5.1 Spatial effect of cTBS on evoked neuronal response to median nerve stimulation

The effect of cTBS on a population of neurons within a ~13 mm^2 area and an average cortical depth of 1 mm is fairly constant. The primary stimulation area of a 70 mm butterfly coil placed at a distance of 10 mm from the target area is estimated at 68 mm × 54 mm (Pascual-Leone, 2002). The array was, therefore, recording neuronal activity from well within the simulated primary stimulation area. This can be observed from the fact that in all three plots of Figure 5-3, the scatter of post vs pre- TMS responses is almost linear which indicates that within the ~13 mm^2 region of interest, TMS has suppressed (as seen by the lower slope value of the linear fit compared to the unity reference line) the response activity of neurons in the ROI. However, more importantly, it has approximately suppressed them by a constant factor (which is given by the slope of the linear fit).

Benali et al. (2011) demonstrated that cTBS applied to the rat cortex affected the evoked response to median nerve stimulation wherein the first SEP response amplitude (which was independent of any cortical recovery function associated with a closely timed previous evoked response) increased after the application cTBS. Our findings are different, showing that cTBS suppressed SEP amplitudes. The critical part of the study by Benali et al. (2011) which may have led to this difference is the site selected for cTBS conditioning, namely the corpus callosum). It has been shown by (Ishikawa et al., 2007; Matsunaga et al., 2009) that the target site of cTBS stimulation has a strong bearing on the outcome effects. When (Ishikawa et al., 2007; Matsunaga et al., 2009) targeted the left primary cortex (M1) of human subjects for cTBS conditioning, SEPs recorded from the left primary somatosensory cortex (resulting from right median nerve stimulation)

showed a significant increase whereas application of cTBS to the left S1 resulted in significant decrease in SEPs.

Our findings are consistent with the studies by (Ishikawa et al., 2007; Matsunaga et al., 2009) with regard to decreased SEP amplitude after cTBS conditioning of S1. We note that the effect of TMS was quite consistent across the 3 experiments. For example, Figure 5-4 shows that the initial effect was a suppression of the responses to the sensory stimuli. This initial effect was followed by a phase in which an overshoot was observed: the responses to sensory stimuli had amplitudes higher than those of the corresponding pre-TMS responses. The most significant variability can be observed in Figure 5-7, that shows a higher level of spiking activity detected in the second (out of 3) primate in comparison to the other two following TMS. We note, however, that a higher level of spiking activity was presented by this animal already before the application of TMS. Such variability can be attributed to different physiological states of the animals. A certain variability in the physiological state is inevitable, which may have affected the baseline state of the neurons.

5.5.2 Duration of the effect of cTBS on evoked neuronal response to median nerve stimulation

Figure 5-4 (a) demonstrates that cTBS suppressed evoked response amplitude for an average period of ~40 minutes (average time taken by the slope curve of all three NHPs to return to 1 after the application of cTBS). cTBS to the primary somatosensory cortex of humans resulted in significant reduction of SEP amplitudes , measured using EEG scalp electrodes, for up to 13 minutes following conditioning (Ishikawa et al., 2007). Interestingly, in our study, the responses from different electrodes were suppressed by approximately the same percentage. This is reflected in the only diminished change in the response pattern calculated by the correlation coefficient, the time-course of which is shown in Figure 5-5. The only visible deviation in the response pattern

after TMS with respect to the response pattern right before TMS occurred in the trial right after TMS in NHP2. Apart from that, the correlation coefficients remain fairly close to unity throughout the course of the experiments. This indicates that TMS suppresses synchronized sensory responses proportionally to the amplitude of these responses pre-TMS.

5.5.3 Effect of cTBS on multi-unit activity (MUA) and firing rate patterns

Increase in MUA (refer Figure 5-7) and the suppressed SEPs indicate that spiking activity is desynchronized after TMS conditioning. Hence, it doesn't synchronize together to generate a local field potential of the same magnitude as in the pre-cTBS period. The MEA used for our neuronal recordings had a depth penetration of 1 mm. Based on the thicknesses of cortical layers (Cauller and Kulics, 1991), our neuronal activity recordings were predominantly from Layer II/III of the primary somatosensory cortex. cTBS is expected to alter cortical excitability due to increase GABAergic interneuronal activity (Stagg et al., 2009). For NHP somatosensory cortex, this could arise from the mediation of activity of any type of chandelier cells (which express parvalbumin, PV) or calbindin (CB-ir) double bouquet cells (Raghanti et al., 2010).

5.5.4 Possible mechanisms

According to Schürmann et al. (2001), the effect of single-pulse TMS on SEPs is proposed to work via two mechanisms: (a) SEPs being purely additive components, independent of background EEG oscillatory activity and the effect of TMS is due to an interaction between descending cortical evoked responses to TMS pulse and the afferent response to median nerve stimulation or, (b) SEPs being dependent on background spontaneous EEG activity arising from the reorganization of spontaneous EEG activity in terms of amplitude enhancement (Başar, 1972, 1980) and phase reordering (Sayers et al., 1974) with TMS disrupting the relationship between EEG oscillations

and SEPs. Our study of the effect of cTBS rTMS on soamtosensery responses supports (but does not prove) a different view of the mechanisms relative to those proposed for single pulses. The decreased response amplitude following cTBS, and the observation that the effect of cTBS can be approximated as a linear gain effect are consistent with a model according to which cTBS reduces the capacity of cortical neurons to respnd synchronously to sensory stimuli due to decreased excitability of cortical neurons. This interpretation is consistent with previous findings of decreased RMT following cTBS (Huang et al., 2005; Ishikawa et al., 2007), since RMT is a peripheral measure of cortical excitability.

5.6 Summary

Continuous theta burst delivered to the primary somatosensory cortex of non-human primates resulted in suppressed evoked response amplitudes for approximately 40 minutes after TMS conditioning. There was no quantifiable effect of cTBS on background spontaneous activity. cTBS TMS induced a linear suppressive gain effect, which was proportional to the SEP response before cTBS. The effect of cTBS might therefore be due to decreased excitability of cortical neurons, which reduces the capacity of cortical neurons to respond to sensory stimuli in a synchronized manner.

Chapter 6 TMS and Response Patterns

Preface

The linear gain effect we show in chapter 5 was obtained in an area responding homogeneously to one stimulus (median nerve stimulation). Our simulations show that the current density elicited by TMS was approximately homogeneous in the region covered by the multi-electrode array, since the effect of TMS spreads out over a much larger area than that covered by the array. But is the extent of the effect of TMS within its effective area the same for all population of neurons within that area? Or is every neuron, be it strongly responding or weakly responding, has its performance after the application of TMS affected by the same percentage relative to its response before the application of TMS, as every other neuron in the effective area? Will the gain effect hold across ensembles of neurons, each with its own specific functional responses? And, is the linear gain effect elicited also with other rTMS protocols, or is it specific to cTBS? Chapter 6 investigates the effect of different rTMS protocols on a spatial area of 3.6 mm × 3.6 mm of the feline brain. The spatial pattern of the responses will be investigated before and after the application of TMS. This was done in order to identify if TMS has different effect on neurons that show discrete response properties.

The effect of theta-burst and 15 Hz rTMS on locally measured cortical response to oriented grating visual stimuli

Ajay Venkateswaran, Sujaya Neupane, Ze-Shan Yao, Martin Villeneuve, Amir Shmuel

Keywords: transcranial magnetic stimulation (TMS), continuous theta burst (cTBS), intermittent theta burst (iTBS), multi electrode array (MEA), Visual cortex, orientation selectivity

Acknowledgements

This work was supported by a grant from the Natural Sciences and Engineering Research Council of Canada and the Canadian Institute of Health Research (**CHRP 385962-10**). We thank Drs. Lisa Koski, Frederic Lesage, and Christophe Grova for their very helpful comments.

6.1 Abstract

The effects of three different repetitive transcranial magnetic stimulation (rTMS) paradigms; continuous theta burst, intermittent theta burst, and 15 Hz on the neuronal processing in cat area 18 were studied. We present the effect of TMS on visual evoked potential components, firing rate and orientation tuning. Each stimulation protocol consisted of 600 pulses at an intensity of 100 % of resting motor threshold (RMT). We demonstrate that the spiking activity response to oriented grating stimuli was suppressed by continuous theta burst and 15 Hz TMS, and was enhanced by intermittent theta burst. We observed a state-dependent effect of TMS on neuronal populations wherein neurons that were more responsive before the application of TMS, were affected more

than neurons that were less responsive before the application of TMS. The effect may be suppressive or facilitatory depending upon the TMS conditioning protocol. In spite of these changes, the response pattern of the region of interest under study, and the orientation tuning of the multi-unit activity remained unaffected. Our findings demonstrate that rTMS does not modify the functional selectivities of ensembles of neurons; rather, it has a linear gain effect on their responses.

6.2 Introduction

Transcranial magnetic stimulation (TMS) involves the application of time-pulsed magnetic fields to cortical tissue by means of a coil positioned near the head. Since its inception (Barker et al., 1985a), TMS has been considered as a potential therapeutic technique for conditions of recovery from stroke (Ernst, 1990; Khedr et al., 2009; Leong, 2009; Rofes et al., 2013; Takeuchi et al., 2005), psychiatric disorders such as depression (Berlim et al., 2012; Berlim et al., 2013), schizophrenia (Prikryl and Kucerova, 2013; Rajji et al., 2013) and others. It has been used in pain research and in studies involving conduction pathways in the brain, the central and the peripheral nervous systems (Awad et al., 2013; Massé-Alarie et al., 2013; Schabrun et al., 2013). TMS has also been commonly used to investigate the relationship between brain and behavior (Rossini et al., 2010). However, the application of TMS has been hindered by the lack of understanding of its mechanism of action, and therewith, the lack of tools for predicting its effect on cortical processing. Therefore, most of the concepts on its mechanisms of action have been speculative.

Various TMS delivery paradigms cause different effects that last for different durations. The effect

of single pulse TMS lasts, at most, a few tens of milliseconds after it (Toga and Mazziotta, 2002). Therefore, it is generally used as an 'instantaneous' paradigm in which TMS is delivered during the performance of a task. Repetitive TMS (rTMS), on the other hand, is used both as an 'instantaneous' and 'prolonged' paradigm, since the duration of its effect is on the order of seconds or minutes, outlasting the application of the pulses (Rossi et al., 2009b; Toga and Mazziotta, 2002). rTMS can be further classified, based upon the frequency of repetition of pulses, into low frequency (<= 1Hz) and high frequency (>1 Hz) rTMS. Low and high frequency rTMS paradigms are known to induce significant effects on cortical excitability and plasticity (Gersner et al., 2011; Siebner, 2010; Vlachos et al., 2012). Low frequency rTMS has been shown to decrease cortical excitability and hence increase seizure threshold (Joo et al., 2007; Prikryl and Kucerova, 2005). The converse may be true for high frequency rTMS, which increases cortical excitability (Berardelli et al., 1998; Tergau et al., 1999), and therefore may be prone to induce seizures.

Several high frequency TMS stimulation protocols currently exist. Our interest lies in a particular rTMS protocol developed by (Huang et al., 2005). This technique conditions the brain with bursts of high frequency rTMS instead of a continuous train of high frequency pulses. Each burst consists of 3 pulses at 50 Hz. These bursts can then further be repeated at a frequency of 5Hz (theta), 10 Hz (alpha) or 20 Hz (beta) to provide an rTMS paradigm which can be referred to as theta-, alpha-, or beta-burst stimulation, respectively (De Ridder et al., 2007).

rTMS (continuous and burst paradigms) paired with invasive electrophysiological recordings have been reported in rodent (Benali et al., 2011; Levkovitz et al., 1999), feline (de Labra et al., 2007; Espinosa et al., 2007; Espinosa et al., 2011; Moliadze et al., 2005; Moliadze et al., 2003; Pasley et al., 2009) and non-human primate (NHP) models (Baker et al., 1995; Dancause et al., 2006). One human intracranial recording study, albeit with a patient who had a history of seizures, has been

reported in the study by Wagner et al. (2004a). The reported effects of TMS paradigms on cortical excitability and function are highly variable. Continuous theta burst (cTBS) applied to the motor cortex suppressed motor evoked potentials (MEPs) amplitudes, which is a peripheral measure of cortical excitability (Huang et al., 2005; Ishikawa et al., 2007). In contrast, Benali et al. (2011) reported an increase in the fundamental (in a train of three) somatosensory evoked potentials (SEPs) P_1N_1 amplitudes following cTBS conditioning. On the contrary, suppression of later component amplitude of SEPs ($P_{25}N_{33}$ or effectively P_2N_2) was reported in (Ishikawa et al., 2007; Zapallow et al., 2012). Zapallow et al. (2012) also showed that P_1N_1 amplitude is significantly suppressed for 5 to 9 minutes following cTBS. Possibly explaining part of the variability, (Noh et al., 2012; Vernet et al., 2013) showed that the effect of cTBS may depend on the site in which activity is measured by demonstrating that cTBS had opposite effects on MEP amplitudes and EEG power, with a suppression of MEP amplitudes and a longer lasting increase in EEG power amplitudes after TMS conditioning. In contrast to the reported effects of cTBS, intermittent theta burst (iTBS) shows consistent facilitatory effect on both MEPs and SEPs (Benali et al., 2011; Di Lazzaro et al., 2008; Huang et al., 2005). However, 15 Hz rTMS, a paradigm that uses single pulses at the average frequency of the bursts used for cTBS, seems to cause variable effects wherein it has shown facilitatory effects on MEPs (Wu et al., 2000) and no effect on MEPs (Huang et al., 2005; Maeda et al., 2000a). Thus, existing reports on the effect of 15 Hz and cTBS on neurophysiological activity are inconsistent.

Not only the sign (suppression or facilitation) of the effect of rTMS on neurophysiological activity is not yet fully determined, the amplitudes of these effects have been neglected too. Based on the dependence of low-frequency rTMS on the spontaneous activity prior to TMS application (Pasley et al., 2009), one may hypothesize that rTMS-induced suppression or facilitation is non-linear,

influencing large-amplitude responses relatively more than low-amplitude responses. An alternative model could be a linear gain effect, according to which the amplitudes of all responses are suppressed in a manner proportional to their amplitude prior to the application of rTMS. Yet another important feature of the effect of rTMS paradigms is their time course. What's the duration of the effect? How long after the application of rTMS do responses go back to their normal amplitudes?

MEP and SEP are two excitability measures that rely on recordings from the scalp or from the surface of cortex. They thus integrate synchronized neurophysiological signals from relatively large regions of cortex, and are prone to missing responses that are less synchronized in space and in time. In order to reconcile these inconsistent reports, we applied intracortical recordings of two more local measures of excitability, namely action potentials and gamma band responses. To this end, we recorded neurophysiological responses to oriented grating stimuli from an array of electrodes implanted in cat area 18. We aimed to determine the sign (suppression or facilitation), amplitude of the response relative to the amplitude prior to rTMS, the time-course and the spatial pattern of the effects of cTBS, iTBS, and 15 Hz rTMS paradigms.

6.3 Materials and Methods

6.3.1 Animals and anesthesia

All procedures were approved by the animal care committees of the Montreal Neurological Institute and McGill University and were carried out with great care according to the guidelines of the Canadian Council on Animal Care. Data were obtained from one male and six female cats, weighing 3.7 to 4.7 Kg. Twelve hemispheres (2 hemispheres from 5 cats and one hemisphere each

from 2 cats) have been used to obtain 12 datasets for each TMS paradigm. Of the 12 datasets, 4 datasets were rejected: three due to unstable baseline activity (which makes it difficult to quantify the effect of TMS) and one due plausible seizure induction.

The experiments have been carried out in an acute paralyzed preparation to prevent eye movements. Glycopyrrolate (0.01-0.05 mg/Kg) was administered intra muscularly (IM). Fifteen minutes later, we administered a cocktail of acepromazine (0.11 mg/Kg SC) and ketamine hydrochloride (20 mg/Kg, IM). The animals were then placed on a heating pad so that their body temperature could be maintained within their normal body temperature (38.0°C-38.5°C). The cats were intubated and ventilated using a respiratory pump, with a mixture of 80 % Medical Air, 20 % Oxygen and isoflurane. Anesthesia was induced with isoflurane. Venous cut-downs were performed to insert cephalic vein catheters into both forelimbs. These two lines were subsequently used for all intra-venous (IV) administrations during the course of the experiment. Throughout the process of cannulation, the animals were pinched on a regular basis to gauge the depth of anesthesia. All cut and pressure points were given local anesthesia in the form of 2 % lidocaine hydrochloride, a long lasting local anesthetic.

The animals were carefully placed on a stereotaxic frame with their heads supported by ear bars coated with lidocaine hydrochloride gel. Electrodes, to monitor ECG activity, and a pulse oximeter were then clamped on to the animals. Contact lenses were placed, to prevent dryness of the cornea. Throughout the experiment, the animals' heart rate (HR), saturation of peripheral oxygen (SPO_2), end-tidal carbon dioxide (Et-CO_2) and body temperature (T), were constantly monitored and stabilized. Once all physiological parameters were stable, Gallamine Triethiodide (5 ml) was injected through one of the IV lines to induce paralysis. All subsequent surgical wounds were then

infused with 2 % lidocaine hydroloride. Glycopyrrolate (IM every 7 hours at 0.01 mg/kg), Buprenorphine (IV every 12 hours at 8.5 μg/kg) and Dexamethasone (IV every 24 hours at 0.3 mg/kg) injections were administered to prevent tracheo-bronchial secretions, post-operative pain and inflammation, respectively.

The cranium was exposed and two holes were drilled for insertion of small metal screws for recording the EEG. For optical imaging and for the subsequent implantation of an electrode array, a larger circular opening (approximately 18 mm in diameter) was made, centered on the midline at Horsley-Clark coordinate A4, and a chamber was attached to the skull. Mannitol (250 mg/kg) was injected (IV) 30 minutes before performing duratomy, in order to prevent edema. The dura mater above area 18 was resected. Artificial cerebro-spinal fluid (aCSF)/Agarose were used to protect the exposed cortex. At the end of the surgical procedures, gas anesthesia was switched from isoflurane to halothane (Sigma-Aldrich). An infusion of 6ml/kg/hr of 5 % Dextrose in Lactated Ringer's solution and 2 % Gallamine Triethiodide (2 mg/Kg/hr) was started and maintained for the duration of the experiment. Throughout the imaging sessions, halothane level was kept at 0.7-1.0 % and the heart rate was maintained at 160-180 BPM. The animal was mechanically ventilated at a rate of 25-40 strokes per minute and a volume of 10-15 ml/kg, maintaining the end-tidal CO2 within 32-38 mm Hg. The gas mixture was adjusted within the range of 100 % medical air to 80 % medical air / 20 % O2, in order to keep the oxygen saturation level at ≥ 94 %. Finally, the animal's temperature was kept between 37.9 and 38.1 degrees.

The pupils were dilated with local application of phenylephrine hydrochloride 2.5 % (Mydfrin®, Aventix Animal Health). The eyes were protected using contact lenses with zero power; they were focused on a tangent screen at a distance of 30 cm using external lenses with power determined by

retinoscopy. The retinal vessels, blind spot and area centralis of each eye were back projected onto the screen.

Responses of neuronal assemblies were imaged optically and subsequently recorded with microelectrode arrays (MEAs).

6.3.2 Visual Stimuli

The visual stimuli generator code was developed by implementing Psychophysics toolbox (Brainard, 1997). The visual stimuli were displayed on a 21" LCD screen with a refresh rate of 60 Hz. The screen was positioned at a distance of 30 cm from the animal, subtending an angle of 30–55° in the visual field, contralateral to the hemisphere investigated. The animals were stimulated binocularly, using 50 %-contrast sinusoidal-wave gratings with a spatial frequency of 0.15 cycles per degree and a temporal frequency of 4 Hz on a luminance-calibrated screen.

Figure 6-1 (a) and Figure 6-1 (b) depict our experimental paradigm. Each visual stimulus consisted of: 1 s of blank (where we presented an iso-luminant gray screen) followed by 1 s of moving grating. Each trial of stimuli spanned the full orientation spectrum at a resolution of 22.5° (hence 16 different directions + 1 blank condition) lasting 34 s. The order of the directions in each trial was randomized to account for adaptation. Seventy-five such trials were run for each TMS paradigm. TMS was given after 15 baseline trials, before the 16th trial started. This made 8.5 minutes of pre-TMS and 34 minutes of post-TMS recording.

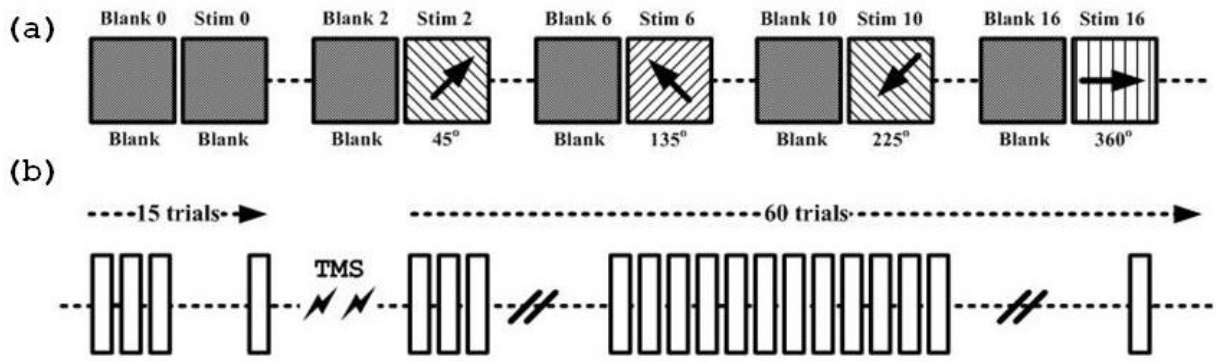

Figure 6-1. Experimental Paradigm. (a) Each trial consists of 16 conditions (8 orientations and 16 directions of motion orthogonal to orientation, at 0 to 360 degrees in steps of 22.5 degrees) and a blank condition. Each stimulus was presented for 1 s, with 1 s inter-stimulus interval during which a blank gray image was presented. (b) Each square block corresponds to one trial. Hence, we have fifteen trials before TMS, followed by the delivery of TMS and, subsequently 60 trials after the application of TMS.

6.3.3 Optical imaging and implantation of a multi-electrode array

The surface of the sealed cortex was imaged using a differential data acquisition system (VDAQ Imager 3001, Optical Imaging Ltd., Rehovot, Israel) equipped with a 12-bit bit depth Pantera 1M60 camera (Teledyne Dalsa, Waterloo, Ontario, Canada) and a macro lens (Nikon, AF Micro Nikkor, 60 mm, 1:2.8 D). The camera was focused on the surface of the cortex, ensuring that the cortical blood vessel architecture was captured. Preferred orientation was mapped parallel to the surface of cortex (Grinvald et al., 1986; Shmuel and Grinvald, 2000). After obtaining the orientation map, an optimally responding region was chosen manually to implant a 10×10 electrode array (4 mm × 4 mm area, 400 μm separation and 1 mm electrode length; Blackrock micro-systems, Salt-Lake Cirt, UT) for electrophysiology recordings. After placing the array on the selected region, a blob of silicone gel (Kwiksil, WPI INC., Sarasota, FL) was dropped on the part of wire bundle that reached the skull, to provide a fulcrum which would prevent the array from being dislodged. The array was then inserted using a pneumatic inserter. Figure 6-2 (a) and

Figure 6-2 (b) show an orientation map obtained during one of the experiments followed by the placement of the electrode array. After the insertion of the array, a laser beam was used to register the location of the array (Figure 6-2 (c)). The array was then covered by a thin layer of Surgifoam soaked in artificial CSF (approximately 1 mm thickness in the soaked state) in order to (i) replicate the CSF layer and keep the brain wet and, (ii) to provide additional precautionary measure against movement of the array during the subsequent steps. The drilled out bit of bone was then placed above the array, now cushioned by a layer of wet Surgifoam. Neurophysiological signals were recorded extra-cellularly at 24,414 Hz using a Tucker Davis Technology (Alachua, FL) data acquisition system.

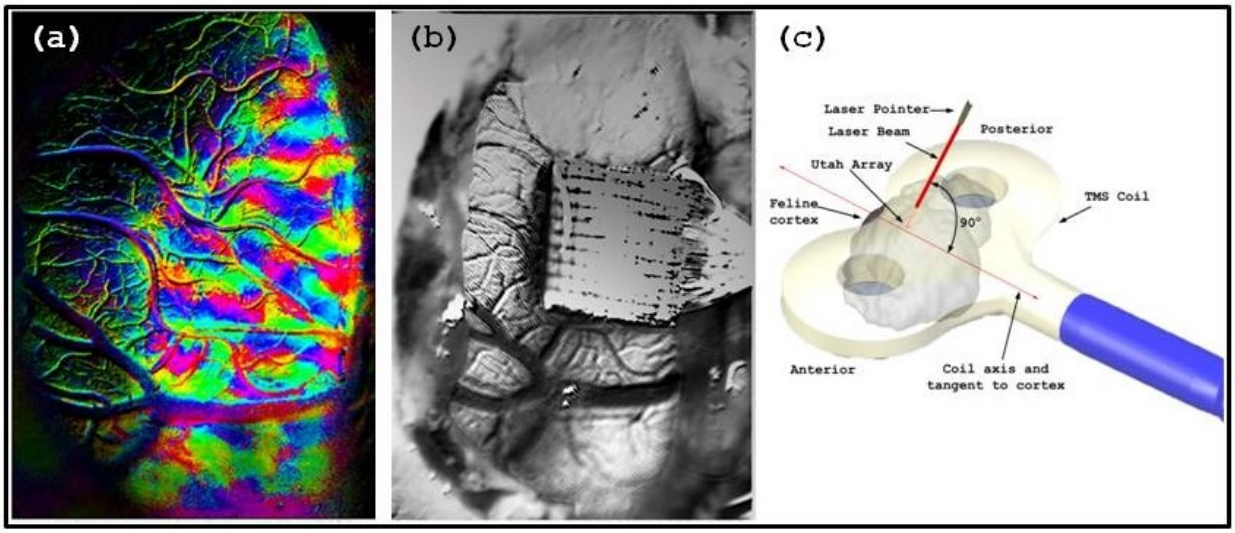

Figure 6-2. Identification of the array implant location followed by coil positioning. (a) Preferred orientation map obtained from optical imaging. (b) The position of the implanted array, determined based on the orientation map. (c) Localization of the array using a laser guided pointer held perpendicularly above the array.

6.3.4 rTMS protocol

TMS was delivered to the cortex using a Magstim Rapid TMS stimulator (Magstim, Whitland Dyfed, UK), producing a biphasic waveform, through a 70 mm butterfly coil.

High frequency continuous theta burst protocol was delivered to cat area 18 (visual area V2). Three different TMS paradigms have been used in this study, a 15 Hz rTMS paradigm (one single train of 15 Hz rTMS pulses for 40 s amounting to a total of 600 pulses) and two theta burst paradigms (three pulses of TMS at 50 Hz repeated in bursts of 200 ms; (Huang et al., 2005); continuous theta burst or cTBS (a single train of TBS for 40 s amounting to 600 pulses) and intermittent theta burst or iTBS (a 2 s train of TBS repeated every 10 s for 190 s amounting to 600 pulses). TMS was delivered after 8.5 minutes of baseline recording. All TMS paradigms were delivered at 55 % MSO, which according to our FEM simulations performed in Chapter 3 translates to 100 % RMT. The goal of the FEM simulations was to induce the same E-field strength on the gray matter segment based on a phantom model of a cat head as the magnitude of E-field that is induced on the gray matter segment in a phantom model of a human head for average RMT TMS stimulator intensity.

The TMS coil was placed above the array approximately 10 mm from the cortical surface. Since the gyrus on which the array was inserted was directed in the anterior-posterior direction, the TMS coil was oriented tangential to the cortex perpendicular to the anterior-posterior axis. This caused the induced current profile to align approximately with medio-lateral axis (perpendicular to the direction of the gyrus). This orientation is important to induce the maximum electric field that can be induced in a gyrus for a particular stimulation intensity (Thielscher et al., 2011).

6.3.5 Data Analysis

Each TMS experiment was of 42 minutes long and consisted of 8.5 minutes baseline activity followed by 34 minutes of post TMS conditioning activity. Each of the two aforementioned segments provided us recordings of local field potentials (specifically visual evoked potentials or VEPs) and spiking activity.

For analysis we re-sampled the 75 time points (each time point representing one trial or 34 s of cumulative data, with 2 s of response per orientation) to 25 time points by averaging 3 consecutive trials together.

Statistical significance of the effect of TMS on all variables being investigated was ascertained using one-tailed t-test with $p<0.05$. Statistically significant decreases are represented by blue (*) markers near the lower y-axis extremity and statistically significant increases are represented by red (*) markers near the upper y-axis extremity. The points of significance on correlation plots were obtained by transforming correlation coefficients to Fisher coefficients and performing a t-test on the Fischer coefficients. However, for presentation purposes, actual correlation coefficient values were used in the correlation plots. For one particular analysis, we used a paired Kolmogorov-Smirnov test to calculate the similarity between two distributions followed by a Chi squared goodness-of-fit test to identify the similarity of those curves to one common normal cumulative distribution function.

Post-hoc false discovery rate (FDR) analysis based on Bejamini and Yekutieli's procedure was performed on all statistical tests.

6.3.6 Sifting orientation selective channels from other channels

Each evoked response to a visual stimulus was split into three segments: spontaneous segment (800 milliseconds baseline activity before the onset of the stimulus), transient segment (first 200 milliseconds after the onset of the stimulus) and, sustained segment (200-1000 milliseconds after the onset of the stimulus). From our observations, we concluded that the sustained segments of evoked responses provided the least noisy and most stable measures for analysis. Hence, the sustained segments of the evoked responses were used for subsequent analyses to quantify the effect of TMS.

In order to determine the effect of TMS on neuronal populations, it was important to first ascertain which channels (out of 96 implanted channels) demonstrated orientation tuning. This was achieved by using circular variance of direction tuning curves as a measure (Ringach et al., 1997; Ringach et al., 2002). In mathematical terms, circular variance (CV) for a bi-modal distribution, such as that expected for direction selectivity (Shmuel and Grinvald, 1996; Swindale et al., 2003), is given by

$$CV = \frac{\sum_{k=0}^{360} R_k e^{i2\theta_k}}{\sum_{k=0}^{360} R_k} \tag{6.1}$$

where, R_k is the response (in terms of firing rate or spiking activity) corresponding to direction *k* of the gratings and θ_k represents the direction angle of drift of the gratings. CV can be further simplified for uni-modal distribution, such as that expected for orientation selectivity (Hubel and Wiesel, 1962)

$$CV = \frac{\sum_{k=0}^{180} R_k e^{i\theta_k}}{\sum_{k=0}^{180} R_k} \tag{6.2}$$

We calculated the CV obtained for each of the 96 channels based on action potential responses. The idea behind this is to weed out channels that show actual tuning from channels that do not show tuning but rather just fire randomly. A threshold of 0.9 in terms of CV was chosen to distinguish between tuned and un-tuned channels.

6.4 Results

6.4.1 Effect of TMS on VEPs

Average VEPs obtained at different time relative to TMS are shown in Figure 6-3. Three distinct early VEP components are identified to be N_{48} (N_1), P_{130} (P_1) and N_{435} (N_2) components which are feline analogues to the N_{75}, P_{100} and N_{135} components in humans (Barnikol et al., 2006). In order to eliminate baseline fluctuations, two relative measures of peak to peak amplitudes were defined; N_1P_1 and P_1N_2. Both the TBS paradigms and 15 Hz rTMS showed non-significant long term increase in both N_1P_1 and P_1N_2 amplitudes, with the effect of 15 Hz > iTBS > cTBS (in terms of duration and stability of facilitation, t-test, $p<0.2$)

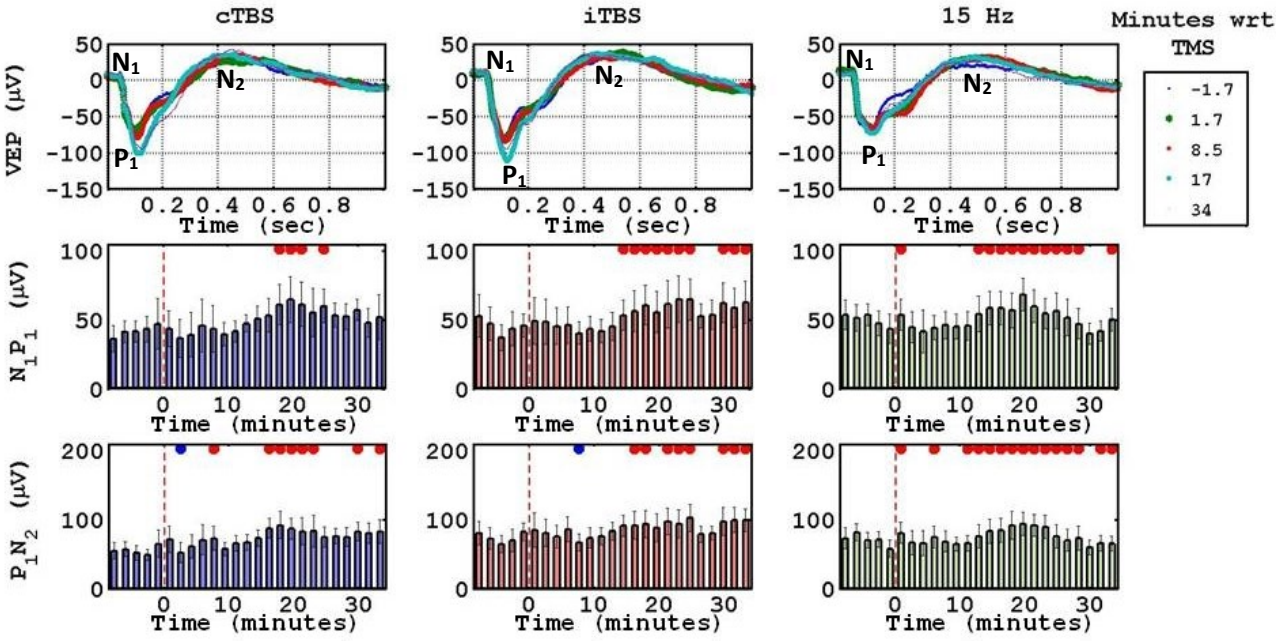

Figure 6-3. The first row shows, from left to right the average VEPs for cTBS, iTBS and 15 Hz rTMS across all orientations and experiments representing VEPs 1.7 minutes before and 1.7, 8.5, 17 and 34 minutes after TMS. Similarly, plots in the middle row are measures of average peak to peak amplitude between N_1 and P_1 components of VEPs before and after TMS (represented by the bar before the 0 time-point). Plots in the bottom row are measures of average peak to peak amplitude between P_1 and N_2 components of VEPs before and after TMS. Statistically significant increase (red *) and decrease (blue *) are represented by the markers near the vertical axis' upper limit of the plots.

In order to analyze the causes of the changes in the relative peak to peak amplitudes, we considered the effect of the individual early VEP components on the relative peak to peak amplitude behavior. In Figure 6-4, we observe the timecourses of the magnitude values of the early VEP components in terms of extracellular potentials. It is to be noted that the P_1 component potential has been reversed in polarity to maintain a consistent depiction of results. cTBS caused non-significant but consistent long term increases in the amplitudes of P_1 and N_2 components. iTBS showed no consistent discernible effect on the early VEP components. 15 Hz rTMS caused non-significant increases in the long term P_1 and N_2 components with the effect on N_1 component being sporadic.

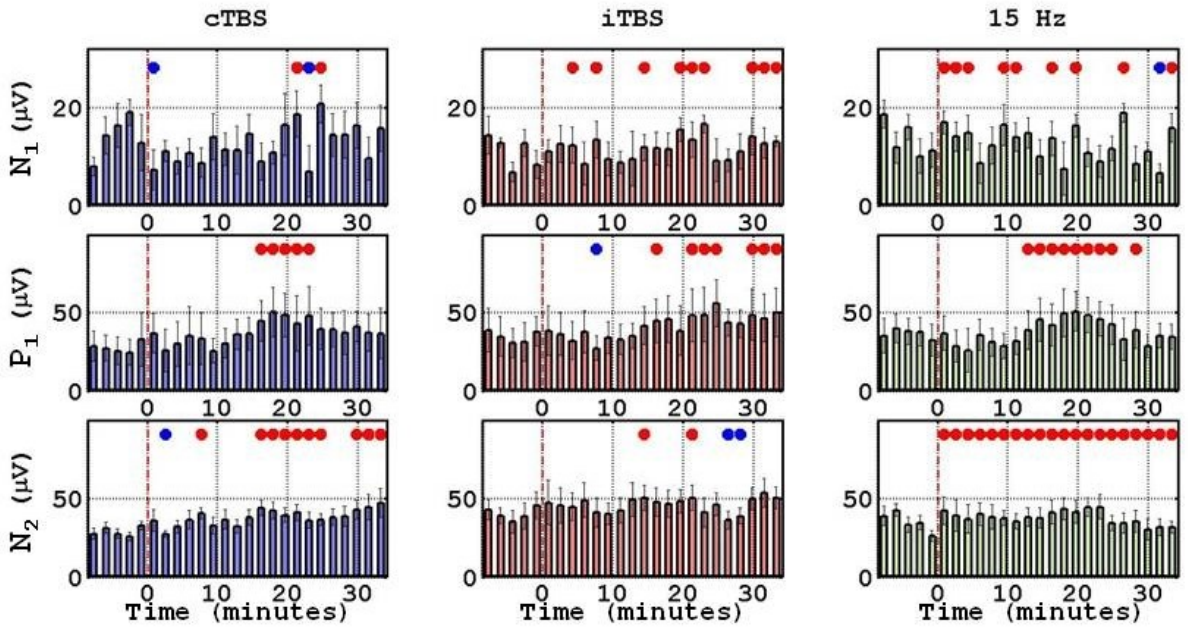

Figure 6-4. Magnitude of early VEP components.

Figure 6-5 depicts the latencies of the aforementioned early VEP components. Interestingly, on comparing Figure 6-4 and Figure 6-5, though there is an increase in N_2 amplitudes caused by cTBS and 15 Hz rTMS, their effects on the latencies of N_2 are exactly opposite, with cTBS resulting in a non-significant decrease in N_2 latency corresponding to the increase in amplitude, whereas 15 Hz rTMS causes an increase in N_2 component latency corresponding to an increase in amplitude of N_2.

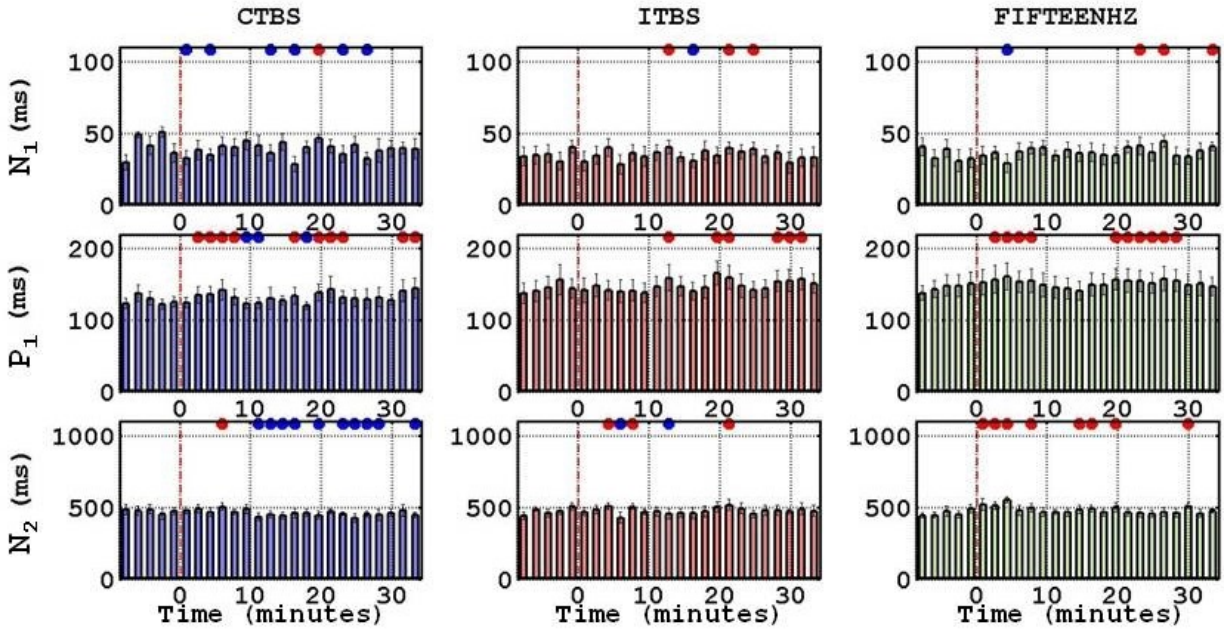

Figure 6-5. Average latencies of N_1, P_1 and N_2 components before and after TMS.

6.4.2 Effect of TMS on Firing Rates and Gamma Band Power

For analysis we re-sampled the 75 time points (each time point representing orientation specific responses in one trial or 34 s of cumulative data) to 25 time points by averaging 3 trials together. Hence, each time point represented an average of 3 trials or, conversely 102 s of data (= 1.7 minutes). We first analyzed the data from the channels that were tuned to orientation, to quantify the effect of TMS right after its delivery. This was achieved by plotting the time courses of firing rates (FRs) and band limited magnitude of gamma activity (gBLM). Figure 6-6 presents the time courses of the averaged FRs, low gBLM (30-57 Hz) and high gBLM (63-150 Hz) for each rTMS paradigm. Each individual measure (FR or low/high gBLM) was first normalized separately for each channel and condition by its pre-TMS value (5th time point on the plots) and the resultant values were averaged across all orientations, tuned channels and, finally across all hemispheres. Both cTBS and 15 Hz rTMS paradigms resulted in considerable suppression of spiking activity

right after their administration; however, iTBS showed a very transient and non-significant suppressive effect after its delivery. cTBS and 15 Hz rTMS suppressed spiking activity for 6.8 and 1.7 minutes, respectively (one-tailed t-test, $p<0.05$, $N = 8$; represented by blue '*' markers near the lower y-axis extremity). iTBS, on the other hand, caused statistically significant but sporadic long term facilitation in spiking activity (represented by red '*' markers near the upper y-axis extremity). In low and high gBLM, the changes were less obvious. However, the trends were similar: cTBS and 15 Hz rTMS suppressed gamma band activity for 1.7 minutes after their administration with no significant long term effects, whereas iTBS, in contrast, showed no short term effects but consistent and significant increase in long term gBLM (more prominent in high gBLM than in low gBLM).

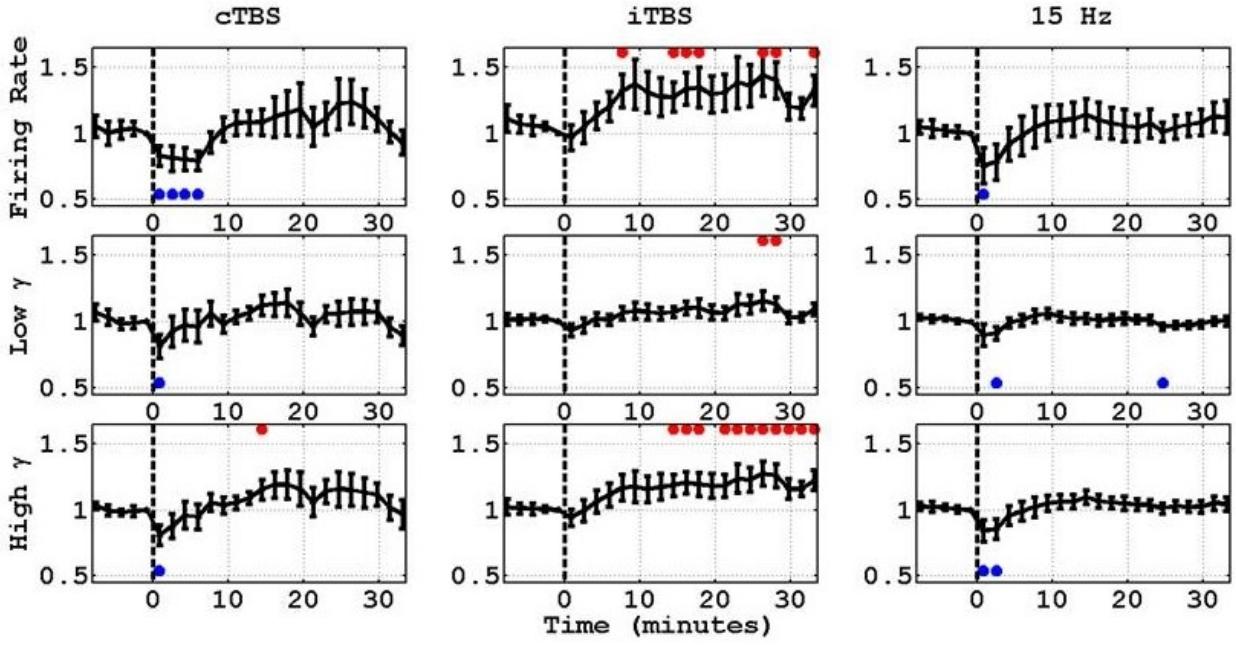

Figure 6-6. Average Normalized action potentials firing rate and gBLM responses in cTBS, iTBS and 15 Hz rTMS experiments. In all cases, normalization was done with respect to values on the time point right before the application of TMS.

6.4.3 Regression analysis

In our previous discussion, we examined the effects of TMS on the average firing rate and gamma activity across all orientations and tuned channels. How these effects influence the spatial pattern of the responses? The subsequent analysis looked at a more global perspective of the effect of TMS. To this end, we analyzed the spatial pattern of response (spiking activity) to each orientation. Specifically, we compared the responses recorded in all channels to all orientations in each trial relative to their counterparts before applying TMS. The comparison was done with respect to the pattern of responses to all orientations and all channels of the reference pre-TMS trial. This gave us a measure of how the response pattern of each trial varied with respect to the pre-TMS trial. A snippet of the analysis is demonstrated in the results presented in Figure 6-7, showing a scatter plot and orthogonal regression of post-TMS responses at different time points (1.7, 6.8 and 18.7 minutes after TMS) with respect to pre-TMS responses to all orientations averaged over the 3 trials (1.7 minutes) before TMS. The scatter plots show an approximate linear behavior of the responses at different time points. The orthogonal regression lines (Leng et al., 2007) for each cluster depicted the major axis of anisotropy. In order to test the possible linear relationship between the pre- and post-TMS responses, we chose not to use simple linear regression, because we present and analyze the post-TMS measure as a function of the pre-TMS measure and both parameters are subject to measurement errors. Therefore, we assume errors in both pre- and post-TMS measurements. Orthogonal regression fits this scenario better than linear regression, which assumes that one of the two variables is given with no errors. The slope of each regression represents a multiplicative factor, the gain associated with that cluster relative to pre-TMS baseline. For the given experiments presented in Figure 6-7, one each for cTBS, iTBS and 15 Hz TMS conditioning selected randomly, we observe that cTBS conditioning resulted in a decrease

in spiking activity after 2 minutes and 7 minutes (slopes of the red and green regression lines vs. the slope of the black unity line) with a return to baseline activity after 19 minutes (slope of blue regression line vs. slope of black unity line). iTBS conditioning resulted in a prolonged increase in cortical activity (shown by the higher slope of the blue regression line with respect to the unity line), with the effect not visible immediately following TMS administration (deduced from the overlap of the red and black regression lines). 15 Hz rTMS resulted in a decrease in cortical activity after the delivery of TMS but after a 19 minute time period seemed to show a small increase in cortical activity. These results were inferred from one experiment and only 3 time-points. Our subsequent analyses meant to test our hypothesis that cortical responses to the three different TMS conditioning paradigms, hence the cortical mechanisms underlying the response behaviors, are generic to them individually but differ from each other.

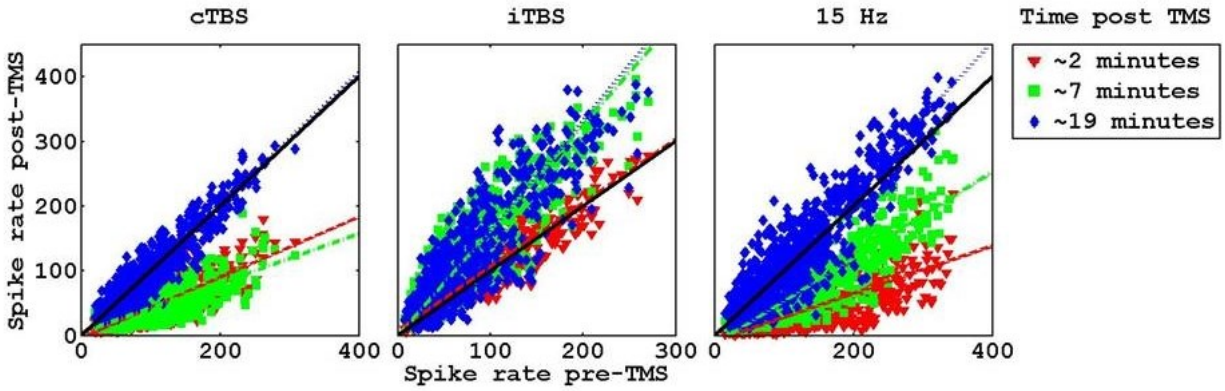

Figure 6-7. Linear gain effect of TMS: Pre- Vs Post TMS responses to oriented grating stimuli for cTBS, iTBS and 15 Hz TMS conditioning. Each plot presents the average spiking activity recorded by tuned channels after the delivery of a particular TMS conditioning paradigm with respect to average spiking activity recorded by the same tuned channels before the delivery of TMS, for a specific experiment run. Average spiking activity refers to the average response recorded during the sustained part of the response by a given tuned channel. First set of averaging took place across the prolonged part of the response (200-1000 ms following the presentation of the stimulus). The second set of averaging was performed by averaging over three consecutive trials, separately for each channel and orientation. Responses obtained 1.7, 6.8 and 18.7 minutes (portrayed by red, green and blue markers, respectively) after the delivery of the particular TMS paradigm were compared to responses averaged over approximately 2 minutes before TMS delivery. The colored scatter plots represent the relationship between post TMS responses to the pre-TMS response. The corresponding colored lines for the scatter plots are the orthogonal regression lines. The black lines represent the lines with slope 1 and intercept 0 (unity slope lines).

In Figure 6-8, the time-courses of the slopes and y-intercepts of the regression lines, along with correlation coefficients, are shown. The three parameters represent global measures of neuronal responses since they represent changes across channels and orientations as a function of time. They present the time courses averaged separately across all cTBS, iTBS and 15 Hz runs. The regression slope represents a multiplicative factor by which responses were either suppressed or facilitated. The y-intercept refers to an additive component of responses relative to the pre-TMS baseline responses.

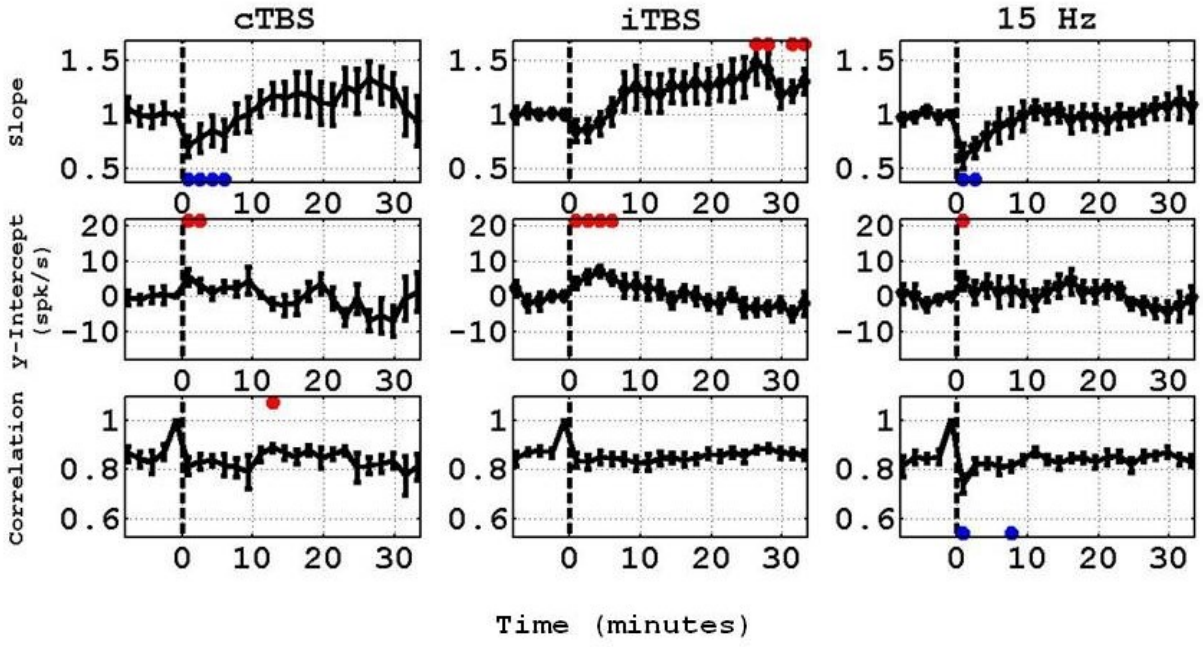

Figure 6-8. Time course of slope, y-intercepts of orthogonal regression lines and correlation coefficients applied to the scatter plots sampled from 3 trials average. The slope and intercept time courses represent the time point by time point results of orthogonal regression of responses to oriented gratings as a function of the baseline responses recorded pre-TMS, for cTBS, iTBS and 15 Hz rTMS. The error bars represent the standard errors of means.

Correlation of the response patterns is shown at every time point, with respect to pre-TMS time point was performed separately for each experiment. The time courses of these correlation coefficients were then averaged across experiments to obtain the time course presented in Figure 6-8. Table 6-I shows the values of mean correlation coefficient values before (time points 1 to 4 or trials 1 through 12) and immediately after (time points 6 to 9 or trials 16 through 27) the application of TMS. Based on these values we conclude that the application of TMS does not significantly change the response patterns (except for a 1.7 minutes transient effect right after the application of 15 Hz TMS).

In summary, in all 3 paradigms, the effect of TMS on spiking activity response is approximately linear relative to pre-TMS responses, showing short term suppression in cTBS and 15Hz, and a

long term facilitation in iTBS (statistically significant) and cTBS (a non-statistically significant trend). However, the response pattern remained unchanged.

Table 6-I Variation of mean correlation coefficient values across trials before and after the delivery of TMS (cTBS, iTBS and 15 Hz rTMS conditioning).

Correlation / rTMS Paradigm	*Pre-TMS trials (1 to 12) (Mean ±SEM)*	*Post-TMS trials (16 to 27) (Mean ±SEM)*
cTBS	0.853 ± 0.035	0.826 ± 0.034
iTBS	0.865 ± 0.020	0.841 ± 0.028
15 Hz	0.840 ± 0.029	0.799 ± 0.030

Table 6-I. The enumerations are mean correlation coefficient values before (time points 1 to 4 or trials 1 through 12) and immediately after (time points 6 to 9 or trials 16 through 27) the application of TMS. Each of the response patterns was compared to the response pattern from time point 5 (trials 13-15), which served as pre-TMS baseline response. Values are reported as mean correlation coefficient values ± standard error of means (SEM). SEM was calculated over the correlation coefficient values obtained from 8 hemispheres.

6.4.4 Effect of TMS on orientation tuning and selectivity

Cortical sites that were classified as tuned to orientation are expected to show different firing rate responses to different orientations. If the effect to TMS is indeed linear relative to responses prior to TMS, we should expect that orientation tuning will not change following the application of TMS. To test this expectation directly, we analyzed orientation tuning before and after TMS. Orientation tuning curves were obtained by first averaging the responses from same orientation but opposite direction. Therefore, the bi-modal direction tuning curves were transformed to unimodal orientation tuning curves spanning 0 to 180 degrees. The tuning curves were fitted with

Von-Mises function (Swindale, 1998; Swindale et al., 2003) with a modification by adding an extra variable to account for DC offset.

$$R(\theta)=Ae^{\frac{\cos(2(\theta-po))-1}{s}}+B$$

where, R is the response at orientation θ degrees, A is the response parameter at preferred orientation, B is the DC offset, po is the preferred orientation and S is the spread parameter. The motive to add DC parameter was to account for spontaneous activity and in most of the cases untuned visual evoked response analogous to a DC offset. In other words, the global signal (untuned evoked responses) was expected to be fitted by the DC offset parameter. The general procedure of tuning curve fitting where the first step is to subtract spontaneous activity from evoked responses, was not done here. The reason is that the effect of TMS was not the same in spontaneous activity and in evoked activity, which was also demonstrated by Pasley et al. (2009). It was shown that the effect of rTMS on spontaneous activity was variable and shorter compared to evoked activity. Therefore, subtracting spontaneous activity from evoked responses in subsequent tuning curves after TMS administration would create variability in the tuning curves. Instead, we added a DC parameter in the Von-Mises model. Addition of the DC parameter in Von-Mises model increased the goodness of fit. Goodness of fit was analyzed by computing correlation coefficient (adjusted r2) and mean squared error (MSE) of fits over average pre-TMS tuning curve obtained from several experiment runs.

We first determined whether TMS changed the preferred orientation of each channel. In Figure 6-9, the upper row presents the preferred orientation of all tuned channels in one experiment, obtained from the fitted tuning curves. The curves show that barring noise, there was no systematic change in preferred orientation as a function of time. In order to quantify the effect of TMS on the

preferred orientation, we obtained the difference in preferred orientation of each channel, relative to its preferred orientation right before TMS. The distributions in the second row in Figure 6-9 depict the preferred orientation at the beginning of the TMS session (time point 1, 6.8-8.5 minutes pre-TMS) and after the TMS conditioning (time point 9, 6.8-8.5 minutes post TMS, relative to time point 5, just before TMS). These distributions are cumulative, including data from all tuned channels from all experiments. There was no statistically significant difference between the two distributions (D = 0.064, 0.057 and 0.039; χ^2 = 5.95, 21.52, 18.72 where D is the Kolmogorov-Smirnov test statistic and χ^2 is the Chi Square goodness of fit statistic at a significance level of $p<0.01$ for the distributions in Figure 6-9 for cTBS, iTBS and 15 Hz rTMS, respectively). Based on the similarity of the distributions before and after TMS, we concluded that TMS did not change the preferred orientation.

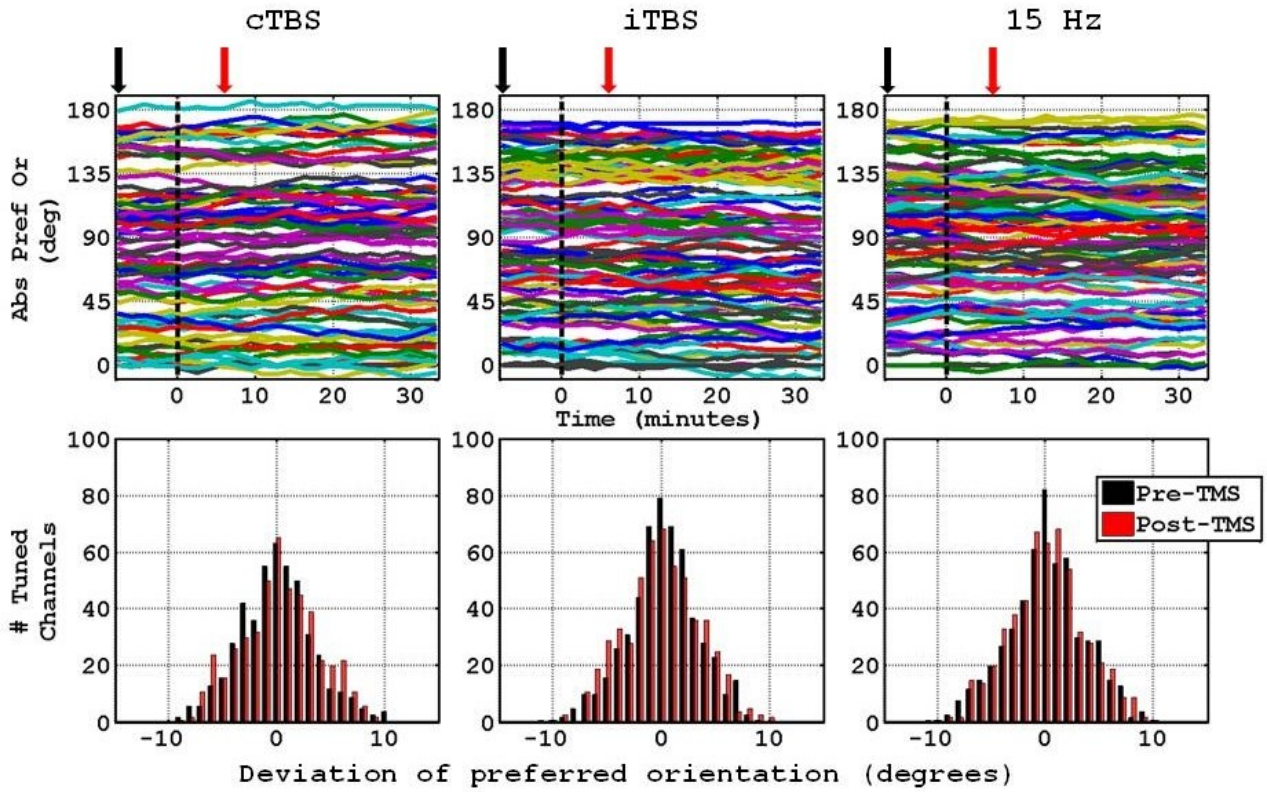

Figure 6-9. Time courses of preferred orientation of each tuned channel, from one experiment with cTBS, iTBS and 15 Hz rTMS. Cumulative distribution of all tuned channels across all experiments based on the maximum relative deviation of their preferred orientations (with respect to their corresponding preferred orientations right before TMS i.e. time point 5) at the beginning of the experiment session (-6.8 to -8.5 minutes with respect to when TMS is applied, denoted by the black arrows in the figures above) and after TMS conditioning (6.8 to 8.5 minutes with respect to when TMS is applied, denoted by the red arrows in the figures above).

In order to analyze the effect of TMS on other parameters of orientation tuning, we aligned all fitted tuning curves according to their preferred orientation such that the preferred orientation corresponded to 90 degrees and then we chart out the rearranged tuning curve.

Figure 6-10 shows plots of the average tuning curves fitted to the average of three trials right before TMS (in dark) and to the average of three trials right after TMS (in red). These tuning curves were averaged across all tuned channels and all experiments. The curves demonstrate the suppressive

effect of cTBS and 15 Hz right after TMS, and the weak suppression following iTBS. Note that the relative change in firing rate for a given orientation following TMS relative to the average firing rate for the same orientation prior to TMS seem to remain approximately equal across all orientations. This means that the response to a stimulus bore a linear relationship with the response to the same stimulus during the pre-TMS baseline period. Additional support to this observation is demonstrated by the vertical lines representing the full-width at half height before and after TMS, which are approximately equal.

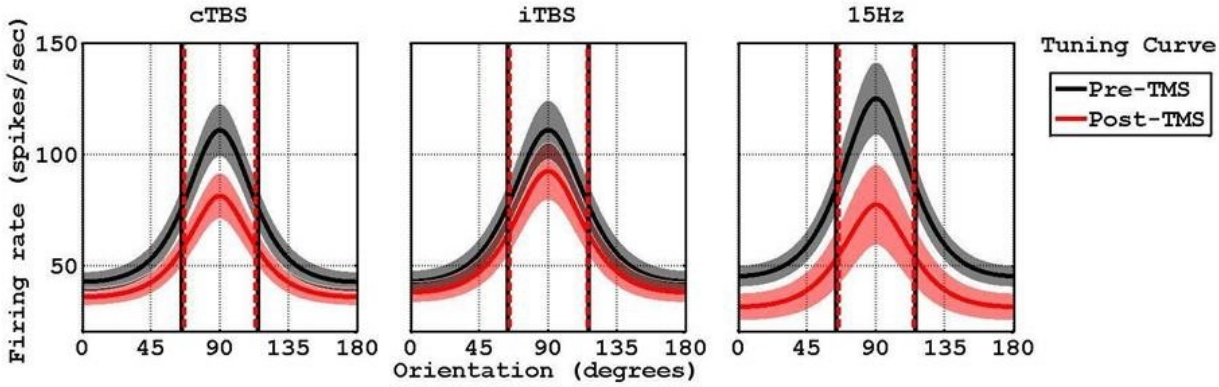

Figure 6-10. Average tuning curves of three trials right before (black) and right after (red) the administration of (a) cTBS (b) iTBS and (c) 15 Hz rTMS. The darker lines represent the mean values whereas the lighter patches around them show the standard error of means across all experiments. The vertical solid black and dotted red lines show the widths of the tuning curves at the corresponding half heights before and after TMS, respectively.

Figure 6-11 shows the time courses of the average tuning curves for the three TMS paradigms. The black and red arrows indicate the time points at which the tuning curves shown in Figure 6-10 were extracted from.

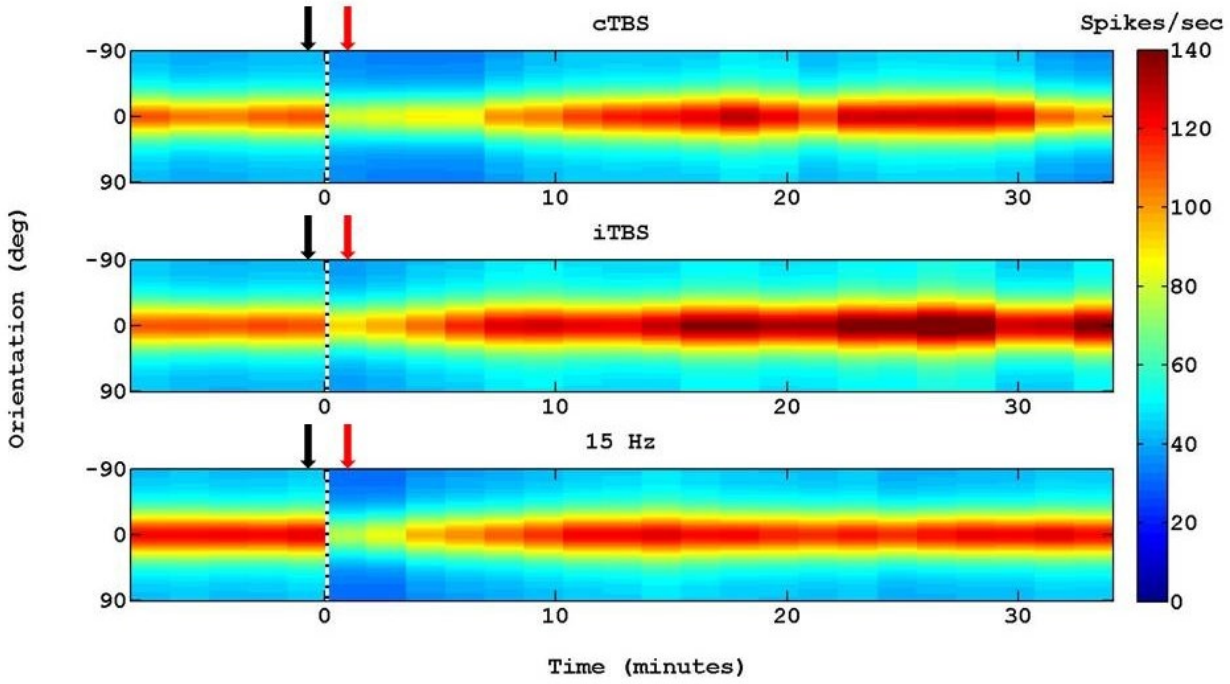

Figure 6-11. Time-courses of average tuning curves fitted with Von-Mises function. The dotted black vertical lines separate the tuning curves into the pre-TMS and post-TMS regions. The spike firing rate tuning curve of each recording site was fitted with Von-Mises function and centered on the preferred orientation before averaging across all recording sites.

Figure 6-12 presents the time courses of 1) the mean relative difference in firing rate response amplitude between the preferred and non-preferred orientation (orientation that elicits the lowest firing rate). Note that 'relative' refers to that same measure in time point 5, just before TMS; 2) non-preferred orientation firing rate (DC parameter); 3) half width at half maximum height (HW@HM), also termed the bandwidth of the tuning curve; and, 4) circular variance (CV). CV is a global measure of tuning and selectivity whereas the bandwidth is a local measure (Ringach et al., 2002). Consistent with the results presented in Figure 6-6 and Figure 6-8, cTBS and 15 Hz TMS suppressed the amplitude of the response of the tuning curve for 6.8 and 1.7-3.4 minutes, respectively. Consistent with the results presented in Figure 6-11, iTBS caused a late (14-32 min

following TMS) increase in tuning curve amplitude. TMS caused a transient (1.7 min long) increase in CV right after cTBS conditioning. No statistically significant changes in tuning bandwidth were observed following each of the 3 TMS paradigms. We concluded that none of the TMS paradigms affected orientation tuning and selectivity, either at the global or local levels. We further concluded that the effect of TMS on the response amplitude is linear relative to the baseline pre-TMS response.

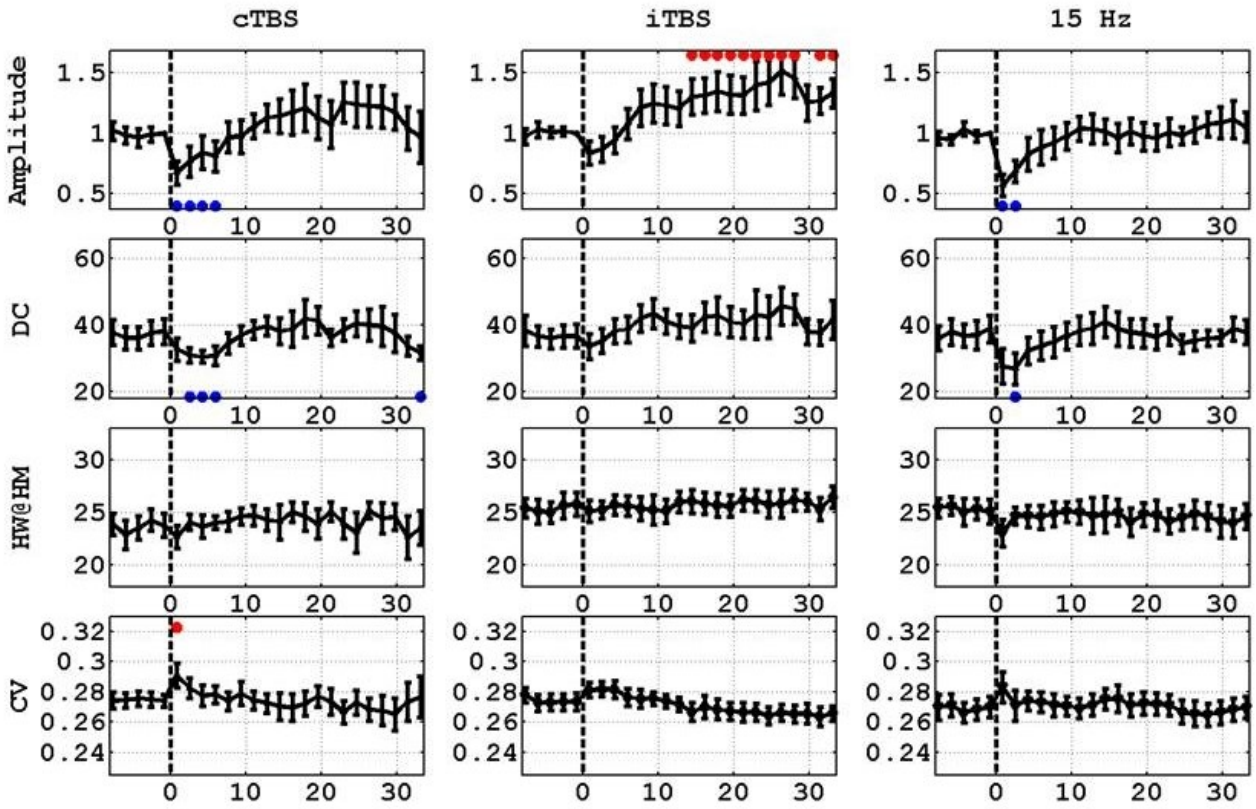

Figure 6-12. Time course of circular variance of fitted tuning curves with the left, middle and right columns representing calculated values corresponding to cTBS, iTBS and 15 Hz rTMS respectively. Similarly, plots in the middle row are measures of orthogonal-to-preferred orientation ratio while plots at the bottom are measures of bandwidth (half width at half maximum).

6.5 Discussion

6.5.1 Effect of TMS on analogous parameters

Analogous parameters recorded from different regions of the brain can be affected differently by the same TMS paradigm. In order to explain the effect of a given TMS paradigm on an evoked

potential, it is critical to identify the input factors that are involved in the generation of these evoked responses. For instance visual evoked potentials are theorized to have input parameters associated with the stimulus (referred to as afferent input), synaptic input currents (from both excitatory and inhibitory neurons) and the membrane currents associated with Na, K and leaky channels (Miyawaki et al., 2012). The synaptic input currents which depend on inputs of the associated neurons to each other may vary due to their intrinsic behavior mechanism. Different neurons may be tuned to different orientations and hence the inputs to a neuron from its associated neurons may not be linear. However, such a structure may not be applicable to SEPs elicited by the stimulation of a particular digit in area S1. The afferent input components are different between the visual cortex and the somatosensory cortex not only due to the different pathways that are involved in the transmission of the stimulus to the cortex but also due to the nature of excitation with somatosensory stimulation being more synchronized, hence more potent than the less synchronized and weaker visual stimulus. Miyawaki et al. (2012) have demonstrated that the effect of TMS is strongly dependent on the above two discussed factors. Hence, the variability in the effects of a given TMS paradigm on different types of evoked potentials could be ascribed to the intrinsic behavior of their input components.

Hence, any TMS paradigm cannot be generalized as predominantly facilitatory or suppressive based on its effect on a given response/basal parameter.

6.5.2 TMS does not affect the global pattern of responses

Linearity and correlation analysis of firing rates revealed that TMS affects every neuron in the defined population the same way (except for a 1.7 minutes transient effect observed in the correlation coefficient time course of Figure 6-8 right after the application of 15 Hz TMS, which

may be due residual chaotic effects of the conditioning TMS pulses (on the pre-amplifier) altering the responses of specifically trial 16. The chaotic effects may be due to saturation of the pre-amplifier of the DAQ owing to its considerably smaller dynamic range compared to the magnitude of the currents induced by TMS). The only measure that does not support this claim is the y-intercept. The y-intercept should effectively be zero across the entire time course for all three TMS paradigms, which is not the case. However, we also observe that the maximum value y-intercept does not even reach ten spikes per second, in all three TMS conditioning experiments. Neurophysiologically, such a value has no significance, nor does negative spiking activity. Hence, the fluctuations in y-intercept can, for all practical reasons, be neglected and the system can be assumed to be demonstrating an approximately linear behavior. In other words, the response of multi-unit activity across all orientations, be it preferred or non-preferred, bears a linear relationship to their corresponding responses after TMS, with the same multiplicative factor across recordings from all electrodes. This was also proven using tuning curve analysis in which we show that TMS did not affect global measures of tuning and selectivity. This occurs precisely because of the fact that all sites and corresponding neuronal ensembles are affected in a similar manner by TMS. In addition, we also show that the preferred orientation of all neurons did not change after the application of TMS. What we postulate is that neurons tuned to a particular orientation maintain their preferred orientation.

The decreased firing rate can be seen as indicative of a decrease in the “perceived” contrast of the stimulus after TMS. One way to justify this is by extending the slope time course of a TMS experiment to a non TMS experiment in which the contrast is varied at every time point. If the correlation between the firing rate profile of the TMS experiment and non-TMS experiment is

high, provided the animal physiology is the same during both experiments, the hypothesis of the perceived contrast variation due to TMS can be supported (although not proven).

In conclusion, TMS affects different stimulus related responses differently. However, for a given response, due to the spatial distribution of TMS with a figure-of-eight coil, the change in state of ensembles of neurons in a population within a constant field distribution is affected to the same extent by TMS. For future studies, it would also be interesting to see how populations of neurons lying in different electric field contours are affected by a TMS paradigm. In order to achieve this, it is likely that two electrodes arrays will be required, with one array targeted to one electric field contour plane whereas the other array will be targeted to another field contour plane. This could further strengthen the observation regarding the effect of field gradient on neuronal responses.

6.6 Summary

TMS conditioning affects a large area of cat area 18, but the effect is consistent in that all population of neurons with discrete functional processing are affected in a similar, multiplicative way. The efficiency of processing is therefore altered to the same extent across neuronal populations, without any loss of functional processing ability. In other words, the functional selectivity shaped by the cortical circuit remain unchanged. The only parameter that does change is the amplitude, or gain of the responses. Neuronal populations that were tuned to specific orientation of gratings, continued to be tuned to that specific orientation even after TMS conditioning, however, their response amplitude to these gratings (as demonstrated by the change in spiking activity of the tuning curves) changed after TMS. Average spiking activity was

suppressed by cTBS and 15 Hz rTMS for a few minutes after the application of rTMS, while it was enhanced by iTBS (demonstrating a pattern of long-term facilitation).

Chapter 7 Overview and Conclusions

There are two key aspects to TMS. The first aspect is the field that is induced in a medium due to the current in the TMS coil placed in its vicinity (which is analogous to induction of magnetism, in say, a piece of iron when a magnet is brought close to it). The second aspect is related to the effects which such changes, due to the field induction, bring about to the neuronal activity and behavior (which can be seen as analogous to movement of the aforementioned piece of iron towards the magnet). The second aspect, dealing with the neuronal and behavioral response to TMS, has been studied in great detail using in-vivo and behavioral experiments, respectively. Multiple TMS protocols and their effects on cortical functionality are available in current literature and are applied for the treatment several disorders. The first aspect, too, which deals with the physics underlying TMS related induction has been investigated considerably, but only analytically or via numerical methods involving finite difference, finite element or boundary element method simulations. Simulation related studies, however, lack experimental validation. Simulation related study pertaining to the actual fields induced because of TMS is therefore not exhaustive and hence, the analytical/numerical results are not conclusive. A fundamental question, therefore, still looms: How do we say that a particular profile of induced field is responsible for a particular kind of neuronal response? The only way to achieve this is by quantifying the relationship between the induced field magnitudes and profiles and, neuronal responses. We know that simulation based studies can be more easily conducted on humans due to the relative ease of obtaining 3D models of the head derived from MRI images. However, in-vivo invasive experimentation in humans is extremely limited on the basis of ethical constraints. Thus, lower order species (rodents, felines and non-human primates) are the candidates to achieve the desired

level of success in understanding how TMS actually works, due the possibility of conducting both theoretical and invasive experimental studies.

rTMS protocols tend to have a prolonged duration of effects compared to single pulse TMS. For instance, single pulse TMS can disrupt cortical activity for a few milliseconds whereas long trains of rTMS can alter cortical excitability for seconds or even minutes after TMS conditioning (Ganis et al., 2000). A relatively new high frequency TMS protocol, theta burst (TBS), has been gaining popularity due to its versatility. It has been used for behavioral studies in humans and invasive studies in small animal models (rodents). Invasive studies on higher order species such as NHPs and felines has not been reported yet. We studied the effect of continuous theta burst (cTBS) protocol on cortical processing in NHPs and of cTBS, intermittent theta burst (iTBS) and 15 Hz rTMS paradigms in felines, in a region (cat area 18) known for its columnar organization of responses to oriented gratings. This allowed us to study the effect of TMS on a functionally homogeneous ensemble of neurons (in monkey somatosensory cortex), as well as on functionally heterogeneous ensembles of neurons (in cat area 18).

Overall, this thesis is directed towards exploring uncharted but viable territories pertaining to transcranial magnetic stimulation. To that end, this doctoral dissertation has achieved and concluded the following:

7.1 Summary of validation study

This study was designed to address the purely engineering aspect of TMS. Hence, neurophysiology is not considered for discussions in this study. The rationale behind this approach is that before we try to understand “why” TMS affects neurophysiology, we need to understand “how”, indeed, does

it affect neurophysiology. The underlying phenomenon behind this question lies in the form of induced fields. These induced fields change the ionic concentration outside the neurons (in the extra cellular fluid), thereby disturbing the neuronal equilibrium established between ions across the neuronal membrane. Currently, there are two ways to calculate these induced fields: through measurement studies and numerical simulation studies. Both methods suffer from drawbacks. Measurement studies are subject to experimental constraints arising from the manner in which the measurements were acquired (species, probe type, data acquisition system characteristics, etc.) while numerical simulations tend to be somewhat exhaustive in terms computational time and resources required. Additionally, numerical studies are also prone to errors based on wrong interpretation of the problem to be solved and wrong assumptions of boundary conditions. Importantly, although simulations have been used to determine the profiles of the fields induced in a given medium, they have never quite been validated experimentally over a large volume of the conducting medium using high resolution of data points. Up until now, validation has been based on estimations obtained at a few data points in the conducting medium, unlike our study where a volumetric analysis has been presented. Since the simulation results have not been validated, researchers are not confident of the results provided by simulations. This gives an impression that simulation studies are not always relevant to reality. Our objective was to calibrate and validate fields induced in a conducting medium by a single pulse of TMS delivered by a stimulating coil placed in the vicinity of the conducting medium. This was achieved by comparing measured values of induced fields in two types of phantom models to simulated values of induced fields in the same phantom models (using finite element analysis) so that we could 1) simplify TMS simulation models to improve the speed of simulations, 2) understand what kind of information does each method (measurement and numerical simulation) of induced E-field

estimation provide, 3) compare and analyze how do these estimations tally with each other and, 4) explain, if they are different, what is the probable cause of this difference and what bearing will this have on future studies.

We directed our efforts to simplify the butterfly stimulating coil model that we intended to use for our TMS FEM problem definition. Time and computation resources with the single turn coil model, compared to simulation time and computational resources of the same problem definition using a realistic stimulating coil model, were minimized. We achieved sufficient confidence in our FEM TMS problem description by comparing magnetic field strength produced by the single turn coil model with values from literature and Magstim data sheets. Further validation of the single turn coil model was obtained by calibrating the single turn coil model's magnetic field strength decay profile with the decay profile of their magnetic field strength of the real stimulating coil (measured using a balanced probe). Following the validation of the coil model and FEM of the TMS simulation, a multi-electrode Utah array (MEA) was used to measure the potentials induced in two phantom models due to a single pulse of TMS. The phantom models consisted of two different glass beakers filled with saline (the conducting medium). One phantom was smaller than the wing span of the coil and was referred to as "small volume" and the second phantom was sufficiently larger than the wing span of the coil and was referred to as "large volume". Single pulse TMS was delivered by a 70 mm butterfly coil. The broadband signals from the electrodes of the array were recorded by a standard electrophysiology data acquisition system. E-field induced in the conducting saline medium in the two phantom models was estimated using mathematical equations applied to potentials measured in the medium using an electrode array, as mentioned in chapter 3. The E-field solutions were also estimated for the same phantom models using finite element model simulations (using the single turn coil model mentioned in the beginning of the paragraph). The

volumetric field distribution in the two phantoms obtained from the two methods (measurement and FEM simulation) was analyzed for closeness of distribution patterns using scatter plots. Linear regression analysis and correlation coefficient calculation provided a measure of closeness of the relationship between the volumetric induced field profile and magnitude estimated using measurement and numerical simulation.

Main findings and conclusions

(a) Reduction in simulation model complexity and, time and resource requirement

Compared to the realistic coil model, the single turn coil model resulted in substantial reduction of the number of tetrahedral elements used to discretize the problem domain. This simplified the simulation model and brought down the simulation time from several hours (for the realistic coil model) to a matter of a few minutes (for the single turn coil mode).

(b) Simulations and measurements in the large volume

Good agreement was reached between measured and simulated results in the large volume demonstrated by a slope of approximately 1 when simulated volumetric current density distribution was expressed as a function of measured volumetric current density distribution. A high correlation coefficient of 0.97 proves that the relationship is approximately linear and that both simulations and measurements estimate similar values of induced fields. Thus, when both methods are applied to a setup simulating an infinite half plane to estimate the same parameter, the results converge to almost same values.

(c) Simulations and measurements in the small volume

The slope and correlation coefficient values of the volumetric current density distribution function are low, pointing to the fact that the two methods result in different estimations. The validation of induced fields in the small volume was not achieved. This is an aspect that needs to be investigated further because similar phenomena may be observed in realistic head models, which are a subset of small volumes.

(d) Existence of secondary E-fields and currents in our simulations

Our overall evaluation of the existence of secondary current in our simulations and measurements is as follows: (1) there is no direct evidence in our measurements for a secondary current. (2) There is no evidence that the simulation is not wrong. (3) Strictly based on our data, one cannot make full proof conclusion about which method, simulation or measured data, is correct. (4) Based on the fact that electromagnetic induction is a fundamental part of electromagnetism, information from the company that produces CST, indirect information from the literature, and indirect evidence from our data, we hypothesize (but do not prove) that our simulations consider secondary E-fields and secondary currents, whereas our measurements cannot measure them.

7.2 Summary of simulation studies

Accurate estimations of total E-fields are especially needed when TMS is used for clinical applications (Salinas et al., 2009). Most clinical applications of TMS involve conditioning of targeted cortical regions with a train of TMS pulses (referred to as repetitive transcranial magnetic stimulation or simply rTMS). Correct estimate of total induced E-fields will provide better per-pulse dose approximations for such clinical studies. These, in turn, will allow clinicians to monitor patient progress and/or treatment effectiveness over time. Accurate dosage information is also

beneficial when comparing treatments across patient groups (e.g. control vs. impaired) because they are a more reliable measure than, for example, using TMS stimulator output settings which are subject to variability depending upon the stimulator/coil parameters (Salinas et al., 2009). For this reason, TMS conditioning is conducted using a generic measure called resting motor threshold (RMT) and not TMS stimulator intensity, because E-field magnitude required to achieve RMT is a relatively stable measure but the TMS intensity that may be used to achieve the desired E-field to achieve RMT is subject to inter-individual variability associated with difference in the different segments of the human head, for example, difference in scalp thickness and the structure of gyri and sulci. In fact, Julkunen et al. (2012) demonstrated that for TMS applications, the induced field is a more stable measure than percentage of maximum stimulator output intensity. In addition to improving the efficiency of clinical studies, accurate E-field estimates will also contribute to safety protocols associated with TMS studies.

Finite element model simulations can be used to estimate induced E-fields on the cortex in response to a single pulse of TMS delivered by a stimulating coil located in the vicinity of the head. In order to quantify our estimations, we chose to estimate E-fields on the cortex at resting motor threshold (RMT) intensities. RMT is a generic measure that is used to define dosage levels of TMS conditioning. The objective of the study was to estimate the E-field magnitude induced on the motor cortex of humans at RMT intensity and investigate if induction of same magnitude of E-field on an animal's motor cortex would correspond to RMT of the animal. The average stimulator intensity which defines the RMT in humans is 44 % of maximum stimulator output (available from literature). The E-field on the human motor cortex at the mentioned value of stimulator output was estimated. This value of E-field magnitude was sought to be induced on the animal's motor cortex by varying the current amplitude on the stimulating coil. Our hypothesis

was tested using FEM simulations involving TMS for two different situations: (1) comparison of induced E-field magnitude between realistic human head and a realistic animal model and, (2) a spherical human head model and a spherical animal head model. The results obtained for situation (1) were validated by measuring RMT of three animals based on the values obtained from FEM simulations. We observed that simulations estimated RMT of NHPs at 55.4 % MSO whereas in-vivo measurements provided an average RMT value of 51± 5.2 % (Mean ± SD) of MSO. We hypothesize that the accuracy can be improved further by using a more detailed FEM model of the NHP head, using optimized segmentation of the NHP head volume.

Simulations should be performed on individual subject models to determine any kind of abnormal distribution of currents even before a surgery is performed on an animal. With a lead time of just about an hour for the results to appear, it is a worthy investment from the perspective of the quality of data that will be subsequently acquired from the subjects because variables which can induce errors in obtained data, such as coil position, wrong TMS intensity, artifacts on the cortex, etc., can be avoided. Our method could be further improved by incorporating neuronavigation providing input to the simulation software so that the position of the coil in the simulation domain could be accurately matched with the actual physical position of the coil in the experiment. For our current study, commercial software was used to perform finite element analysis but in future, scripted analysis software specific to this purpose could be developed to increase the speed at which solutions are obtained. One set of simulations should be performed for motor threshold determination followed by another set of simulations over the targeted region of cortex for the study. This would help us quantify the effect of TMS based on the field induced in the region of interest. This may aid us in explaining some of the discrepancies that currently exist between different studies.

Main findings and conclusions

(a) Finite element simulation on realistic human head model

Significant differences exist in the estimation of E-field magnitudes at activation thresholds depending on

i. choice of stimulation method (TES, tDCS, TMS, etc.)
ii. choice of TMS stimulator used to perform the estimation (monophasic or biphasic stimulator)
iii. the measure that is used to define activation threshold (cortical activation, peripheral measure of activation in the form of AMT or RMT)

We used a Magstim Rapid biphasic stimulator as our reference stimulator model and used RMT as a measure of activation threshold. Since we present a novel study, we were unable to compare our results with other studies which performed TMS simulations on NHP head models. We could only reference studies which pursue NHP head volume stimulations but differ from our study in either points (i), (ii) or (iii). Any difference in choice of stimulation method, choice of stimulator or definition of activation threshold will result in a different estimate of stimulation intensity required to achieve motor threshold. We, therefore, hypothesize that the difference in our estimated value of E-field at RMT compared to other studies found in the literature was due to a difference in either points number (i), (ii) and/or (iii) between our study and those available in those studies.

(b) Finite element simulation on realistic NHP head model

Verification of motor threshold, based on induced E-field estimates from NHP cortex was satisfactory and provided good basis for future studies. Such studies may include more accurate segments of the NHP head volumes which may result in a better match between simulated and

measured RMT estimates. Future studies could also use simulations on NHP head models to develop more optimized coil sizes (using parametric coil size-to-head ratio) that could create a more focal stimulation than the those elicited by the conventional 70 mm FOE coil, for NHP related TMS experiments.

(c) Simulation on spherical human head model

The simulations on spherical head model, which was used to estimate E-field magnitude (100 V/m) on a spherical human head model, resulted in lower estimates of E-field magnitude compared to a realistic head model (176 V/m).

(d) Comparison between E-field estimates from simulation on realistic human head model and spherical human head model

We hypothesize that the spherical head volume have resulted in lower E-field estimates due to its simplistic definition (not involving gyral and sulcal convolutions) compared to the realistic head model. Gyral and sulcal definitions result in added geometrical inhomogenities in the brain (in addition to inhomogenities resulting from conductivity jumps between different segments of the head volume). Due to the law of conservation of charges, charges (ions or electrons) tend to accumulate in regions of such inhomogenities. Therefore, field estimates at such gyral crowns and sulcal walls may tend to be higher than the corresponding regions on a surface with a smooth profile (as in the case of spherical volumes). The motor cortex lies on such a gyral crown (the pre-central gyrus). Spherical head volumes lack such definitions and have a smoother geometry compared to a realistic brain. This results in a more unified field distribution on their surface compared to a real brain. Therefore, E-field magnitudes at corresponding points on the spherical and realistic brain volumes may be different. The sphere model could be improved further by using

sensor-weighted overlapping sphere method to define the head geometry along with the inclusion of non-linear electrical properties in the medium definition.

7.3 Summary of TMS on NHPs

The previous two studies give us an idea about the spread of the induced current in a medium from one TMS pulse. However, it is also important to investigate what this induced current is capable of doing. More interestingly, how would a train of TMS pulses affect neuronal responses? The induced current profile would be the same for each of the TMS pulses in the train but an additional component is added in terms of periodicity of the pulses. The periodic properties of a train can result in a range neuronal effects over varying durations. In this study we investigated effects of a particular train of TMS pulses, referred to as continuous theta burst (cTBS), on neuronal responses. The effects of cTBS on non-human primate models have not been explored. The effect of cTBS over a relatively large region of interest incorporating a large neuronal populations has also not been investigated. Our goal was to observe the neuronal responses of populations having similar response function over a large region of interest and identify the effect of TMS on their function. Continuous theta burst is a transcranial magnetic stimulation paradigm (three pulses of TMS at 50 Hz repeated in bursts of 200 ms for 40 s duration resulting in a total of 600 pulses) which has been known to reduce cortical excitability in rat and human models. We delivered cTBS conditioning to the primary somatosensory cortex of three NHPs using a 70 mm butterfly coil at 90 % resting motor threshold (RMT) of the NHPs and studied the effect of cTBS on neuronal response to median nerve stimulation of the NHPs. The primary somatosensory cortex was engaged by electrically stimulating the median nerves of the NHPs on the contralateral side. The optimum site

for implantation was chosen by observing responses to electrical stimuli to the contralateral median nerve using a surface EcoG array. A MEA encompassing an observation region of 13 mm^2 was then implanted at the optimum location of the somatosensory cortex to record neuronal responses. Twenty one (21) minutes of spontaneous activity and evoked responses (event related potentials), which together constituted our measure of baseline activity, was recorded before a train of six hundred (600) pulses using cTBS protocol was delivered to the implanted somatosensory cortex (the cTBS conditioning duration was forty (40) s). Following cTBS conditioning, we recorded ninety (90) minutes of post conditioning spontaneous activity and evoked responses.

The relationship between changes in somatosensory evoked potential (SEP) amplitude, firing rate of neuronal populations and oscillatory cortical activity in the form of local field potentials (LFP) activity categorized into six bands ((a) Delta band (1-4 Hz), (b) Theta band (5-8 Hz), (c) Alpha band (8-12 Hz), (d) Beta band (15-30 Hz), (e) Low Gamma band (30-57 Hz) and (f) High Gamma band (63-150 Hz)) was studied. We studied the distribution pattern of SEP amplitudes from the neuronal populations in the recording area using scatter plots and performed linear regression analysis on these distributions to analyze the spatial effect of TMS. Firing rate patterns of neuronal populations for 500 ms on either side of median nerve stimulus were presented. We also studied the relationship between response amplitude and spontaneous LFP activity to postulate how these parameters could be related to each other.

Main findings and conclusions

(a) Effect of cTBS on evoked neuronal response to median nerve stimulation

The effect of cTBS on a population of neurons within a 13 mm^2 area and an average cortical depth of 1 mm is fairly constant. This can be observed from the fact that in all three plots the scatter of

post vs pre- TMS activity cluster is almost linear. This shows that within the region of interest, TMS has suppressed (as seen by the lower slope value of the linear fit compared to the unity reference line) the response activity of all the neurons in the ROI, however, more importantly, it has suppressed them by approximately a constant factor (which is given by the slope of the linear fit). Interestingly, even though the responses were suppressed, all the responses were suppressed by the approximately the same percentage which is reflected in the non-significant change in the response pattern demonstrated by the high correlation between the response patterns before and after TMS.

(b) Duration of the effect of cTBS on evoked neuronal response to median nerve stimulation

cTBS suppressed evoked response amplitude for an average period of 40 minutes (average time taken by the slope curve of all three NHPs to return to 1 after the application of cTBS). cTBS to the primary somatosensory cortex of humans resulted in significant reduction of SEP amplitudes for a range of 13 to 30 minutes following conditioning (Ishikawa et al., 2007; Zapallow et al., 2012).

(c) Effect of cTBS on multi-unit activity

cTBS resulted in an increase in multi-unit activity.

(d) Probable mechanisms

The decreased response amplitude following cTBS, and the observation that the effect of cTBS can be approximated as a linear gain effect are consistent with a model according to which cTBS reduces the capacity of cortical neurons to respnd synchronously to sensory stimuli due to decreased excitability of cortical neurons. This interpretation is consistent with previous findings

of decreased RMT following cTBS (Huang et al., 2005; Ishikawa et al., 2007), since RMT is a peripheral measure of cortical excitability.

7.4 Summary of TMS on felines

In spite of the rapidly growing use of repetitive TMS (rTMS), its biophysical principles remain poorly understood. Our goal was to investigate the effect of TBS (cTBS and iTBS) and 15 Hz rTMS on the spiking activity and LFPs elicited in response to visual stimuli in the cat visual cortex (Brodmann area 18).

Electrophysiological recordings were obtained from the visual cortex (area 18) of cats. The animals were stimulated binocularly, using 50 %-contrast sinusoidal-wave gratings, repeated in cycles of 34 s. Neurophysiological recordings were pursued using an ICS 96 MEA (BlackRock). The area for implantation was selected based on optimum response to visual stimulus using orientation maps acquired through optical imaging. The delivery of the magnetic field pulses was achieved through a regular 70 mm butterfly coil. Three different TMS paradigms were used in this study, a 15 Hz rTMS paradigm (one single train of 15 Hz rTMS pulses for 40 s amounting to a total of 600 pulses) and two theta burst (three pulses of TMS at 50 Hz repeated in bursts of 200 ms) paradigms (Huang et al., 2005); continuous theta burst or cTBS (a single train of TBS for 40 s amounting to 600 pulses) and intermittent theta burst or iTBS (2 s train of TBS repeated every 10 s for 190 s amounting to 600 pulses). All TMS paradigms were delivered at 55 % MSO, which according to our FEM simulations performed in Chapter 4 translates to 100 % RMT. The neurophysiology electrodes were positioned within cortex, such that they were ¾ of the way towards the point below the “sweet spot” of the TMS coil. TMS was delivered after 8.5 minutes

of baseline recording. Data were obtained for cTBS, iTBS and 15 Hz rTMS. In all, 12 resultant hemispheres have been used to obtain 12 datasets for each TMS paradigm. Off the 12 datasets, 4 datasets have been rejected due to unstable baseline activity (which makes it difficult to quantify the effect of TMS) or plausible seizure induction (one dataset). Thus, datasets from 8 hemispheres were used to derive conclusions for our work.

We studied the average firing rates and band limited magnitude of gamma activity (low gBLM (30-57 Hz) and high gBLM (63-150 Hz)). We performed regression analysis and orientation tuning curve analysis; both based on spiking activity of neuronal populations. Effect of TMS on the function of orientation selectivity was also investigated along with changes in tuning curve characterizes.

Main findings and conclusions

(a) 15 Hz and cTBS rTMS suppressed evoked spiking activity response

cTBS and 15 Hz rTMS suppressed evoked spiking activity response to oriented grating stimuli, whereas intermittent theta burst enhanced this response. 15 Hz rTMS had no effect on motor evoked potentials (MEPs) in humans (Huang et al., 2005). In our study, we observed a suppression of evoked spiking activity response in the feline visual cortex. These results show that the same TMS paradigm can have different effects on different cortical areas.

(b) TMS does not affect the spatial pattern of responses

Consistent with the gain effect model elicited from neuronal behaviour in the NHP somatosenry cortex, neurons that were more responsive before the application of TMS were affected more than neurons that were less responsive before the application of TMS. In spite of these changes, the response pattern of the region of interest, and the orientation tuning of the multi-unit activity

remained unaffected. Our findings demonstrate that even in neuronal populations with diverse and selective functional characteristics, TMS does not modify the functional selectivities of ensembles of neurons; rather, it has a linear gain effect on their responses.

Tuning curve analysis revealed that suppression following any TMS was higher in response to preferred- than to non-preferred orientation, in agreement with a more general observation on the effect of TMS: a linear gain effect with gain changing with time and pattern of activity remains approximately unchanged. The mechanisms may involve increased GABAergic tone over the entire stimulated region.

7.5 Directions for future work

Suggestions for future work pertaining to simulations and experimental studies are summarized as follows:

7.5.1. Suggestions for future simulation related work

The best way to address questions about the effect of TMS and variability associated with experiments would be to have a watertight experiment procedure involving neuro-navigation (to correctly localize the position of the TMS coil), a simulation (resulting in a visual presentation of the spread of the TMS induced current profile based on the relative position suggested by the neuro-navigation setup) followed by an actual measurement of the neuronal responses to TMS. Neuronal responses could be studied for different orientations and positions of the coil. The role of the “sweet spot” or the most effective spot for neural activation (MESNA) on neuronal responses can be investigated further.

Neural models could be included in the 3D simulation models to trace the propagation of current between two hemispheres intra cortically, rather than just over the csf-gray matter interface. This could shed light on the role of the corpus callosum and neural bundles in the redistribution of the induced current.

This way, changes in the neuronal activity can be traced back to the source, which in our case are the induced currents. This will help build up a database which can contain information about how a variation in the actual delivery of TMS to the cortex can result in a variation in the neuronal effects. We see that there are limitations to frequency domain simulations and we demonstrated some of these aspects in this dissertation, most importantly the inability to separate out primary and secondary induced currents. However, frequency domain simulations are a good conservative estimate of induced fields (since they take both primary and secondary currents into consideration) and provide a good baseline value of induced currents. Such simulations, which can be fast and accurate, should be implemented in all major experiments and medical procedures involving TMS. The most prominent gain of these simulations will be observed in subjects who may have infarcts on the cortex due to stroke or injury. Such patients are more susceptible to effects of TMS due to the inhomogenities brought about by these infarcts which tend to have a strong influence on the distribution of the induced fields. In the long run, for all other cases, simulations with experiments will help to build up a database of cause and effect(s) which will in turn make it possible to eliminate variability in results. An additional leap in the form of time-domain solvers will push this method to near perfection because experimental data (which is obtained in time domain) can be directly correlated with time domain solver data. Our current simulation software cannot address the time domain solution well due to constraints in the software itself. A different low

frequency time domain solver (e.g. COMSOL Multiphysics or ANSYS) may be more suited for the time domain analysis.

A simple example of how simulation studies can be beneficial is as follows:

With regard to invasive studies in animals

The subject animal could be scanned with an MRI prior to the experiment. Automated segmentation tools/codes may be used to segment the head volume and create 3D head models from the acquired MRI images. With the right tools/codes, this process would take just a few hours at the maximum. Coil positioning required to induce maximum field strength at a target area is an important parameter that governs neuronal activation. This could be optimized before the experiment using numerical analysis and provides a tool to make the induction reproducible.

Experiments also tend to have certain variability associated with them, for example due to variability in physiological state of the animal. Each anomaly tends to alter the geometrical configuration of the target area. A simple simulation at this stage could provide us information about how the field distribution would alter because of inhomogeneity caused by the anomaly. The reason behind this is the ease of altering the 3D models to match the current situation. An inhomogeneity could result in alteration of the induced fields resulting in an alteration in the neuronal responses. If the field alteration could be identified, the observation could be used during neuronal data analysis.

With regard to non-invasive human studies

It is important to understand that effects of TMS are due to the fields induced on the target area due to TMS. Some of the important factors that influence the effect of TMS are the stimulation

intensity, coil position, coil geometry and subject-specific structure of gyri and sulci. The reason behind this is that the induced field profile and magnitude is a function of these factors. If we consider the hypothetical case study involving healthy subjects, let us assume that the same coil (assuming a 70 mm butterfly coil), stimulation intensity (90% of resting motor threshold) and coil position is used to condition the same target area on the cortex of each subject. This is what is followed in most TMS studies. However, we have discussed in this dissertation how additional factors can result in variability in results. For example, the individual structure of gyri and sulci where the target region and neighboring regions can explain a substantial part of the variability. In addition, the presence or absence of hair, presence of a hematoma on the scalp at the target area, scalp thickness, etc., can have an influence on the results. These are inter-individual factors that can result in inter-individual variability because they are additional components of inhomogeneity on the head volume. Any additional inhomogeneity in any of the five major segments (scalp, skull, CSF, gray matter or white matter) results in an alteration of induced field magnitude and/or profile at the target area. Currently, it is not possible to measure the induced fields on healthy human subjects. However, these fields can be estimated for each subject using numerical analysis tools, which could be modeled to include the additional inhomogeneity. Similar to our study, FEA could be used and the coil position/intensity could then be varied on the simulation models to reproduce the same magnitude and profile of induced field on every subject under study. This could help quantify the effects of TMS better because the underlying cause (induced E-field) of the effects will be identical in all subjects. This could contribute to the reduction of inter-individual variability in TMS results.

7.5.2. Suggestions for future experimental work

The above mentioned simulations using time domain solvers can be further validated experimentally by recording induced fields from the cortices of NHPs. Although frequency domain solutions are sufficient for fast analysis of the induced fields, the trust quotient in simulations can be further improved by estimating the induced E-fields using time domain analysis or by using a frequency sweep in frequency domain analysis. This can be compared with fields measured using electrode recordings from NHP cortices.

The effect and mechanisms of action of a TMS pulse can be studied by varying the timing of the TMS pulses with respect to an externally applied stimulus. A small (one second) window can be defined around the external stimulus trigger, with the trigger in the center of the window temporally, and the TMS pulse delivered at different times within the window. This can provide information about how the evoked response changes when TMS alters the baseline spontaneous activity (which would occur when the TMS pulse would precede the external stimulus) and what happens to the evoked response when TMS is applied during the initialization of the evoked response (which would occur when the TMS pulse would follow the external stimulus).

For invasive studies with different TMS conditioning protocols, single electrode recordings in conjunction with immuno-histochemistry can be used to identify the sources of inhibition or facilitation for a given TMS protocol. Single electrode recordings are more beneficial for clustering and spike sorting owing to their higher impedances compared to MEAs which have lower impedance resulting from larger recording surface areas. Immunohistochemistry will be able to further quantify the neuronal cells responsible for producing the effects of TMS.

TMS pulse intensities can have a profound effect on the neuronal behavior. This has been brought to attention by Pascual-Leone (2002) where sub- and supra-threshold intensities of the same TMS

protocol show different effects. This aspect needs to be explored for cTBS TMS protocol and can be achieved by varying the intensity of the cTBS conditioning from 60-120 % RMT.

For TMS conditioning, the size of the coil relative to the subjects' head plays a vital role in defining the effects of TMS conditioning. The optimum size of the coil can be determined analytically using simulations and the results can be validated experimentally by performing analyses on neuronal recordings by using the amplitude and duration of suppression/facilitation of evoked responses as the defining parameter.

In continuation with feline experiments, it would be interesting to identify the behavioral effect of TMS on visual perception. In order to achieve this, the contrast of the gratings used in feline experiments can be varied as a function of the slope obtained from our work, without incorporating TMS conditioning. The baseline values of the contrast could be chosen to be the same as the one used in our work. The neuronal responses due to a variation in contrast can be then compared to the neuronal responses obtained with experiments involving TMS (similar to one presented in this thesis) to characterize what is it that the feline subjects actually see when their cortex is conditioned by a given TMS protocol. We hypothesize before and after cTBS perception of gratings to be similar to what has been shown in Figure 7-1

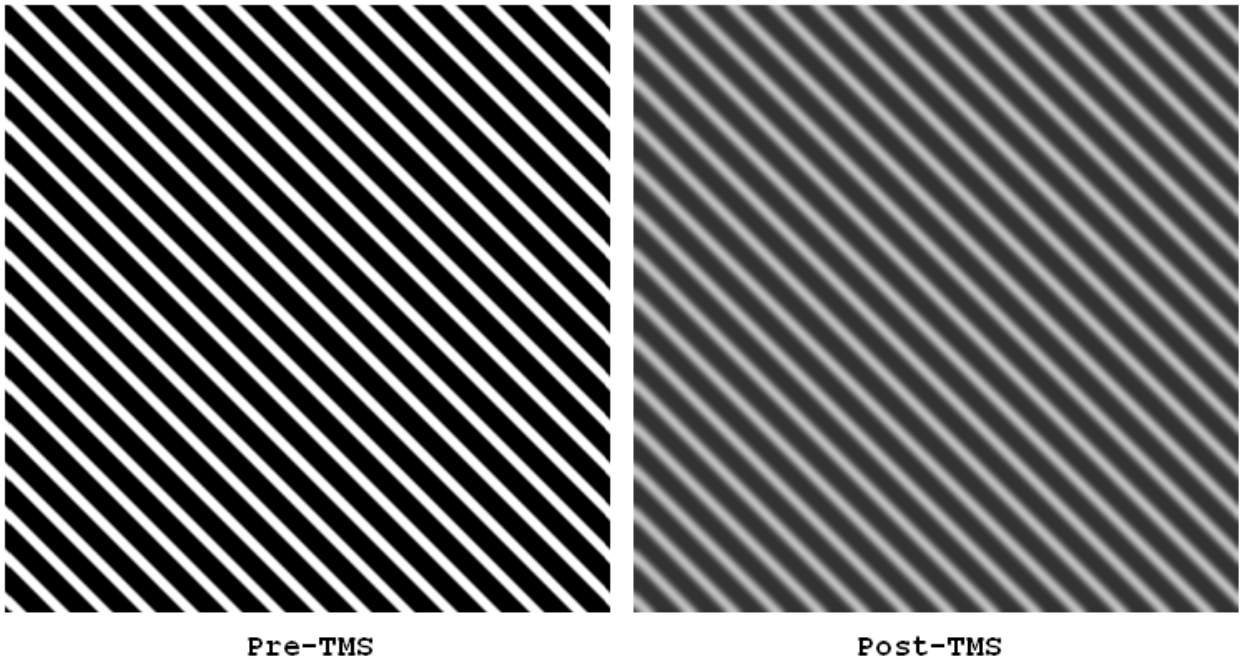

Figure 7-1. Hypothesized visual perception of gratings, before and after cTBS conditioning.

Layer specific effect of TMS is an area that needs to be explored further. Current source density analysis of event related potentials can shed light on how the generator components (N_1, P_1, etc.) of an evoked potential are affected by TMS. A laminar electrode array can be used in conjunction with a customized coil. The customized coil can house a hole in the center through which the laminar probe can be passed to be inserted in the cortex. This way, it would be possible to record cortical activity before and after the delivery of TMS. A sample LFP evoked response to visual stimulus, in the absence of any TMS conditioning, obtained from a feline experiment has been presented in Figure 7-2. The different components of an evoked potential, based on existing literature, have been marked. It is common knowledge that current induced by TMS tends to accumulate at intersection boundaries between two different media. It would be interesting to see if this current source density plot would change in accordance with the above theory. If it is true,

then it would be interesting to note, which generator component is strengthened and which component is weakened due to the ionic redistribution caused by TMS.

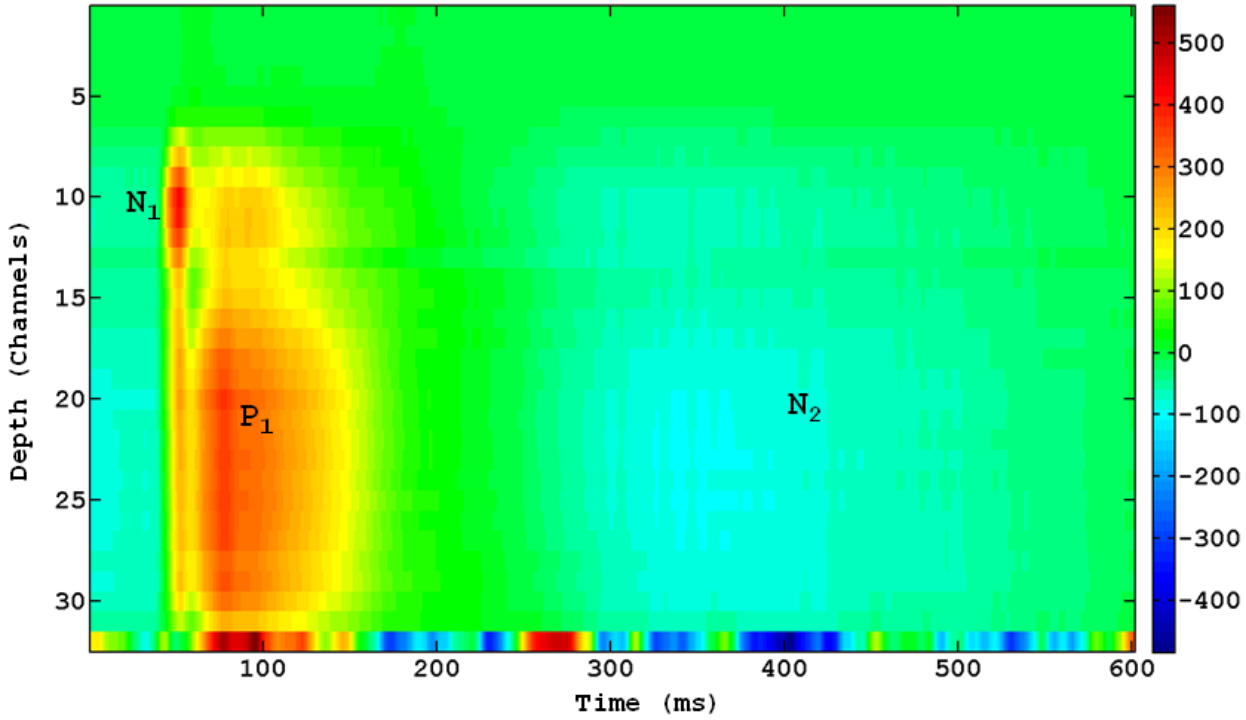

Figure 7-2. Local field potential of visual stimulus related evoked potential obtained from a feline experiment.

7.5.3. Potential application in cognitive and therapeutic studies

The effect of TMS on brain function and cognition is an area of enhanced interest. Shang et al. (2016) demonstrated that 5 Hz rTMS significantly increased the expressions of brain-derived neurotrophic factor (BDNF), presynaptic protein synaptophysin (SYP) and postsynaptic protein (NR2B). This led to the conclusion that 5 Hz rTMS significantly enhanced the synaptic plasticity and spatial cognition in normal animals. Galletly Cherrie et al. (2016) demonstrated that rTMS

could be used as efficient and safe treatment option for patients suffering from major depressive disorder (MDD). They used a combination of 10 Hz and 1 Hz rTMS to condition the right and left dorsolateral prefrontal cortex (DLPFC). Hamilton Depression Rating Scale was used to as marker for the effect of rTMS. It was reported that rTMS improved cognitive function and was associated with a decrease in depressive symptoms. A recent review by Tatti et al. (2016) investigated the feasibility of non-invasive brain stimulation (NiBS) as an effective interventional approach to hinder cognitive decline in healthy aging individuals. Tatti et al. (2016) concluded that, based on the available experimental data, NiBS can be easily coupled to cognitive trainings to bolster positive effects and could be a feasible and safe tool to partly counteract physiological age-related decline of cognitive functions. However, it was also mentioned that variability and volatility of the induced neuro-enhancement effects are a persisting challenge that can be addressed using a multidisciplinary approach to the study of NiBS.

Our proposed subject-specific simulation can potentially reduce this variability, by using subject-specific MRI data to predict the current density elicited by applying magnetic field of various amplitude. The approach we propose is to fix the current density elicited in the region of interest, by subject specific pre-experiment simulation, which will conclude the subject-specific TMS power required to elicit the same current density in the region of interest across all subjects.

TMS has also gained popularity in the therapeutic effects in the recovery and rehabilitation from stroke (Ernst, 1990; Khedr et al., 2009; Koski et al., 2004; Maulden et al., 2005; Mayo et al., 1999; Nakayama H, 1994 Apr; Takeuchi et al., 2005), depression (Fitzgerald et al., 2003; John et al., 2007; George et al., 1995; Mosimann et al., 2002; Pascual-Leone et al., 1996) and other psychiatric and neurological disorders. However, a meta-analysis of numerous studies performed by Martin

et al. (2016) demonstrated that rTMS conditioning does not result in robust cognitive enhancement. The studies were conducted on patients subjected to rTMS conditioning administered to the dorsolateral prefrontal cortex (DLPFC). The effect of rTMS on cognitive functions such as Global cognitive function, executive function, attention, working memory, processing speed, visual memory, verbal memory and visuospatial ability were analyzed. In fact, the effect of TMS protocols and duration of these effects on neuronal behavior is still elusive.

As mentioned in this dissertation, we hypothesize that the reason behind this persistent elusiveness lies in the fact that to this date, no conclusions on how TMS affects the neurons exist. The reason behind this is the proclivity to perform TMS sessions and analyze the effects on neuronal behavior later. This is what we could refer to as action-and-effect mode of investigation which resembles a Brute force method of investigation. With novel TMS conditioning protocols being developed, it could become more challenging to quantify the effect of every single TMS conditioning protocol using an investigation method being followed today. A more reasonable approach would be to identify the induced field-neural network relationship based on the study of a few TMS conditioning protocols and identify/establish the basic mechanistic functional equation of this relationship.

Current literature allows us a good starting point for such an investigative study. For example, we have acquired the knowledge that TMS affects GABAergic interneurons (Stagg et al., 2009) which results in long term depression (LTD) like effects (Suppa et al., 2016). An interesting question would be about investigating the specificity of the effect of cTBS on different classes of interneuron. Each class of interneuron influences the neurons that it targets, resulting in the modulation of transfer of the neurotransmitter associated with its synapses. This is a very complex

relationship that needs to be investigated and understood in order to steer from action-and-effect mode to cause-and-effect mode with regard to TMS studies. This can be achieved by

(a) Developing robust simulation models by including neural models in head geometries. This would allow us to investigate how the induced fields affect different types of neurons and interneurons, when the neurons and interneurons have their own associated activation functions.

(b) Performing in vivo studies followed by immunohistochemistry to identify how the neurons plausibly affected by cTBS (in simulations) resulted in neurotransmitter modulations, which caused modulations of their associated protein expressions.

Additional studies involving iTBS, 15 Hz, and other rTMS protocols can be conducted to obtain a robust relationship between periodicity of the TMS protocols, the fields induced by them and, their corresponding effect on different classes of neuronal entities. Understanding the relationship between the TMS induced fields and a neurotransmitter modulation is the key to quantify the effects of TMS. To this end, “Neural correlates of TMS” is a topic worth investing effort in.

7.6 Concluding remarks

Finally, in closing, transcranial magnetic stimulation is an exciting non-invasive technique that has the potential to not just alleviate but potentially treat neurological and psychiatric disorders, provided the duration of effects of TMS can be prolonged. Future work with regard to achieving plasticity may be able to extend the effect of TMS for longer durations than is currently achievable. In order to achieve this though, a strong grasp of the fundamentals of how TMS works is essential.

A lot of work is still pending with regard to this aspect which is what makes TMS a very interesting field of study filled with innumerable possibilities.

7.7 List of publications

Conference abstracts

- **Venkateswaran A.,** Yao Z.S., Reed S., Neupane S., Kropf P., Villeneuve M. Y., Shmuel A. The effect of continuous theta-burst rTMS on locally measured cortical response to visual stimuli. (2012). Society for Neuroscience, New Orleans, USA.
- Neupane S., **Venkateswaran A.**, Yao Z.S., Kropf P., Villeneuve M.Y., Shmuel A. The effect of high-frequency (20 Hz) rTMS on locally measured cortical response to visual stimuli. (2012). Society for Neuroscience, New Orleans, USA.
- **Venkateswaran A.**, Thomas S.T., Neupane S, Villeneuve M.Y, Shmuel A. The effect of Theta-burst (TBS) rTMS on locally measured cortical response to somatosensory stimuli. (2011). Society for Neuroscience, Washington, USA.
- Thomas S.T., **Venkateswaran A.**, Neupane S, Shmuel A. The effects of Theta-burst (TBS) rTMS on locally measured cortical response to somatosensory stimuli. (2011). Organization for Human Brain Mapping, Quebec City, Canada.

Conference papers

- Sabouni, A., **Venkateswaran, A.**, Shmuel, A., Pouliot, P., & Lesage, F. (2013, 7-13 July 2013). An automated technique to determine the induced current in transcranial magnetic stimulation. Paper presented at the Antennas and Propagation Society International Symposium (APSURSI), 2013 IEEE.
- Lankarany, M., **Venkateswaran, A.**, Wei Ping, Z., Swamy, M. N. S., & Shmuel, A. (2012, 25-30 March 2012). TMS artifact removal from neurophysiological recordings using a novel iterative adaptive filtering. Paper presented at the Acoustics, Speech and Signal Processing (ICASSP), 2012 IEEE International Conference on.

Journal paper manuscripts (To be sent for publication)

- **Venkateswaran A.,** Mohanty N., Baig M.A., Lesage F., Shmuel A. Validating and calibrating a simulated finite element model of transcranial magnetic stimulation (TMS): simulation based estimation of resting motor threshold in non-human primates and cats. **(**Chapter 3 and Chapter 4 merged together)
- **Venkateswaran A.**, Thomas S., Baig M.A., Kropf P., Shmuel A. Effects of continuous theta burst transcranial magnetic stimulation on neuronal processing in the primate's somatosensory cortex. (Chapter 5)
- **Venkateswaran A.**, Neupane S., Yao Z.S., Villeneuve M. Y., Shmuel A. The effect of theta-burst and 15 Hz rTMS on locally measured cortical response to oriented grating visual stimuli. (Chapter 6)
- Ghatas M.P., **Venkateswaran A.**, Shmuel A. Ferrite attachment for optimization of induced electric field from TMS coils.

References

1989. Electrical conductivity of acqueous solutions. In: Weast R C (Ed.), CRC Handbook of Chemistry and Physics. CRC Press, Boca Raton, FL.

1990. The Magstim Company Ltd Whitland, Dyfed, UK.

n.d. Growth characteristics, survival and brain volumetric changes in WNIN/Ob obese rats [pdf]. Retrieved from http://shodhganga.inflibnet.ac.in/bitstream/10603/44330/7/07_chapter_2.pdf.

Abdeen, M.A., Stuchly, M.A., 1994. Modeling of magnetic field stimulation of bent neurons. Biomedical Engineering, IEEE Transactions on 41, 1092-1095.

Adeloye, A., Kattan, K.R., Silverman, F.N., 1975. Thickness of the normal skull in the American blacks and whites. American Journal of Physical Anthropology 43, 23-30.

Allen, E.A., Pasley, B.N., Duong, T., Freeman, R.D., 2007. Transcranial magnetic stimulation elicits coupled neural and hemodynamic consequences. Science 317, 1918-1921.

Awad, B.I., Carmody, M.A., Zhang, X., Lin, V.W., Steinmetz, M.P., 2013. Transcranial Magnetic Stimulation After Spinal Cord Injury. World Neurosurgery.

Awada, K.A., Jackson, D.R., Baumann, S.B., Williams, J.T., Wilton, D.R., Fink, P.W., Prasky, B.R., 1998. Effect of conductivity uncertainties and modeling errors on EEG source localization using a 2-D model. Biomedical Engineering, IEEE Transactions on 45, 1135-1145.

Aydin-Abidin, S., Moliadze, V., Eysel, U.T., Funke, K., 2006. Effects of repetitive TMS on visually evoked potentials and EEG in the anaesthetized cat: dependence on stimulus frequency and train duration. J Physiol 574, 443-455.

Aydin-Abidin, S., Trippe, J., Funke, K., Eysel, U.T., Benali, A., 2008. High- and low-frequency repetitive transcranial magnetic stimulation differentially activates c-Fos and zif268 protein expression in the rat brain. Exp Brain Res 188, 249-261.

Baker, S.N., Olivier, E., Lemon, R.N., 1995. Task-related variation in corticospinal output evoked by transcranial magnetic stimulation in the macaque monkey. The Journal of Physiology 488, 795-801.

Barker, A.T., Freeston, I.L., Jalinous, R., Jarratt, J.A., 1985a. Non-invasive stimulation of motor pathways within the brain using time-varying magnetic fields. Electroencephalography and Clinical Neurophysiology 61, S245-S246.

Barker, A.T., Jalinous, R., Freeston, I.L., 1985b. Non-invasive magnetic stimulation of human motor cortex. Lancet 1, 1106-1107.

Barnikol, U.B., Amunts, K., Dammers, J., Mohlberg, H., Fieseler, T., Malikovic, A., Zilles, K., Niedeggen, M., Tass, P.A., 2006. Pattern reversal visual evoked responses of V1/V2 and V5/MT as revealed by MEG combined with probabilistic cytoarchitectonic maps. NeuroImage 31, 86-108.

Başar, E., 1972. A study of the time and frequency characteristics of the potentials evoked in the acoustical cortex. Kybernetik 10, 61-64.

Başar, E., 1980. EEG-brain dynamics: relation between EEG and brain evoked potentials. Elsevier-North-Holland Biomedical Press.

Bashir, S., Perez, J., Horvath, J.C., Pascual-Leone, A., 2013. Differentiation of motor cortical representation of hand muscles by navigated mapping of optimal TMS current directions in healthy subjects. Journal of clinical neurophysiology : official publication of the American Electroencephalographic Society 30, 390-395.

Basso, C., 2012. Designing Control Loops for Linear and Switching Power Supplies: A Tutorial Guide. Artech House.

Benali, A., Trippe, J., Weiler, E., Mix, A., Petrasch-Parwez, E., Girzalsky, W., Eysel, U.T., Erdmann, R., Funke, K., 2011. Theta-Burst Transcranial Magnetic Stimulation Alters Cortical Inhibition. The Journal of Neuroscience 31, 1193-1203.

Benninger, D.H., Iseki, K., Kranick, S., Luckenbaugh, D.A., Houdayer, E., Hallett, M., 2012. Controlled Study of 50-Hz Repetitive Transcranial Magnetic Stimulation for the Treatment of Parkinson Disease. Neurorehabilitation and Neural Repair 26, 1096-1105.

Berardelli, A., Inghilleri, M., Rothwell, J.C., Romeo, S., Currà, A., Gilio, F., Modugno, N., Manfredi, M., 1998. Facilitation of muscle evoked responses after repetitive cortical stimulation in man. Experimental Brain Research 122, 79-84.

Berger, U., Korngreen, A., Bar-Gad, I., Friedman, A., Wolfus, S., Yeshurun, Y., Lavidor, M., 2011. Magnetic stimulation intensity modulates motor inhibition. Neuroscience Letters 504, 93-97.

Berlim, M.T., Van den Eynde, F., Daskalakis, Z.J., 2012. A systematic review and meta-analysis on the efficacy and acceptability of bilateral repetitive transcranial magnetic stimulation (rTMS) for treating major depression. Psychological Medicine FirstView, 1-10.

Berlim, M.T., Van den Eynde, F., Daskalakis, Z.J., 2013. Efficacy and acceptability of high frequency repetitive transcranial magnetic stimulation (rTMS) versus electroconvulsive therapy (ECT) for major depression: A systematic review and meta-analysis of randomized trials. Depression and Anxiety, n/a-n/a.

Bindman, L.J., Lippold, O., Redfearn, J., 1964. The action of brief polarizing currents on the cerebral cortex of the rat (1) during current flow and (2) in the production of long-lasting after-effects. The Journal of Physiology 172, 369-382.

Blankenburg, F., Ruff, C.C., Bestmann, S., Bjoertomt, O., Eshel, N., Josephs, O., Weiskopf, N., Driver, J., 2008. Interhemispheric effect of parietal TMS on somatosensory response confirmed directly with concurrent TMS–fMRI. The Journal of Neuroscience 28, 13202-13208.

Bolognini, N., Ro, T., 2010. Transcranial magnetic stimulation: disrupting neural activity to alter and assess brain function. The Journal of Neuroscience 30, 9647-9650.

Brainard, D.H., 1997. The Psychophysics Toolbox. Spatial Vision 10, 433-436.

Brückner, S., Kiefer, M., Kammer, T., 2013. Comparing the after-effects of continuous theta burst stimulation and conventional 1Hz rTMS on semantic processing. Neuroscience 233, 64-71.

Casula, E.P., Tarantino, V., Basso, D., Arcara, G., Marino, G., Toffolo, G.M., Rothwell, J.C., Bisiacchi, P.S., 2014. Low-frequency rTMS inhibitory effects in the primary motor cortex: Insights from TMS-evoked potentials. NeuroImage 98, 225-232.

Cauller, L.J., Kulics, A.T., 1991. The neural basis of the behaviorally relevant N1 component of the somatosensory-evoked potential in SI cortex of awake monkeys: evidence that backward cortical projections signal conscious touch sensation. Experimental Brain Research 84, 607-619.

Chakravarty, M.M., Steadman, P., van Eede, M.C., Calcott, R.D., Gu, V., Shaw, P., Raznahan, A., Collins, D.L., Lerch, J.P., 2013. Performing label-fusion-based segmentation using multiple automatically generated templates. Human Brain Mapping 34, 2635-2654.

Chen, M., Mogul, D.J., 2009. A structurally detailed finite element human head model for simulation of transcranial magnetic stimulation. Journal of Neuroscience Methods 179, 111-120.

Chunye, R., Tarjan, P.P., Popovic, D.B., 1995. A novel electric design for electromagnetic stimulation-the Slinky coil. Biomedical Engineering, IEEE Transactions on 42, 918-925.

Cohen, D., Cuffin, B.N., 1991. Developing a more focal magnetic stimulator. Part I: Some basic principles. J Clin Neurophysiol 8, 102-111.

Cohen, L.G., Roth, B.J., Nilsson, J., Dang, N., Panizza, M., Bandinelli, S., Friauf, W., Hallett, M., 1990. Effects of coil design on delivery of focal magnetic stimulation. Technical considerations. Electroencephalography and Clinical Neurophysiology 75, 350-357.

Collins, D.L., Evans, A.C., 1997. Animal: Validation and Applications of Nonlinear Registration-Based Segmentation. International Journal of Pattern Recognition and Artificial Intelligence 11, 1271-1294.

Collins, D.L., Holmes, C.J., Peters, T.M., Evans, A.C., 1995. Automatic 3-D model-based neuroanatomical segmentation. Human Brain Mapping 3, 190-208.

Cooke, S.F., Bliss, T.V., 2006. Plasticity in the human central nervous system. Brain 129, 1659-1673.

Coupé, P., Manjón, J.V., Fonov, V., Pruessner, J., Robles, M., Collins, D.L., 2011. Patch-based segmentation using expert priors: Application to hippocampus and ventricle segmentation. NeuroImage 54, 940-954.

Dancause, N., Barbay, S., Frost, S.B., Zoubina, E.V., Plautz, E.J., Mahnken, J.D., Nudo, R.J., 2006. Effects of Small Ischemic Lesions in the Primary Motor Cortex on Neurophysiological Organization in Ventral Premotor Cortex. Journal of Neurophysiology 96, 3506-3511.

Day, P., 1999. The philosopher's tree: a selection of Michael Faraday's writings. CRC Press.

De Gennaro, L., Fratello, F., Marzano, C., Moroni, F., Curcio, G., Tempesta, D., Pellicciari, M.C., Pirulli, C., Ferrara, M., Rossini, P.M., 2008. Cortical plasticity induced by transcranial magnetic stimulation during wakefulness affects electroencephalogram activity during sleep. PloS one 3, e2483.

de Labra, C., Rivadulla, C., Grieve, K., Mariño, J., Espinosa, N., Cudeiro, J., 2007. Changes in Visual Responses in the Feline dLGN: Selective Thalamic Suppression Induced by Transcranial Magnetic Stimulation of V1. Cerebral Cortex 17, 1376-1385.

De Ridder, D., van der Loo, E., Van der Kelen, K., Menovsky, T., van de Heyning, P., Moller, A., 2007. Theta, alpha and beta burst transcranial magnetic stimulation: brain modulation in tinnitus. International journal of medical sciences 4, 237-241.

Deng, Z.-D., Lisanby, S.H., Peterchev, A.V., 2013. Electric field depth–focality tradeoff in transcranial magnetic stimulation: Simulation comparison of 50 coil designs. Brain Stimulation 6, 1-13.

Di Lazzaro, V., Pilato, F., Dileone, M., Profice, P., Oliviero, A., Mazzone, P., Insola, A., Ranieri, F., Meglio, M., Tonali, P.A., Rothwell, J.C., 2008. The physiological basis of the effects of intermittent theta burst stimulation of the human motor cortex. The Journal of Physiology 586, 3871-3879.

Dong-Hun, K., Georghiou, G.E., Won, C., 2006. Improved field localization in transcranial magnetic stimulation of the brain with the utilization of a conductive shield plate in the stimulator. Biomedical Engineering, IEEE Transactions on 53, 720-725.

Durand, D., Ferguson, A.S., Dalbasti, T., 1992. Effect of surface boundary on neuronal magnetic stimulation. Biomedical Engineering, IEEE Transactions on 39, 58-64.

Epstein, C.M., Davey, K.R., 2002. Iron-Core Coils for Transcranial Magnetic Stimulation. Journal of Clinical Neurophysiology 19, 376-381.

Epstein, C.M., Schwartzberg, D.G., Davey, K.R., Sudderth, M., David B., 1990. Localizing the site of magnetic brain stimulation in humans. Neurology 40, 666.

Ernst, E., 1990. A review of stroke rehabilitation and physiotherapy. Stroke 21, 1081-1085.

Eshel, N., Ruff, C.C., Spitzer, B., Blankenburg, F., Driver, J., 2010. Effects of parietal TMS on somatosensory judgments challenge interhemispheric rivalry accounts. Neuropsychologia 48, 3470 - 3481.

Eskildsen, S.F., Coupé, P., Fonov, V., Manjón, J.V., Leung, K.K., Guizard, N., Wassef, S.N., Østergaard, L.R., Collins, D.L., 2012. BEaST: Brain extraction based on nonlocal segmentation technique. NeuroImage 59, 2362-2373.

Espinosa, N., de Labra, C., Rivadulla, C., Mariño, J., Grieve, K.L., Cudeiro, J., 2007. Effects on EEG of Low (1Hz) and High (15Hz) Frequency Repetitive Transcranial Magnetic Stimulation of the Visual Cortex: A Study in the Anesthetized Cat. The Open Neuroscience Journal 1, 20-25.

Espinosa, N., Mariño, J., de Labra, C., Cudeiro, J., 2011. Cortical Modulation of the Transient Visual Response at Thalamic Level: A TMS Study. PloS one 6, 1-11.

Filipović, S.R., Rothwell, J.C., Bhatia, K., 2010. Slow (1Hz) Repetitive Transcranial Magnetic Stimulation (rTMS) Induces Sustained Change in Cortical Excitability in Patients with Parkinson's Disease. Clinical neurophysiology : official journal of the International Federation of Clinical Neurophysiology 121, 1129-1137.

Fitzgerald, P.B., Brown, T.L., Marston, N.A.U., Daskalakis, Z.J., de Castella, A., Kulkarni, J., 2003. Transcranial Magnetic Stimulation in the Treatment of Depression: A Double-blind, Placebo-Controlled Trial. Arch Gen Psychiatry 60, 1002-1008.

Fitzgerald, P.B., Fountain, S., Daskalakis, Z.J., 2006. A comprehensive review of the effects of rTMS on motor cortical excitability and inhibition. Clin Neurophysiol 117, 2584-2596.

Ganis, G., Keenan, J.P., Kosslyn, S.M., Pascual-Leone, A., 2000. Transcranial Magnetic Stimulation of Primary Motor Cortex Affects Mental Rotation. Cerebral Cortex 10, 175-180.

Garry, M.I., Thomson, R.H.S., 2009. The effect of test TMS intensity on short-interval intracortical inhibition in different excitability states. Experimental Brain Research 193, 267-274.

Galletly Cherrie, C., Gill, S., Rigby, A., Carnell, B.L., Clarke, P., 2016. Assessing the Effects of Repetitive Transcranial Magnetic Stimulation on Cognition in Major Depressive Disorder Using Computerized Cognitive Testing. Journal of ECT 32, 169-173

Gershon, 2003. Transcranial Magnetic Stimulation in the Treatment of Depression. American Journal of Psychiatry 160, 835-845.

Gersner, R., Kravetz, E., Feil, J., Pell, G., Zangen, A., 2011. Long-Term Effects of Repetitive Transcranial Magnetic Stimulation on Markers for Neuroplasticity: Differential Outcomes in Anesthetized and Awake Animals. The Journal of Neuroscience 31, 7521-7526.

Gilio, F., Rizzo, V., Siebner, H.R., Rothwell, J.C., 2003. Effects on the right motor hand-area excitability produced by low-frequency rTMS over human contralateral homologous cortex. The Journal of Physiology 551, 563-573.

Grinvald, A., Lieke, E., Frostig, R.D., Gilbert, C.D., Wiesel, T.N., 1986. Functional architecture of cortex revealed by optical imaging of intrinsic signals. Nature 324, 361-364.

Gu, C., Corneil, B.D., 2014. Transcranial magnetic stimulation of the prefrontal cortex in awake nonhuman primates evokes a polysynaptic neck muscle response that reflects oculomotor activity at the time of stimulation. The Journal of Neuroscience 34, 14803-14815.

Guizhi, X., Yong, C., Shuo, Y., Mingshi, W., Weili, Y., 2005. The Optimal Design of Magnetic Coil in Transcranial Magnetic Stimulation. Engineering in Medicine and Biology Society, 2005. IEEE-EMBS 2005. 27th Annual International Conference of the, pp. 6221-6224.

Hamalainen, M.S., Sarvas, J., 1989. Realistic conductivity geometry model of the human head for interpretation of neuromagnetic data. IEEE Transactions on Biomedical Engineering 36, 165-171.

Han, B.H., Chun, I.K., Lee, S.C., Lee, S.Y., 2004. Multichannel magnetic stimulation system design considering mutual couplings among the stimulation coils. Biomedical Engineering, IEEE Transactions on 51, 812-817.

Hanakawa, T., Mima, T., Matsumoto, R., Abe, M., Inouchi, M., Urayama, S.-i., Anami, K., Honda, M., Fukuyama, H., 2009. Stimulus–Response Profile during Single-Pulse Transcranial Magnetic Stimulation to the Primary Motor Cortex. Cerebral Cortex 19, 2605-2615.

Hanus, X., Luong, M., Lethimonnier, F., 2005. Electromagnetics Fields and SAR Computations in a Human Head with a Multi-port Driven RF Coil at 11.7 Tesla. Proc. Intl. Soc. Mag. Reson. Med. 13.

Heaviside, O., 2011. Electrical papers. Cambridge University Press.

Heller, L., van Hulsteyn, D.B., 1992. Brain stimulation using electromagnetic sources: theoretical aspects. Biophysical Journal 63, 129-138.

Herwig, U., Kölbel, K., Wunderlich, A.P., Thielscher, A., von Tiesenhausen, C., Spitzer, M., Schönfeldt-Lecuona, C., 2002. Spatial congruence of neuronavigated transcranial magnetic stimulation and functional neuroimaging. Clinical Neurophysiology 113, 462-468.

Hori, H., Moretti, G., Rebora, A., Crovato, F., 1972. The Thickness of Human Scalp: Normal and Bald. Journal of Investigative Dermatology 58, 396-399.

Horvath, J.C., Forte, J.D., Carter, O., 2015. Evidence that transcranial direct current stimulation (tDCS) generates little-to-no reliable neurophysiologic effect beyond MEP amplitude modulation in healthy human subjects: A systematic review. Neuropsychologia 66, 213-236.

Hovey, C., Jalinous, R., 2006. The guide to magnetic stimulation [pdf]. Retrieved from http://www1.icts.uci.edu/neuroimaging/GuidetoMagneticStimulation2008.pdf.

Huang, M.X., Mosher, J.C., Leahy, R.M., 1999. A sensor-weighted overlapping-sphere head model and exhaustive head model comparison for MEG. Physics in Medicine and Biology 44, 423.

Huang, Y.-Z., Edwards, M.J., Rounis, E., Bhatia, K.P., Rothwell, J.C., 2005. Theta Burst Stimulation of the Human Motor Cortex. Neuron 45, 201-206.

Hubel, D.H., Wiesel, T.N., 1962. Receptive fields, binocular interaction and functional architecture in the cat's visual cortex. J Physiol 160, 106-154.

Ilmoniemi, R.J., Ruohonen, J., Karhu, J., 1999. Transcranial magnetic stimulation--a new tool for functional imaging of the brain. Crit Rev Biomed Eng 27, 241-284.

Ishikawa, S., Matsunaga, K., Nakanishi, R., Kawahira, K., Murayama, N., Tsuji, S., Huang, Y.-Z., Rothwell, J.C., 2007. Effect of theta burst stimulation over the human sensorimotor cortex on motor and somatosensory evoked potentials. Clinical Neurophysiology 118, 1033-1043.

John, J.E., John, C.M., Sylvain, B., Richard, M.L., 2001. Rapidly recomputable EEG forward models for realistic head shapes. Physics in Medicine and Biology 46, 1265.

John, P.O.R., Solvason, H.B., Philip, G.J., Shirlene, S., Keith, E.I., Ziad, N., William, M.M., David, A., Paul, B.F., Colleen, L., Mark, A.D., Mark, S.G., Harold, A.S., 2007. Efficacy and Safety of Transcranial Magnetic Stimulation in the Acute Treatment of Major Depression: A Multisite Randomized Controlled Trial. Biological Psychiatry 62, 1208-1216.

Joo, E.Y., Han, S.J., Chung, S.-H., Cho, J.-W., Seo, D.W., Hong, S.B., 2007. Antiepileptic effects of low-frequency repetitive transcranial magnetic stimulation by different stimulation durations and locations. Clinical Neurophysiology 118, 702-708.

Julkunen, P., Säisänen, L., Danner, N., Awiszus, F., Könönen, M., 2012. Within-subject effect of coil-to-cortex distance on cortical electric field threshold and motor evoked potentials in transcranial magnetic stimulation. Journal of Neuroscience Methods 206, 158-164.

Kai-Hsiung, H., Durand, D.M., 2001. A 3-D differential coil design for localized magnetic stimulation. Biomedical Engineering, IEEE Transactions on 48, 1162-1168.

Kammer, T., Beck, S., Thielscher, A., Laubis-Herrmann, U., Topka, H., 2001. Motor thresholds in humans: a transcranial magnetic stimulation study comparing different pulse waveforms, current directions and stimulator types. Clinical Neurophysiology 112, 250-258.

Kang, C., Liu, Y., Li, D., 2011. Analysis of output voltage on a planar insulating core transformer. Nucl. Sci. Tech 22, 15-18.

Katayama, T., Suppa, A., Rothwell, J.C., 2010. Somatosensory evoked potentials and high frequency oscillations are differently modulated by theta burst stimulation over primary somatosensory cortex in humans. Clinical Neurophysiology 121, 2097-2103.

Katayama, Y., Iramina, K., 2009. Equivalent Circuit Simulation of the Induced Artifacts Resulted From Transcranial Magnetic Stimulation on Human Electroencephalography. Magnetics, IEEE Transactions on 45, 4833-4836.

Khedr, E.M., Abdel-Fadeil, M.R., Farghali, A., Qaid, M., 2009. Role of 1 and 3 Hz repetitive transcranial magnetic stimulation on motor function recovery after acute ischaemic stroke. European Journal of Neurology 16, 1323-1330.

Kim, D.H., Georghiou, G.E., Choi, J.W., Yun, W., 2004. Optimization of the Electric Field Distribution induced in the Brain during Transcranial Magnetic Stimulation (TMS) using the Continuum Design Sensitivity Analysis (CDSA). A A 1, 2-2.

Kim, T., Kim, S.-G., 2011. Temporal dynamics and spatial specificity of arterial and venous blood volume changes during visual stimulation: implication for BOLD quantification. J Cereb Blood Flow Metab 31, 1211-1222.

Klarica, M., Radoš, M., Draganić, P., Erceg, G., Orešković, D., Maraković, J., Bulat, M., 2006. Effect of Head Position on Cerebrospinal Fluid Pressure in Cats: Comparison with Artificial Model. Croatian medical journal 47, 233-238.

Kobayashi, M., Pascual-Leone, A., 2003. Transcranial magnetic stimulation in neurology. The Lancet Neurology 2, 145-156.

Kobayashia, M., Ueno, S., Kurokawa, T., 1997. Importance of soft tissue inhomogeneity in magnetic peripheral nerve stimulation. Electroencephalography and Clinical Neurophysiology/Electromyography and Motor Control 105, 406-413.

Komssi, S., Kähkönen, S., Ilmoniemi, R.J., 2004. The effect of stimulus intensity on brain responses evoked by transcranial magnetic stimulation. Human Brain Mapping 21, 154-164.

Komssi, S., Savolainen, P., Heiskala, J., Kähkönen, S., 2007. Excitation threshold of the motor cortex estimated with transcranial magnetic stimulation electroencephalography. Neuroreport 18, 13-16.

Koops, S., Dellen, E.v., Schutte, M.J.L., Nieuwdorp, W., Neggers, S.F.W., Sommer, I.E.C., 2015. Theta Burst Transcranial Magnetic Stimulation for Auditory Verbal Hallucinations: Negative Findings From a Double-Blind-Randomized Trial. Schizophrenia Bulletin.

Koski, L., Mernar, T.J., Dobkin, B.H., 2004. Immediate and Long-Term Changes in Corticomotor Output in Response to Rehabilitation: Correlation with Functional Improvements in Chronic Stroke. Neurorehabilitation and Neural Repair 18, 230-249.

Krasteva, V., Papazov, S., Daskalov, I., 2002. Magnetic stimulation for non-homogeneous biological structures. BioMedical Engineering OnLine 1, 3.

Kupers, R., Fumal, A., de Noordhout, A.M., Gjedde, A., Schoenen, J., Ptito, M., 2006. Transcranial magnetic stimulation of the visual cortex induces somatotopically organized qualia in blind subjects. Proceedings of the National Academy of Sciences 103, 13256-13260.

Lee, C., Im, C.-H., Jung, H.-K., 2007. Analysis and design of whole-head magnetic brain stimulators: a simulation study. International Journal of Control Automation and Systems 5, 337-342.

Leng, L., Zhang, T., Kleinman, L., Zhu, W., 2007. Ordinary least square regression, orthogonal regression, geometric mean regression and their applications in aerosol science. Journal of Physics: Conference Series 78, 012084.

Leong, K.W., 2009. Predicting the response to neural stimulation in rehabilitation of stroke-related motor impairment. McGill University, Montreal.

Levkovitz, Y., Marx, J., Grisaru, N., Segal, M., 1999. Long-Term Effects of Transcranial Magnetic Stimulation on Hippocampal Reactivity to Afferent Stimulation. The Journal of Neuroscience 19, 3198-3203.

Lisanby, S.H., Gutman, D., Luber, B., Schroeder, C., Sackeim, H.A., 2001. Sham TMS: intracerebral measurement of the induced electrical field and the induction of motor-evoked potentials. Biological Psychiatry 49, 460-463.

Luft, A.R., Kaelin-Lang, A., Hauser, T.K., Cohen, L.G., Thakor, N.V., Hanley, D.F., 2001. Transcranial magnetic stimulation in the rat. Exp Brain Res 140, 112-121.

M.S. George, E.M.W., W.A. Williams , A.Callahan, T.A. Ketter ,P. Basser ,M. Hallett ,R.M. Post 1995 Oct 2. Daily repetitive transcranial magnetic stimulation (rTMS) improves mood in depression. Neuroreport 6(14):, 1853-1856.

Maccabee, P.J., Eberle, L., Amassian, V.E., Cracco, R.Q., Rudell, A., 1990. Spatial distribution of the electric field induced in volume by round and figure ‘8’ magnetic coils: relevance to activation of sensory nerve fibers. Electroencephalography and Clinical Neurophysiology 76, 131-141.

Maeda, F., Keenan, J.P., Tormos, J.M., Topka, H., Pascual-Leone, A., 2000a. Interindividual variability of the modulatory effects of repetitive transcranial magnetic stimulation on cortical excitability. Experimental Brain Research 133, 425-430.

Maeda, F., Keenan, J.P., Tormos, J.M., Topka, H., Pascual-Leone, A., 2000b. Modulation of corticospinal excitability by repetitive transcranial magnetic stimulation. Clinical Neurophysiology 111, 800-805.

Magstim, In: Magstim (Ed.), Whitland Dyfed, UK.

Maidment, D.R., 1993. Handbook of hydrology. McGraw-Hill. pp 11.3, New York.

Makris, N., Angelone, L., Tulloch, S., Sorg, S., Kaiser, J., Kennedy, D., Bonmassar, G., 2008. MRI-based anatomical model of the human head for specific absorption rate mapping. Medical & Biological Engineering & Computing 46, 1239-1251.

Martin, D.M., McClintock, S.M., Forster, J., Loo, C.K., 2016. Does Therapeutic Repetitive Transcranial Magnetic Stimulation Cause Cognitive Enhancing Effects in Patients with

Neuropsychiatric Conditions? A Systematic Review and Meta-Analysis of Randomised Controlled Trials. Neuropsychology Review 26, 295-309

Massé-Alarie, H., Flamand, V.H., Moffet, H., Schneider, C., 2013. Peripheral Neurostimulation and Specific Motor Training of Deep Abdominal Muscles Improve Posturomotor Control in Chronic Low Back Pain. The Clinical Journal of Pain Publish Ahead of Print, 10.1097/AJP.1090b1013e318276a318058.

Matsunaga, K., Sağlam, M., Murayama, N., Hayashida, Y., Nakanish, R., 2009. Effect of theta burst stimulation on sensorimotor cortex in humans. Complex Medical Engineering, 2009. CME. ICME International Conference on. IEEE, pp. 1-6.

Maulden, S.A., Gassaway, J., Horn, S.D., Smout, R.J., DeJong, G., 2005. Timing of Initiation of Rehabilitation After Stroke. Archives of Physical Medicine and Rehabilitation 86, 34-40.

Mayo, N.E., Wood-Dauphinee, S., Ahmed, S., Gordon, C., Higgins, J., McEwen, S., Salbach, N., 1999. Disablement following stroke. Disability & Rehabilitation 21, 258-268.

McIntosh, A.M., Semple, D., Tasker, K., Harrison, L.K., Owens, D.G.C., Johnstone, E.C., Ebmeier, K.P., 2004. Transcranial magnetic stimulation for auditory hallucinations in schizophrenia. Psychiatry Research 127, 9-17.

Merton, P., Morton, H., 1980. Stimulation of the cerebral cortex in the intact human subject.

Mishra, B.R., Sarkar, S., Praharaj, S.K., Mehta, V.S., Diwedi, S., Nizamie, S.H., 2011. Repetitive transcranial magnetic stimulation in psychiatry. Annals of Indian Academy of Neurology 14, 245-251.

Miyawaki, Y., Shinozaki, T., Okada, M., 2012. Spike suppression in a local cortical circuit induced by transcranial magnetic stimulation. Journal of Computational Neuroscience 33, 405-419.

Moliadze, V., Giannikopoulos, D., Eysel, U.T., Funke, K., 2005. Paired-pulse transcranial magnetic stimulation protocol applied to visual cortex of anaesthetized cat: effects on visually evoked single-unit activity. The Journal of Physiology 566, 955-965.

Moliadze, V., Zhao, Y., Eysel, U., Funke, K., 2003. Effect of transcranial magnetic stimulation on single-unit activity in the cat primary visual cortex. The Journal of Physiology 553, 665-679.

Mosimann, U.P., Marre, S.C., Werlen, S., Schmitt, W., Hess, C.W., Fisch, H.U., Schlaepfer, T.E., 2002. Antidepressant Effects of Repetitive Transcranial Magnetic Stimulation in the Elderly: Correlation Between Effect Size and Coil-Cortex Distance. Arch Gen Psychiatry 59, 560-561.

Nakayama H, J.H., Raaschou HO, Olsen TS., 1994 Apr. Recovery of upper extremity function in stroke patients: the Copenhagen Stroke Study. Arch Phys Med Rehabil 75(4):, 394-398.

Noh, N.A., Fuggetta, G., Manganotti, P., Fiaschi, A., 2012. Long Lasting Modulation of Cortical Oscillations after Continuous Theta Burst Transcranial Magnetic Stimulation. PloS one 7, e35080.

Oersted, H.C., 1820. Experiments on the effect of a current of electricity on the magnetic needles. Annals of Philosophy 16, 273-277.

Opitz, A., Legon, W., Mueller, J., Barbour, A., Paulus, W., Tyler, W.J., 2015. Is sham cTBS real cTBS? The effect on EEG dynamics. Frontiers in Human Neuroscience 8.

Opitz, A., Windhoff, M., Heidemann, R.M., Turner, R., Thielscher, A., 2011. How the brain tissue shapes the electric field induced by transcranial magnetic stimulation. NeuroImage 58, 849-859.

Pal, G., 2001. Textbook of practical physiology. Orient Blackswan.

Pascual-Leone, A., 2002. Handbook of transcranial magnetic stimulation. Arnold ;

Oxford University Press [distributor], London

New York, NY.

Pascual-Leone, A., Davey, N.J., Rothwell, J., Wassermann, E.M., Puri, B.K., 2002. Handbook of Transcranial Magnetic Stimulation. Arnold.

Pascual-Leone, A., Rubio, B., Pallardó, F., Catalá, M.D., 1996. Rapid-rate transcranial magnetic stimulation of left dorsolateral prefrontal cortex in drug-resistant depression. The Lancet 348, 233-237.

Pascual-Leone, A., Tormos, J.M., Keenan, J., Tarazona, F., Canete, C., Catala, M.D., 1998a. Study and modulation of human cortical excitability with transcranial magnetic stimulation. J Clin Neurophysiol 15, 333-343.

Pascual-Leone, A., Tormos, J.M., Keenan, J., Tarazona, F., Cañete, C., Catalá, M.D., 1998b. Study and modulation of human cortical excitability with transcranial magnetic stimulation. Journal of Clinical Neurophysiology 15, 333-343.

Pascual-Leone, A., Wagner, T., 2007. A brief summary of the history of noninvasive brain stimulation. Annu Rev Biomed Eng 9, 527-565.

Pasley, B.N., Allen, E.A., Freeman, R.D., 2009. State-dependent variability of neuronal responses to transcranial magnetic stimulation of the visual cortex. Neuron 62, 291-303.

Peinemann, A., Reimer, B., Löer, C., Quartarone, A., Münchau, A., Conrad, B., Siebner, H.R., 2004. Long-lasting increase in corticospinal excitability after 1800 pulses of subthreshold 5 Hz repetitive TMS to the primary motor cortex. Clinical Neurophysiology 115, 1519-1526.

Prikryl, R., Kucerova, H., 2005. Occurrence of epileptic paroxysm during repetitive transcranial magnetic stimulation treatment. Journal of Psychopharmacology 19, NP.

Prikryl, R., Kucerova, H.P., 2013. Can Repetitive Transcranial Magnetic Stimulation Be Considered Effective Treatment Option for Negative Symptoms of Schizophrenia? The Journal of ECT 29, 67-74 10.1097/YCT.1090b1013e318270295f.

Purves, D., Augustine, G.J., Fitzpatrick, D., Katz, L.C., LaMantia, A.-S., McNamara, J.O., Williams, S.M., 2001. Neuroscience. Sunderland, MA: Sinauer Associates 3.

Quartarone, A., Bagnato, S., Rizzo, V., Morgante, F., Sant'Angelo, A., Battaglia, F., Messina, C., Siebner, H.R., Girlanda, P., 2005. Distinct changes in cortical and spinal excitability following high-frequency repetitive TMS to the human motor cortex. Experimental Brain Research 161, 114-124.

Ragert, P., Becker, M., Tegenthoff, M., Pleger, B., Dinse, H.R., 2004. Sustained increase of somatosensory cortex excitability by 5 Hz repetitive transcranial magnetic stimulation studied by paired median nerve stimulation in humans. Neuroscience Letters 356, 91-94.

Raghanti, M.A., Spocter, M.A., Butti, C., Hof, P.R., Sherwood, C.C., 2010. A Comparative Perspective on Minicolumns and Inhibitory GABAergic Interneurons in the Neocortex. Frontiers in Neuroanatomy 4, 3.

Rajji, T.K., Rogasch, N.C., Daskalakis, Z.J., Fitzgerald, P.B., 2013. Neuroplasticity-Based Brain Stimulation Interventions in the Study and Treatment of Schizophrenia: A Review. Les interventions de stimulation cérébrale basée sur la neuroplasticité dans l'étude et le traitement de la schizophrénie: une revue. 58, 93-98.

Ringach, D.L., Hawken, M.J., Shapley, R., 1997. Dynamics of orientation tuning in macaque primary visual cortex. Nature 387, 281-284.

Ringach, D.L., Shapley, R.M., Hawken, M.J., 2002. Orientation Selectivity in Macaque V1: Diversity and Laminar Dependence. The Journal of Neuroscience 22, 5639-5651.

Rofes, L., Vilardell, N., Clavé, P., 2013. Post-stroke dysphagia: progress at last. Neurogastroenterology & Motility, n/a-n/a.

Rossi, S., Hallett, M., Rossini, P.M., Pascual-Leone, A., 2009a. Safety, ethical considerations, and application guidelines for the use of transcranial magnetic stimulation in clinical practice and research. Clin Neurophysiol 120, 2008-2039.

Rossi, S., Hallett, M., Rossini, P.M., Pascual-Leone, A., 2009b. Safety, ethical considerations, and application guidelines for the use of transcranial magnetic stimulation in clinical practice and research. Clinical Neurophysiology 120, 2008-2039.

Rossini, P.M., Rossini, L., Ferreri, F., 2010. Brain-Behavior Relations: Transcranial Magnetic Stimulation: A Review. Engineering in Medicine and Biology Magazine, IEEE 29, 84-96.

Rotenberg, A., Muller, P.A., Vahabzadeh-Hagh, A.M., Navarro, X., Lopez-Vales, R., Pascual-Leone, A., Jensen, F., 2010. Lateralization of forelimb motor evoked potentials by transcranial magnetic stimulation in rats. Clin Neurophysiol 121, 104-108.

Roth, B.J., Cohen, L.G., Hallett, M., 1994a. The electric field induced during magnetic stimulation. Electroencephalography and Clinical Neurophysiology-Supplements only, 268-278.

Roth, B.J., Maccabee, P.J., Eberle, L.P., Amassian, V.E., Hallett, M., Cadwell, J., Anselmi, G.D., Tatarian, G.T., 1994b. In vitro evaluation of a 4-leaf coil design for magnetic stimulation of peripheral nerve. Electroencephalography and Clinical Neurophysiology/Evoked Potentials Section 93, 68-74.

Roth, B.J., Saypol, J.M., Hallett, M., Cohen, L.G., 1991. A theoretical calculation of the electric field induced in the cortex during magnetic stimulation. Electroencephalography and Clinical Neurophysiology/Evoked Potentials Section 81, 47-56.

Rothwell, J.C., 1993. Evoked-potentials, magnetic stimulation studies, and event-related potentials. Current opinion in neurology [1350-7540] 6, 715 - 723.

Rothwell, J.C., Hallett, M., Berardelli, A., Eisen, A., Rossini, P.M., Paulus, W., 1999. Magnetic stimulation: motor evoked potentials. The International Federation of Clinical Neurophysiology. Electroencephalography and clinical neurophysiology. Supplement 52, 97.

Rudiak, D., Marg, E., 1994. Finding the depth of magnetic brain stimulation: a re-evaluation. Electroencephalography and Clinical Neurophysiology/Evoked Potentials Section 93, 358-371.

Ruohonen, J., 1998. Transcranial magnetic stimulation: modelling and new techniques [Dissertation]. Helsinki university of technology, laboratory of biomedical engineering (BioMag), pp. 16.

Ruohonen, J., Ravazzani, P., Grandori, F., Ilmoniemi, R.J., 1999. Theory of multichannel magnetic stimulation: toward functional neuromuscular rehabilitation. Biomedical Engineering, IEEE Transactions on 46, 646-651.

Salinas, F.S., Lancaster, J.L., Fox, P.T., 2007. Detailed 3D models of the induced electric field of transcranial magnetic stimulation coils. Physics in Medicine and Biology, 2879.

Salinas, F.S., Lancaster, J.L., Fox, P.T., 2009. 3D modeling of the total electric field induced by transcranial magnetic stimulation using the boundary element method. Physics in Medicine and Biology 54, 3631.

Sayers, B.M., Beagley, H., Henshall, W., 1974. The mechanism of auditory evoked EEG responses. Nature.

Schabrun, S.M., Jones, E., Kloster, J., Hodges, P.W., 2013. Temporal association between changes in primary sensory cortex and corticomotor output during muscle pain. Neuroscience 235, 159-164.

Schambra, H.M., Sawaki, L., Cohen, L.G., 2003. Modulation of excitability of human motor cortex (M1) by 1 Hz transcranial magnetic stimulation of the contralateral M1. Clinical Neurophysiology 114, 130-133.

Schimpf, P., Haueisen, J., Ramon, C., Nowak, H., 1998. Realistic computer modelling of electric and magnetic fields of human head and torso. Parallel Computing 24, 1433-1460.

Schmitt, R., 2002. Electromagnetics explained: a handbook for wireless/RF, EMC, and high-speed electronics. Newnes.

Schürmann, M., Nikouline, V.V., Soljanlahti, S., Ollikainen, M., Başar, E., Ilmoniemi, R.J., 2001. EEG responses to combined somatosensory and transcranial magnetic stimulation. Clinical Neurophysiology 112, 19-24.

Seyal, M., Ro, T., Rafal, R., 1995. Increased sensitivity to ipsilateral cutaneous stimuli following transcranial magnetic stimulation of the parietal lobe. Annals of neurology 38, 264-267.

Shang, Y., Wang, X., Shang, X., Zhang, H., Liu, Z., Yin, T., Zhang, T., 2016. Repetitive transcranial magnetic stimulation effectively facilitates spatial cognition and synaptic plasticity associated with increasing the levels of BDNF and synaptic proteins in Wistar rats. Neurobiology of Learning and Memory 134, Part B, 369-378

Shibuya, K., Park, S.B., Geevasinga, N., Huynh, W., Simon, N.G., Menon, P., Howells, J., Vucic, S., Kiernan, M.C., 2016. Threshold tracking transcranial magnetic stimulation: Effects of age and gender on motor cortical function. Clinical Neurophysiology 127, 2355-2361

Shmuel, A., Grinvald, A., 1996. Functional Organization for Direction of Motion and Its Relationship to Orientation Maps in Cat Area 18. The Journal of Neuroscience 16, 6945-6964.

Shmuel, A., Grinvald, A., 2000. Coexistence of linear zones and pinwheels within orientation maps in cat visual cortex. Proceedings of the National Academy of Sciences of the United States of America 97, 5568-5573.

Shoham, D., Grinvald, A., 2001. The cortical representation of the hand in macaque and human area SI: high resolution optical imaging. The Journal of Neuroscience 21, 6820-6835.

Siebner, H.R., 2010. Can we enhance training-induced plasticity by modulating inhibitory cortical circuits with transcranial stimulation? (Commentary on Mix et al.). European Journal of Neuroscience 32, 1573-1574.

Siebner, H.R., Tormos, J.M., Baumann, A.O.C.-., Auer, C., Catala, M.D., Conrad, B., Pascual-Leone, A., 1999. Low-frequency repetitive transcranial magnetic stimulation of the motor cortex in writer's cramp. Neurology 52, 529.

Stagg, C.J., Wylezinska, M., Matthews, P.M., Johansen-Berg, H., Jezzard, P., Rothwell, J.C., Bestmann, S., 2009. Neurochemical Effects of Theta Burst Stimulation as Assessed by Magnetic Resonance Spectroscopy. Journal of Neurophysiology 101, 2872-2877.

Stogryn, A., 1971. Equations for Calculating the Dielectric Constant of Saline Water (Correspondence). Microwave Theory and Techniques, IEEE Transactions on 19, 733-736.

Suppa, A., Huang, Y.Z., Funke, K., Ridding, M.C., Cheeran, B., Di Lazzaro, V., Ziemann, U., Rothwell, J.C., 2016. Ten Years of Theta Burst Stimulation in Humans: Established Knowledge, Unknowns and Prospects. Brain Stimulation 9, 323-335.

Swindale, N.V., 1998. Orientation tuning curves: empirical description and estimation of parameters. Biological Cybernetics 78, 45-56.

Swindale, N.V., Grinvald, A., Shmuel, A., 2003. The Spatial Pattern of Response Magnitude and Selectivity for Orientation and Direction in Cat Visual Cortex. Cerebral Cortex 13, 225-238.

Takeuchi, N., Chuma, T., Matsuo, Y., Watanabe, I., Ikoma, K., 2005. Repetitive Transcranial Magnetic Stimulation of Contralesional Primary Motor Cortex Improves Hand Function After Stroke. Stroke 36, 2681-2686.

Tay, G., Chilbert, M., Battocletti, J., Sances, A., Jr., Swiontek, T., Kurakami, C., 1989. Measurement of magnetically induced current density in saline in vivo. Engineering in Medicine and Biology Society, 1989. Images of the Twenty-First Century., Proceedings of the Annual International Conference of the IEEE Engineering in, pp. 1167-1168 vol.1164.

Tatti, E., Rossi, S., Innocenti, I., Rossi, A., Santarnecchi, E., 2016. Non-invasive brain stimulation of the aging brain: State of the art and future perspectives. Ageing Research Reviews 29, 66-89.

Terao, Y., Ugawa, Y., Sakai, K., Miyauchi, S., Fukuda, H., Sasaki, Y., Takino, R., Hanajima, R., Furubayashi, T., Pütz, B., Kanazawa, I., 1998. Localizing the site of magnetic brain stimulation by functional MRI. Experimental Brain Research 121, 145-152.

Tergau, F., Naumann, U., Paulus, W., Steinhoff, B.J., 1999. Low-frequency repetitive transcranial magnetic stimulation improves intractable epilepsy. The Lancet 353, 2209.

Thielscher, A., Kammer, T., 2002. Linking Physics with Physiology in TMS: A Sphere Field Model to Determine the Cortical Stimulation Site in TMS. NeuroImage 17, 1117-1130.

Thielscher, A., Opitz, A., Windhoff, M., 2011. Impact of the gyral geometry on the electric field induced by transcranial magnetic stimulation. NeuroImage 54, 234-243.

Todd, G., Flavel, S.C., Ridding, M.C., 2006. Low-intensity repetitive transcranial magnetic stimulation decreases motor cortical excitability in humans.

Todd, G., Rogasch, N.C., Flavel, S.C., Ridding, M.C., 2009. Voluntary movement and repetitive transcranial magnetic stimulation over human motor cortex. Journal of Applied Physiology 106, 1593-1603.

Tofts, P.S., 1990. The distribution of induced currents in magnetic stimulation of the nervous system. Physics in Medicine and Biology 35, 1119.

Toga, A.W., Mazziotta, J.C., 2002. Brain mapping: The methods , chap 11. Academic Press.

Valero-Cabre, A., Payne, B.R., Pascual-Leone, A., 2007. Opposite impact on 14C-2-deoxyglucose brain metabolism following patterns of high and low frequency repetitive transcranial magnetic stimulation in the posterior parietal cortex. Exp Brain Res 176, 603-615.

Valero-Cabré, A., Payne, B.R., Rushmore, J., Lomber, S.G., Pascual-Leone, A., 2005. Impact of repetitive transcranial magnetic stimulation of the parietal cortex on metabolic brain activity: a 14C-2DG tracing study in the cat. Experimental brain research. Experimentelle Hirnforschung. Expérimentation cérébrale 163, 1-12.

Vatta, F., Meneghini, F., Esposito, F., Mininel, S., Salle, F.D., 2010. Realistic and spherical head modeling for EEG forward problem solution: a comparative cortex-based analysis. Computational intelligence and neuroscience 2010, 13.

Veniero, D., Bortoletto, M., Miniussi, C., 2013. Cortical modulation of short-latency TMS-evoked potentials. Frontiers in Human Neuroscience 6.

Vernet, M., Bashir, S., Yoo, W.-K., Perez, J.M., Najib, U., Pascual-Leone, A., 2013. Insights on the neural basis of motor plasticity induced by theta burst stimulation from TMS–EEG. European Journal of Neuroscience 37, 598-606.

Virjoghe, E.O., Enescu, D., Caciula, I., 2008. Numerical computation of the capacitance for the spherical capacitor. Scientific Bulletin of the Electrical Engineering Faculty, Valahia University of Targoviste, Romania.

Vlachos, A., Müller-Dahlhaus, F., Rosskopp, J., Lenz, M., Ziemann, U., Deller, T., 2012. Repetitive Magnetic Stimulation Induces Functional and Structural Plasticity of Excitatory Postsynapses in Mouse Organotypic Hippocampal Slice Cultures. The Journal of Neuroscience 32, 17514-17523.

Volz, L.J., Benali, A., Mix, A., Neubacher, U., Funke, K., 2013. Dose-dependence of changes in cortical protein expression induced with repeated transcranial magnetic theta-burst stimulation in the rat. Brain Stimulation.

von Ellenrieder, N., Beltrachini, L., Muravchik, C.H., 2012. Electrode and brain modeling in stereo-EEG. Clinical Neurophysiology 123, 1745-1754.

Wagner, T., Eden, U., Fregni, F., Valero-Cabre, A., Ramos-Estebanez, C., Pronio-Stelluto, V., Grodzinsky, A., Zahn, M., Pascual-Leone, A., 2008. Transcranial magnetic stimulation and brain atrophy: a computer-based human brain model study. Experimental Brain Research 186, 539-550.

Wagner, T., Fregni, F., Eden, U., Ramos-Estebanez, C., Grodzinsky, A., Zahn, M., Pascual-Leone, A., 2006. Transcranial magnetic stimulation and stroke: A computer-based human model study. NeuroImage 30, 857-870.

Wagner, T., Gangitano, M., Romero, R., Théoret, H., Kobayashi, M., Anschel, D., Ives, J., Cuffin, N., Schomer, D., Pascual-Leone, A., 2004a. Intracranial measurement of current densities induced by transcranial magnetic stimulation in the human brain. Neuroscience Letters 354, 91-94.

Wagner, T., Valero-Cabre, A., Pascual-Leone, A., 2007. Noninvasive Human Brain Stimulation. Annual Review of Biomedical Engineering 9, 527-565.

Wagner, T., Zahn, M., Grodzinsky, A.J., Pascual-Leone, A., 2004b. Three-dimensional head model simulation of transcranial magnetic stimulation. Biomedical Engineering, IEEE Transactions on 51, 1586-1598.

Wang, H., Wang, X., Scheich, H., 1996. LTD and LTP induced by transcranial magnetic stimulation in auditory cortex. Neuroreport 7, 521-525.

Wang, X., Chen, Y., Guo, M., Wang, M., 2005. Design of multi-channel brain magnetic stimulator and ANSYS simulation. IJBEM 7, 259-262.

Weissman, J.D., Epstein, C.M., Davey, K.R., 1992. Magnetic brain stimulation and brain size: relevance to animal studies. Electroencephalography and Clinical Neurophysiology/Evoked Potentials Section 85, 215-219.

Westin, G.G., Bassi, B.D., Lisanby, S.H., Luber, B., 2014. Determination of motor threshold using visual observation overestimates transcranial magnetic stimulation dosage: Safety implications. Clinical Neurophysiology 125, 142-147.

Weyh, T., Wendicke, K., Mentschel, C., Zantow, H., Siebner, H.R., 2005. Marked differences in the thermal characteristics of figure-of-eight shaped coils used for repetitive transcranial magnetic stimulation. Clinical Neurophysiology 116, 1477-1486.

Windhoff, M., Opitz, A., Thielscher, A., 2011. Electric field calculations in brain stimulation based on finite elements: An optimized processing pipeline for the generation and usage of accurate individual head models. Human Brain Mapping, n/a-n/a.

Won Hee, L., Lisanby, S.H., Laine, A.F., Peterchev, A.V., 2015. Electric Field Model of Transcranial Electric Stimulation in Nonhuman Primates: Correspondence to Individual Motor Threshold. Biomedical Engineering, IEEE Transactions on 62, 2095-2105.

Wu, T., Sommer, M., Tergau, F., Paulus, W., 2000. Lasting influence of repetitive transcranial magnetic stimulation on intracortical excitability in human subjects. Neuroscience Letters 287, 37-40.

Yadav, N., Ludlam, D., Ciuffreda, K., 2012. Effect of different stimulus configurations on the visual evoked potential (VEP). Documenta Ophthalmologica 124, 177-196.

Yunokuchi, K., Cohen, D., 1991. Developing a more focal magnetic stimulator. Part II: Fabricating coils and measuring induced current distributions. J Clin Neurophysiol 8, 112-120.

Zangaladze, A., Epstein, C.M., Grafton, S.T., Sathian, K., 1999. Involvement of visual cortex in tactile discrimination of orientation. Nature 401, 587-590.

Zapallow, C., Asmussen, M., Bolton, D.A., Lee, K.G., Jacobs, M., Nelson, A., 2012. Theta burst repetitive transcranial magnetic stimulation attenuates somatosensory evoked potentials from the lower limb. BMC Neuroscience 13, 133.

Zhang, Y., Li, E., Chada, A., Fan, J., 2009. Calculation of the via-plate capacitance of a via with pad using finite difference method for signal/power integrity analysis. Int. Electromagn. Compat. Symp, pp. 20-24.